Markus Hupp

Simulating Star Formation and Turbulence in Models of Isolated Disk Galaxies

A FEARLESS Project

Fluid m**E**chanics with **A**daptively **R**efined **L**arge **E**ddy **S**imulation**S**

NGC 7331

Doctoral Dissertation

Julius-Maximilians-
UNIVERSITÄT
WÜRZBURG

Simulating Star Formation and Turbulence in Models of Isolated Disk Galaxies

A FEARLESS Project

Dissertation zur Erlangung des
naturwissenschaftlichen Doktorgrades
der Julius-Maximilians-Universität Würzburg

Markus Hupp

aus Würzburg

Institut für Theoretische Physik und Astrophysik
Fakultät für Physik und Astronomie
Universität Würzburg

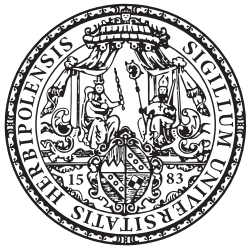

Würzburg
Dezember 2008

Eingereicht am:

bei der
Fakultät für Physik und Astronomie

Gutachter und Prüfer im Promotionsverfahren:

1. Gutachter Prof. Dr. Jens C. Niemeyer
2. Gutachter Prof. Dr. Karl Mannheim

der Dissertation

1. Prüfer Prof. Dr. Jens C. Niemeyer
2. Prüfer Prof. Dr. Karl Mannheim
3. Prüfer Prof. Dr. Thomas Trefzger

im Promotionskolloquium

Tag des Promotionskolloquiums:

Doktururkunde ausgehändigt am:

Simulating Star Formation and Turbulence in Models of Isolated Disk Galaxies

A FEARLESS Project

Fluid m**E**chanics with **A**daptively **R**efined **L**arge **E**ddy **S**imulation**S**

Gutachter / Referees:

Prof. Dr. Jens C. Niemeyer – Prof. Dr. Karl Mannheim

Abstract. We model Milky Way like isolated disk galaxies in high resolution three-dimensional hydrodynamical simulations with the adaptive mesh refinement code Enzo. The model galaxies include a dark matter halo and a disk of gas and stars. We use a simple implementation of sink particles to measure and follow collapsing gas, and simulate star formation as well as stellar feedback in some cases. We investigate two largely different realizations of star formation. Firstly, we follow the classical approach to transform cold, dense gas into stars with an fixed efficiency. These kind of simulations are known to suffer from an overestimation of star formation and we observe this behavior as well. Secondly, we use our newly developed FEARLESS approach to combine hydrodynamical simulations with a semi-analytic modeling of unresolved turbulence and use this technique to dynamically determine the star formation rate. The subgrid-scale turbulence regulated star formation simulations point towards largely smaller star formation efficiencies and henceforth more realistic overall star formation rates. More work is necessary to extend this method to account for the observed highly supersonic turbulence in molecular clouds and ultimately use the turbulence regulated algorithm to simulate observed star formation relations.

Key words. astrophysics - hydrodynamics - turbulence - star formation - simulation:subgrid-scale model - ISM:turbulence - galaxies:formation:evolution:general

---

Abriss. In dieser Arbeit beschäftigen wir uns mit der Modellierung und Durchführung von hoch aufgelösten dreidimensionalen Simulationen von isolierten Scheibengalaxien, vergleichbar unserer Milchstraße. Wir verwenden dazu den Simulations-Code Enzo, der die Methode der adaptiven Gitterverfeinerung benutzt um die örtliche und zeitliche Auflösung der Simulationen anzupassen. Unsere Galaxienmodelle beinhalten einen Dunkle Materie Halo sowie eine galaktische Scheibe aus Gas und Sternen. Regionen besonders hoher Gasdichte werden durch Teilchen ersetzt, die fortan die Eigenschaften des Gases beziehungsweise der darin entstehenden Sterne beschreiben. Wir untersuchen zwei grundlegend verschiedene Darstellungen von Sternentstehung. Die erste Methode beschreibt die Umwandlung dichten Gases einer Molekülwolke in Sterne mit konstanter Effektivität und führt wie in früheren Simulationen zu einer Überschätzung der Sternentstehungsrate. Die zweite Methode nutzt das von unserer Gruppe neu entwickelte FEARLESS Konzept, um hydrodynamische Simulationen mit analytischen-empirischen Modellen zu verbinden und bessere Aussagen über die in einer Simulation nicht explizit aufgelösten Bereiche treffen zu können. Besonderes Augenmerk gilt in dieser Arbeit dabei der in Molekülwolken beobachteten Turbulenz. Durch die Einbeziehung dieser nicht aufgelösten Effekte sind wir in der Lage eine realistischere Aussage über die Sternentstehungsrate zu treffen. Eine zukünftige Weiterentwicklung dieser von uns entwickelten und umgesetzten Technik kann in Zukunft dafür verwendet werden, die Qualität des durch Turbulenz regulierten Sternentstehungsmodells noch weiter zu steigern.

Schlagwörter. Astrophysik - Hydrodynamik - Turbulenz - Sternentstehung - Simulation:Subgrid-Skalen Modell - ISM:Turbulenz - Galaxien:Entstehung:Entwicklung:Allgemein

---

Würzburg, December 2008

Simulating Star Formation and Turbulence in Models of Isolated Disk Galaxies

---

This thesis is based upon the following publications:

▶ *FEARLESS – A new modelling approach for turbulent astrophysical flows*

W. Schmidt, A. Maier, M. Hupp, L. Iapichino and J. C. Niemeyer; Astronomische Nachrichten **328**: 663-+, 2007;

▶ *FEARLESS* – Subgrid-Scale Turbulence modeling and Applications to Star Formation*

M. Hupp, A. Maier, J. C. Niemeyer, W. Schmidt, L. Iapichino, J. Adamek and C. Federrath; Astronomische Nachrichten **328**: 664-+, 2007;

▶ *Numerical simulations of compressively driven interstellar turbulence: I. Isothermal gas*

W. Schmidt, C. Federrath, M. Hupp, S. Kern, J. C. Niemeyer; Astronomy and Astrophysics, *accepted by A&A, 2008*;

▶ *Simulating Star Formation and Turbulence in Models of Isolated Disk Galaxies*

M. Hupp, W. Schmidt, A. Maier, J. C. Niemeyer; *in preparation*;

The work contained in this thesis is part of the research done within the DFG-funded International Research Training Group (GRK 1147/1) entitled as *Theoretical Astrophysics and Particle Physics*. This graduate school is a joint project of the Department of Physics (Theoretical Astrophysics and Theoretical High Energy Physics) and the Department of Mathematics of the Julius-Maximilians-Universität Würzburg; it is funded by the Deutsche Forschungsgemeinschaft (DFG) and so was the author.

PhD thesis
Author: Markus Hupp
E-mail address: `hupp@astro.uni-wuerzburg.de`
Typeface: Computer Modern Roman 8pt, 9pt, 10pt, 11pt, 12pt
Distribution: LaTeX 2ε using AMS-LaTeX and hyperref

Compiled on February 26, 2009 as a native `dvi` document

Contents

Notation

This thesis makes use of the common astrophysical labeling of quantities and several of our own definitions of parameters and variables. Below is a complete list of all used quantities, their meaning and their standard values.

General Notation:

pc	Parsec	$3.0856 \cdot 10^{18}\,\mathrm{cm}$
kpc	Kiloparsec	$3.0856 \cdot 10^{21}\,\mathrm{cm}$
Mpc	Megaparsec	$3.0856 \cdot 10^{24}\,\mathrm{cm}$
yr	Year	$3.1536 \cdot 10^{7}\,\mathrm{s}$
Myr	Megayear	$3.1536 \cdot 10^{13}\,\mathrm{s}$
Gyr	Gigayear	$3.1536 \cdot 10^{16}\,\mathrm{s}$
$\mathrm{M}_\odot$	Solar Mass	$1.989 \cdot 10^{33}\,\mathrm{g}$
m_h	Proton Mass	$1.67 \cdot 10^{-24}\,\mathrm{g}$
k_b	Boltzmann Constant	$1.38 \cdot 10^{-16}\,\mathrm{g\,cm^2/s^2\,K}$
G	Gravitational Constant	$6.67 \cdot 10^{-8}\,\mathrm{cm^3/g\,s^2}$
μ	Mean Molecular Weight	1.2
γ	Heat Capacity Ratio	1.6667
π	Pi	3.14159

Scaling Parameters:

$\mathbb{R}$	scaling factor Density	$1.0 \cdot 10^{-25}\,\mathrm{g/cm^3}$
$\mathbb{L}$	scaling factor Length	1.0 Mpc
$\mathbb{G}_0$	scaling factor Gravitational Constant	$6.67 \cdot 10^{-8}\,\mathrm{cm^3/g\,s^2}$
$\mathbb{G}$	scaling factor Acceleration	
$\mathbb{T}$	scaling factor Time	
$\mathbb{M}$	scaling factor Mass	
$\mathbb{E}$	scaling factor Energy	
$\mathbb{V}$	scaling factor Velocity	
$\mathbb{C}$	scaling factor Cooling	
$\mathbb{H}$	scaling factor Heating	

Standard values are used whenever not indicated otherwise.

Abbreviations:

AMR	Adaptive Mesh Refinement
CDM	Cold Dark Matter
GMC	Giant Molecular Cloud
IMF	Initial Mass Function
ISM	Interstellar Medium
KS	Kennicutt-Schmidt
MC	Molecular Cloud
MHD	Magnetohydrodynamical
NFW	Navarro-Frenk-White
KM05	Krumholz and McKee [2005]
PDE	Partial Differential Equations
PDF	Probability Distribution Function
PPM	Piecewise Parabolic Method
SF	Star Formation
SFR	Star Formation Rate
SGS	Subgrid-Scale
SPH	Smoothed Particle Hydrodynamics
TB06	Tasker and Bryan [2006]
ULIRG	Ultraluminous Infrared Galaxy
YSO	Young Stellar Objects

to All Mankind

Preface

How we conceive the world around us is mostly determined by our current situation. On a bright sunny day at the beach we listen to the wind and waves, in the woods we hear the leaves rustling and during a clear night we watch the stars. Luckily, most often we can just enjoy the beauty within, although pondering about who put the stars on the canopy intrigues the mind.
In public talks, television reports, books and via literally all media we are frequently made aware of how little we know about the very things around us.
Starting at the smallest scales, there is the question of how the mass of the most elemental building blocks of matter is generated, as the common sense of summing up pieces to get an entity fails. How do neurons in the human brain work and what makes up the conscious mind? How about sociological interactions and what are the prospectives of human evolution? What do we know about our planet? Are there more or even less hidden resources than mankind has assumed during the last decades of industrial evolution and how about the deep sea? What species are waiting for us in the depths hidden by darkness and pressure or the remoteness of their habitats? What is the inner structure of our planet and how about its core, which seems to be so important for the blue planet's magnetic field, shielding all its life from solar and cosmic radiation? Are there other planets like the one we claim to know at least to some extent and is the moon a scattered fraction of our own home? How did the solar system come to existence and how can we conceive the extent of the Milky Way? What does it mean that space-time expands and how did the Big Bang create time? After all, what is the Universe made of?
To most of these questions science has given at least vague ideas, more often conceptual frameworks accompanied by diverse theories, and sometimes even formal concepts. Some questions are rather attributed to metaphysics, others are currently under heavy attack by scientists and experiments all over the world.

Figure (0.1) summarizes what has emerged as answer to the last question about the composition of the Universe. This picture is part of what astronomers call the standard model of cosmology and again reflects how little we really know about the Universe we live in.
Roughly 70% of the Universe is made of some kind of mysterious dark energy that permeates all of space. One of the few conceptual ideas we can attribute seems to be the fact that this form of energy does not show any tendency to clump together. Of course, theoretically, dark energy can explain recent observations that the Universe appears to be expanding at an accelerating rate and that is only one reason for its triumphal success in the standard model. Theorists have already proposed different forms for dark energy, for example, a realization of Einstein's famous cosmological constant or dynamic scalar field quantities. Nevertheless, its existence has yet to be prooven and its effects need further investigation.
Dark energy aside, approximately another 25% of the Universe seems to consits of what is called dark matter. The terminology of *dark* matter stems from the fact that this matter only interacts via gravity and not via electromagnetic interactions. The vast majority of mass in the observable universe is made of dark matter and it plays the most important role during the formation of

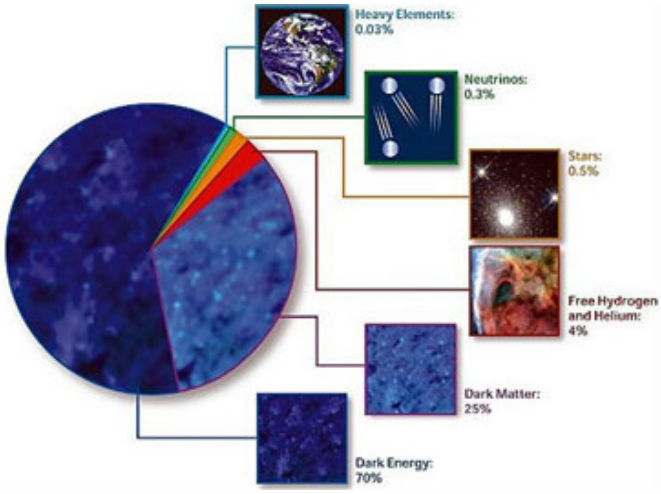

FIGURE 0.1. This NASA chart displays what most astronomers believe is the energy distribution in the Universe.

structure in the Universe. Again, theory gives candidates of exotic particles which can be the constituents of dark matter and experiments scanning for cosmic radiation as well as collider experiments are searching for them – yet waiting.
Leaving the dark side of the Universe behind, we are left with approximately 5% of what we call baryonic matter – that is essentially what we are familiar with as tangible material. Following the standard model of high energy physics, we talk about fermions such as leptons (electrons, muons, taus, neutrinos) and quarks (up, down, charm, strange, top, bottom) as well as bosons (gluon, photon, vectorbosons) and mesons. These fundamental building blocks make up the atoms which themselves can build molecules and more complex chemical compounds.
Free hydrogen and helium gas are the most important constituents of baryonic matter in the astrophysical context and make up roughly 4% of the mass-energy in the Universe. This free elementary gas is the natal material out of which stars form, which contribute approximately 0.5% to the energy content of the Universe, themselves. After all, stars generate neutrinos and fuse simple chemical species to heavy elements which are the chemical basis of life.

So much about what we believe to know or not to know about the content of our universe. While there is tremendous knowledge to gain and yet inconceivable conceptions to make about 95% of the Universe, the following thesis will try to shed some more light on the remaining 5% and look into the details of how stars are coming to existence out of free gas consisting of the simplest chemical elements.

Non est ad astra mollis e terris via

Seneca, Hercules furens
(Der wildgewordene Herkules)

Part I

Nursery of Stars

CHAPTER 1

Motivation

1.1. Introduction

Free hydrogen and helium gas and the stars that form therein are the basis of our observational knowledge of the Universe. Essentially, stars are the fundamental building blocks of the Universe and by transforming gas into stars the star formation process shapes the structure of galaxies and governs their global evolution. The most simplified picture of star formation is that free hydrogen gas falls into a dark matter potential, which grew itself from inhomogeneities produced during inflation, and starts to accumulate there. Eventually, the gas becomes dense enough to start cooling efficiently and fragmentation begins. At the end of this fragmentation process there are patches of gas which are highly unstable and finally become dense enough to ignite the fusion process – a star is formed.

McKee and Ostriker [2007] review star formation theory and divide the extensive problem into two categories separated by the scales of the processes. All the physics that influence the formation and evolution of single stars or binary systems[a] are termed *microphysics* of star formation. Research in this category investigates how stellar mass distributions arise as a result of gravitational collapse. What imprints of the host medium out of which stars form can be found in the stellar populations? How do magnetic fields influence the accumulation process of gas and how is angular momentum transferred when protostellar disks are formed? Once stars are formed they strongly influence their surroundings. What are the properties of young stellar objects (YSO) and how do their outflows, jets and radiation pressure interact with the interstellar medium (ISM).
The physics of star formation on larger scales is termed *macrophysics* of star formation and deals with whole systems and associations of stars. They are typically formed in giant molecular clouds (GMCs) which are believed to be the birthplace of most stars. Here, star formation theory tackles the questions of how GMCs are formed from the diffuse intergalactic gas and what their properties are. Are they gravitationally bound long-lived entities or do they have rather short life cycles and get dispersed shortly after they have formed the first stars? How much gas of such clouds is transformed into stars and at what rate does it happen? Moreover, how do the properties of the natal material influence the star formation process and what are the effects from the interstellar medium? How do the overall properties of the available gas in a galaxy determine the distribution of stars in that galaxy and how do stars influence the evolution of the host galaxy?
In this thesis we will mostly be concerned with the explicit treatment of macrophysics of star formation while the microphysics will be parameterized by a subgrid model approach. However, it is already obvious from the above overview that all the physics involved in the formation of stars cannot always be clearly and independently separated into two regimes. A supernova explosion of a single massive star would be attributed to the category of evolution of a single star and therefore be considered microphysics. However, the influence of such an event on the

[a] It is assumed that roughly 50% of all stars form as binary systems.

ISM might be quite dramatic and may have effects on scales much larger than GMCs, therefore it would belong to the macrophysics category. Nevertheless, it is very intuitive to use the terminology introduced by McKee and Ostriker to distinguish between different scales involved in star formation theory as well as to emphasize the focus of our work on the large scale properties of star formation.

To investigate the macrophysics of star formation it is intuitive to consider a framework like our own galaxy, and the Galaxy is also a good example to outline some of the basic problems in star formation theory. The Galaxy contains roughly $10^9\,\mathrm{M}_\odot$ of molecular gas. Most of this gas is located in GMCs which have typical masses of $10^6\,\mathrm{M}_\odot$ and number densities of $n_H \approx 100\,\mathrm{cm}^{-3}$. If this gas could simply gravitationally collapse without any opposing force, its free–fall time $\tau_{\mathrm{ff}} = \sqrt{3\pi/(32\,G\rho)}$ would approximately be 5 Myr. Using $\rho = n_H m_h \mu$ we get $\tau_{\mathrm{ff}} = 4.7\,\mathrm{Myr}$. It follows that the Galaxy should turn gas into stars at a rate of $200\,\mathrm{M}_\odot\,\mathrm{yr}^{-1}$. However, McKee and Williams [1997] state an observed star formation rate in the Galaxy of $\sim 3\,\mathrm{M}_\odot\,\mathrm{yr}^{-1}$. Obviously, the picture of pure gravitational collapse is wrong by almost two orders of magnitude.
This discrepancy is not only apparent in the Galaxy but also in other more extreme environments. Considering the closest Ultraluminous Infrared Galaxy (ULIRG), namely Arp 220, Downes and Solomon [1998] state a molecular mass of $2 \cdot 10^9\,\mathrm{M}_\odot$ and typical number densities of $n_H \approx 10^4\,\mathrm{cm}^{-3}$. In this case we calculate a free–fall time of roughly 0.5 Myr and subsequently a star formation rate (SFR) of $4000\,\mathrm{M}_\odot\,\mathrm{yr}^{-1}$ while the authors state an observed SFR of only $50\,\mathrm{M}_\odot\,\mathrm{yr}^{-1}$. Again, the simple free-fall calculation and observations are off by almost two orders of magnitude.
Furthermore, Krumholz and Tan [2007] also analyze high density star formation traced by HCN. They find an observed correlation of $SFR \sim M_{HCN}/30\,\mathrm{Myr}$ which again contradicts the calculated free-fall time of $\tau_{\mathrm{ff}} \approx 0.2\,\mathrm{Myr}$ by a factor of almost 100.
Although it is not really surprising that the assumption of pure gravitational free-fall collapse does not sufficiently describe the physics of star formation, it is very interesting to see that the differences appear in a systematic fashion and hold for vastly different star formation scenarios. It is very tempting to draw the conclusion that some general process available in all star forming environments plays the crucial role of synchronizing theory and observations. We will come back to this hypothesis in the next paragraph where we touch upon the physics opposing gravity.

In a typical star formation scenario gravity certainly plays a key role but there are also other physical processes which have to be taken into consideration. The literature has extensively discussed the physics of thermodynamics in the ISM, large scale galactic dynamics such as rotational shear, magnetic fields and turbulence, and we will investigate these processes in Chapter (3) in detail. We will show that a realistic evaluation and incorporation of turbulence effects can indeed have a significant influence on controlling star formation processes and alleviate the contradictions, mentioned earlier, to a certain extend. Turbulence is in fact important in essentially all branches of astrophysics that involve gas dynamics and this universality has also been one of the first hints which led theorists to the idea that it might be a excellent candidate to counteract gravity in various star formation scenarios. Today, we conceive turbulence in star formation theory to play a dual role. Turbulence counteracts gravity in overdense regions while at the same time generating seeds for gravitational contraction and collapse by gas compression. Various sources have been identified as the origin and driving mechanisms of the observed turbulent motions, among them gravity [Wada et al., 2002], stellar winds, supernovae [Mac Low and Klessen, 2004], magneto-rotational instabilities [Sellwood and Balbus, 1999], and radiative heating [Kritsuk and Norman, 2002]. Most likely some combination of these processes generates

the turbulence that globally opposes gravitational collapse while locally producing density enhancements [Mac Low and Klessen, 2004] which can become gravitationally unstable and exceed the density threshold for star formation.
These density enhancements are initially generated by shocks in the supersonic flow of a turbulent gas cloud. The density of the postshock gas increases by $\sim \mathscr{M}^2$ in an isothermal gas, where $\mathscr{M}$ is the Mach number. Therefore, the Jeans length, the length scale of a collapsing cloud of self-gravitating gas, drops by a factor proportional to $\mathscr{M}$ and may render the shocked gas able to collapse while the surrounding flow is still supported by turbulence.
Star formation is essential for the evolution of galaxies and molecular clouds. Stars heat and stir up their surrounding material. In the case of massive OB stars, this may have important consequences on a large fraction of the molecular cloud's gas. Feedback from stars can interrupt the accretion process or even destroy the molecular cloud itself and end the overall star formation. Additionally, star formation and the eventual death of stars leads to metallicity enrichment of the gas which influences the further development of the system by enhancing the metal-line cooling efficiency.

Another problem in star formation theory is to explain the observed correlations of the star formation rate and gas surface density. The surface density is a projection of a 3-dimensional quantity on a 2-dimensional face. In imitation of the 2-dimensional information an observer envisions when looking at a distant stellar object, the surface density is generated mathematically by integrating the 3-dimensional quantity along the line of projection (sight).
Surveys of vastly different star formation locations in numerous galaxies covering a large range of star formation rates and gas surface densities show clear correlations of the latter quantities [Schmidt, 1959, 1963, Kennicutt, 1989, 1998a,b]. While Schmidt proposed a power law correlation of gas density and star formation rate, Kennicutt investigated the normalization and power law index. The Kennicutt-Schmidt law can be stated

$$\Sigma_{\mathrm{SFR}} = (2.5 \pm 0.7) \cdot 10^{-4} \left(\frac{\Sigma_{\mathrm{gas}}}{1\,\mathrm{M}_\odot\,\mathrm{pc}^{-2}} \right)^{1.4\pm0.15} \mathrm{M}_\odot\,\mathrm{yr}^{-1}\,\mathrm{kpc}^{-2} \tag{1.1}$$

as done by the latter author. Here Σ_{SFR} is the star formation rate (the mass of stars formed per unit area and unit time) and Σ_{gas} is the gas surface density. Remarkably, this correlation holds over more than four orders of magnitude in gas surface density and more than six orders in star formation rate.

1.2. Goals of this Thesis

A good theory of star formation has to be able to give convincing answers to the two major problems outlined above. Moreover, the arguments have to be valid for the whole margin from low star formation rates in disk galaxies to orders of magnitude larger rates in ULIRGs. To date, no such theory exists. The essential goal of this work is therefore to contribute along the way towards a better understanding of the physics of star formation and to investigate the ideas which might eventually lead to a general theory of star formation.

Along this path, we have decided to focus on three major tasks:

- Construction of a toy model galaxy simulation

Neither can stars and star formation be studied in isolation from their galactical environment, nor can galaxies and the star formation therein be studied without understanding how stars and their life cycles influence the host galaxy. It was therefore our first goal to set up a toy model

galaxy as a numerical simulation.

- Investigation of simulation parameters and implementation of a turbulence regulated star formation formulation

With the numerical setup at hand the plan was to reinvestigate what is commonly referred to as density threshold star formation in the literature. Although there is plenty of literature on numerical simulations of star formation, only recently full scale galaxy simulations of star formation in three dimensions have become available. We wanted to test our setup through comparisons and in a further step evolve the simulation framework in some details.
In particular, we wanted to take advantage of the FEARLESS[b] code which has recently been developed in our group. It enables us to implement the theory of turbulence regulated star formation proposed by Krumholz and McKee [2005] as a subgrid-scale (SGS) model in our galaxy simulations.

- Extensive numerical experimentation with galaxy simulations and different star formation (SF) algorithms some of which including stellar feedback

In order to model star formation in disk galaxies from first principles, one needs a good understanding of the evolution and lifetime of molecular clouds, the influence of turbulence, rotation and magnetic fields on gravitational instability, as well as feedback from supernovae, ionizing radiation, stellar outflows and galactic winds. Obviously, this challenging program is beyond our current abilities. Instead, we invoke Occam's razor and propose to ignore all effects but supersonic turbulence, as formulated by Krumholz and McKee. In some cases we also include a simple realization of star formation feedback to close the star formation cycle.

This thesis is organized as follows:
In Part (I) we give a brief review of the most relevant theoretical aspects of contemporary star formation theory. In Chapter (2) we draw the global picture of a star forming disk galaxy, followed by a detailed discussion of the most relevant physical processes in Chapter (3). Subsequently, in Chapter (4) we discuss important aspects of turbulence theory and its implications on star formation.
Part (II) deals with the numerical aspects of this dissertation. In Chapter (5) we give a detailed description of our simulation framework and disscuss in Chapter (6) how we set up isolated galactic disks. Chapter (7) is devoted to the description of the numerical implementation of the subgrid model and a discussion of its functionality and parameters. As an amendment, we discuss in Chapter (8) the particular aspect of probability gas density distributions in molecular clouds as this is an important ingredient in the turbulence regulated star formation algorithm.
The last part, Part (III) of this thesis is devoted to our numerical results. In Chapter (9) we present simulations with a classical star formation algorithm and study the global evolution of galaxies as well as the influence of certain important parameter choices. Eventually, we investigate the expected effects as a result of including unresolved turbulence effects in Chapter (10) and present our full subgrid-scale simulations with turbulence regulated star formation. Finally, in Chapter (11) we sum up our conclusions and discuss improvements and limitations, and point out some future prospects.

[b] **F**luid m**E**chanics with **A**daptively **R**efined **L**arge **E**ddy **S**imulation**S**

CHAPTER 2

Star Formation in Disk Galaxies

Galactic disk systems are rather complex entities. Here we introduce the basic concepts of disk galaxies and their properties. We will begin this section with an introduction of the hydrodynamical framework which we use to describe the gas dynamics of galactic disk systems. We continue with a general description of the formation process of galaxies via hierarchical collapse, followed by a description of the galactic scales in more detail. Subsequently, we look into the interstellar medium and end with a discussion of molecular clouds.

2.1. Hydrodynamical Framework

Astrophysical applications usually deal with plasma of gas typically composed of dilute mixtures of atoms, molecules and electrons. The direct numerical simulation at the microscopic level, which is completely described by the distribution functions of the involved particle species, and the calculation of the time evolution of the system using the Boltzmann equation, is unmanageable in most astrophysical applications. Luckily, whenever particle collisions are frequent enough, or equivalently, the mean free path of a particle is short compared to the dimension of the system itself, we can resort to much simpler statistical methods involving only the conserved, macroscopic quantities of the plasma.

The Basic Hydrodynamical Equations. Here, we introduce the most general equations used to describe a compressible, viscous, self-gravitating fluid exposed to an external force:

$$\frac{\partial}{\partial t}\rho + \boldsymbol{\nabla}\cdot(\rho\boldsymbol{v}) = 0 \tag{2.1}$$

$$\frac{\partial}{\partial t}(\rho\boldsymbol{v}) + \rho(\boldsymbol{v}\cdot\boldsymbol{\nabla})\boldsymbol{v} = -\boldsymbol{\nabla}p - \rho\boldsymbol{\nabla}\Phi + \boldsymbol{\nabla}\cdot\mathbb{S}' + \boldsymbol{F} \tag{2.2}$$

$$\frac{\partial}{\partial t}(\rho e) + \boldsymbol{\nabla}\cdot\boldsymbol{v}\rho e = -\boldsymbol{\nabla}\cdot\boldsymbol{v}p - \rho\boldsymbol{v}\cdot\boldsymbol{\nabla}\Phi + \boldsymbol{\nabla}\cdot\boldsymbol{v}\,\mathbb{S}' + \boldsymbol{v}\cdot\boldsymbol{F} \tag{2.3}$$

Here we have the continuity Equation (2.1) which expresses the conservation of mass, the Equations (2.2) of motion expressing the conservation of momentum and the Equation (2.3) for the gas' internal energy. The dependent variables $\rho, \boldsymbol{v}$ and e are the mass density, the velocity and the specific energy, respectively.
The second term on the right hand side of both Equations (2.2) and (2.3) accounts for the influence of gravitational effects, while the third term includes the viscous stress tensor $\mathbb{S}'$, describing viscous forces. The last terms in each of the latter equations, $\boldsymbol{F}$, encodes the external or body forces (per unit volume) acting on the fluid.
Gravitational forces are described by the Poisson equation

$$\Delta\Phi = 4\pi G\rho. \tag{2.4}$$

Equation of state. Additionally, the fluid equations are closed by an equation of state, correlating gas pressure p with gas density and internal energy. From the ideal gas law $pV = nRT$ we get

$$\frac{p}{\rho} = \frac{N}{m} k_b T. \tag{2.5}$$

Furthermore, the ratio of specific heats is

$$\gamma = \frac{c_p}{c_V} = 1 + \frac{2}{f}, \tag{2.6}$$

where f describes the number of degrees of freedom in the gas. Using Equation (2.5) and (2.6) in the equation of the specific energy of an ideal gas

$$e_{int} = \frac{f}{2} \frac{N}{m} k_b T, \tag{2.7}$$

finally yields the desired equation of state:

$$p = (\gamma - 1) \rho e_{int}, \tag{2.8}$$

where $e_{int} = e - \frac{1}{2} v^2$ is the internal energy.

For the work presented in this thesis, we use a general value of $\gamma = 5/3$ for our calculations and simulations. However, as we discuss in Section (5.3), in dense and cold gas, the cooling time becomes much smaller than the dynamical time and energy from adiabatic heating processes is radiated away immediately. Therefore, our simulations mimic isothermal behavior of cold clouds while explicitly using an adiabatic equation of state.

The Navier-Stokes Equation. We make use of different forms of the hydrodynamical equations throughout this work. For example, in Chapter (4) we will introduce the general concepts of incompressible turbulence. For this discussion we use Equation (2.2) but neglect explicit gravitational terms. Furthermore, the stress tensor, encoding the force per unit volume of the fluid is obtained by considering the stresses acting upon an infinitesimal cube of the fluid, and calculating the net forces on the cube by taking the differences in the stress acting on different faces. We can have internal stresses as a result of fluid pressure p as well as stress owed to viscous forces. The results are derivatives of the stress tensor $\sigma_{ij} = -p\delta_{ij} + \sigma'_{ij}$ which we write:

$$\sum_{j=1}^{3} \frac{\partial}{\partial x_j} \sigma_{ij} = -\frac{\partial p}{\partial x_i} + \sum_{j=1}^{3} \frac{\partial}{\partial x_j} \sigma'_{ij} \tag{2.9}$$

Evaluating the last sum, we get

$$\begin{aligned} \sum_{j=1}^{3} \frac{\partial}{\partial x_j} \sigma'_{ij} &= \eta \boldsymbol{\nabla}^2 v_i + \underbrace{\eta \frac{\partial}{\partial x_i} \boldsymbol{\nabla} \cdot \boldsymbol{v}}_{\boldsymbol{\nabla} \cdot \boldsymbol{v} = 0} \\ &= \eta \boldsymbol{\nabla}^2 \boldsymbol{v} = \rho \nu \boldsymbol{\nabla}^2 \boldsymbol{v} \end{aligned} \tag{2.10}$$

Consequently, we can deduce the Navier-Stokes equation for an incompressible fluid from Equation (2.2):

$$\rho \left(\frac{\partial \boldsymbol{v}}{\partial t} + (\boldsymbol{v} \cdot \boldsymbol{\nabla}) \boldsymbol{v} \right) = -\boldsymbol{\nabla} p + \rho \nu \boldsymbol{\nabla}^2 \boldsymbol{v} + \boldsymbol{F} \tag{2.11}$$

Basic Scales. From the momentum equation, we can infer the equation of hydrostatic equilibrium. We use Equation (2.2) and neglect the time derivative as well as the velocity terms. Hence, we get

$$-\frac{1}{\rho}\boldsymbol{\nabla} p - \boldsymbol{\nabla}\Phi = 0. \tag{2.12}$$

With the gravitational potential $\Phi = -GM/R$ we gain the equation of hydrostatic equilibrium

$$\frac{dp}{dR} + \frac{GM\rho}{R^2} = 0, \tag{2.13}$$

which we can use to evaluate the balance of pressure and gravitational forces of a spherical cloud of radius R and mass M. If forces are out of equilibrium a net acceleration $\ddot{r}$ will result on the right hand side of Equation (2.13). We can express this acceleration as fraction of the overall gravitational force $\ddot{r} = fg(r)$. For molecular clouds we can assume the gravitational acceleration to change only marginally with location and approximate $g(r) \equiv g = \text{const}$. Integrating over a time interval τ yields the translation of a gas element as $\Delta r = fg\frac{1}{2}\tau^2$. As we now use $g = \frac{GM}{R^2}$ with $M = \frac{4}{3}\pi R^3\rho$ and assume the same fraction of radial translation as of gravitational force $\Delta r = fR$, we get

$$\tau = \tau_{\text{ff}} \approx \sqrt{\frac{1}{G\rho}}, \tag{2.14}$$

within an order of unity. This is the dynamical or free-fall time scale of a molecular cloud.

For the sound-crossing time, we simply write

$$\tau_s = \frac{R}{c_s}. \tag{2.15}$$

Considering a slightly compressed spherical gas cloud, this is the time it takes for sound waves to cross the region R, in an attempt to push back and re-establish the system in pressure balance. Directly comparing both latter time scales we can estimate the stability of the gas cloud. When the sound-crossing time is less than the free-fall time, pressure forces are dominant, and the system evolves back to a stable equilibrium. In case of a shorter free-fall time, gravitational collapse occurs. From these considerations we get the condition for gravitational collapse:

$$R_J = \sqrt{\frac{k_b T}{G\rho m_h \mu}} \tag{2.16}$$

$$M_J = \left(\frac{k_b T}{G m_h \mu}\right)^{3/2} \rho^{-1/2} \tag{2.17}$$

All scales of a system larger than the Jeans length R_J are unstable to gravitational collapse. The Jeans mass M_J gives the mass of such a spherical system of diameter R_J.

These are the basic equations and concepts we use throughout this work and on which we base the theoretical as well as numerical modeling in the following chapters. However, before we get into the details of our model approach, we discuss more of the theoretical aspects of galactic evolution.

2.2. The Formation of Galaxies

Modern ideas and models describe galaxy formation as a process in a universe in which cosmic structures build up hierarchically through gravitational instability. Baugh [2006] gives a recent review on the details of galaxy formation. Here, we will only include a brief outline and introduce

the general concepts.
We use the cosmological standard model of a cold dark matter universe with cosmological constant (ΛCDM) as the starting point of our description. The initial density fluctuations, assumed to follow a Gaussian random distribution, are the seeds of structure formation in the universe. The driving force behind the amplification of fluctuations in the dark matter is gravitational instability which leads to a continuous growth of perturbations until dark matter collapses into dark halos. These dark halos are believed to continue growing their mass by subsequently merging with other halos.
The baryonic gas component follows the gravitational potential of the dominating dark matter and starts to accumulate in the potential wells created by dark halos. During infall, the gas is heated by shocks until it eventually reaches the virial temperature of the halo. The inner parts of the hot halo gas start to cool and form a rotationally supported disk as angular momentum is transferred away in axial direction during contraction. Furthermore, the radius within which the gas has had time to cool becomes larger and advances towards the virial radius of the halo. Meanwhile, the cooling gas settles down on the disk which correspondingly grows in size.
At this time, the galaxy formation process becomes more and more complicated, and a more detailed description is rather difficult owing to the lack of understanding of all the included processes such as gas dynamics, star formation and feedback. However, following the model of hierarchical structure formation, galaxies continue to evolve and grow via merging events with other galaxies. In this picture, early galaxies emerged as small entities which evolved via mergers and violent acquisitions of smaller galactic objects to become today's galaxies like our Milky Way or even larger systems.
Disk galaxies are hereby assumed to result from rotating collapsing clouds of gas during the above described evolution. Their main source of growth are much smaller, nearby galaxies which are accreted into the disk and dissolve therein. Elliptical galaxies on the other hand are believed to result from subsequent collisions of massive, evolved disk galaxies.

While it has become possible during the last decade to study the dynamical evolution of dark matter, which only interacts gravitationally, in tremendous detail (see e. g. the Virgo Consortium's Millennium Simulation [Springel et al., 2005]), the study of the dynamical evolution of galaxies is still in its infancy. The reason is that the involved plethora of processes in galaxies is much more difficult to deal with than gravitational instability which creates dark matter halos. Additionally, gas physics of galaxies is mostly dissipative and highly nonlinear. Nevertheless, a better understanding and more detailed knowledge of the properties and evolution of disk galaxies resides at the basis of a more complete understanding of hierarchical structure formation. Therefore, in this work, we try to combine hydrodynamical simulations of galactic gas disks with semi-analytic modeling of the involved processes to contribute a better model for galaxy scale systems in cosmological structure formation simulations.

2.3. Disk Galaxies

The most efficient cooling process in the young universe was thermal Bremsstrahlung where an electron is decelerated in the Coulomb potential of a proton and therefore loses energy via electromagnetic radiation. The time scale of this cooling process is $t_{\rm cool} \sim \epsilon/\dot{\epsilon}$, where $\epsilon \propto nkT$ and $\dot{\epsilon} \propto n^2(k_bT)^{1/2}$. The timescale of gravitational collapse of a gas cloud is estimated as $t_{\rm grav} \sim (GM/R^3)^{-1/2}$, where R and M are the radius and mass, respectively. Comparing these timescales it is possible to deduct the length scale of a system able to collapse without the buildup of thermal pressure (cooling is efficient) to oppose its contraction. More details on the calculation can be found in Appendix (A). The typical length scale of such a system is roughly 75 kpc. Using an additional lower limit of temperature owing to a limiting ionizing potential it

is also possible to calculate a corresponding mass scale of approximately $10^{11}\,M_\odot$. These are the gross numbers of systems that are able to cool efficiently and at the same time they are typical values for early galaxies. As the gas continues to cool slowly, the system contracts and the galactic disk approaches a typical radius of the order of 10-20 kpc.

Our own galaxy is a very good example. Classified as barred spiral galaxy of type SBbc,

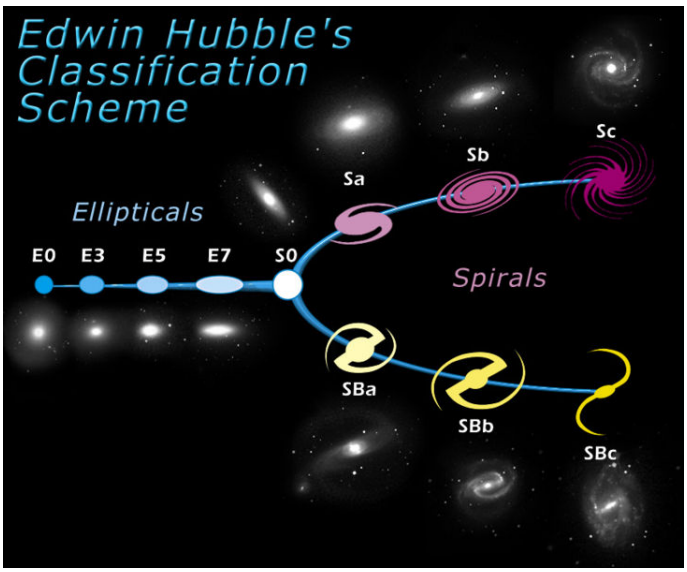

FIGURE 2.1. Edwin Hubble's classification scheme of galaxies, developed in 1926. The material was created for NASA by STScI under Contract NAS5-26555 and for ESA by the Hubble European Space Agency Information Centre.

according to the Galaxy Morphological Classification by Edwin Hubble. 'S' and 'B' describe the galactic shape as of Spiral structure with a significant Bar feature and it has slightly loose defined spiral arms 'bc', not so tightly wound arms as an 'a' and 'b' types but also not so loose arms as 'c' and 'd' types. We believe it to be approximately 13.2 Gyr of age. Actually, it is very hard to measure the age of the Galaxy. However, the oldest object found within the Galaxy is a Pop II red giant star (at HE 1523-0901) of the cited age. Today, the galaxy has a very thin stellar disk with radius of ~ 15 kpc. The gas disk is much thicker and has a scale radius of roughly 3.5 kpc and scale height of a couple of hundred of parsecs. The total mass of the disk is determined to range of the order of approximately $4 \cdot 10^{10}\,M_\odot$ (see i. e. [Klypin et al., 2002]) and we believe the Galaxy to reside in a dark halo - an almost spherical envelope of dark matter with mass up to two orders of magnitude larger than baryonic gas and star components.

As we turn towards other galaxies, their wide variety and morphological differences are enormous as are their broad dispersion in the pattern of star formation (see i. e. Stahler and Palla [2005]). Although the connections are not always obvious and a complete theory of star formation has to account for all types of galaxies, here we will focus mostly on disk galaxies as this is the scenario which we will later present in our numerical simulations.

Henceforth, we are back to the cooling system which settles into a disk like structure while angular momentum is transferred away in direction of a designated axis of rotation during the process of contraction. While gravity tries to fragment the disk and form dense clouds it is counteracted by thermal pressure, rotational shear, magnetic fields, heating from UV background radiation, and turbulence. In his work, Toomre [1964], developed the classical condition for the stability of

disk systems. The Toomre Q parameter is defined as

$$Q_g = \frac{\kappa c_s}{\pi G \Sigma_g}. \tag{2.18}$$

Here we follow Rafikov [2001] and name Q_g to indicate that this parameter is valid for the gas disk. κ is the epicyclic frequency of the disk, where $\kappa \approx \sqrt{2}\Omega$ with $\Omega = v_{rot}/r$ is the angular velocity and r is the distance to the center of the disk. c_s is the sound speed, G is the gravitational/Newton's constant and Σ_g is the gas surface density. Most generally, disk instability arises for values $Q_g < 1$. The Q parameter encodes that a thin rotating gaseous disk can become gravitationally unstable to local axisymmetric perturbations as first shown by Safronov [1960]. More directly interpreted, the Q parameter encodes shear effects from large scale rotation and pressure effects determining the effective speed of sound to estimate the suppression of large and small scale perturbations, respectively. While we are not so much interested in the large scale rotation it is the encoded pressure that we want to focus on. It is not clear which combination and to what magnitude the above mentioned mechanisms counteracting gravity contribute to this pressure. However, during the last years the conception has emerged that supersonic turbulence is the leading candidate [Mac Low and Klessen, 2004, McKee and Ostriker, 2007] to supply this pressure. The speed of sound in Equation (2.18) can be replaced by the effective sound speed $c^2_{\mathrm{s,eff}} \sim c_s^2 + 1/3\ v^2$ which includes the effects of turbulent motions v. Originally, Chandrasekhar [1951a,b] proposed the effective sound speed to include the rms velocity dispersion of turbulent motions $\langle v^2 \rangle$, while later work by Bonazzola et al. [1987], Vazquez-Semadeni and Gazol [1995] suggested a wave-length dependent effective sound speed $v^2(k)$. See Mac Low and Klessen [2004, Chap. (III)] for a more detailed discussion. Governing the stability condition, turbulence has a channel to directly regulate the stability of the gas disk. Therefore, as instability leads to fragmentation and fragmentation possibly to the formation of star forming molecular clouds, this is a channel for turbulence to control the star formation efficiency.
In Chapter (3) we will discuss the strength and influence of turbulence as well as of the other candidates on a quantitative basis. But first we proceed to the interstellar material inside the galactic disk.

2.4. The Interstellar Medium

The ISM consists almost entirely of hydrogen gas in its different chemical states. We can sort the hydrogen gas into the three forms - molecular, atomic, ionized - and loosely associate these forms with their temperature regimes - cold, warm and hot. Of course, things are more complicated and atomic hydrogen, for example, exists as warm medium, as well as in bound cold structures. Similarly, there are also ionized regions in the proximity of massive stars which have temperatures still considered warm. Table (2.1) gives the details of our current understanding of the interstellar medium and its components and phases.

The essential ingredient to understand the physics of the ISM is gas pressure. We start with the atomic component of the Cold Neutral Medium (CNM). The typical values of such HI clouds are $n = 30\,\mathrm{cm}^{-3}$ and $T = 80\,\mathrm{K}$ which results in an average gas pressure of approximately $P/k_b = nT = 2400\,\mathrm{K\,cm}^{-3}$. Interestingly, this pressure is matched within a factor of two by the Warm Neutral Medium (WNM) $n = 0.5\,\mathrm{cm}^{-3}$ and $T = 8 \cdot 10^3\,\mathrm{K}$ giving $P/k_b = 4000\,\mathrm{K\,cm}^{-3}$. Field et al. [1969] first drew the conclusion that there are two coexisting phases in the ISM, cold neutral HI clouds and warm neutral diffuse HI gas. Indeed, this conclusion follows as well from theoretical considerations.

Stahler and Palla [2005] lay out the following idea: The gas pressure directly correlates with the thermal energy of the gas. This energy content is the result of the combined effects of all

Component	Temperature [K]	Density [cm^{-3}]	f_V	Chemical State	Common Name
Molecular Clouds	$10 - 20$	$10^2 - 10^6$	< 0.01	H_2	
Cold Neutral Medium (CNM)	$50 - 100$	$20 - 50$	$0.01 - 0.05$	HI	Cold
Warm Neutral Medium (WNM)	$6 \cdot 10^3 - 10^4$	$0.2 - 0.5$	$0.1 - 0.2$	HI	
Warm Ionized Medium (WIM)	8000	$0.2 - 0.5$	$0.2 - 0.5$	HII	Warm
HII regions	8000	$10^2 - 10^4$	< 0.01	HII	
Hot Ionized Medium (HIM)	$10^6 - 10^7$	$10^{-4} - 10^{-2}$	$0.3 - 0.7$	HII	Hot

Table 2.1. Phases of the interstellar medium. f_V is the volume fraction taken by the different components of gas. The values are taken from Ferrière [2001].

involved cooling and heating processes. Although we do not want to get into the details of heating and cooling yet (see Section (5.3)) we assume some equilibrium between the processes and calculate the corresponding pressure values P/k_b for each density and temperature as shown by the solid curve in Figure (2.2). This curve effectively sets apart the two regimes where either one, cooling or heating, is more efficient than the other. Consequently, a parcel of gas with some pressure value above the solid curve cools until it reaches equilibrium and the opposite is true for gas below the curve. We have also indicated the assumed equilibrium pressure of the ISM by a horizontal dashed line at $P/k_b = 4000\,\mathrm{K\,cm^{-3}}$. Figure (2.2) shows three intersections of the pressure curve with this line. If we consider gas at point B and slightly compress it, while it maintains pressure equilibrium with the surrounding material, the gas enters the regime where cooling is more efficient than heating and cools until it reaches point C. Contrarily, if the gas is slightly expanded, it will heat up until reaching the stable point A. Hence, we see that there are two naturally stable points and these points match the observed CNM and WNM specifications quite well.

Aside the neutral medium there is the molecular component. From the values in Table (2.1) it is obvious that this gas can have much higher gas pressure. This component exists in confined molecular clouds which are sufficiently dense that their own mass weight can play a significant role. These clouds are held in mechanical equilibrium mostly through the addition of self-gravity. Deep inside the clouds high density regions are hold together by gravity while the less dense outer layers are mostly in pressure equilibrium with their surroundings.

Next, there is ionized hydrogen gas. This extremely hot gas, blistering up from supernova explosions or more precisely from interacting bubbles of hot gas, each the result of a supernova explosion, has very low number densities $n = 0.003\,\mathrm{cm^{-3}}$ accompanying the high temperatures $T = 10^6\,\mathrm{K}$. Thus, their thermal pressure $P/k_b = 3000\,\mathrm{K\,cm^{-3}}$ again corresponds to the pressure of CNM and WNM. For this reason it is legitimate to speak of a third phase of the ISM - the hot ionized or hot intercloud medium is in pressure equilibrium with both other phases. The latter

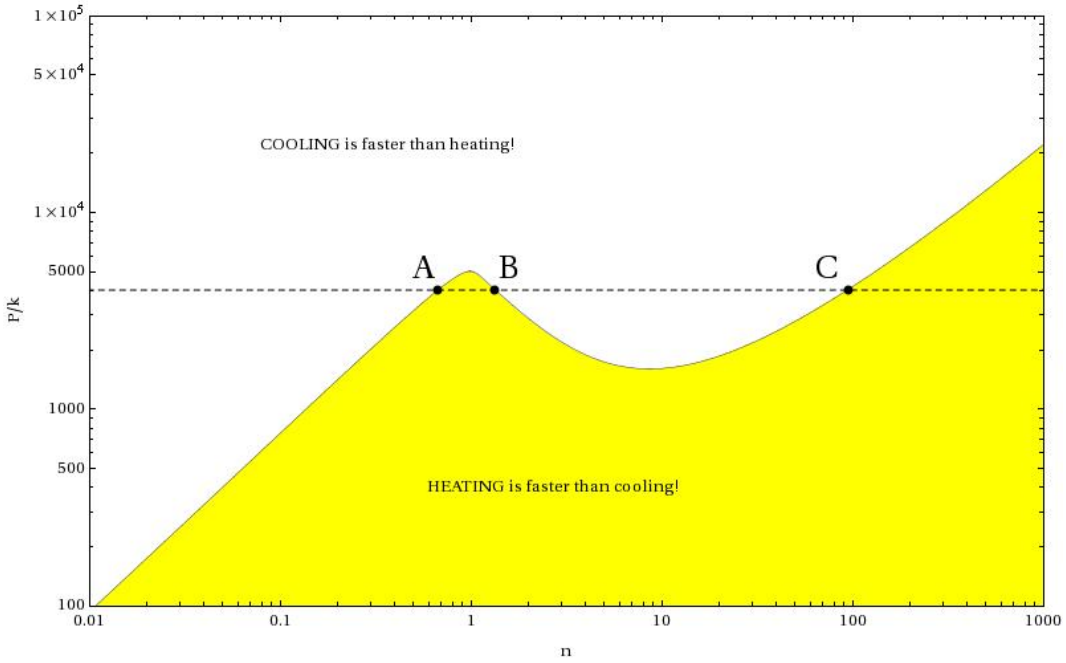

FIGURE 2.2. Equilibrium pressure nT as a function of number density. The horizontal dashed line indicates our empirical nT-value for the ISM.

label stresses the fact that we are talking about loosely stirred low density gas.
Finally, HII regions, clouds of hot gas and plasma with densities as high as a million particles per cm^{-3} are hosts of active star formation. Young, hot, recently formed blue OB stars illuminate their surrounding gas envelopes with large amounts of UV light. These regions can give birth to an enormous amount of stars until supernovae of recently formed massive stars disperse the clouds, probably leaving a cluster of stars behind.

While we have only touched upon the description of the ISM and left out all about the physics of interstellar dust as well as the detailed heating and cooling mechanisms, we have provided some background on the physics of interstellar gas out of which stars form. However, these basic principles will be sufficient in the subsequent discussion of star formation in disk galaxies. A more detailed treatment of the multiphase ISM can be found in Lequeux [2005], Stahler and Palla [2005], Tielens [2005] but is not part of this thesis.
We rather sum up the above discussion and head on towards star formation. We have outlined the existence of three vastly different gas phases, with elementary differences in their physical conditions, yet, in pressure equilibrium. Most of the volume in the ISM is occupied by the hot and some warm gas. Contrarily, most of the mass is located in the cool and dense regions of molecular clouds. This molecular component has mass of the same order of magnitude as the much more volume filling neutral component and will be in focus in the next Section (2.5).

2.5. Giant Molecular Clouds and Star Formation

Giant molecular clouds or cloud complexes are numerous in the Galaxy. A well known example of these GMCs is the Orion Nebula. Typically, these dense, self-gravitating gas clouds have extensions of roughly 50 pc and number densities of order $n = 100\,\mathrm{cm}^{-3}$. Assuming a spherical

configuration this results in an approximate mass of $M_{\mathrm{GMC}} \approx 10^5\,\mathrm{M}_\odot$.
Within the Galaxy over 80 % of the molecular gas resides in GMCs and most of the actual star formation is happening within these clouds. Typical lifetimes are of the order of 30 Myr, too short for a significant "bottom-up" formation scenario in which the massive cloud complexes form through subsequent collisions and mergers of smaller cold HI clouds. McKee and Ostriker [2007] calculate the details of the collision processes and draw the conclusion that destructive feedback from star formation would also prohibit GMC masses to reach the observed values.
It seems more favorable to focus on a "top-down" formation scenario, where GMCs form from large scale instabilities in the diffuse interstellar medium and fragment subsequently to develop their observed complex internal structures. This hierarchical structure then stretches from the scale of the cloud down to clumps out of which clusters of stars can form, and ends at the smallest scale locations of the formation of individual stars, termed cores. The detailed structure as well as the properties of lower density gas permeating the space between individual clumps and cores is not yet known in detail.

However, the relatively short lifetimes indicated above and the overall structural alterability are strong hints towards the dynamical nature of giant molecular clouds. Furthermore, there is strong observational evidence for supersonically turbulent gas motions through the broadening of molecular emission lines attributed to the turbulent velocity dispersion inside the clouds. This emission line broadening is directly correlated with the size of the molecular cloud itself, as first noted by Larson [1981]. As stated earlier and conceptually derived in Section (2.1), the free-fall time of a GMC is conventionally defined as

$$\tau_{\mathrm{ff}} = \sqrt{\frac{3\pi}{32\,G\rho}}. \tag{2.19}$$

Here, we make the approximation of a spherical geometry and a constant density or, likewise, take a volume averaged density for the whole cloud. Equation (2.19) gives a result of several Myr for standard GMC values. Although roughly in the same order of magnitude as the typical GMC lifetimes, the free-fall time appears to be only a fraction of the total lifetime. This lead historically to the early conclusion that GMCs are indeed gravitationally bound and collapsing entities. However, today it is still controversial whether GMCs are gravitationally bound or rather transient objects [Mac Low and Klessen, 2004, McKee and Ostriker, 2007]. Theories supporting the latter case argue that the timescale for interacting shock fronts, which can pile up enough gas to form clouds which reach densities high enough to build up a significant molecular fraction and form stars, is in concordance with the typical cloud lifetime. Additionally, whether the clouds are destroyed by supernova explosions or gas exhaustion from within or by subsequent shocks in the interstellar medium is also an open controversy.
Again, most likely some combination of the above scenarios is best matching the real nature of giant molecular clouds. Henceforth, we will now investigate the different physical forces important in GMCs to get a better understanding of their importance and influence on the evolution of the cloud and the star formation therein.

CHAPTER 3

Major Physical Processes in Star Formation

As we have seen from the discussion of the ISM in the earlier Section (2.4), molecular clouds are self-gravitating, bound objects which can contain strong pressure gradients. The detailed structure of molecular clouds as well as the chemistry and physics of these objects, from scales of tenth of a parsec down to single protostars, is a highly nontrivial and very active field of research. Before we start the discussion of the most relevant processes involved, we briefly outline the standard textbook star formation scenario for completeness.

3.1. From Molecular Clouds towards the Initial Mass Function

Star formation starts in dense nebulae, where gas densities become high enough to shield their interiors against photo-dissociation as a result of ultraviolet background radiation. In these locations, large amounts of molecular gas can form and accumulate, called molecular clouds. If such a cloud is massive enough that its gas pressure is insufficient to support it, gravitational collapse will start to contract the cloud. The critical mass above which a cloud becomes gravitationally unstable and consequently undergoes collapse is called the Jeans Mass. The Jeans instability thereby causes the collapse of interstellar gas clouds once the hydrostatic equilibrium is perturbed and the disturbance is not damped away but amplified. The Jeans mass determines the limit at which the cloud in question becomes gravitationally unstable. We have already discussed the Jeans mass and its derivation in Section (2.1). Typical masses range from thousands to tenth of thousands of solar masses. At high masses, there is a sharp cutoff of cloud masses at $\sim 6 \cdot 10^6\,\mathrm{M}_\odot$ indicating a general, limiting physical process such as disrupting feedback effects form massive stars [Williams et al., 2000].
Star formation can be triggered in previously stable clouds by several events which might occur in the ISM and result in a compression of molecular clouds and subsequent gravitational collapse. Molecular clouds can collide with each other, supernova shock waves can produce compressions or introduce shocked material at high speeds into clouds and galactic interactions, such as fly bys, collisions and mergers, can impose strong forces on interstellar clouds as a result of tidal interactions.
Once a cloud has become unstable it collapses and breaks into several smaller pieces. This process of fragmentation and subfragmentation is accompanied by the release of gravitational potential energy into thermal energy and a corresponding increase of gas pressure. Furthermore, fragments start to settle into rotating spheres of gas. Once the pressure is again large enough to support the fragment against further collapse it is commonly called a protostar.
During the further evolution of a protostar surrounding gas settles into a circumstellar disk from which it is transferred via accretion onto the central object. Once density and temperature are high enough, first fusion processes begin and slow the gravitational collapse via radiation pressure effects. The protostar follows the Hayashi track on the Hertzsprung-Russell diagram until the Hayashi limit is reached. Further contraction and evolution depends on the mass of the protostar, but finally, hydrogen fusion begins, ending the protostellar phase and starting the main sequence evolution of the star.

The Initial Mass Function (IMF) describes the relative fraction of stars of different mass at their birth [Lequeux, 2005]. The IMF can be considered for all kind of stellar populations, ranging from star clusters and associations over field stars and large galactic regions to whole galaxies. While it is rather difficult to observationally determine the exact distribution of stellar masses owing to observational difficulties, the IMF is on average approximated by a power law of the form (cf. latter reference)

$$\Psi(M) = \frac{dn(M)}{d\ln M} = \frac{M dn(M)}{dM} \propto M^{-x}, \qquad M_{\min} < M < M_{\max}, \tag{3.1}$$

where $n(M)$ describes the number of stars with masses in the interval $M + dM$. For masses in the range of $M_{\min} \approx 1\,\mathrm{M}_\odot$ to $M_{\max} \approx 100\,\mathrm{M}_\odot$ first studies [Salpeter, 1955] as well as recent observations state a power law index of $x \approx 1.35$. For masses smaller than one solar mass, the distribution is observed to become approximately flat. Aside the uncertainties of the exact form of the IMF, which is very actively discussed by several authors (see e. g. Miller and Scalo [1979], Kroupa [2001], Chabrier [2003]), its origin is also rather controversial. However, the IMF appears to be relatively invariant from one group of stars to another which, after all, renders it an important and powerful tool to model stellar populations and their influence, without detailed information about the particular stellar distribution at hand.

3.2. The Virial Theorem

We now return to the processes on larger scales of entire clouds. For our subsequent work, we are solely interested in the overall properties of molecular clouds in a statistical sense. For example, we assume that most star formation takes place in molecular clouds and calculate a star formation rate as some fraction of mass of an average cloud that is turned into stars during a certain amount of time. One can deduct such an efficiency parameter from observational statistics and apply it as a general property to all objects identified as molecular clouds in a simulation. This procedure will give rise to a globally averaged star formation rate, which might in the statistical sense, correspond to observations.
Indeed, the global Kennicutt-Schmidt law in Equation (1.1) describes such a statistical relation. The analytic equation follows from a fit to data where each galaxy is represented by a single data point, giving the star formation rate and the average gas surface density of that galaxy.

Although the Kennicutt-Schmidt relation in particular and other global averages, depending on the underlying statistics, illustrate the gross properties of the corresponding systems quite well, we are nevertheless interested in a more detailed understanding of the processes which give rise to the observed statistical behavior.
Therefore, we break the problem of molecular clouds into several parts choosing only the most important for understanding their dynamical evolution.

Here and beyond we follow Krumholz and McKee [2005] and only assume that star formation occurs mostly in molecular clouds that are in virial equilibrium. To equate their energy content and, henceforth, determine the agents governing the evolution of clouds we introduce the virial theorem and discuss the importance of gravity, thermal pressure, magnetic forces and kinetic energy from turbulent motions.

The virial theorem provides a general equation to relate the globally averaged energies of a system. The derivation of the theorem for long term stability of a self-gravitating gas cloud has

been rolled out to Appendix (B). The simplified result of that calculation is the balance Equation (B.34).

$$\frac{1}{2}\frac{\partial^2 I}{\partial t^2} = 2\mathfrak{T} + 2\mathfrak{U} + \mathcal{W} + \mathcal{M} \tag{3.2}$$

If the cloud is in virial equilibrium, the net moment of inertia vanishes and the gravitational potential energy $\mathcal{W}$ has to be balanced by the sum of kinetic energy $\mathfrak{T}$, thermal energy $\mathfrak{U}$ and magnetic energy $\mathcal{M}$.
From this simplified picture we deduce some qualitative information about the magnitude of the available energy components inside molecular clouds. Henceforth, we can start our discussion about how to implement the dominant components in our treatment of star formation in galaxies and comment on shortcomings and possible errors of our realization.

3.3. Gravitational Potential

To see the importance of each component, we follow Stahler and Palla [2005] and relate each term to the potential gravitational self-energy

$$\mathcal{W} \equiv \frac{1}{2}\int \rho \Phi_g d^3\boldsymbol{x}, \tag{3.3}$$

where ρ is an averaged cloud density and Φ_g is the potential.
Note that this evaluation is only valid if gravitational acceleration as a result of mass outside the system in consideration is negligible. Fortunately, this is generally the case for dense clouds embedded in a diffuse turbulent interstellar background medium.
Integrating Equation (3.3) we get within a factor of unity a simplistic term, roughly describing the gravitational energy of the cloud

$$\mathcal{W} \approx -\frac{GM^2}{R}. \tag{3.4}$$

Here, the radius of the cloud R is just $L/2$, G is the gravitational constant and M is the total mass of the cloud.

Evaluating the potential energy with standard values for typical molecular clouds gives

$$|\mathcal{W}| \approx 3.5 \cdot 10^{49}\,\mathrm{erg}\,\left(\frac{M}{10^5\,\mathrm{M}_\odot}\right)^2\left(\frac{R}{25\,\mathrm{pc}}\right)^{-1}. \tag{3.5}$$

Aside the following discussion about different energy terms, this number is also interesting with respect to the discussion about the destruction mechanism of molecular clouds. If stars form inside MCs, evolve and eventually end up as core collapse supernova, typical energies of such type II events would be in the same range of magnitude. Without discussing the details of such an explosion and how efficient kinetic and thermal energy can affect the parent MC, we note the fact that already from our very simple analysis, it appears reasonable that forming stars might significantly impact on the life-cycle of their natal clouds. We will come back to the discussion of feedback in Section (5.5).

3.4. Thermal Pressure

To equate the thermal pressure inside a molecular cloud as a result of the random thermal motion in the gas we integrate

$$\mathfrak{U} \equiv \frac{3}{2}\int n k_b T d^3\boldsymbol{x}. \tag{3.6}$$

Here, n is the number density, k_b is Boltzmann's constant and T is the assumed average temperature of the cloud. Again, we use $\rho = nm_h\mu$ and derive a simplified equation for thermal energy

$$\mathcal{U} \approx \frac{k_b}{m_h\mu} MT. \tag{3.7}$$

The last equation gives us the energy contained in random thermal motion and has again to be considered a qualitative approximation.
Forming the ratio of thermal to potential energy and inserting typical numbers, we get

$$\begin{aligned} \frac{\mathcal{U}}{|\mathcal{W}|} &\approx \frac{k_b}{m_h\mu} MT \frac{R}{GM^2} \\ &= \frac{k_b}{m_h\mu G} RTM^{-1} \\ &\approx 6.0 \times 10^{-3} \left(\frac{R}{25\,\mathrm{pc}}\right) \left(\frac{T}{15\,\mathrm{K}}\right) \left(\frac{M}{10^5\,\mathrm{M}_\odot}\right)^{-1}. \end{aligned} \tag{3.8}$$

Hence, it is quite obvious that, using the above approximations, the energy constituting thermal pressure is almost three orders of magnitude smaller than the gravitational energy trying to collapse the cloud. Molecular clouds, which roughly allow for the simplifications we have introduced in their description are certainly not held up against collapse by thermal energy.
We have already made the same physical argument earlier, when we stated the discrepency of expected to observed star formation rate in Section (1.1) and the life-time of molecular clouds in Section (2.5). The sole consideration of gravitational forces in comparison to thermal gas properties can not explain the observed stability of molecular clouds.

At this point, it is worth taking a little detour, quickly discussing HII regions. These regions, also known as emission nebula, have typical densities which roughly coincide with those of molecular clouds. This stems from the fact that the progenitor systems are giant molecular clouds. However, HII regions are physically very different as the inherent temperatures are larger by a factor of several hundred, owing to the continuous heating of young, hot, blue stars that have formed within the region. Considerable star formation is known to take place there. However, note that typical HII regions at temperatures of 8000 K contain enough thermal energy to fully dominate gravitational energy on global scales. For a more detailed analysis, one has to include the substructure in a more realistic way and account for steep density gradients resulting in highly complex shapes. This is certainly beyond our current scope. We therefore leave the detailed explicit treatment as possible future improvement to our model. Yet, we are only able to include a uniform UV background in our simulations. Nevertheless, the feeback algorithm itself can introduce large amounts of thermal energy into dense patches of gas, heating them to rather high temperatures, probably mimicking gas with some properties of real HII clouds.

3.5. Magnetic Fields

The influence of magnetic fields has long been discussed in star formation theory. The method at hand to measure magnetic field strengths in molecular clouds relies on measuring the Zeeman splitting of molecular lines. The typical lines are either the 21 cm line of HI or a cluster of lines near the 18 cm from OH, which is observationally very challenging (see [Crutcher et al., 1993]). Mac Low and Klessen [2004] summarize recent work on such magnetic field measurements and point out that significant measurements above the 3σ confidence level are very rare. A larger compilation of field values by Crutcher [1999] and Bourke et al. [2001] shows typical values in

the regime of $B_{\rm los} \approx 1 \sim 1000\,\mu$G for column densities of $N(H_2) \approx 10^{21} \sim 10^{24}\,{\rm cm}^{-2}$. Here the magnetic field is measured along the line of sight and can be deprojected to gain an absolute B field value. However, the latter authors also stress the fact that almost all of their observed cloud cores have mass-to-flux ratios $(\Phi/M)_n < 1$. This corresponds to the magnetically super-critical regime where the magnetic field is not strong enough to support the cores against collapse.

Lacking a clear analytical understanding of the influence of magnetic fields Stahler and Palla [2005] resort to a representative B-value which is deduced from measurements in nearby dark clouds. The value of $|\boldsymbol{B}| \approx 20\,\mu$G is assumed to match the observed field strength in the warm HI gas surrounding giant complexes.
In the frame of our approximations we can evaluate the magnetic term in Equation (3.2) by integration of

$$\mathcal{M} \equiv \frac{1}{8\pi} \int |\boldsymbol{B}|^2 d^3\boldsymbol{x}. \tag{3.9}$$

Thus, we can simplify the magnetic energy to

$$\mathcal{M} \approx \frac{|\boldsymbol{B}|^2 R^3}{6\pi}. \tag{3.10}$$

Again, relating the approximate magnetic energy to potentail energy gives

$$\begin{aligned} \frac{\mathcal{M}}{|\mathcal{W}|} &\approx \frac{|\boldsymbol{B}|^2 R^3}{6\pi} \frac{R}{GM^2} \\ &= \frac{1}{6\pi G} |\boldsymbol{B}|^2 R^4 M^{-2} \\ &\approx 0.3 \times \left(\frac{B}{20\,\mu{\rm G}}\right)^2 \left(\frac{R}{25\,{\rm pc}}\right)^4 \left(\frac{M}{10^5\,{\rm M}_\odot}\right)^{-2}. \end{aligned} \tag{3.11}$$

This result seems to contradict the above discussion as a ratio of almost 1/3 clearly points to the conclusion that magnetic terms indeed can contribute to the clouds stability. However, the problem of magnetic support is very complex. In the derivation of the virial theorem we describe the magnetic term as force acting on a fluid element orthogonal to the magnetic field $\boldsymbol{B}$. Therefore, self-gravity could freely contract the cloud along the direction of the field lines until an almost planar configuration is realized. As observations do not indicate that the majority of clouds has settled into such oblate configurations the assumption of a smooth uniform internal magnetic field has to be rejected. However, in case of a highly complex B–field configuration it is not possible to use any simple statistical description to approach the problem. Obviously unable to come up with a direct solution or general answer to the problem we summarize our understanding that magnetic fields might have an important influence on the dynamics and evolution of molecular clouds, although it appears that magnetic fields cannot stabilize clouds against gravitational collapse on their own in a general fashion.

3.6. Kinetic Energy and Turbulence

The final term of Equation (3.2) we need to analyze describes the kinetic energy of the system. The total kinetic energy in the cloud can be described as thermal plus bulk energy. Likewise, the velocity $\boldsymbol{v}$ can be split into thermal and nonthermal or turbulent part. From observations of nonthermal linewidths we know that the velocity dispersion in molecular clouds is dominated through the turbulent part. We term the mean value of these random velocity fluctuations Δv and use this in

$$\mathcal{T} \equiv \frac{1}{2} \int \rho |\boldsymbol{v}|^2 d^3\boldsymbol{x} \tag{3.12}$$

to express the kinetic energy term by

$$\mathcal{T} \approx \frac{1}{2} M (\Delta v)^2. \tag{3.13}$$

A representative example of such an molecular cloud complex can be inferred from the Rosette giant molecular cloud. Taking the one dimensional line-of-sight velocity dispersion of $2.3\,\mathrm{km\,s^{-1}}$ [Stahler and Palla, 2005] and multiplying by a dimensional factor of $\sqrt{3}$ to convert as appropriate for a random three dimensional velocity field, we get $\Delta v \approx 4\,\mathrm{km\,s^{-1}}$.
We use the typical temperature from Section (3.4) to calculate the speed of sound in the gas $c_s \approx 0.4\,\mathrm{km\,s^{-1}}$ and use it to get the turbulent Mach number $\mathscr{M} \approx 10$. This shows that highly supersonic Mach numbers are realized in molecular clouds.
Again, we can use our typical numbers and express the final ratio of turbulent to gravitational energy. Hence we write

$$\begin{aligned} \frac{\mathcal{T}}{|\mathcal{W}|} &\approx \frac{1}{2} M (\Delta v)^2 \frac{R}{GM^2} \\ &= \frac{1}{2G} M^{-1} (\Delta v)^2 R \\ &\approx 0.5 \times \left(\frac{M}{10^5\,\mathrm{M_\odot}} \right)^{-1} \left(\frac{\Delta v}{4\,\mathrm{km\,s^{-1}}} \right)^2 \left(\frac{R}{25\,\mathrm{pc}} \right). \end{aligned} \tag{3.14}$$

We see that this result features the most simple formulation of the virial theorem $2\mathcal{T} = |\mathcal{W}|$, which can be interpreted to justify the assumption of virial equilibrium of molecular clouds in the first place. More practically, this result shows that the observed velocity dispersion of MCs contains enough kinetic energy to significantly stabilize clouds against gravitational collapse. If there were no perturbations such as shocks passing through the cloud and a mechanism were present to supply turbulence inside the cloud, we would not see any fragmentation after all. However, this static picture is of course far from reality and the dynamical evolution quickly alters the substructure of clouds leading away from equipartition of energy.
Nevertheless, we deduce from this simplified analysis once more that turbulence is the leading candidate to shape the overall evolution of molecular clouds. We see that turbulent motions carry sufficient energy to oppose gravitational forces. We also know that at the same time turbulent shock fronts can induce the seeds for local perturbations in the molecular gas. This is the idea and theoretical basis on which we build the turbulent subgrid-scale star formation algorithm.

3.7. Uncertainties and Errors

From the above discussion we can also deduce some qualitative statements about uncertainties and errors we introduce in our realization of turbulence regulated star formation in galaxy simulations.

First, we investigate how the amount of thermal energy might change as we consider values other than our standard numbers of mass, size and temperature. The largest margin of uncertainty in this respect stems certainly from the density value. In Table (2.1) we have noted possible values in the range $n = 10^2 \sim 10^6\,\mathrm{cm^{-3}}$. Despite the fact that the assumption of uniform density is certainly not true, we see that the assumed mass of $10^5\,\mathrm{M_\odot}$ is at the lower end of possible values. Higher masses, however, would increase gravitational forces and render thermal energy even less important.
Next, the temperature range appears to be rather tight varying only by a factor of order unity. Henceforth, variation in the appropriate temperature limit cannot significantly tip the ratio of energies. Even assuming an unrealistically high temperature of several hundred Kelvin, which

is the lower temperature limit in our simulations, does not alleviate thermal energy to a level significantly impeding gravitational collapse.
The same line of argumentation goes for the range of possible cloud sizes and geometrical configurations. The extremely low ratio obtained with the standard values is just too small for any reasonable change in the latter numbers to really yield some dominant thermal energy contribution.

Second, for the magnetic field we have already discussed the lack of observational as well as theoretical understanding of the involved processes. For now, we can really just comfort ourselves with ignorance as we are yet technically incapable of simulating any magnetohydrodynamical properties. This might indeed pose one of the largest sources of error in the current work.

Third and last at this point, we consider variations in the nonthermal part of the velocity fluctuations. Lequeux [2005] gives a form of the linewidth-size relation in the form

$$\sigma_{v,\mathrm{nt}} \propto L^{0.5(\pm 0.1)}, \tag{3.15}$$

where $\sigma_{v,\mathrm{nt}}$ is the velocity dispersion we named Δv, and L is the size of the structure. Solomon et al. [1987] determine the proportionality constant for GMCs in the first Galactic quadrant as 0.72 ± 0.07 when $L = (R/1\,\mathrm{pc})$. In the spirit of our approximations we take our standard values and assume

$$\Delta v \equiv 0.8\,\mathrm{km\,s^{-1}} \cdot R_{\mathrm{pc}}^{0.5} \approx 4\,\mathrm{km\,s^{-1}}, \tag{3.16}$$

where R_{pc} is the radius of the cloud in parsec. The squareroot in this relation reduces the quadratic dependence of Equation (3.15) on Δv to a linear one on R. Again, reasonable variations in radius and mass only alter the ratio of energies within plausible values, rendering none of both, neither gravitational nor turbulent energy, a solely dominating component.

CHAPTER 4

Nature and Effects of Turbulence

At this point, we briefly discuss the concepts of turbulence, its role in the interstellar medium and its duality in star formation theory. Owing to the obvious importance of turbulence for this work we give a short theoretical introduction.
We will start with a short summary introducing the general concepts of incompressible turbulence. Subsequently, we will extend this approach to the more general and also more difficult case of turbulence in the interstellar medium. At this point we will focus our discussion on aspects directly related to star formation rather than the ambitious field of general turbulence theory and conclude with our description of a turbulence regulated star formation process.

The Encyclopædia Britannica defines turbulence as

> "type of fluid (gas or liquid) flow in which the fluid undergoes irregular fluctuations, or mixing, in contrast to laminar flow, in which the fluid moves in smooth paths or layers. In turbulent flow the speed of the fluid at a point is continuously undergoing changes in both magnitude and direction [...]".

4.1. A Brief Summary of Incompressible Turbulence

The most elementary and universal features of turbulence are random velocity fluctuations at many scales. These fluctuations result in an overall gas flow. This basic idea is common in all theories of turbulence.
Most studies of turbulence treat incompressible flows, where velocities are subsonic and density changes scale as $\frac{\delta\rho}{\rho} \sim \mathscr{M}^2$, with small Mach numbers ($\mathscr{M} \ll 1$). In this classical picture of turbulence, energy is supplied to the system on the largest scales and subsequently cascades from the largest scales of the system to smaller ones. This transfer of energy ends where the dynamical scale is much shorter than a viscous scale (the length scale on which viscosity acts) and energy is dissipated in the smallest scale structures of the system. Kolmogorov [1941] first introduced an analytic treatment of turbulence in his celebrated theory of incompressible fluid flows.

We can tackle this by starting off with the Navier-Stokes equation (Equation (2.11)). We repeat it here for convenience:

$$\rho\left(\frac{\partial \boldsymbol{v}}{\partial t} + \boldsymbol{v}\cdot\boldsymbol{\nabla}\boldsymbol{v}\right) = -\boldsymbol{\nabla}p + \boldsymbol{F} + \rho\nu\boldsymbol{\nabla}^2\boldsymbol{v} \tag{4.1}$$

Here, we write $\boldsymbol{F}$ as general external force term, i. e. gravity. Note that the term including the viscosity describes the force per unit volume from stresses owing to viscous forces. Relating the two terms in this equation which account for the transport of momentum, namely the nonlinear advection term $\rho\boldsymbol{v}\cdot\boldsymbol{\nabla}\boldsymbol{v}$ and the linear diffusion term $\rho\nu\boldsymbol{\nabla}^2\boldsymbol{v}$, we gain a ratio which determines whether a flow becomes chaotic or not. More precisely, laboratory experiments have shown that large scale velocity fluctuations occur whenever the ratio of advection to diffusion becomes larger than about 100. This either happens when the velocity of the flow becomes very large or when

the viscosity becomes very small. When this ratio approaches the critical regime of chaotic behavior, a transition towards turbulence sets in and vortices, also called eddies, appear in the flow. This transition regime can be identified by a Reynolds number Re which is larger than the above mentioned value.
Aside from experimental observations, the Reynolds number can also be deduced from theoretical considerations. The typical approach is to perform a dimensional analysis on the advection and diffusion terms. Both terms contain the gradient of the characteristic fluid velocity $\boldsymbol{\nabla v}$. We can estimate this gradient within an order of magnitude by relating the absolute value of the characteristic velocity v_l at scale l to that scale. In other words, an eddy of size l inherits an approximate velocity gradient equal to the ratio of its size to the velocity on its largest scale $\boldsymbol{\nabla v} \sim v_l/l$.
From here we can estimate the advection term at the scale l as $\rho v_l^2/l$. Equivalently, the diffusion term can be stated as $\rho\nu v_l/l^2$. Hence we get

$$Re = \left(\frac{\rho v_l^2}{l}\right)\left(\frac{\rho\nu v_l}{l^2}\right)^{-1} = \frac{v_l l}{\nu}. \tag{4.2}$$

For large Reynolds numbers, the advection term dominates over the diffusion term, which stems from the viscous forces. As viscosity damps instabilities, large Reynolds numbers are a prerequisite for the production of turbulence.

In his theory, Kolmogorov [1941] describes turbulence as a cascade of energy from large scales to subsequently smaller ones. Instability of the larger eddies leads to continuous buildup of more numerous but smaller eddies. Energy is transferred from scale to scale until the size of eddies reaches the domain where diffusion becomes more dominant than the other transport terms. The largest scale, where the cascade starts and energy is injected, is called the integral scale L. The scale where advection and diffusion terms become comparable and, therefore, the Reynolds number becomes approximately $Re \sim 1$, is termed dissipative or Kolmogorov scale l_d. At this scale, viscous dissipation starts to transform kinetic energy into heat. The intermediate regime, where energy can freely cascade is known as inertial scale. Here, advection is dominant and dissipation as a result of the diffusion term can be neglected.
Kolmogorov drew two major conclusions from this picture. First, in the inertial domain, statistical properties of the flow are independent of the scale. This is also known as scale invariance or self-similarity of turbulence. Second, the dynamics of a certain scale are dominated by those of adjacent scales.
From the first hypothesis, one can infer the rate of transfer of specific energy, which is energy per unit mass, ϵ. Assuming v_l^2 as kinetic energy per units mass and dividing by some time τ_l for the transfer of that energy we get an order of magnitude estimate of

$$\epsilon \sim \frac{v_l^2}{\tau_l}. \tag{4.3}$$

Deducing the actual transfer time from the time for the inversion of the direction of the characteristic velocity in an eddy of scale l, we can write $\tau_l \sim l/v_l$, and get $v_l \sim (\epsilon l)^{1/3}$. Using this together with the definition of $Re \sim 1$ at the dissipation scale and therefore, $v_d \sim \nu/l_d$, we can calculate an expression for the dissipation scale.

$$l_d \sim \left(\frac{\nu^3}{\epsilon}\right)^{1/4}. \tag{4.4}$$

Switching to Fourier space and using $k = 2\pi/l$ we finally look at the power spectrum $E(k)$ of kinetic energy of turbulence. By definition we set the average kinetic energy per unit mass

between wavenumber k and $k + dk$ to be $E(k)dk$. Integration over all wavenumbers larger than k (equivalently over all scales smaller than l) gives the total specific energy at scale l.

$$\langle v_l^2 \rangle = \int_k^\infty E(k')dk' \tag{4.5}$$

From above we see that this is of order of $(\epsilon l)^{2/3}$ or equivalently $(\epsilon/k)^{2/3}$. Differentiating this with respect to k while ϵ is assumed to be constant for the inertial range, we arrive at the Kolmogorov law

$$E(k) \sim \epsilon^{2/3} k^{-5/3}, \tag{4.6}$$

from which it is obvious that most of the energy is contained in the largest scales.

Another form to express this statistical relation is to correlate the increments of the velocity field with the separation of the corresponding sample points. Taking the n^{th} moment M_n of the absolute value of the difference of two representative velocities $\boldsymbol{v}(\boldsymbol{x})$ and $\boldsymbol{v}(\boldsymbol{x} + \boldsymbol{r})$ separated by the distance $|\boldsymbol{r}|$ is

$$M_n = \langle |\boldsymbol{v}(\boldsymbol{x} + \boldsymbol{r}) - \boldsymbol{v}(\boldsymbol{x})|^n \rangle \propto (\epsilon r)^{n/3}. \tag{4.7}$$

In order to compute these functions one has to average over all positions $\boldsymbol{x}$ and directions $\boldsymbol{r}$. Obviously, Kolmogorov's theory predicts $M_2 \propto r^{2/3}$ for the second order moment. This is also known as the structure function of incompressible turbulence.

4.2. Turbulence in the Interstellar Medium

In most astrophysical applications, we are dealing with situations significantly different from the idealized picture summarized above. The three major caveats are incompressibility, the validity of the fluid approximation, and the diversity of vastly different energy sources.

Certainly, the ISM is a highly compressible medium containing vastly different Mach numbers. These range from subsonic to transsonic in the hot phase and particularly in the warm phase of the diffuse ISM ($\sim 10^4$ K). Moreover, Mach numbers reach the highly supersonic regime with values up to 10 in the cold cloud phase (~ 10 K), and possibly even higher deep inside molecular clouds (up to 50, cf. [Mac Low, 1999]). This means that gas motions are much faster than the sound velocity in the gas. Therefore, the structural appearance of the interstellar gas is highly different from what the incompressible theory can describe. Density spans over almost ten orders of magnitude (see Table (2.1)) with structure on all spatial scales. Moreover, shocks temporarily compress gas to densities high enough for the gas to become self-gravitating and probably trigger its gravitational collapse.

Additionally, it should not go unmentioned that there are potential difficulties considering the fluid approximation. The approximation that the scale of viscus dissipation is always much larger than the mean free path of the atoms and molecules, is basic to all our work. However, for the diffuse cold neutral medium ($T \approx 100$ K, $n \approx 30\,\mathrm{cm}^{-3}$) the approximation appears to be at least questionable. Lequeux [2005] gives an order of magnitude estimate for the viscous dissipation scale in the cold medium of $l_d \approx 3$ AU. The mean free path $\lambda = 1/(n\sigma)$, where $\sigma \approx 10^{-15}\,\mathrm{cm}^2$ is the elastic collision cross-section for hydrogen atoms, evaluates to $\lambda \approx 3.3 \cdot 10^{13}$ cm or roughly $\lambda \approx 2.2$ AU[a]. The actual cross-section is temperature dependent, however, this is neglected here for simplicity. Hence, both scales are getting rather close and the approximation may break

[a] $1\,\mathrm{AU} = 1.49598 \cdot 10^{13}$ cm

down in this regime.

Yet, another source of difficulties is manifest through the different sources of energy input in the ISM. In the classical turbulence theory, energy is always supplied at the largest scales and subsequently cascades to smaller scales. The ISM, however, is essentially driven on all scales. Considering the Galaxy as example, the largest scale energy input is from galactic rotation which shears the gas on kpc scales, injecting large amounts of energy. Supernova explosions are responsible for the input of energy on scales of order up to 100 pc. At roughly 10 pc, we can identify gas motions driven by expanding HII regions as energy sources. Finally, the direct consequences of star formation, namely, outflows and jets deposit energy in the ISM on scales down to tenth of a pc.
Although it is quite difficult to attribute some hierarchy of importance to these mechanisms owing to the fact that their individual couplings to the ISM are rather complex and depending on various parameters, it is obvious that the simple large to small scale propagation of energy is intermittet with additional energy supply on all scales. Additionally, the injection events might be distributed very inhomogeneously in space and time.

We also have seen earlier that magnetic fields seem to influence molecular clouds, and although it is more difficult to obtain reliable values for the magnetic field strength in diffuse gas, where Zeeman splitting measurements are again the best agents for this task, several authors have investigated magnetic fields in the ISM [Ferriere, 1992, Goldreich and Sridhar, 1997, 1995, She and Leveque, 1994]. Especially in recent years, accompanied by the growing feasibility of numerical studies in this field, more attention has been devoted to this interesting task. However, the treatment and effects of magnetic fields is beyond our current scope and we refer interested readers to the literature.

4.3. Driving and Effect of Supersonic Turbulence

Keeping the big picture in mind, we now concentrate towards smaller scales of individual molecular clouds to see how they in return influence the ISM. Since the observation of supersonic motions in these clouds, it has been clear that the inherent turbulence would decay quickly without some effective mechanism preventing the draining of energy. Moreover, supersonic turbulence was believed to decay more quickly than subsonic turbulence as a result of the extreme dissipative nature of shocks, naturally occurring in supersonic turbulence. Theoretical modeling and numerical experiments, however, show this to be incorrect. Mac Low et al. [1998] show indeed that supersonic turbulence decays somewhat more slowly than subsonic one, even though the difference is only marginal and after all, both decay much faster than the a typical free-fall time of a molecular cloud. Mac Low [1999] calculates the cloud's formal dissipation time $\tau_{\rm decay} = E_{\rm kin}/\dot{E}_{\rm kin}$ and examines its ratio to the free-fall time to quantitatively evaluate whether turbulence can delay gravitational collapse of molecular clouds. The authors derive

$$\frac{\tau_{\rm decay}}{\tau_{\rm ff}} = \frac{1}{4\pi\eta_v}\left(\frac{32}{3}\right)^{1/2}\frac{\kappa}{\mathscr{M}_{\rm rms}} \simeq 3.9\frac{\kappa}{\mathscr{M}_{\rm rms}}, \tag{4.8}$$

where $\mathscr{M}_{\rm rms} = v_{\rm rms}/c_s$ is the rms Mach number of the turbulence, the energy-dissipation coefficient is determined as $\eta_v = 0.21/\pi$ and κ is the ratio of driving wavelength to the Jeans wavelength. While typical values for the rms Mach number are observed to be of order 10 and larger in molecular clouds, it is less clear what the ratio of wavelengths κ is. Especially, the driving wavelength remains uncertain owing to the lack of knowledge concerning the exact large scale driving mechanism. Additionally, it is unclear to what we shall determine the Jeans length

in a strongly inhomogeneous medium. Mac Low states a value of $\kappa \leq 1$, not yet confirmed observationally.
However, we know from observations that molecular clouds appear to be several free-fall times of age. If we assume larger values up to $\kappa \lesssim 4$ then turbulence would still vanish within one free-fall time without significant driving. Hence, continuous energy input appears to hold up molecular clouds against gravitational free-fall collapse and prolongs the cloud's lifetime by a factor of several. As discussed in the last section, several different sources of energy are available to produce and maintain or at least delay the decay of the observed turbulent motions. Energy input can stem from the external sources as well as from inside during the lifetime of molecular clouds. Internal sources appear as soon as the cloud has started the formation of stars.

It is this internal feedback which illustrates the dual role of turbulence in molecular clouds. While continuously driven turbulence can support molecular clouds against gravitational collapse, numerical simulations have also shown that local collapse occurs even though turbulent motions carry enough energy to counterbalance gravity in global scales [Klessen et al., 2000].
The idea of a two-faced effect of turbulence on different scales is quite old and was first suggested by Hunter [1979], based on calculations of the virial theorem. The reason for this duality, however, is simple. Any gas flow which is dominated by turbulence, in the sense that turbulent support is much stronger than thermal pressure support, the turbulent support itself stems from supersonic flows. While these high Mach number motions stabilize the flow on their inherent large scales they compress gas in spatially constrained shock regions at the same time. The density of the postshock gas increases by $\sim \mathscr{M}^2$ in an isothermal gas. Therefore, the Jeans length drops by a factor proportional to $\mathscr{M}$ and may render the shocked gas able to collapse while the surrounding flow is still supported by the overall supersonic motions.
In order for turbulence to prohibit collapse completely, it would be necessary to not only counteract gravitational collapse of gas at average molecular cloud density, but especially, at high density of shock compressed gas. Elmegreen [1993], Vazquez-Semadent et al. [1995] pointed out that this is only the case when the rms velocity is sufficiently high, and at the same time, the driving wavelength is sufficiently small. Otherwise, local collapse of overdense regions is inevitable.

Turbulent Fragmentation and the Mass Distribution of Dense Cores. Moreover, supersonic turbulence is believed to be responsible to shape the substructure of molecular clouds. It fragments the clouds in dense sheets, filaments, cores and large low-density voids. Padoan and Nordlund [2002] refer to this process as *turbulent fragmentation* of molecular clouds. The fragmentation will eventually lead to the formation of protostars and is therefore particularly important for generating the initial distribution of stellar masses. In the latter reference and subsequent work [Padoan et al., 2007a], the authors develop and numerically test the model of turbulent fragmentation and derive the mass distribution of gravitationally unstable cores in turbulent clouds based on the probability density function of gas density and the scaling of velocity differences (cf. Equation (4.7)). The Padoan and Nordlund model of turbulent fragmentation is able to produce the power-law distribution of mass for cores larger than $1\,\mathrm{M}_\odot$ in concordance with the slope of the stellar initial mass function $x = 1.4$ (cf. Equation (3.1)) for the case of magnetohydrodynamical considerations. For the hydrodynamical case without magnetic fields, as most probable for primordial star formation where magnetic fields are known to play subordinate role, a slope of $x = 2.5$ is predicted. The slope of these high mass dependencies are directly dependent on the velocity differences in the turbulent medium. The distribution of masses smaller than $1\,\mathrm{M}_\odot$ is determined by the probability distribution of gas density.

In recent work [Schmidt et al., 2008a] we have studied the effects of different numerical realizations of energy input in supersonically turbulent gas and found that physically motivated, compression dominated driving of turbulence produces significant differences in the structure of velocity fluctuations compared to driving by rotational modes. Moreover, compressive driving also influences the distribution of gas densities and causes deviations from lognormal statistics fundamental to the turbulent fragmentation calculations by Padoan et al..
Additionally, we will see in the next Section (4.4) how the turbulence regulated star formation model also includes the assumption of a lognormal distribution of gas densities in molecular clouds. Because of the obvious importance of this issue we come back to the topic in detail in Chapter (8). However, we again stress that studying the detailed physics as well as the distribution of stellar masses is not part of this work.

4.4. Turbulence Regulated Star Formation

Star formation is assumed to take place in the densest clumps of molecular gas. Considering such a core, Krumholz and McKee [2005] (hereafter KM05) use the model of a Bonnor-Ebert sphere [Ebert, 1955, Bonnor, 1956] to describe the star forming clump and calculate gravitational potential energy, thermal energy and the average turbulence kinetic energy of the object which mimics the birthplace of stars. The potential, thermal and kinetic energies are comparable when the Jeans length at the mean density, λ_J, and the sonic length scale, λ_s, defined as the transition scale from supersonic to subsonic turbulence, are equal. If the Jeans length is smaller than the sonic length, $\lambda_J \leq \lambda_s$, collapse will occur. Since the Jeans length is density dependent ($\lambda_J \sim \rho^{-1/2}$) this translates into a density threshold x_{crit} for gravitational collapse and defines the gas overdensity x:

$$x \geq x_{\rm crit} \equiv \left(\phi_x \frac{\lambda_{\rm J0}}{\lambda_s}\right)^2 . \tag{4.9}$$

Here, the definition of the Jeans length at overdensity x, $\lambda_J(x) = \lambda_{\rm J0}/\sqrt{x}$ is used.
Starting from a lognormal density probability distribution function (PDF) of supersonically turbulent gas [e. g., Vazquez-Semadeni, 1994, Ostriker et al., 1999, Padoan and Nordlund, 2002],

$$dp(x) = \frac{1}{\sqrt{2\pi\sigma_\rho^2}} \exp\left[-\frac{\left(\ln x - \overline{\ln x}\right)^2}{2\sigma_\rho^2}\right] \frac{dx}{x} \tag{4.10}$$

$$\overline{\ln x} = -\frac{\sigma_\rho^2}{2} \tag{4.11}$$

$$\sigma_\rho \approx \left[\ln\left(1 + \frac{3\mathscr{M}^2}{4}\right)\right]^{1/2} , \tag{4.12}$$

where $x = \rho/\rho_0$ is the normalized density, $\overline{\ln x}$ is the mean of the log of density, and σ_ρ describes the dispersion of the PDF [Krumholz and McKee, 2005], one can calculate the amount of gas with densities higher than x_{crit}. ϕ_x is a model parameter that needs to be determined by fitting to numerical simulations (see below).
Assuming that the collapsed structures become decoupled from the surrounding turbulence, the remaining gas loses pressure support and new gas begins to collapse. The time scale for this process is approximately the gas' free-fall time, $\tau_{\rm ff}$, multiplied by a second model parameter, ϕ_t. The star formation rate per free-fall time, $\mathrm{SFR_{ff}}$, which is the fraction of an object's gaseous mass that is transformed into stars in one free-fall time at the objects mean density, can then be

computed from

$$\begin{aligned} \mathrm{SFR_{ff}} &= \frac{\epsilon_{\mathrm{core}}}{\phi_t}\int_{x_{\mathrm{crit}}}^{\infty} xp(x)dx \\ &= \frac{\epsilon_{\mathrm{core}}}{2\phi_t}\left[1+\mathrm{erf}\left(\frac{-2\ln x_{\mathrm{crit}}+\sigma_\rho^2}{2^{3/2}\sigma_\rho}\right)\right]. \end{aligned} \tag{4.13}$$

The factor ϵ_{core} is introduced to account for the outflows from star-forming cores and is defined as the fraction of mass that undergoes collapse. It is set to a fiducial value of $\epsilon_{core} = 0.5$ for all numerical calculations by KM05.
The authors determine the two model parameters, ϕ_x and ϕ_t, from a set of 12 smoothed particle hydrodynamics (SPH) simulations of non-magnetic turbulent flows using 205,379 particles. The simulations performed and reported by Vázquez-Semadeni et al. [2003] include self-gravity, random forcing at wavenumbers around $k = 2, 4, 8$ and four different Mach numbers $\mathscr{M} = 2, 3.2, 6, 10$.
In order to derive an equation for $\mathrm{SFR_{ff}}$ depending only on the physical properties of a star-forming cloud, KM05 use the definition of the virial parameter,

$$\alpha_{\mathrm{vir}} = \frac{5\sigma_{\mathrm{tot}}^2 R}{GM} \tag{4.14}$$

[Bertoldi and McKee, 1992], where σ_{tot} is the (one-dimensional) thermal plus turbulent velocity dispersion of the cloud, R is its radius, and M is its mass. As described by KM05, this parameter has to be interpreted as ratio of turbulent kinetic to gravitational energy and is used to describe the stability criterion.
Assuming that at large scales $\sigma_{\mathrm{tot}} \gg c_s$ and, therefore, that the velocity dispersion at the largest scale, $\sigma_{2\mathrm{R}}$, is approximately equal to the turbulent velocity, x_{crit} and hence $\mathrm{SFR_{ff}}$ can be computed in terms of the two dimensionless numbers α_{vir} and $\mathscr{M} = \sigma_{2\mathrm{R}}/c_s$. In turn, $\sigma_{2\mathrm{R}} = (2e_t)^{1/2}$, where e_t is the turbulence kinetic energy. Considering a star-forming region following the linewidth-size relation

$$\sigma_l = \sigma_{2\mathrm{R}}\left(\frac{l}{2\mathrm{R}}\right)^p, \tag{4.15}$$

with $p \approx 0.5$ [Larson, 1981, Solomon et al., 1987, Heyer and Brunt, 2004], the sonic scale is defined as

$$\lambda_s = 2R\left(\frac{c_s}{\sigma_{2\mathrm{R}}}\right)^{1/p}. \tag{4.16}$$

The Jeans length at the mean density ρ_0 is

$$\lambda_{\mathrm{J0}} = \sqrt{\frac{\pi c_s^2}{G\rho_0}} = 2\pi c_s\sqrt{\frac{R^3}{3GM}}, \tag{4.17}$$

and, therefore, the critical overdensity translates into:

$$x_{\mathrm{crit}} = \left(\phi_x\frac{\lambda_{\mathrm{J0}}}{\lambda_s}\right)^2 = \frac{\pi^2\phi_x^2}{15}\alpha_{\mathrm{vir}}\mathscr{M}^{\frac{2}{p}-2}. \tag{4.18}$$

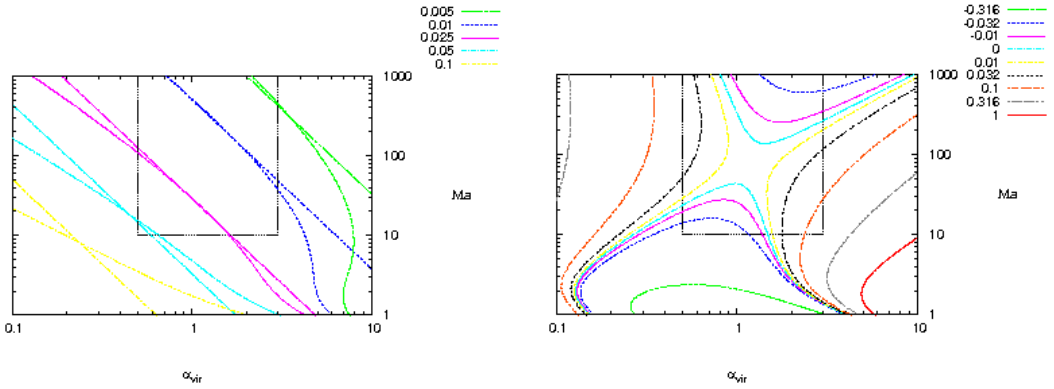

(a) Contour lines depicting the star formation rate per free-fall time in dependence of the virial parameter and the Mach number. The straight lines represent the power-law fit to the contours computed with the actual model.

(b) Contour lines showing the error in the power-law fit, defined as error = (fit - $\mathrm{SFR_{ff}}$)/$\mathrm{SFR_{ff}}$.

FIGURE 4.1. Comparison of the star formation model and its best fit as presented by Krumholz and McKee [2005].

Now, $\mathrm{SFR_{ff}}$ can be derived from Equation (4.13) with the help of Equation (4.12) and (4.18):

$$\begin{aligned} \mathrm{SFR_{ff}} &= \frac{\epsilon_{\mathrm{core}}}{2\phi_t}\left[1+\mathrm{erf}\left(\frac{-2\ln\left(\frac{\pi^2\phi_x^2}{15}\alpha_{\mathrm{vir}}\mathscr{M}^{\frac{2}{p}-2}\right)+\sigma_\rho^2}{2^{3/2}\sigma_\rho}\right)\right] \\ &= \frac{\epsilon_{\mathrm{core}}}{2\phi_t}\left[1+\mathrm{erf}\left(\frac{-2\ln\left(\frac{\pi^2\phi_x^2}{15}\alpha_{\mathrm{vir}}\mathscr{M}^{\frac{2}{p}-2}\right)+\ln\left(1+\frac{3\mathscr{M}^2}{4}\right)}{2^{3/2}\left[\ln\left(1+\frac{3\mathscr{M}^2}{4}\right)\right]^{1/2}}\right)\right] \end{aligned} \tag{4.19}$$

The total star formation rate per free-fall time within a cloud with molecular gas mass M_{mol} is

$$\dot{M}_* = \mathrm{SFR_{ff}}\frac{M_{\mathrm{mol}}}{t_{\mathrm{ff}}}. \tag{4.20}$$

Note that although Equation (4.19) appears massive, it only has α_{vir} and $\mathscr{M}$ as dependend parameters. KM05 give that $\epsilon_{\mathrm{core}} = 0.5$ is set on physical grounds and $\phi_x = 1.12$ as well as $\phi_t = 1.91$ are determined by fitting to numerical simulations.
The latter authors also give a power-law fit to the predictions of the model equation. Using the above stated values KM05 calculate

$$\mathrm{SFR_{ff}} = 0.014\left(\frac{\alpha_{\mathrm{vir}}}{1.3}\right)^{-0.68}\left(\frac{\mathscr{M}}{100}\right)^{-0.32} \tag{4.21}$$

In Figure (4.1) we show the dependence of $\mathrm{SFR_{ff}}$ on the model parameters for both, the analytical equation and the presented power-law fit. Additionally, we follow the original authors and also show the error in the power-law fit approximation. We have marked the region of $\alpha_{\mathrm{vir}} = 0.5 - 3$ and $\mathscr{M} = 10 - 1000$ in these plots to highlight the domain where most of star formation is claimed to be happening. Indeed, the error in this regime is rather small, of the order of a few percent.

More technically, with respect to simulations, the information needed to compute the local value

of the total star formation rate, $\dot{M}_*$, (cf. Equation (4.20)) in a grid cell of a simulation consists of the local free-fall time $\tau_{\rm ff}$, the molecular mass $M_{\rm mol}$, and the star formation rate $\mathrm{SFR}_{\rm ff}$. The first two quantities can be directly computed from suitably averaged local state variables. Moreover, $\mathrm{SFR}_{\rm ff}$ can be parameterized in terms of $\mathscr{M}$ and $\alpha_{\rm vir}$.
Note that, by virtue of the subgrid-scale nature of the proposed model, $\mathscr{M}$ here stands for the amplitude of velocity fluctuations on scales below the grid cutoff Δ (as opposed to the grid scale fluid velocity provided by the hydro code) which has to be calculated from the SGS turbulent kinetic energy, $e_t(l \leq \Delta) \equiv e_{\rm sgs}$, provided by FEARLESS. Similarly, $\alpha_{\rm vir}$ follows from the ratio of the local turbulent kinetic energy on subgrid-scales and potential energy, $\alpha_{\rm vir} \propto e_{\rm sgs}/E_{\rm pot}$. The ability of FEARLESS to predict $e_{\rm sgs}$ enables us to directly calculate the star formation rate per free-fall time, implementing the KM05 model as a subgrid-scale model for star formation.

To summarize, the star formation rate proposed by KM05 depends sensitively on the amplitude of turbulent velocity fluctuations on the scale of the collapsing cloud region. If this region is numerically unresolved, as is the case in simulations on galaxy scales or larger, a subgrid-scale model for unresolved turbulence is required in order to determine e_t and, hence, $\mathrm{SFR}_{\rm ff}$. The implementation of the semi-localized turbulence SGS model described in Schmidt et al. [2006a] into the cosmological hydrocode ENZO as part of the FEARLESS project in our group, provides us with the unique ability to model turbulence regulated star formation on subgrid-scales as proposed by KM05.

Summary of Theory

In this first Part (I) we have presented the most important physical concepts relevant for our work. With our eventual goal in mind to study turbulence regulated star formation in simulations of galactic systems we have described the gross properties of such systems. Furthermore, we have discussed the structure of galaxies in a hierarchical manner starting at the overall shape, subsequently broaching the issues of interstellar material and the substructures that form therein. We have illustrated the picture of a multiple, three-phase interstellar medium and reasoned for its theoretical as well as observed existence. Additionally, we have discussed how cold dense clouds, the hosts of most of star formation, emerge and how they evolve.
Next, we have given a quantitative evaluation of the most often discussed physical processes in star formation theory. We wanted this to serve two objectives. Firstly, we motivated our focus on turbulence in the star formation process as one of, or probably, the most important agent opposing gravitational contraction. Secondly, acquiring a general basis of comparison enabled us to estimate the error margin contained in our work as we necessarily omit several aspects of the full star formation problem in order to retain a manageable problem. The exclusion of magnetic fields appeared to be likely the most severe shortcoming we have to cope with and bear in mind when drawing our conclusions.
We completed the theoretical part with an introduction to the earlier singled out star formation regulation mechanism, turbulence. Here, we constructed the most elementary concepts which we will use in the following parts as fundament for the implementation and understanding of the model we use to capture turbulence effects in our simulations. Concluding this first part, we gave a description of the turbulence regulated star formation algorithm we will employ in these simulations.

Now, we will proceed to Part (II) and describe the numerical endeavors we have gone for along the plan of this work.

Part II

Toy Models and the Playground

CHAPTER 5

The Simulation Framework

In order to model star formation in disk galaxies from first principles, one needs a good understanding of the evolution and lifetime of molecular clouds, the influence of turbulence, rotation and magnetic fields on gravitational instability, as well as feedback from supernovae, ionizing radiation, stellar outflows, and galactic winds. Obviously, this challenging program is beyond our current abilities and would certainly exceed the scale of this thesis.
Instead, we invoke Occam's razor and ignore in our explicit treatment all effects but one, supersonic turbulence, as formulated in the KM05 model assumptions. We refer to Section (4.4) for a description of the approach.
Most galaxy simulations include a dark matter halo (either static or dynamical), a disk of stars, and a gas component. One of the basic tests for simulations of star formation in galaxies is their reproduction of the Kennicutt-Schmidt (KS) law, Equation (1.1), with the eventual goal to understand the mechanisms which lead to the observed behavior.
In this Part (II) we will therefore develop and describe the numerical techniques and methods used for the simulation of star formation in isolated disk galaxies.

5.1. The Hydrodynamics Code Enzo

The simulation framework we use for our numerical simulations is the adaptive mesh refinement (AMR), grid-based hybrid code (hydrodynamics + N-Body) Enzo which was originally designed to do simulations of cosmological structure formation. Enzo's home is the *Laboratory for Computational Astrophysics, LCA, University of California, San Diego*. The code is publically available in its original version (1.0.1) released March 1st, 2004 from
`http://lca.ucsd.edu/portal/software/enzo`.
O'Shea et al. [2004] published a general description of the simulation code. Enzo was designed to perform 3-dimensional cosmological simulations of structure formation. As a result of its general ability to solve the equations of Eulerian hydrodynamics it can readily be applied to a variety of different astrophysical problems.
In order to operate on massively parallel computational infrastructures, Enzo is parallelized using the application programming interface MPI (Message Passing Interface). The adaptive mesh refinement works in a block-structured fashion and is controlled via several parameterized refinement criteria such as threshold values, differences and gradients of calculated simulation quantities.
Furthermore, Enzo includes a full scale N-body solver to simulate particle evolution, such as a dynamical dark matter distribution, using the particle-mesh technique. The Poisson equation is solved using a combination of fast Fourier transform and multigrid techniques for a periodic basis/root grid and non-periodic refinement grids, respectively.
The equations of hydrodynamics are solved either with an implementation of the piecewise parabolic method (PPM) or a much more stable implementation of the Zeus algorithm. The latter is significantly more dissipative during the treatment of strong shocks and discontinuities while

the former has severe numerical problems when combined with additional physics in some simulations.
Enzo comes with a whole set of such physics packages like implementations for radiative cooling or global ultraviolet background radiation. In some non-official pre and post release versions there are also additional packages for cosmological star formation and even feedback. However, all the additional packages were initially conceptualized for cosmological structure formation simulations. Although it has turned out that some of the general infrastructure of Enzo can conveniently be adopted to include additional physics, the packages themselves have to be carefully reconsidered and strongly adopted to the simulation problem, without loosing track of the original intension of the package, in order not to introduce severe numerical and physical errors.

Additional references to the code are, Norman et al. [2007] who again describe the technical side of Enzo in details, Wang et al. [2008], Regan et al. [2007], Hallman et al. [2007] which are just a selection of most recent applications and Collins and Norman [2004], Xu et al. [2008] who report the ongoing development and implementation of a magnetohydrodynamics module.

5.2. The Zeus Algorithm and its Implementation

Originally built into Enzo for testing and verification of the PPM implementation, the Zeus hydrodynamics algorithm [Stone and Norman, 1992a] is a complete alternative to the former. The Enzo documentation states that the staggered grid, finite difference method uses artificial viscosity as a shock-capturing technique and is formally first-order-accurate when using variable timesteps.
Although we would have preferred to use the PPM algorithm for our simulations we had to resort to the Zeus solver owing to the infeasibility of operating PPM in combination with our cooling physics for interstellar gas. For PPM a more complex high-order Godunov method is implemented [Woodward and Colella, 1984]. As stated earlier, PPM appears to be less diffusive and can follow strong gradients in more detail than the implementation of the Zeus algorithm in Enzo is capable of. However, Zeus employs artificial viscosity to ensure that the difference equations will give correct Rankine-Hugoniot relations across shocks and the correct shock velocity. The Rankine-Hugoniot equations govern the behavior of shock waves normal to the oncoming flow. The idea is to consider one-dimensional, steady flow of a fluid subject to the Euler equations and require that mass, momentum, and energy are conserved. A shortcoming is that shocks will be spread unphysically across several computational zones. Hence, one loses the details of the flow structure as a result of shocks and cannot study the details of the shock themselves unless adaptive mesh techniques are used to increase the shock resolution. Therefore, we employed AMR to resolve down to the overall scale of roughly a molecular cloud. We argue that for the physical regime we aim to explicitly simulate, the accuracy of the Zeus solver is sufficient to yield reliable and physically meaningful results. The detailed structure and physics within molecular cloud scale is approximated via implicit subgrid models. More importantly, we are capable to combine the Zeus hydrodynamics with the additional cooling, star formation and feedback physics we consider essential for our simulation of galactic scale star formation. Although we invested some serious effort, it was not possible to operate cooling and star formation with the PPM implementation in Enzo.

The algorithm encoded in Enzo to solve the hydrodynamical equations is a 3-dimensional version of the code described in a series of publications by Stone and Norman [1992a,b], Stone et al. [1992], Clarke et al. [1990].

Details of the ZEUS Algorithm. At the most fundamental level, the ZEUS hydrocode is an implementation of certain specific numerical algorithms to solve the equations of hydrodynamics (Equation (2.1), (2.2) and (2.3)). The implementation in ENZO is based on the method of finite-differences and takes advantage of the high degree of simplicity as well as the robustness and speed of this method. These are also the reasons which make it feasible to add the additional physics described in the next sections.
Note that while the PPM implementation in ENZO uses the conservation law of total energy, ZEUS uses the internal energy equation in order to achieve high accuracy in supersonic flows. When using PPM it is necessary for ENZO to use a so called dual-energy formalism, which computes the internal energy explicitly in an additional step and synchronizes internal and total values to be consistent, to reach comparable accuracy and therefore numerical stability in this regime. The ENZO user guide states that the use of the dual-energy implementation is needed to make total energy scheme PPM stable and accurate when the ratio of thermal energy to total energy is significantly smaller than one. ZEUS does not have these problems.

For a more detailed description on the ZEUS algorithm and the equations which are actually solved, we closely follow the description in Stone and Norman [1992a]. For simplicity and better comprehensibility we stick to the two-dimensional formulation of the latter authors, although an extension to three dimensions is straightforward.
The method of finite-differences for solving hyperbolic PDEs is based on the discretization of the dependent variables over the entire spatial computational domain. The algebraic finite-difference approximations to the evolution equations can then be computed as solutions on the discrete mesh. In order to identify boundaries, cells and coordinates on the mesh, Stone and Norman define two computational grids, using coordinate vectors. Zone boundaries are described by the 'a-grid' while zone or cell centers are specified by the 'b-grid'. Following the original authors' formalism, we introduce the discrete notation of any quantity x, i. e. position, and write $x1$ for the *left* boundary and $x2$ for the *lower* boundary of any cell. We use i and j as coordinates in a two-dimensional mesh to identify the (i, j)-zone. Consequently, $x1a_i$ is the left boundary of any ith cell and $(x1b_i, x2b_j)$ is the unique coordinate position of the center of cell (i, j). Figure (5.1) illustrates the usage of the coordinate and grid definitions.
Using the coordinate description, ZEUS works with cell centered scalar quantities and boundary or face-centered vector quantities. Therefore, the authors use this formalism to write the hydrodynamical variables as

$$\begin{aligned}
\rho(x_1, x_2) &\rightarrow d(x1b_i, x2b_j) = d_{ij}, \\
e(x_1, x_2) &\rightarrow e(x1b_i, x2b_j) = e_{ij}, \\
v_1(x_1, x_2) &\rightarrow v1(x1a_i, x2b_j) = v1_{ij}, \\
v_2(x_1, x_2) &\rightarrow v2(x1b_i, x2a_j) = v2_{ij}, \\
v_3(x_1, x_2) &\rightarrow v3(x1b_i, x2b_j) = v3_{ij}, \\
\Phi_1(x_1, x_2) &\rightarrow \Phi(x1b_i, x2b_j) = \Phi_{ij}.
\end{aligned}$$

We use this notation to formulate the equations solved by the numerical algorithm. The individual parts of the solution procedure of the ZEUS solver are grouped into two major steps. The first is called *source* step and solves for the finite-difference approximations to

$$\frac{\partial}{\partial t}(\rho \boldsymbol{v}) = -\boldsymbol{\nabla} p - \rho \boldsymbol{\nabla} \Phi - \boldsymbol{\nabla} \cdot \boldsymbol{Q}, \tag{5.1}$$

$$\frac{\partial}{\partial t}(\rho e) = -\boldsymbol{\nabla} \cdot \boldsymbol{v} p - \boldsymbol{Q} \times \boldsymbol{\nabla} \boldsymbol{v}. \tag{5.2}$$

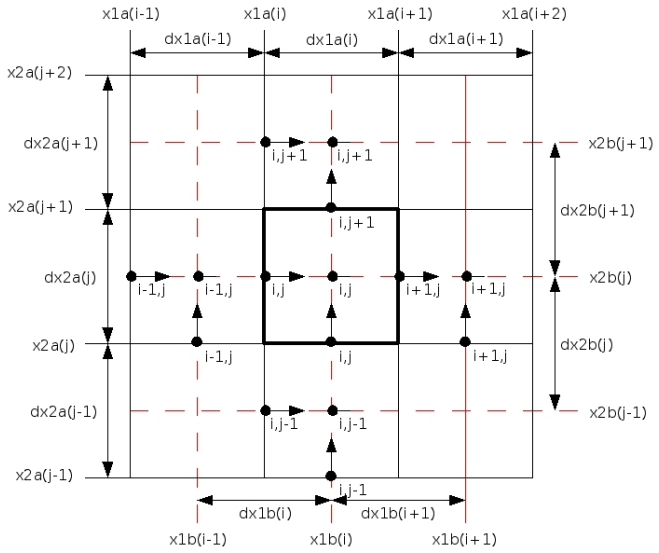

FIGURE 5.1. Illustration of the vector coordinates in a two-dimensional mesh. Zone edges are described by the a-mesh, while the b-mesh locales the cell centers.

The additional terms appearing here are introduced into the equations to account for viscous stresses and dissipation as a result of artificial viscosity $\boldsymbol{Q}$. As mentioned earlier, this artificial viscosity acts to smooth possibly occurring discontinuities in the flow, where otherwise the finite-difference equations break down. In order to minimize these effects in smooth parts of the flow, the artificial viscosity is chosen nonlinearly to be large in shocks, but small or better negligible otherwise.
The second step, named *transport* step, solves the finite-difference approximations to the integral equations to account for the fluid advection.

$$\frac{d}{dt}\int_V \rho dV = -\int_{dV} \rho \boldsymbol{v}\cdot\boldsymbol{dS} \tag{5.3}$$

$$\frac{d}{dt}\int_V \rho \boldsymbol{v} dV = -\int_{dV} \rho \boldsymbol{v}\boldsymbol{v}\cdot\boldsymbol{dS} \tag{5.4}$$

$$\frac{d}{dt}\int_V e dV = -\int_{dV} e\boldsymbol{v}\cdot\boldsymbol{dS} \tag{5.5}$$

These integral equations can be derived from the continuity equation and the divergence theorem. Note that while the original algorithm includes terms to account for a moving coordinate grid, we have omitted these additional complications here. The authors state to have chosen to solve the integral form of the equations in order to use a conservative differencing scheme. The major advantage of such a scheme is that the total quantity of the advected variable on the grid is preserved to high accuracy.

To compute the solution, the source step is subdivided into three substeps using the operator split method.

The Source Step. In the first *substep I* the code updates the velocities owing to pressure gradients and gravitational forces (again we omit terms for moving coordinates). In the following,

Stone and Norman use the superscript n to denote quantities at hand after the completion of a full calculation cycle, therefore also initial quantities at the beginning of the next cycle. $n+a$, $n+b$ and $n+c$ denote partially updated quantities after each of the following substeps, respectively. In *substep I* velocities are updated:

$$\frac{v1_{i,j}^{n+a} - v1_{i,j}^{n}}{\Delta t} = -\frac{p_{i,j}^{n} - p_{i-1,j}^{n}}{dx1b_i(d_{i,j}^{n} + d_{i-1,j}^{n})/2} - \frac{\Phi_{i,j}^{n} - \Phi_{i-1,j}^{n}}{dx1b_i} \tag{5.6}$$

$$\frac{v2_{i,j}^{n+a} - v2_{i,j}^{n}}{\Delta t} = -\frac{p_{i,j}^{n} - p_{i,j-1}^{n}}{dx2b_j(d_{i,j}^{n} + d_{i,j-1}^{n})/2} - \frac{\Phi_{i,j}^{n} - \Phi_{i,j-1}^{n}}{dx2b_j} \tag{5.7}$$

At the beginning of this step, the pressure $p_{i,j}^{n}$ is computed from the equation of state and the gravitational potential $\Phi_{i,j}^{n}$ is derived as solution to the Poisson equation. For details, please refer to the cited reference of the original authors, here we only present major steps of the hydrodynamical algorithm.

In the second *substep II* the code adds the terms of artificial viscous stress and gas heating.

$$\frac{v1_{i,j}^{n+b} - v1_{i,j}^{n+a}}{\Delta t} = -\frac{q1_{i,j} - q1_{i-1,j}}{dx1b_i(d_{i,j}^{n} + d_{i-1,j}^{n})/2} \tag{5.8}$$

$$\frac{v2_{i,j}^{n+b} - v2_{i,j}^{n+a}}{\Delta t} = -\frac{q2_{i,j} - q2_{i,j-1}}{dx2b_j(d_{i,j}^{n} + d_{i,j-1}^{n})/2} \tag{5.9}$$

$$\frac{e_{i,j}^{n+b} - e_{i,j}^{n}}{\Delta t} = -q1_{i,j}\left(\frac{v1_{i+1,j} - v1_{i,j}}{dx1a_i}\right) - q2_{i,j}\left(\frac{v2_{i,j+1} - v2_{i,j}}{dx2a_j}\right) \tag{5.10}$$

For the multidimensional realization, these equations use the zone-centered viscous pressure q to separately update each dimension. Therefore, the pressure is defined as

$$q1_{i,j} = \begin{cases} C_2 d_{i,j}(v1_{i+1,j} - v1_{i,j})^2 & \text{if } (v1_{i+1,j} - v1_{i,j}) < 0 \\ 0 & \text{otherwise} \end{cases}, \tag{5.11}$$

$$q2_{i,j} = \begin{cases} C_2 d_{i,j}(v2_{i,j+1} - v2_{i,j})^2 & \text{if} (v2_{i,j+1} - v2_{i,j}) < 0 \\ 0 & \text{otherwise} \end{cases}, \tag{5.12}$$

where the dimensionless constant $C_2 = l/\Delta x$ measures the number of cells over which the artificial viscosity will spread shocks when l is a dimensionless length determining the strength of the viscosity.

To complete the source step, the code adds the term for compressional heating in *substep III*. As we are using an equation of state for an ideal gas an implicit update technique can be used, involving the time-centered pressure $p^{n+1/2}$. This additionally improves energy conservation. We get

$$(e^{n+1} - e^{n})/(\Delta t) = -p^{n+1/2}\boldsymbol{\nabla} \cdot \boldsymbol{v}, \tag{5.13}$$

where the time-centered pressure is defined as $p^{n+1/2} = (p^{n} + p^{n+1})/2$. Together with the equation of state $p = (\gamma - 1)e$ this gives an explicit expression for e^{n+1} to be differenced as

$$e_{i,j}^{n+c} = \left[\frac{1 - (\Delta t/2)(\gamma - 1)(\boldsymbol{\nabla} \cdot \boldsymbol{v})_{i,j}}{1 + (\Delta t/2)(\gamma - 1)(\boldsymbol{\nabla} \cdot \boldsymbol{v})_{i,j}}\right] e_{i,j}^{n+b}. \tag{5.14}$$

Hereby, the source step is completed. Next, the code proceeds with the transport step and to solve the finite-difference approximations to Equations (5.3-5.5).

The Transport Step. The latter equations state that the rate of change of any variable q within the volume of a zone centered on q, named control volume, is equal to the divergence of the flux of q through the faces of the control volume. A space and time second-order-accurate approximation of time evolution of finite-differences can be written as

$$[(q_{i,j}^{n+1} - q_{i,j}^{n})\tau_{i,j}]/(\Delta t) = -(\mathcal{F}_{i+1,j}^{1} - \mathcal{F}_{i,j}^{1} + \mathcal{F}_{i,j+1}^{2} - \mathcal{F}_{i,j}^{2})^{n+1/2}, \tag{5.15}$$

where τ is the constant control volume and $\mathcal{F}^k$ is the flux in the kth direction. Using directional splitting, the advection problem can be simplified for multidimensional problems. For the above two-dimensional problem two one-dimensional updates can be used. The first step is a sweep in 1-direction

$$\frac{(q_{i,j}^{n+a} - q_{i,j}^{n})\tau_{i,j}}{\Delta t} = -[\langle v1_{i+1,j} q_{1,i+1,j}^{*} A_{1,i+1,j}\rangle - \langle v1_{i,j} q_{1,i,j}^{*} A_{1,i,j}\rangle], \tag{5.16}$$

completed by a second sweep in 2-direction

$$\frac{(q_{i,j}^{n+1} - q_{i,j}^{n})\tau_{i,j}}{\Delta t} = -[\langle v2_{i,j+1} q_{2,i,j+1}^{*} A_{2,i,j+1}\rangle - \langle v2_{i,j} q_{2,i,j}^{*} A_{2,i,j}\rangle]. \tag{5.17}$$

Here, $q_{k,i,j}^{*}$ is the value of q interpolated to the surface of the control volume $A_{k,i,j}$ and describes the area of the control volume interface, both in kth direction. All quantities on the right hand side of the latter equations are time centered, denoted by the angle brackets.
One of the most difficult aspects of the calculation is now to compute the time-averaged, interpolated value of the variable q at the faces of the control volume. For a detailed discussion of different methods, i. e. donor cell method (first-order), van Leer method (second-order) and piecewise parabolic advection method (third-order), we again refer to the original paper [Stone and Norman, 1992a]. Note, piecewise parabolic advection in Zeus is not equivalent to the alternative piecewise parabolic method solver in Enzo. Here we complete the discussion by presenting the van Leer method used in Enzo. This method is popular owing to its high accuracy while still being a fast algorithm.
The method uses a piecewise linear function to represent the distribution of q within a zone. Thus, we get

$$q_i^{*} = \begin{cases} q_{i-1} + (\Delta x_{i-1} - v_i \Delta t)(dq_{i-1}/2) & \text{if } v_i > 0 \\ q_i + (\Delta x_i - v_i \Delta t)(dq_i/2) & \text{if } v_i < 0 \end{cases}. \tag{5.18}$$

The monotonized van Leer slopes dq_i are computed from harmonic averages

$$dq_i = \begin{cases} \frac{2(\Delta q_{i-1/2} \Delta q_{i+1/2})}{\Delta q_{i-1/2} + \Delta q_{i+1/2}} & \text{if } \Delta q_{i+1/2} \Delta q_{i-1/2} > 0 \\ 0 & \text{otherwise} \end{cases}. \tag{5.19}$$

Here, $\Delta q_{i+1/2} = (q_{i+1} - q_i)/\Delta x_i$.

Summing up, the hydrodynamic variables are computed via two major steps. Beginning with the source step and its three substeps, followed by the transport step, the code updates all variable values. The full algorithm has several additional amendments which we have not presented here. Among them, the algorithm solving for the Poisson equation, symmetry considerations during the computation of fluxes and the problem of numerical diffusion minimized through the application of consistant transport which accounts for better local conservation of the variables. Finally, although the original algorithms are formulated including variable coordinates such as moving grids, we have deliberately re-written all presented equations without the respective terms. Firstly, we do not use any variable coordinates throughout this work, and secondly, this renders the equations somewhat more readable.

Differences and Problems with PPM. Most generally, PPM is an implementation of the high-order Godunov method developed by Woodward and Colella [1984]. It combines a third-order interpolation, which can be conceptualized as an improved version of the second-order algorithm presented above, with a Riemann solver to evolve the hydrodynamic equations. Although there are several methodical differences, the problem of evolving the hydrodynamical variables in PPM can be reduced to the problem of finding the variable values at the left and right edges of a zone [Bryan et al., 1995]. The authors state this to be simple in principle, although accuracy requirements as well as the need for monotonicity complicate issues. Although complicated, the desired values are still straight forward to calculate and the complete equations are given in Woodward and Colella [1984, Eq. (1.7) and (1.10)]. Using these interpolated values one can compute the characteristic domain of any zone edge. The characteristic domain of a zone edge is the farthest a sound wave can travel in order to reach the interface by the end of a timestep [Bryan et al., 1995]. Therefore, this domain holds all the information possibly available in that zone during the timestep. By averaging all characteristic domains, two constant states are created, separated by a discontinuity. This is called a Riemann problem, its solution is well-known, self-similar and relatively easy to compute. The application of a Riemann solver enforces the Rankine-Hugoniot conditions across shocks and therefore avoids the necessity of artificial viscosity. In the limit of a smooth flow, the characteristic equations yield time-centered quantities.

Generally, PPM would be the method of choice for most astrophysical applications owing to the higher order accuracy and its ability to capture shocks and strong gradients without the need of artificial smoothing by viscosity terms. However, these advantages come at the cost of computational resources and the acceptance of a more complicated numerical realization of the algorithm. Usually, one would present a comparison of both methods for the problem at hand and then argue for a particular choice based on physical feasibility, resources or other practical issues. In our case such a comparison was only possible without the additional complication of a radiative cooling realization. However, as cooling is essential for our work and this additional manipulation of the energy equations resulted in severe problems and perpetual errors in the numerical algorithms, we could not perform any simulation with PPM including radiative cooling. Most likely, large, hypersonic bulk flows with high ratio of kinetic energy to internal gas energy are the source of errors here. Although Enzo has the possibility to treat energies in the so called dual-energy formalism to account for this problem, the algorithms have never been intended for our extended cooling mechanism which realizes cooling close to the temperature of the cold ISM phase.

As it was not the goal of this thesis to study the effects and differences of different numerical methods, we decided, after some unsuccessful effort to resolve the problem, to follow recent work [Tasker and Bryan, 2006] and use the Zeus algorithm which uses internal energy rather than the conservation of total energy, to improve the accuracy of internal energy and temperature computations for highly supersonic flows, in the first place.
Henceforth, all discussion of simulations refers to work using Zeus. Next, we detail the above mentioned radiative cooling routine.

5.3. Thermodynamical Processes and their Realization

The public Enzo 1.0.1 webrelease includes the general possibility to explicitly treat heating and cooling. This is realized by simply adding new terms to the energy Equation (2.3) or more technically by modifying the particular energy content of simulation cells.

Enzo features two different techniques to calculate heating and cooling rates. The first method is a multi-species calculation where the code directly computes the abundance of up to twelve species (H, H+, He, He+, He++, e-, H2, H2+, H-, D, D+ and HD) based on a backward differenced multi-step algorithm, tailored for cosmological simulations.
The second possibility is to use tabulated equilibrium cooling data which consist of pairs of temperature values and corresponding cooling rates. Again, these data and their algorithmic implementation were originally intended for cosmological simulations. The tabulated temperature ranges from $10^4 - 10^9$ K in the table that comes with Enzo's web-release and the calculation of the energy update uses an implicit (hard coded) mean molecular weight of $\mu = 0.6$.
For this work, we choose to use and adopt the second method of tabulated cooling data, as described hereafter, while for other simulations our group has also developed dynamical procedures to calculate the cooling rate in the fashion presented by Audit and Hennebelle [2005].

Cooling laws and Cooling Rates. Gas cooling in the ISM is a very broad topic. Depending on the specific problem one wants to investigate it might be necessary to develop a very detailed treatment of the various physical mechanisms involved. Contrarily, it might also be possible to use major simplifications when parameter space can be physically constrained.
For our galaxy scale simulations, where the resolution is limited to the largest scale of molecular clouds, it is possible to find and motivate some simplifications and introduce a general and rudimentary solution.

Fine-structure line cooling dominates almost everywhere in the ISM. Exceptions to this are only very hot gas and the insides of molecular clouds. To be complete, other mechanisms may be of importance within strong shocks and in HII regions [Lequeux, 2005].
However, here we first focus on line cooling and discuss different temperature regimes, starting at the low temperatures of the order of ~ 100 K. The cooling efficiency of atomic and molecular line transitions obviously depends on the abundance of trace elements, and the fact that these have fine-structure levels that are easy to excite. At low temperatures, typical candidates existent in sufficient numbers and having energy levels close to their fundamental level are CII and OI. Depending on the degree of ionization, some heavier elements like Si^+ and Fe^+ might also contribute significantly. At temperatures above several hundreds of Kelvin, the cooling ability starts to rise slowly and above roughly 6000 K the excitation of low-lying Oxygen and Nitrogen starts.
Increasing the temperature further above 10^4 K cooling by collisional excitation of neutral Hydrogen becomes more efficient. We observe the famous Lyman-α emission. The extraordinary steep increase of the cooling rate at this temperature is not only a result of the fact that Lyman-α cooling becomes dominant, but, moreover, it is owed to a sharp increase in collisional ionization that occurs, rendering the excitation process much more efficient [Tielens, 2005].
Additionally, highly ionized trace elements of C, O and Fe can again contribute importantly to the cooling for even higher temperatures.
Above roughly 10^5 K ionization is almost completely realized and most species retain very little bound electrons. Therefore, the cooling rate starts to decline. Additionally, Bremsstrahlung becomes the dominant cooling agent and dielectric recombination of He and heavier elements can contribute in high temperature plasma.

This picture of an interstellar cooling curve for the different temperature regimes can be resampled with the previously mentioned simplified model. To reach this goal, we have omitted the influence of interstellar dust and molecular hydrogen H_2. Furthermore, we assume some

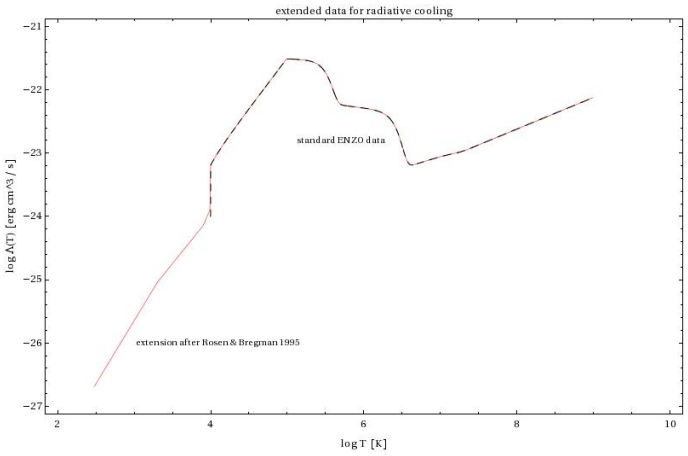

FIGURE 5.2. Cooling curve as function of temperature assumed in our simulations.

constant ionization state above 10^4 K for all elements (usually the approximation of a fully ionized medium is considered). And we ignore the depletions of some of the cooling species (most importantly carbon and oxygen). With these assumptions we are left with a static cooling curve as depicted in Figure (5.2).

The first simplification is indeed the most cruel one, since especially low temperature H_2 cooling and dust chemistry shape the physics at the level below several hundred Kelvin. The inclusion of these processes is, however, highly nontrivial. It would require not only to simulate the full multi-species gas content, but at least to some extent also the microphysics of interstellar gas. Again, we can state that our resolution limit prevents the study of these effects, however, they are still important for the physics we want to describe. We argue to indirectly account for the neglected direct treatment by including the gross effects of low temperature cooling in the subgrid treatment of molecular clouds. In other words, as we are not going to resolve inside MCs, we model their inherent properties by global averages.
The second simplification of a fully ionized ISM above 10^4 K is less critical since we can assume the abundance of the relevant trace elements to be relatively low at this point.
With respect to the previous two simplifications and the errors we have to accept in order to arrive at our simplified solution, the third simplification, namely neglecting elemental depletions, is a minor caveat. The relative elemental abundances and the rates of their evolution are highly speculative and differ vastly for different galaxies and within the ISM of individual galaxies. By neglecting the depletion completely, we only add a very small error to our cooling model, with respect to the best we could do otherwise, but finally achieve a general solution.

Figure (5.2) shows the tabulated cooling data we employ for our simulations. The black dashed line depicts to original data supplied with the ENZO web release. Again, these data are intended for cosmological simulations and therefore do not include any cooling mechanisms below 10^4 K. The reason is that in high redshift cosmological simulations there are essentially no elements for fine-structure cooling processes below 10^4 K. We can apply these high temperature cooling rates to our simulations for galactic and intergalactic gas. Additionally, we have to extend the data to somewhat lower temperatures. The red, continuous line depicts our full, extended cooling rates which range from ~ 300 to 10^9 K.
We have extensively experimented with different numerical and analytic derivations of cooling

data. We tested data calculated by a numerical implementation of Audit and Hennebelle who followed closely the analytic work of Wolfire et al. [1995, 2003]. Vázquez-Semadeni et al. [2007] give an analytic expression based on the work of Koyama and Inutsuka [2002, 2000]. The authors Kritsuk and Norman [2002] where so kind to provide us with their tabulated cooling data and we also followed Tasker and Bryan [2006] and extended the Enzo cooling table with values computed with the analytic expressions in Rosen and Bregman [1995]. The last option actually goes back to the early work of Dalgarno and McCray [1972] and Raymond et al. [1976].
Without presenting detailed analysis and results here, we only summarize that the resulting differences of these approaches, however, showed to imply only marginal effects. The temperature and gas phase distributions in galaxy test simulations developed differences of the order of a few percent, much less than the systematic errors introduced by the gross basic simplifications.
Additionally, we note that the cooling time is much less than the dynamical time for high density, rapidly cooling gas. Therefore most gas in this phase will quickly reach the minimum temperature. The details of the cooling process can be completely neglected as a result of the speed of the process. We can estimate the cooling timescale when we ratio thermal energy and its rate of change

$$\tau_{\text{cool}} \approx \frac{k_b T}{n\Lambda(T)}. \tag{5.20}$$

Using our temperature cutoff value of 300 K, a number density $n = 100\,\text{cm}^{-3}$ of cold dense gas and the relatively small cooling rate $\Lambda(300\,\text{K}) \approx 10^{-27}\,\text{erg}\,\text{cm}^3\,\text{s}^{-1}$ we get a value of several thousand years, three orders of magnitude less than the dynamical time of several Myr (cf. Section (1.1)). Hence, variations of the cooling data do literally have tiny effects.
Consequently, we decided to resort back to the original Enzo data and chose the Rosen and Bregman extension, also because already the high temperature cooling rate data in the Enzo table have been computed based on the work of Raymond et al.. This is essentially the red continuous line in Figure (5.2).

These cooling data are cut at a lower temperature value of 300 K. Tasker and Bryan [2006] cite the original authors [Rosen and Bregman, 1995] to argue that this artificially high temperature cutoff may compensate for neglected physical processes like cosmic-ray pressure or magnetic fields, which can possibly have some limiting influence on the cooling ability of gas.
We neither support nor deny this argument, we state that with the simplifications discussed above it seems very questionable whether cooling below a certain temperature limit can yield any physically meaningful results. Taking all this into consideration, we decided to follow Rosen and Bregman [1995] and extend[a] the cooling rates only down to $\sim 300\,\text{K}$. Aside physical reasoning, this also enables us to preserve comparability to the work of Tasker and Bryan.

5.4. Sink Particle Implementation

When simulating interstellar gas and its gravitational collapse, one inescapably faces the problem that some gas eventually reaches extreme densities. Almost singular densities pose a strong problem for numerical schemes and most codes crash without precautions to deal with extremely dense gas. This is also true for our galaxy simulations with Enzo.
Aside the issue of numerical stability, we can also attribute some physical particularities to extraordinarily dense gas. Most simply, a significantly dense parcel of gas in the ISM can, for example, be interpreted as molecular cloud. Although density alone is certainly not sufficient to

[a] As a technical remark, it is important to realize that Enzo interpolates between two subsequent tabulated temperature values to get a cooling rate for some specific temperature value not tabulated itself. This interpolation routine is designed to deal with temperature values which are equally spaced in log space.

characterize molecular clouds, we use the idea here to clarify our interpretation. Once identified, the gas of the molecular cloud can be removed from the simulation, and replaced by a lagrangian particle which carries the attributes of the removed gas, i. e. mass, temperature. Additionally, the particle somehow has to represent the important dynamics of the modeled cloud. Examples are outflows or the formation of stars inside the cloud.
Therefore, we avoid numerical problems and use the possibility of physical interpretation to construct a model for high density gas.

The authors of the Enzo code have implemented such a replacement of gas by particles but not included the routines in the public release. Nevertheless, the authors have been so kind to share their work with us so we could start off from there.
The Enzo documentation and also the code itself refer to the algorithms as *star formation* algorithms and to the particles as *star particles*. However, the original design was for particles to represent galaxies in cosmological structure formation simulations. We use the algorithms to mimic gas clouds and clusters of stars. Therefore, we refer to the particles in our simulations as *sink particles*.
The original sink particle algorithm in Enzo is based on the work by Cen and Ostriker [1992]. To distinguish from other algorithms and changes we have made, we call this original version *SF1* algorithm.

Before a sink particle is generated, SF1 requires six conditions to be fulfilled.

(a) The first condition is that all sink forming cells are not refined further at higher levels.

This is a numerical criterion which ensures that the best information (most refined) is taken to determine the properties of a possibly created sink particle.

(b) The second condition is a density threshold which requires the cell to have at least some critical density.

This is a standard requirement which is employed in most structure formation simulations and simply compares the density of the cell at hand to some predefined fixed value.

(c) The third condition requires negative divergence of the velocity field in the cell at question.

$$\boldsymbol{\nabla} \cdot \boldsymbol{v} < 0 \tag{5.21}$$

This requirement is supposed to encode whether the flow is converging or not. In particular it is supposed to exclude cells which have high densities as a result of the compression by shocks, but are not gravitationally bound. Such regions would quickly disperse again and are not supposed to be considered for particle creation.

(d) The fourth condition compares the dynamical time and the cooling time of the gas in the cell and only allows sink formation when the cooling time is shorter than the free-fall time.

$$\tau_{\mathrm{cool}} < \tau_{\mathrm{ff}} \equiv \sqrt{\frac{3\pi}{32 G \rho_{\mathrm{tot}}}} \tag{5.22}$$

This encodes the requirement that gas can cool rapidly and gravitational contraction is not significantly opposed by a buildup of thermal pressure. For technical reasons, the check for

this criterion is switched of for cells which have already reached the minimal gas temperature. Moreover, it is important to note that ρ_{tot} is the sum of densities of baryonic and dark matter (cf. Section (6.1)).

(e) The fifth condition checks whether the mass in a cell is equal to or larger than the Jeans mass.

$$m_b > m_J \equiv \frac{1}{6}\frac{\pi^{5/2} c_s^3}{\rho^{1/2} G^{3/2}} \tag{5.23}$$

This checks whether gas pressure is sufficient to prevent gravitational collapse. Note that in Enzo, the Jeans mass is computed for a sphere while it is compared to the mass of a cubic cell.

(f) The sixth condition finally requests that the sink particle which is created has at least a certain minimal mass $M_{\mathrm{min}}^{\mathrm{sink}}$.

Again, this is a purely numerical criterion to ensure the code does not produce a large number of tiny/light particles. This had appeared to be a problem in earlier simulations as the computational demands for high number N-body part of the simulation were too expensive. However, one has to be very careful with this criterion, as it introduces an artificial density threshold which might dramatically dominate over the intended density threshold parameter.
Example: In our simulations the highest refined cells, which host most particle formation, have a length of $l_{\mathrm{cell}} \approx 30\,\mathrm{pc}$. A typical lower mass limit for this criterion was $10^5\,\mathrm{M}_\odot$ [Tasker and Bryan, 2006] which translates into a density of $\rho_{\mathrm{cell}} \approx 2.5 \cdot 10^{-22}\,\mathrm{g/cm^3}$ or a number density of $n \approx 125\,\mathrm{cm}^{-3}$. This is exactly in the critical regime in galaxy scale star formation simulations where one wants to use typical density limits of this magnitude.
This last criterion is somewhat softened by an additional option to switch on a bypass called *stochastic star formation*. When this option is turned on, sink particles with mass less then the mass threshold can be formed. The probability for such an event is calculated from the ratio of potential star mass to minimum threshold particle mass. The created particle would have the threshold mass or half the mass of the gas in the cell, whichever is smaller.
Again, we stress that in our opinion, this softening does not alleviate but masks the problem of an additional density threshold. With this probabilistic addition, it is basically impossible to distinguish the effects of the different criteria, which is a nontrivial task even without the stochastic process. The authors of the code comment themselves, not to be convinced of the proper implications of the subroutine. For all of our simulations, we do *not* use this option of stochastic star formation.

Once all the above criteria are validated, the code generates a sink particle. The particle mass is calculated as

$$m_{\mathrm{sink}} = \epsilon \frac{\Delta t}{\tau_{\mathrm{ff}}} \rho_{\mathrm{gas}} \Delta x^3. \tag{5.24}$$

ϵ is the efficiency parameter and set by hand for the SF1 algorithm. However, it is limited so that at most 90 % of the gas in a cell is transformed into a single particle in one timestep. The other parameters describe the timestep Δt and the cell length Δx. The corresponding amount of gas is removed from the grid. Particles are placed at the center of the creating cell and get the same velocity components as the natal gas. Additionally, particles also carry several attributes, such as the time of their creation and the dynamical time at creation.

5.5. Star Formation Rate and Feedback

The original particle routine discussed above comes together with a star formation and feedback part. While for the creation, sink particles are created instantaneously, the star formation feedback algorithm calculates the forming mass and generates back reactions over an extended period of time. Particles are modeled to lose mass in an exponentially decaying fashion as described by Cen and Ostriker [1992] and the code only keeps track of the actual mass of each particle.
One can conceptualize a sink particle as a molecular cloud. The initial particle mass is the mass of all gas available in the cloud. The star formation feedback algorithm converts gas into stars while at the same time generating feedback from the formed stars.
In order to calculate this process, the algorithm first recomputes the initial mass of a particle in question. With the information about the elapsed time since the particle creation, the mass that would have formed during the timestep is calculated. From this mass, the algorithm determines the mass loss owing to feedback such as winds or supernovae.

The mass[b] evolution of sink particles is modeled as

$$\begin{aligned} m(t) &= m_0 \int_{t_0}^{t} \frac{t'-t_0}{\tau_{\mathrm{ff}}^2} \exp\left(-\frac{t'-t_0}{\tau_{\mathrm{ff}}}\right) dt' \\ &= m_0 \left[1 - \left(1 + \frac{t-t_0}{\tau_{\mathrm{ff}}}\right) \exp\left(-\frac{t-t_0}{\tau_{\mathrm{ff}}}\right)\right]. \end{aligned} \tag{5.25}$$

The particle mass exponentially increases as it evolves. $m(t)$ is the particle mass at some arbitrary time t. m_0 is the final mass of the particle and t_0 is the creation time of the particle.

Mass feedback is coupled to the evolved mass $m(t)$. Hence, the feedback mass m_{fb} is

$$m_{\mathrm{fb}} = f_{\mathrm{ej}} \cdot m(t), \tag{5.26}$$

where f_{ej} is the fraction of stellar mass ejected back into interstellar gas.
Vice versa, these equations can be used to calculate m_0 during a simulation,

$$m_0 = m(t) \left[1 - f_{\mathrm{ej}} \left(1 - (1 + \frac{t-t_0}{\tau_{\mathrm{ff}}}) \exp\left(-\frac{t-t_0}{\tau_{\mathrm{ff}}}\right)\right)\right]^{-1}, \tag{5.27}$$

and deduct the actual amount of mass formed during the timestep:

$$m_{\mathrm{dt}} = m_0 \left[\left(1 + \frac{t-t_0}{\tau_{\mathrm{ff}}}\right) \exp\left(-\frac{t-t_0}{\tau_{\mathrm{ff}}}\right) - \left(1 + \frac{t+dt-t_0}{\tau_{\mathrm{ff}}}\right) \exp\left(-\frac{t+dt-t_0}{\tau_{\mathrm{ff}}}\right)\right]. \tag{5.28}$$

Now it is straightforward to update the particle mass

$$m(t+dt) = m(t) - m_{\mathrm{dt}} * f_{\mathrm{ej}}, \tag{5.29}$$

and gas mass correspondingly. The important quantity, however, is the mass formed during the current calculation m_{dt}, which is used to analyze the *star formation rate*.

Additionally to the mass feedback of gas, the code also allows the possibility to include energy feedback. This is modeled as feedback from explosions of massive stars and can be associated with type II supernova.

[b] Note, however, that the Enzo code always employs density instead of mass. This is a implication of the particle-in-mesh algorithm and makes it much easier to compute the potential on the grid. A consequence of this is that particles migrating between different resolution levels change their density values correspondingly. Although several parameters and variables are labeled *mass* in the code, real masses always have to be calculated by multiplication with the local cell volume.

The explosive energy released at the death of stars is encoded as efficiency parameter and defined as

$$f_{\rm SN} = \frac{E_{\rm SN}}{M_{\rm SN}c^2}, \tag{5.30}$$

where $E_{\rm SN}$ is the assumed feedback energy for a cumulative $M_{\rm SN}$ mass of stars formed. Tasker and Bryan [2006] use an energy of $E_{\rm SN} = 10^{51}$erg for $M_{\rm SN} = 55{\rm M}_\odot$ of stars formed to calculate a feedback efficiency of $f_{\rm SN} = 10^{-5}$.
In order to compute a specific energy per unit density $e_{\rm SN}$, the effective supernovae feedback energy $f_{\rm SN}m_{\rm dt}c^2$ is divided by the overall available gaseous mass to which it supplies the thermal energy:

$$e_{\rm SN}(dt) = \frac{f_{\rm SN}m_{\rm dt}c^2}{m_{gas} + m_{\rm dt}f_{\rm ej}} \tag{5.31}$$

All the thermal energy from the simulated supernova feedback goes into the cell where the particle resides. To update the energy content of that cell, the original energy value is rescaled to the new mass in the cell owing to mass feedback and summed with the actual feedback energy:

$$e_{\rm cell}(t+dt) = \frac{e_{\rm cell}(dt)m_{\rm gas}}{m_{\rm gas} + m_{\rm dt}f_{\rm ej}} + e_{\rm SN}(dt) \tag{5.32}$$

In the last steps, the code updates the gas mass,

$$m_{\rm gas}(t+dt) = m_{\rm gas}(t) + m_{dt}f_{\rm ej}, \tag{5.33}$$

and computes the momentum feedback on the gas:

$$\boldsymbol{v}_{\rm gas}(t+dt) = \frac{\boldsymbol{v}m_{\rm gas}(t) + m_{\rm dt}f_{\rm ej}v_{\rm sink}(t)}{m_{\rm gas}(t+dt)}. \tag{5.34}$$

The sink particle and feedback algorithm SF1 is completed with these computations for each timestep. Sink particles are handled by the N-body solver and the code proceeds with the hydro calculations.

With this description of particle generation and feedback we end the discussion of parts that have already been implemented into Enzo. Although we already included some of our additional work, especially on the cooling implementation, we will now discuss our setup and new routines.

CHAPTER 6

Setting up an Isolated Disk Galaxy

In this chapter, we describe our numerical setup. We used the recent work by Tasker and Bryan [2006] as a guideline and tried to follow their description closely enough to have a reasonable basis for comparison. We tried to rebuild their simulations for these comparisons but, furthermore, developed our own extensions, star formation algorithms, as well as several other modifications. We will explain our full setup in detail, show similarities to Tasker and Bryan [2006] (hereafter TB06) and stress differences to our realization and reason for them.
We will follow an intuitive order for the construction of our simulations. Therefore, we start with the largest scales and proceed from dark matter halo to gas disk to star formation. We will physically motivate our model and provide extensive technical details on the realization.

We design our simulations to mimic the gross properties of the Milky Way in several aspects. However, we are not simulating the formation of galaxies but build a model with several basic properties which include unrealistic conditions. We therefore stress that our toy model galaxies neither claim nor realize the behavior of the Galaxy. Nontheless, our simulations are built to research galatic scale star formation in an isolated disk galaxy. Consequently, we employ data of the Galaxy as outlined and try to model the interstellar medium as realistically as possible.
Although it is unquestionable that magnetic fields have various implications for the problem at hand we do not include them in our simulations. Currently, our version of Enzo lacks the technical capability of magnetohydrodynamical (MHD) simulations. Nevertheless, Collins and Norman [2004], Xu et al. [2008] report on recent developments in this direction and it might be possible to augment our simulations with magnetic fields in the future.

6.1. Cosmological Framework and Dark Matter Halo

All of our simulations are based on a three-dimensional periodic box with a linear scale of 1 Mpc. We employ a root-grid resolution of 128^3 grid cells and allow for an additional adaptive refinement with up to eight levels based on a density resolution criterion. Hence, the finest resolved grid cells have an extension of approximately $1 \cdot 10^6\,\mathrm{pc}/128/2^8 \approx 30\,\mathrm{pc}$ in each dimension. The extremely large simulation volume with respect to the comparably small galaxy scale $\sim 60\,\mathrm{kpc}$, is chosen in order to avoid potential perturbations from the technical realization of periodic boundaries. We chose the separation of periodic repeated potential sources so large that their influence becomes negligible. Fortunately, as a result of the employment of AMR which only resolves the huge empty boundary regions on the root grid level, the computation of these regions uses a negligible amount computational recources.
We simulate our disk galaxies to rest in a dark matter halo. This galactic halo is assumed to be completely virialized and the galaxy within is unaffected by cosmological expansion. In other words, there is neither motivation nor reason to simulate cosmological expansion. Moreover, the inclusion of the expansion, although it might cause only small effects owing to the relatively short galactic timescales compared to cosmological ones, complicates simulations and especially analysis considerably.

Moreover, a typical galactic timescale like the turnover time of the galactic disk – approximately 250 Myr at the position of the Sun – is significantly larger than the light crossing time of the simulation domain 3.26 Myr for 1 Mpc. Consequently, contributions of general relativity and the finite speed of gravity can be ignored.

Simulations in a Static Coordinate System. We deactivated the calculation of comoving coordinates for all of our simulations. This can be achieved by switching off the cosmological expansion parts in the code with a parameter flag set to zero. However, Enzo has no routines to account for the scaling of physical units when run without its cosmology module. Nevertheless, correct scaling relations of physical units are crucial when simulating gravity or thermodynamical processes with Enzo. Hence, we had to rebuild the ability for treating units in essentially all modules of Enzo not working exclusively in code units.
Fortunately, it was possible to use the technical framework kindly provided by Tasker and Bryan to rebuild the treatment of units in close correlation to the cosmological routines. Whenever the code needs to scale some quantity from or to physical units these newly implemented routines provide the correct scaling factors. Only, the conversion of thermodynamical properties needed some extra attention. We will discuss this in Section (6.2).

Simulating our galaxies without comoving expansion is certainly the largest technical difference to the work of TB06. The reader should keep in mind to scale numbers correctly when comparing data. For example, the latter authors use a simulation box of size $1h^{-1}\,\mathrm{Mpc}$ in a ΛCDM universe with $H = 67\,\mathrm{km\,s^{-1}\,Mpc}$. This denotes a scaled length of almost $\sim 1.5\,\mathrm{Mpc}$ which would be the quantity one wants to compare to our simulations. However, most of the numbers stated in TB06 appear to be comoving data, although comoving units are omitted in the description.

Static Gravitational Potential. For the implementation of the dark matter potential, we follow TB06 and set up a fixed gravitational potential with the classical profile described by Navarro et al. [1996, 1997]. These authors used N-body simulations to study cosmological structure formation and the evolution of dark matter halos. Klypin et al. [2002] deduce that the dark matter distribution in the Galaxy may be compatible with such a NFW profile.
For our implementation we start with the analytic equation for the density distribution of dark matter in a galactic halo given by Navarro et al. [1996]

$$\frac{\rho_{\mathrm{DM}}(r)}{\rho_{\mathrm{crit}}} = \frac{\delta_c}{\frac{r}{r_s}\left(1+\frac{r}{r_s}\right)^2}. \tag{6.1}$$

Here, $\rho_{\mathrm{DM}}(r)$ is the dark matter density at a certain radius r. $r_s = r_{200}/c$ is the characteristic radius of the halo profile, where r_{200} is the virial radius and c the concentration parameter. $\rho_{\mathrm{crit}} = 3H^2/8\pi G$ is the critical density (H is the current value of Hubble's constant) and δ_c is a dimensionless parameter which is linked to the concentration factor by the requirement that the mean density within the virial radius r_{200} is 200 times the critical density ρ_{crit}.

$$\delta_c = \frac{200}{3}\frac{c^3}{\ln(1+c) - \frac{c}{1+c}} \tag{6.2}$$

To calculate the dark matter mass from which we deduce the radially dependent gravitational potential we integrate spherically over the radial dependencies of the density distribution

$$\int_0^R \frac{1}{\frac{r}{r_s}\left(1+\frac{r}{r_s}\right)^2} 4\pi r^2 dr = -4\pi r_s^3 \left[\frac{R}{R+r_s} + \ln(r_s) - \ln(R+r_s)\right] \tag{6.3}$$
$$= 4\pi r_s^3 \left[\ln\left(\frac{R+r_s}{r_s}\right) - \frac{R}{R+r_s}\right]$$
$$= 4\pi r_s^3 \left[\ln(1+x) - \frac{x}{1+x}\right].$$

Here, we have set $x = R/r_s$.
We can use this to rewrite density distribution as a mass profile

$$M_{\rm DM}(R) = \int_0^R \rho_{\rm DM}(r) 4\pi r^2 dr \cdot \delta_c \cdot \rho_{\rm crit} \tag{6.4}$$
$$= 4\pi r_s^3 \left[\ln(1+x) - \frac{x}{1+x}\right] \cdot \frac{200}{3}\frac{c^3}{f(c)} \cdot \rho_{\rm crit}$$
$$= \frac{M_{200}}{f(c)} \left[\ln(1+x) - \frac{x}{1+x}\right].$$

Again, we have made new substitutions and used

$$f(c) = \ln(1+c) - \frac{c}{1+c}. \tag{6.5}$$

as well as

$$M_{200} = \frac{4\pi}{3} 200 \rho_{\rm crit} r_{200}^3 \tag{6.6}$$

to simplify the equations. Note that $r_{200} = r_s c$.

For the numerical implementation we use the same numbers as described by TB06 which appear to match the results of Klypin et al. [2002] for the Galaxy quite well. We set a virial mass $M_{200} = 10^{12}\,{\rm M}_\odot$ and adopt a concentration parameter $c = 12$. Furthermore, we assume $H = 67\,{\rm km\,s^{-1}\,Mpc^{-1}}$ and calculate a virial radius of $r_{200} \simeq 212\,{\rm kpc}$ as well as a characteristic scale radius for the gravitational potential of $r_s \simeq 17.7\,{\rm kpc}$.
As this calculation involves no dynamical quantities, we use the above equations in the initialization of the simulation and calculate the virial mass from the input parameters. In a second step we normalize the acceleration force of the gravitational potential to get the magnitude of gravitational acceleration of a unit mass object at a distance of one length unit. Based on this quantity, the code calculates the acceleration of gas or particles during runtime.

6.2. The Baryonic Gas Disk

Here we describe how we set up the initial gas disk for our galaxy simulations. We will describe the baryonic gas density profile and its technical realization as well as the scaling of units to initialize the proper thermodynamical energy content of the gas.

The Density Profile of Baryonic Gas. We set up the profile of the baryonic gas of our disks, again following the work of TB06. The analytic profile

$$\rho(r,z) = \rho_0 \exp\left(-\frac{r}{r_0}\right) \operatorname{sech}^2\left(\frac{1}{2}\frac{z}{z_0}\right) \tag{6.7}$$

is based on a fixed central density ρ_0 and has an exponential radial as well as a hyperbolic secant dependence on the height z above the disk midplane. The scale radius r_0 and scale height z_0 as well as the central density are chosen to give a gas mass in correspondance with the baryonic mass we assume in the Galaxy.

Note that for all simulations reported here, we start with an entirely gaseous disk and no stellar component. However, we have experimented with an initial stellar component as described by Li et al. [2005, 2006][a] but decided to run our simulations without the additional complication of an initiall stellar disk. The reasons are that, first, comparability to TB06 is preserved and, second, star formation can be studied in a larger parameter regime as galactic properties significantly change during the temporal evolution. This allows us to study the formation of stars on much wider regime of gas densities as in the case where already 50% or more of mass is present only as stellar component.

We set $r_0 = 3.5\,\mathrm{kpc}$, $z_0 = 325\,\mathrm{pc}$ and choose a total gas mass of $M_{\mathrm{gas}} = 4 \cdot 10^{10}\,\mathrm{M}_\odot$ as reported by Klypin et al. [2002] for the Galaxy. To calculate the central gas density in the disk we integrate the density distribution

$$\begin{aligned} M_{\mathrm{gas}} &= \int_0^{2\pi}\int_{-\infty}^{\infty}\int_0^R \rho(r,z)\; r\; drdzd\varphi \\ &= 8\pi r_0 z_0 \rho_0 \left(r_0 - \exp(-\frac{R}{r_0})(R + r_0)\right) \\ &\overset{\mathrm{R}\to\infty}{=} 8\pi r_0^2 z_0 \rho_0. \end{aligned} \tag{6.8}$$

which yields a central gas density $\rho_0 \simeq 2.7 \cdot 10^{-23}\,\mathrm{g\,cm^{-3}}$.

Figure (6.1) shows the gas density profile and how it depends on the distance to the galactic center for both the radial direction and height above the midplane of the disk.

Technically it is important to note that a cell centered value, computed based on the radial distance of the cell center to the galactic center and the distance of the cell center to the galactic midplane, cannot properly represent the average gas density in that cell, as a result of the nonlinear dependencies of the density profile on radius as well as on height above the midplane. This becomes most important in the outer region of the gas disk where refinement changes and the resolution decreases.
To account for this effect, we calculate the density value of a grid cell by averaging 100 randomly sampled analytic density values with coordinates within the cell. Therefore, nonlinearities in radial as well as azimuthal dependence of the density profile are properly included in the setup of the numerical disk density profile. Note that without this procedure, proper coding of the analytic profile does not yield the desired profile itself. Moreover, without calculating proper averages, the density profile inherits unphysical breaks as well as kinks at crossovers of different refinement levels.

[a] The authors have been so kind to provide their initial condition generator which enabled us to produce a realistic initial stellar component inside the gaseous disk.

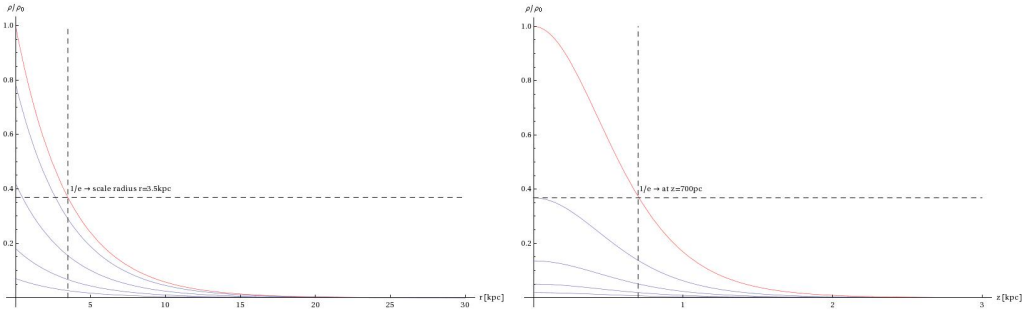

(a) Exponential radial gas density profile.

(b) Hyperbolic secant gas density profile above the disk midplane.

FIGURE 6.1. Illustration of the radial and height dependence of gas density in the disk. The red curve depicts the gas density in the disk midplane or along the axis of rotation, while the additional plots in each figure show the density at one, two, three and four radial or vertical scale heights. The dashed lines indicate a decline of $1/e$ in the density.

Finally, we add the components of baryonic gas mass and presumed dark matter mass, according to the corresponding density profiles, to calculate the total mass within a certain radius prescribed within the galactic plane. From this total mass we deduce the circular velocity of gas in the disk and initialize the differential rotation of the galaxy.

$$v_{\rm cir} = \left(\frac{GM_{\rm tot}(r)}{r}\right)^{1/2} \tag{6.9}$$

Temperature and Thermal Energy. We set the initial temperature in the whole simulation domain, including the gas disk, to a value of $T = 10^4$ K. As ENZO usually does not explicitly calculate the gas temperature during runtime, it is more convenient to focus on thermal energy than temperature. Thermal energy is usually defined as

$$\varepsilon_{int} = T\rho\frac{k_b}{m_h\mu(\gamma-1)} \tag{6.10}$$

For ENZO, first, we use the specific energy per units mass $e = \varepsilon/\rho$. Second, we split the calculation into two parts for technical reasons, one step including all fixed natural constants and a second one including variable parameters which might be different for different simulations. Finally, we rescale units as described in Appendix (C), see Equation (C.5). As this has led to confusion in the past, we summarize the calculation here:

$$\hat{T}_{enzo} = T\frac{k_b}{m_h}/(\mathbb{G}\mathbb{L}) \tag{6.11}$$

$$e_{int,enzo} = \hat{T}_{enzo}\frac{1}{\mu(\gamma-1)} \tag{6.12}$$

$$e_{int,enzo} = T\frac{k_b}{m_h\mu(\gamma-1)}/(\mathbb{G}\mathbb{L}). \tag{6.13}$$

Here, $\mathbb{G}$ and $\mathbb{L}$ are scaling factors and all other quantities have their usual meaning. $\hat{T}_{enzo}$ is only used to encode the temperature but is not itself used for any computation.

In the same spirit, we describe the implementation of cooling and heating (cf. Section 5.3). Most generally, we can write the cooling function as

$$\mathcal{L} = n^2\Lambda(T) - n\Gamma(T_0), \tag{6.14}$$

where n is the number density, Λ is the temperature dependent cooling rate and Γ is the heating rate. Here we have written $\Gamma(T_0)$ to indicate that, we only use a constant heating term for simplicity. Considering Enzo and its use of specific energy, we can express the change of internal energy owing to cooling and heating as

$$e'_{int} = e_{int} - \frac{\mathcal{L}}{\rho} \cdot dt, \tag{6.15}$$

where e' is the energy content after the temporal evolution dt of the simulation cell. We now separate cooling and heating and write $\mathcal{L} = n^2\Lambda - n\Gamma$ with $\mathcal{L}^c = n^2\Lambda$ and $\mathcal{L}^h = -n\Gamma$ for simplicity.
To calculate the energy contribution from cooling we write

$$\begin{aligned} \frac{\mathcal{L}^c}{\rho} &= n^2\frac{\Lambda}{\rho} \\ &= \Lambda\frac{1}{\mu^2 m_h^2}\rho. \end{aligned} \tag{6.16}$$

Therefore, we can write the cooling term in the numerical implementation as

$$e'_{enzo} = e_{enzo} - \Lambda_{enzo}\frac{1}{\mu^2}\rho_{enzo} \cdot dt_{enzo}, \tag{6.17}$$

where we have used the subscript to stress that the apparent quantities are now in code units. μ is dimensionless and the square of the constant m_h as well as its units have been absorbed into the scaling of $\Lambda_{enzo} = \Lambda/\mathbb{C}$. Consequently, we have

$$\begin{aligned} \left[\frac{\mathrm{g\,cm^2}}{\mathrm{s^2}}\frac{\mathrm{cm^3}}{\mathrm{s}}\frac{1}{\mathrm{g^2}}\right] : \mathbb{C} &= \frac{\mathbb{M}\mathbb{L}^5}{\mathbb{T}^3\mathbb{M}^2}m_h^2 \\ &= \frac{\mathbb{L}^2}{\mathbb{T}^3\mathbb{R}}m_h^2. \end{aligned} \tag{6.18}$$

Please refer again to Appendix (C) for details on the scaling parameters. For completeness, we state that Λ in units of $\mathrm{erg\,cm^3\,s^{-1}}$ is the quantity tabulated in the input table file for the radiative cooling routine.

Equivalently, we treat the heating term and get

$$\begin{aligned} \frac{\mathcal{L}^h}{\rho} &= -n\frac{\Gamma}{\rho} \\ &= -\frac{\Gamma}{\mu m_h}. \end{aligned} \tag{6.19}$$

For the implementation of this heating term we write

$$e'_{enzo} = e_{enzo} + \Gamma_{enzo}\frac{1}{\mu} \cdot dt_{enzo}, \tag{6.20}$$

where we have again absorbed m_h and its units into the scaling factor $\Gamma_{enzo} = \Gamma/\mathbb{H}$. We get

$$\left[\frac{\mathrm{g\,cm^2}}{\mathrm{s^2}}\frac{1}{\mathrm{s}}\frac{1}{\mathrm{g}}\right] : \mathbb{H} = \frac{\mathbb{L}^2}{\mathbb{T}^3}m_h. \tag{6.21}$$

The constant heating term Γ can be defined for a simulation in units of $\mathrm{erg\,s^{-1}}$.

6.3. Amendments to Star Formation and Feedback Algorithms

Once the gas disk is in place and the dynamical evolution starts, gas quickly starts to cool and becomes gravitationally unstable – fragmentation starts. In Section (5.4) we have already described the sink particle creation framework we are using for our simulations. Here, we present the details of our changes to SF1 as well as different algorithmic realizations of how gas is converted into sink particles, representing dense clouds of gas and stellar objects. We will also anticipate the detailed introduction of our turbulence subgrid model in Chapter (7) and present how star formation can be parameterized based on the input of the SGS model. Finally, we will discuss our changes and amendments to the standard star formation and feedback algorithm presented in Section (5.5).

Changes to the Original Algorithm SF1. The first important amendment to SF1 appears in the calculation of the dynamical time, τ_{ff}, in a cell forming a sink particle. This calculation affects the sink formation criterion (d), comparing cooling and dynamical time scales. Equation (5.22) contains the total density of matter in the cell. This includes not only the gas mass, but also dark matter and the mass of clouds and stars already encoded in other sink particles.
The gas density is readily available during the calculation and needs no additional attention. The opposite is true for dark matter: as a result of our realization of a static dark matter potential, we have unintentionally circumvented the inclusion of dark matter in the calculation as we simply have no dark matter field component. In other words, originally, dark matter was meant to be treated as particles and a particle-in-cell algorithm was used to compute the dark matter density on the grid. This density went into the calculation of the total density in a cell. Now, while this treatment ensures we readily include all mass already transformed into particles (stars and clouds) we have to additionally account for the dark matter mass.
In order to calculate the dark matter density in any cell, we first determine the radial distance of the center of the cell to the galactic center, which corresponds to the epicenter of the fixed gravitational potential. As the potential is spherically symmetric, the radius is the only variable information we need to calculate the dark matter density using the equations presented in Section (6.1) (Equation (6.1)).
Subsequently, we sum up gas density, dark matter density and the mass density from particles provided by the particle-in-cell algorithm and use this for the computation of the dynamical time. However, we also note that the dark matter density is usually several orders of magnitude smaller than both other density contributions. Nevertheless, it is physically correct and computationally simple to include the effect.

Secondly, sink formation criterion (e) concerning the limiting factor whether a cell exceeds the local Jeans mass or not is altered. Equation (5.23) contains the squared isothermal speed of sound of the gas in the cell in question. The originally used calculation of this sound speed squared was realized by multiplying a recalculated constant with the temperature value of the cell. Using the definition $c_s^2 = R_s \cdot T$ with $R_s = \frac{k_b}{m_h \mu}$ this essentially encodes a fixed mean molecular weight μ. Originally, $\mu = 0.6$ was used. Consequently, we replaced the precalculated constant R_s by the latter relation.

Deducing a Simplified Algorithm SF2. In order to be able to sort out the significance of the star formation density threshold, sink formation criterion (b), we deduced a new version of the original SF1 where we omit all criteria but this density threshold and the requirement that particles are only generated on the most refined levels (a). Hence, this is only a stripped version of the original algorithm. Nevertheless, in the spirit of simplifying things in order to tackle the key issues, this approach proved useful as we will see when we discuss the results in Part (III).

Turbulence Regulated Algorithm SF3. Starting from SF1 as well as the simplified version SF2, using only density as the criterion to decide whether a cell forms a sink particle or not, the next step was to replace the unknown efficiency parameter ϵ in Equation (5.24). While we have extensively experimented with different values for this parameter, one of the major goals of this work was to implement the theory proposed by KM05 to determine this parameter dynamically from simulation quantities.
Comparing Equations (4.20) and (5.24) we find that the desired efficiency parameter appears in the work of KM05 as star formation rate per free-fall time $\mathrm{SFR}_{\mathrm{ff}}$. We have already summarized the concepts of this theory in Section (4.4). Most important for the numerical implementation is the fact that Krumholz and McKee are able to compute the star formation rate solely based on two dimensionless parameters, the virial parameter α_{vir} and the turbulent Mach number $\mathscr{M}_t$.

In order to compute these parameters we recall their physical meaning. Beginning with the virial parameter, one can conceptualize it to represent a balance condition of thermal plus kinetic energy versus the gravitational energy. We assume sink formation to be representative of molecular cloud physics. Therefore, we focus the analysis on the properties of molecular clouds. Consequently, we deal with situations were the thermal energy is totally dominated by the kinetic turbulent energy of the random velocity motions inherent to molecular clouds. This justifies to interpret the total velocity dispersion σ_{tot} to be completely determined by the turbulent velocity fluctuations of the gas. Consequently, the kinetic turbulent energy can be used for the calculation of the virial parameter. Put in numerical terms, we obtain

$$\alpha_{\mathrm{vir}} = \frac{5\ 2e_t \frac{\Delta x}{2}}{G\rho(\Delta x)^3}. \tag{6.22}$$

By virtue of our subgrid-model (cf. Chapter (7)) and references therein for a detailed presentation of the subgrid model), we are in the unique situation to have the turbulent energy e_t available for the computation in each grid cell. All other quantities are commonly available in numerical simulations.

Furthermore, the Mach number appearing in the equation of $\mathrm{SFR}_{\mathrm{ff}}$ can also be expressed in terms of the turbulent energy. Krumholz and McKee state it as the ratio of turbulent velocity on the largest scale of the region under consideration and the sound speed of this region, $\mathscr{M}_t = \sigma_{2R}/c_s$. Again, the turbulent velocity on the grid scale is exactly what we can calculate from the turbulence energy. Therefore, we get the turbulent Mach number as

$$\mathscr{M}_t = \frac{\sqrt{2e_t}}{\sqrt{\frac{k_b}{m_h \mu}T}}. \tag{6.23}$$

Henceforth, we are able to use the fit presented by Krumholz and McKee [2005] to calculate the star formation rate per free-fall time or, correspondingly, the sink particle creation efficiency using Equation (4.21). We call this algorithm SF3.

Computing the Amount of Star Formation. We have made one significant, although purely technical amendment to the original feedback formulation. The original algorithm used to subsequently sum up all masses of sink particles generated in every cell during each timestep. This resulted in a recorded amount of star formation depicting only an integrated star formation rate. To compute the amount of star formation including all the information available at the maximum resolution level of the simulation, we incorporated a new field to capture the amount of gas turned into particles within each cell. The additional field allows us to gain synchronized information about the amount of star formation with the maximum temporal and spatial precision.

Summarizing, we have described how we set up our models of an isolated disk galaxy from the largest cosmological scales down to our resolution limit where we turn gas into sink particles. Additionally, we have discussed the formulation of feedback and how we approach the calculation of the actual rate of the formation of stars numerically. Nevertheless, before we can begin with the discussion of simulation results we have to describe the subgrid model and the aspect of gas distribution properties in galaxies. Therefore, we use the next Chapter (7) to present the details of the previously mentioned subgrid-scale model of turbulence.

CHAPTER 7

Turbulence and Subgrid-Scale Physics

Owing to the infeasibility to solve the hydrodynamical equations on all problem relevant dynamical scales it is a common approach in astrophysical applications to introduce a separation of scales. Resolved scales are simulated explicitly while unresolved ones are either neglected or treated implicitly via models trying to mimic the behavior of a flow below grid resolution.
Using the experience and numerical techniques developed by our group we follow this approach of subgrid-scale treatment of turbulence to account for the unresolved effects of turbulent velocity fluctuations in simulations of galaxy scale star formation. The numerical methods and tests are described in Schmidt et al. [2006a] while a first application to type Ia supernovae is discussed in Schmidt et al. [2006b]. Furthermore, Maier et al. [2008] applies our subgrid-scale modeling to a galaxy cluster. Here, we will briefly introduce the formalism, including only those derivations necessary to arrive at the governing equations. We will show how to close these equations with appropriate subgrid-scale closures and discuss how we use our model on an adaptive grid. Finally, we will comment on differences to our earlier work and describe some limitations we still have in the SGS implementation.

7.1. The Subgrid-Scale Model

To separate resolved from unresolved scales, we decompose the hydrodynamical equations into a large-scale and a fluctuating part. To start with this decomposition, we want to rewrite the governing equations and present a new notation. Moreover, we introduce the formal concepts of filtering using the Favre-Germano formalism.

The idea of filtering is to split any quantity a into its mean value $\langle a \rangle$ and fluctuations a' around this mean. This filtering process can be realized by a low-pass filter. Mathematically, we apply a convolution opterator:

$$\langle a(x) \rangle = \int_{-\infty}^{\infty} G(x - x') \; a(x') \; dx'. \tag{7.1}$$

To separate the resolved mean flow from unresolved fluctuations in the flow, we follow Germano [1992] and decompose the hydrodynamical equations into a large-scale and a fluctuating part. Henceforth, we use the same notation as Maier et al. [2008] and write

$$\begin{array}{rll} \text{ideal/exact} & a & \overset{\infty}{a} \\ \text{filtered/smoothed} & \langle a \rangle & \langle \overset{\infty}{a} \rangle_G = a \\ \text{fluctuating} & a\text{'}, & \end{array}$$

where we have also quoted the ∞ overline notation of Schmidt et al. [2006a] for better comparison. Henceforth, we write plain symbols for theoretical ideal quantities. Filtered quantities, on the other hand, with fluctuations smoothed out, are computed as the numerical solution and written in brackets $\langle\rangle$. In addition to the filter formalism by Germano we define density weighted filtered

quantities as

$$\hat{a} = \frac{\langle \rho a \rangle}{\langle a \rangle}. \tag{7.2}$$

With this definition of density weighted quantities similar to Favre [1969], Schmidt et al. [2006a] are able to define the moments appearing in the filtered equations of compressible fluid dynamics.

$$\hat{\tau}(a,b) = \langle \rho ab \rangle - \langle \rho \rangle \hat{a}\hat{b} \tag{7.3}$$

$$\hat{\tau}(a,b,c) = \langle \rho abc \rangle - \langle \rho \rangle \hat{a}\hat{b}\hat{c} - \hat{a}\hat{\tau}(b,c) - \hat{b}\hat{\tau}(a,c) - \hat{c}\hat{\tau}(a,b) \tag{7.4}$$

$$...$$

For these quantities $\hat{\tau}()$ the same rules apply as for the generalized central moments first introduced by Germano. For details, please refer to Schmidt et al. [2006a], Maier et al. [2008] and the references therein. Here, we use this formalism in the context of the fluid equations.

The equations, describing a compressible, viscous, self-gravitating fluid flow are the hydrodynamical equations (Equation (2.1), (2.2) and (2.3)). We rewrite them here in component form, without the additional term for external forces F. We have the equation of continuity of mass

$$\frac{\partial}{\partial t}\rho + \frac{\partial}{\partial r_j}(v_j \rho) = 0, \tag{7.5}$$

the equation of momentum conservation

$$\frac{\partial}{\partial t}(\rho v_i) + \frac{\partial}{\partial r_j}(v_j \rho v_i) = -\frac{\partial}{\partial r_i}p + \frac{\partial}{\partial r_j}\sigma'_{ij} + \rho g_i \tag{7.6}$$

and the equation of energy conservation

$$\frac{\partial}{\partial t}(\rho e) + \frac{\partial}{\partial r_j}(v_j \rho e) = -\frac{\partial}{\partial r_j}(v_j p) + \frac{\partial}{\partial r_j}(v_i \sigma'_{ij}) + v_i \rho g_i, \tag{7.7}$$

where symbols have their usual meaning, p is pressure, g_i is the gravitational acceleration and σ'_{ij} is the viscous stress tensor.

These are the equations describing ideal quantities, including fluctuations. The next step is to filter them and separate mean and fluctuating parts.
Assuming that the implicit filter is homogeneous and independent of time, i. e. the kernel is a function of $|x = x'|$ only, the operation of filtering commutes with time derivatives and spatial gradients. Therefore, we can express the conservation of mass density of the smoothed field by an equation for $\langle \rho \rangle$, equal to the classical continuity equation. This yields the filtered equation of mass conservation:

$$\frac{\partial}{\partial t}\langle \rho \rangle + \frac{\partial}{\partial r_j}\hat{v}_j \langle \rho \rangle = 0. \tag{7.8}$$

Next, we filter the momentum Equation (7.6). Again, we apply our formalism and get

$$\frac{\partial}{\partial t}\langle \rho \rangle \hat{v}_i + \frac{\partial}{\partial r_j}\langle v_j \rho v_i \rangle = -\frac{\partial}{\partial r_i}\langle p \rangle + \frac{\partial}{\partial r_j}\langle \sigma'_{ij} \rangle + \langle \rho g_i \rangle \tag{7.9}$$

$$\frac{\partial}{\partial t}\langle \rho \rangle \hat{v}_i + \frac{\partial}{\partial r_j}\hat{v}_j \langle \rho \rangle \hat{v}_i = -\frac{\partial}{\partial r_i}\langle p \rangle + \frac{\partial}{\partial r_j}\langle \sigma'_{ij} \rangle + \langle \rho \rangle g_i - \frac{\partial}{\partial r_j}\hat{\tau}(v_i, v_j) \tag{7.10}$$

Here we have used Equation (7.3) of generalized moments to replace

$$\langle v_j \rho v_i \rangle = \hat{v}_j \langle \rho \rangle \hat{v}_i + \hat{\tau}(v_i, v_j). \tag{7.11}$$

Note that the arguments inside the operator commute, $\hat{\tau}(v_j, v_i) = \hat{\tau}(v_i, v_j)$.

Last, we apply our filtering to the energy Equation (7.7) and write

$$\frac{\partial}{\partial t}\langle\rho\rangle\hat{e} + \frac{\partial}{\partial r_j}\langle v_j \rho e\rangle = -\frac{\partial}{\partial r_j}\langle v_j p\rangle + \frac{\partial}{\partial r_j}\langle v_i \sigma'_{ij}\rangle + \langle v_i \rho g_i\rangle \tag{7.12}$$

$$\begin{aligned}\frac{\partial}{\partial t}\langle\rho\rangle\hat{e} + \frac{\partial}{\partial r_j}\langle\rho\rangle\hat{v}_j\hat{e} &= -\frac{\partial}{\partial r_j}\langle v_j p\rangle + \frac{\partial}{\partial r_j}\langle v_i \sigma'_{ij}\rangle + \langle\rho\rangle\hat{v}_i\hat{g}_i \\ &\quad -\frac{\partial}{\partial r_j}\hat{\tau}(v_j, e) + \hat{\tau}(v_i, g_i),\end{aligned} \tag{7.13}$$

where we have again used the equations of generalized moments to expand the equation.

Consequently, we have arrived at the equations for the filtered density, the filtered momentum and the filtered total energy. Next, we split the total energy equation into two equations, one for kinetic and one for internal/thermal energy, and filter those. Filtering the kinetic energy, we get

$$\begin{aligned}\frac{\partial}{\partial t}\langle\rho\rangle\hat{e}_{kin} + \frac{\partial}{\partial r_j}\langle\rho\rangle\hat{v}_j\hat{e}_{kin} &= -\langle v_i \frac{\partial}{\partial r_i} p\rangle + \langle v_i \frac{\partial}{\partial r_j}\sigma'_{ij}\rangle + \langle\rho\rangle\hat{v}_i\hat{g}_i \\ &\quad -\frac{\partial}{\partial r_j}\hat{\tau}(v_j, e_{kin}) + \hat{\tau}(v_i, g_i).\end{aligned} \tag{7.14}$$

The filtered equation for the internal energy reads very similar

$$\frac{\partial}{\partial t}\langle\rho\rangle\hat{e}_{int} + \frac{\partial}{\partial r_j}\langle\rho\rangle\hat{v}_j\hat{e}_{int} = -\langle p\frac{\partial}{\partial r_j}v_j\rangle + \langle\sigma'_{ij}\frac{\partial}{\partial r_j}v_i\rangle - \frac{\partial}{\partial r_j}\hat{\tau}(v_j, e_{int}). \tag{7.15}$$

Now, we have derived the equations for the filtered kinetic and internal energies. Before we can write the total resolved energy we need the equation for the resolved kinetic energy. To get it we contract the filtered Equation (7.10) of momentum with the filtered velocity $\hat{v}_i$. We get

$$\frac{\partial}{\partial t}\langle\rho\rangle\frac{1}{2}\hat{v}_i\hat{v}_i + \frac{\partial}{\partial r_j}\hat{v}_j\langle\rho\rangle\frac{1}{2}\hat{v}_i\hat{v}_i = -\hat{v}_i\frac{\partial}{\partial r_i}\langle p\rangle + \hat{v}_i\frac{\partial}{\partial r_j}\langle\sigma'_{ij}\rangle + \langle\rho\rangle\hat{v}_i\hat{g}_i - \hat{v}_i\frac{\partial}{\partial r_j}\hat{\tau}(v_i, v_j), \tag{7.16}$$

where we have used $\hat{v}_i\frac{\partial}{\partial t}\hat{v}_i = \frac{\partial}{\partial t}\frac{1}{2}\hat{v}_i\hat{v}_i$ to write the above equation.

Subsequently, we can now add Equation (7.16) of the resolved kinetic energy to the Equation (7.15) of the filtered internal energy to get the desired equation for the total resolved energy as $e_{res} = \hat{e}_{int} + \frac{1}{2}\hat{v}_i\hat{v}_i$:

$$\begin{aligned}\frac{\partial}{\partial t}\langle\rho\rangle e_{res} + \frac{\partial}{\partial r_j}\langle\rho\rangle\hat{v}_j e_{res} &= -\hat{v}_i\frac{\partial}{\partial r_i}\langle p\rangle + \hat{v}_i\frac{\partial}{\partial r_j}\langle\sigma'_{ij}\rangle + \langle\rho\rangle\hat{v}_i\hat{g}_i - \hat{v}_i\frac{\partial}{\partial r_j}\hat{\tau}(v_i, v_j) \\ &\quad -\langle p\frac{\partial}{\partial r_i}v_i\rangle + \langle\sigma'_{ij}\frac{\partial}{\partial r_j}v_i\rangle - \frac{\partial}{\partial r_j}\hat{\tau}(v_j, e_{int})\end{aligned} \tag{7.17}$$

This last equation contains the coupling of unresolved fluctuations on the filtered resolved flow. Particularly, the four terms $\langle p\frac{\partial}{\partial r_i}v_i\rangle$, $\langle\sigma'_{ij}\frac{\partial}{\partial r_j}v_i\rangle$, $\hat{\tau}(v_i, v_j)$ and $\hat{\tau}(v_j, e_{int})$ represent this coupling. Instead of trying to calculate each of those terms from quantities known from the resolved flow Schmidt et al. [2006a] showed that the first three of these terms are directly connected to what we call turbulent energy ε_t. We will get those terms by modeling the balance equation for the turbulent energy and only the last term $\hat{\tau}(v_j, e_{int})$ has to be modelled independently.
Taking $\varepsilon_t = \langle\rho\rangle e_t = \frac{1}{2}\hat{\tau}(v_i, v_i)$ we use Equations (7.14) and (7.16) to calculate $e_t = \hat{e}_{kin} - \frac{1}{2}\hat{v}_i\hat{v}_i$.

To do this, we subsequently subtract the left and right hand sides of Equation (7.14) and Equation (7.16) from each other:

$$\begin{aligned}\frac{\partial}{\partial t}\langle\rho\rangle e_t + \frac{\partial}{\partial r_j}\langle\rho\rangle\hat{v}_j e_t &= -\left[\langle v_i\frac{\partial}{\partial r_i}p\rangle - \hat{v}_i\frac{\partial}{\partial r_i}\langle p\rangle\right] \\ &\quad +\left[\langle v_i\frac{\partial}{\partial r_j}\sigma'_{ij}\rangle - \hat{v}_i\frac{\partial}{\partial r_j}\langle\sigma'_{ij}\rangle\right] \\ &\quad +\langle\rho\rangle\hat{v}_i\hat{g}_i - \frac{\partial}{\partial r_j}\hat{\tau}(v_j, e_{kin}) + \hat{\tau}(v_i, g_i) \\ &\quad -\langle\rho\rangle\hat{v}_i\hat{g}_i + \hat{v}_i\frac{\partial}{\partial r_j}\hat{\tau}(v_i, v_j).\end{aligned} \tag{7.18}$$

We expand the second order generalized moment $\hat{\tau}(v_j, e_{kin})$ in the third line of the last equation as follows:

$$\begin{aligned}-\frac{\partial}{\partial r_j}\hat{\tau}(v_j, e_{kin}) &= -\frac{\partial}{\partial r_j}\frac{1}{2}\hat{\tau}(v_j, v_i v_i) \\ &= -\frac{1}{2}\frac{\partial}{\partial r_j}\hat{\tau}(v_j, v_i, v_i) - \frac{\partial}{\partial r_j}\hat{v}_i\hat{\tau}(v_j, v_i) \\ &= -\frac{1}{2}\frac{\partial}{\partial r_j}\hat{\tau}(v_j, v_i, v_i) - \hat{\tau}(v_j, v_i)\frac{\partial}{\partial r_j}\hat{v}_i - \hat{v}_i\frac{\partial}{\partial r_j}\hat{\tau}(v_j, v_i)\end{aligned} \tag{7.19}$$

where we have used the rule $\hat{\tau}(a, bc) = \hat{\tau}(a, b, c) + \langle b\rangle\hat{\tau}(a, c) + \langle c\rangle\hat{\tau}(a, b)$ to expand the kinetic term in the second step, and the chain rule in the last step.

Inserting Equation (7.19) into Equation (7.18) we get

$$\begin{aligned}\frac{\partial}{\partial t}\langle\rho\rangle e_t + \frac{\partial}{\partial r_j}\langle\rho\rangle\hat{v}_j e_t &= -\left[\langle v_i\frac{\partial}{\partial r_i}p\rangle - \hat{v}_i\frac{\partial}{\partial r_i}\langle p\rangle\right] \\ &\quad +\left[\langle v_i\frac{\partial}{\partial r_j}\sigma'_{ij}\rangle - \hat{v}_i\frac{\partial}{\partial r_j}\langle\sigma'_{ij}\rangle\right] \\ &\quad +\hat{\tau}(v_i, g_i) \\ &\quad -\frac{1}{2}\frac{\partial}{\partial r_j}\hat{\tau}(v_j, v_i, v_i) - \hat{\tau}(v_j, v_i)\frac{\partial}{\partial r_j}v_j.\end{aligned} \tag{7.20}$$

It is convenient to use the following chain-rule expansions to rewrite the above equation [Schmidt et al., 2006a].

$$\langle v_i\frac{\partial}{\partial r_i}p\rangle = \frac{\partial}{\partial r_i}\langle v_i p\rangle - \langle p\frac{\partial}{\partial r_i}v_i\rangle \tag{7.21}$$

$$\hat{v}_i\frac{\partial}{\partial r_i}\langle p\rangle = \frac{\partial}{\partial r_i}\hat{v}_i\langle p\rangle - \langle p\rangle\frac{\partial}{\partial r_i}\hat{v}_i \tag{7.22}$$

$$\langle v_i\frac{\partial}{\partial r_j}\sigma'_{ij}\rangle = \frac{\partial}{\partial r_j}\langle v_i\sigma'_{ij}\rangle - \langle\sigma'_{ij}\frac{\partial}{\partial r_j}v_i\rangle \tag{7.23}$$

$$\hat{v}_i\frac{\partial}{\partial r_j}\langle\sigma'_{ij}\rangle = \frac{\partial}{\partial r_j}\hat{v}_i\langle\sigma'_{ij}\rangle - \langle\sigma'_{ij}\rangle\frac{\partial}{\partial r_j}\hat{v}_i \tag{7.24}$$

With these expressions we finally arrive at the equation of conservation of turbulent energy. We get

$$
\begin{aligned}
\frac{\partial}{\partial t}\langle\rho\rangle e_t + \frac{\partial}{\partial r_j}\langle\rho\rangle\hat{v}_j e_t \quad = \quad & \overbrace{-\frac{\partial}{\partial r_j}\left[\frac{1}{2}\hat{\tau}(v_j,v_i,v_i) + \overbrace{\langle v_i p\rangle - \hat{v}_i\langle p\rangle}^{-\mu} - \overbrace{\langle v_i\sigma'_{ij}\rangle + \hat{v}_i\langle\sigma'_{ij}\rangle}^{-\kappa}\right]}^{\mathcal{D}} \\
& \overbrace{-\left[\langle p\rangle\frac{\partial}{\partial r_i}\hat{v}_i - \langle p\frac{\partial}{\partial r_i}v_i\rangle\right]}^{\langle\rho\rangle\lambda} \\
& \overbrace{+\left[\langle\sigma'_{ij}\rangle\frac{\partial}{\partial r_j}\hat{v}_i - \langle\sigma'_{ij}\frac{\partial}{\partial r_j}v_i\rangle\right]}^{-\langle\rho\rangle\epsilon} \\
& \overbrace{+\hat{\tau}(v_i,g_i)}^{\Gamma} - \hat{\tau}(v_j,v_i)\frac{\partial}{\partial r_j}\hat{\tau}_i,
\end{aligned}
\tag{7.25}
$$

where we have used the overbraces to introduce a new series of substitutions. Accordingly, we can write the balance equation of turbulent energy as

$$
\frac{\partial}{\partial t}\langle\rho\rangle e_t + \frac{\partial}{\partial r_j}\langle\rho\rangle\hat{v}_j e_t \;=\; \mathcal{D} + \Gamma - \langle\rho\rangle\lambda - \langle\rho\rangle\epsilon - \hat{\tau}(v_j,v_i)\frac{\partial}{\partial r_j}\hat{v}_i. \tag{7.26}
$$

Moreover, using the two expansions from Equations (7.22) and (7.24) and the substitutions from Equation (7.25) we can also rewrite Equation (7.17) of the total resolved energy:

$$
\begin{aligned}
\frac{\partial}{\partial t}\langle\rho\rangle e_{res} + \frac{\partial}{\partial r_j}\langle\rho\rangle\hat{v}_j e_{res} \quad = \quad & -\frac{\partial}{\partial r_i}\hat{v}_i\langle p\rangle + \frac{\partial}{\partial r_j}\hat{v}_i\langle\sigma'_{ij}\rangle + \langle\rho\rangle\hat{v}_i\hat{g}_i \\
& +\langle\rho\rangle(\lambda+\epsilon) - \hat{v}_i\frac{\partial}{\partial r_j}\hat{\tau}(v_i,v_j) - \frac{\partial}{\partial r_j}\hat{\tau}(v_j,e_{int})
\end{aligned}
\tag{7.27}
$$

Therefore, we have succeeded in deriving a complete set of equations to describe the dynamics of a fluid flow split into a smoothed and a fluctuating part.

Summarizing, we again state this set of partial differential equations:

$$
\frac{\partial}{\partial t}\langle\rho\rangle + \frac{\partial}{\partial r_j}\hat{v}_j\langle\rho\rangle \;=\; 0 \tag{7.28}
$$

$$
\frac{\partial}{\partial t}\langle\rho\rangle\hat{v}_i + \frac{\partial}{\partial r_j}\hat{v}_j\langle\rho\rangle\hat{v}_i \;=\; -\frac{\partial}{\partial r_i}\langle p\rangle + \frac{\partial}{\partial r_j}\langle\sigma'_{ij}\rangle + \langle\rho\rangle\hat{g}_i - \frac{\partial}{\partial r_j}\hat{\tau}(v_i,v_j) \tag{7.29}
$$

$$
\begin{aligned}
\frac{\partial}{\partial t}\langle\rho\rangle e_{res} + \frac{\partial}{\partial r_j}\langle\rho\rangle\hat{v}_j e_{res} \quad = \quad & -\frac{\partial}{\partial r_i}\hat{v}_i\langle p\rangle + \frac{\partial}{\partial r_j}\hat{v}_i\langle\sigma'_{ij}\rangle + \langle\rho\rangle\hat{v}_i\hat{g}_i \\
& +\langle\rho\rangle(\lambda+\epsilon) - \hat{v}_i\frac{\partial}{\partial r_j}\hat{\tau}(v_i,v_j) - \frac{\partial}{\partial r_j}\hat{\tau}(v_j,e_{int})
\end{aligned}
\tag{7.30}
$$

$$
\frac{\partial}{\partial t}\langle\rho\rangle e_t + \frac{\partial}{\partial r_j}\langle\rho\rangle\hat{v}_j e_t \;=\; \mathcal{D} + \Gamma - \langle\rho\rangle\lambda - \langle\rho\rangle\epsilon - \hat{\tau}(v_j,v_i)\frac{\partial}{\partial r_j}\hat{v}_i. \tag{7.31}
$$

Together with the equation of state (Equation (2.8)) as well as the Poisson equation (Equation (2.4)) to solve for the gravitational potential these are essentially the equations which we use in our version of Enzo to simulate turbulent astrophysical systems.
The terms of viscous dissipation σ_{ij} in Equations (7.29) and (7.30) can be neglected for sufficiently

large Reynolds numbers, this is equivalent to the transition form Navier-Stokes equation to Euler's equation for the resolved flow. Consequently, dissipation is completely accounted for by the ϵ-term in Equation (7.31) of turbulent energy.
Note that we can split Equation (7.30) into two separate equations for resolved kinetic and resolved thermal energy, respectively. This features the use of the SGS model in combination with the ZEUS solver.

$$\frac{\partial}{\partial t}\langle\rho\rangle\hat{e}_{kin} + \frac{\partial}{\partial r_j}\langle\rho\rangle\hat{v}_j\hat{e}_{kin} = -\hat{v}_i\frac{\partial}{\partial r_i}\langle p\rangle + \hat{v}_i\frac{\partial}{\partial r_j}\langle\sigma'_{ij}\rangle + \langle\rho\rangle\hat{v}_i\hat{g}_i - \hat{v}_i\frac{\partial}{\partial r_j}\hat{\tau}(v_i, v_j) \tag{7.32}$$

$$\frac{\partial}{\partial t}\langle\rho\rangle\hat{e}_{int} + \frac{\partial}{\partial r_j}\langle\rho\rangle\hat{v}_j\hat{e}_{int} = -\langle p\rangle\frac{\partial}{\partial r_j}\hat{v}_j + \langle\sigma'_{ij}\rangle\frac{\partial}{\partial r_j}\hat{v}_i + \langle\rho\rangle(\lambda+\epsilon) - \frac{\partial}{\partial r_j}\hat{\tau}(v_j, e_{int}) \tag{7.33}$$

The major missing piece is to model the explicitly unknown quantities $\mathcal{D}$, Γ, λ, ϵ, and $\hat{\tau}(v_i, v_j)$ in terms of the turbulence energy e_t and to find a model for $\hat{\tau}(v_j, e_{int})$ which is independent of this energy. In the following section we will discuss the relevant closures for our star formation simulations. For a complete account of the SGS model, see Schmidt et al. [2006a,b]. For more details on the formalism of filtering, operator rules and the decomposition of equations, please also refer to the Ph. D. thesis of Maier 2008. This thesis describes this abridgment of our model in a more extended fashion.

7.2. Closures for the Production of Turbulence Energy

To close the Equations (7.28) to (7.31) and allow for their numerical use, we now need to find appropriate assumptions to handle the five unknown terms within. The most simple assumption would just be to completely neglect a term. Fortunately, we are able to do this for two of our terms. Therefore, we will start the following discussion of subgrid closures with those simplest model assumptions.

We begin with the only term independent of turbulent energy $\hat{\tau}(v_j, e_{int})$. The divergence of this generalized moment of velocity and internal energy appearing in Equation (7.30) describes the turbulent transport of heat. This is the first effect we omit in our subgrid model. This is a rather imperfect approximation since we are not able to resolve all relevant thermal properties of the flow. However, we consider this turbulent diffusion of internal energy as a secondary effect and postpone a more realisitic treatment to future work.
Furthermore, the second term we ignore is Γ, which describes small-scale gravitational effects. Again, this is not close to a desired final solution since we are not able to resolve down to a Jeans length in our simulations and therefore should not neglect all unresolved gravitational effects. However, this effect also appears to be rather insignificant for our modeling of molecular cloud subgrid-scales in the current framework.

To account for the remaining terms $\mathcal{D}$, λ, ϵ and $\hat{\tau}(v_i, v_j)$ we introduce the interpretation of the density weighted trace of $\hat{\tau}(v_i, v_j)$ as squared velocity fluctuations q^2. Therefore, we write

$$e_t = \frac{1}{2}\frac{\hat{\tau}(v_i, v_i)}{\langle\rho\rangle} := \frac{1}{2}q^2. \tag{7.34}$$

These velocity fluctuations q are henceforth used to describe the characteristic velocity of turbulent motions below the grid cutoff. Moreover, the grid cutoff itself constitutes the characteristic

length scale of the subgrid model. In our simulations, this characteristic length l_Δ is the size of the grid cell.

With these definitions, we turn to the subgrid-scale transport of turbulent energy described by $\mathcal{D}$. This transport of energy is modeled by a gradient-diffusion hypothesis where it is assumed that the nonlinear term is proportional to the turbulent velocity gradient (see Sagaut [2006] for more details). Consequently, we realize the computation of $\mathcal{D}$ as

$$\mathcal{D} = \frac{\partial}{\partial r_i} C_\mathcal{D} \langle\rho\rangle l_\Delta q^2 \frac{\partial}{\partial r_i} q. \tag{7.35}$$

The global constant diffusion coefficient $C_\mathcal{D}$ has to be determined from numerical experiments. Schmidt et al. [2006a] find a fiducial value of $C_\mathcal{D} = 0.4$.

Next, we turn to the effects of unresolved pressure fluctuations in compressible turbulence which are encoded in term λ. A simple closure for this term is

$$\lambda = C_\lambda q^2 \frac{\partial}{\partial r_i} \hat{v}_i, \tag{7.36}$$

where the global coefficient $C_\lambda = -0.2$ is used.

ϵ is the term which accounts for the turbulent dissipation as a result of viscosity on subgrid-scales. Although viscosity can be completely neglected for high enough Reynolds numbers on large scales, subgrid viscosity converts turbulent energy to internal energy on subgrid scales. The most simple term which corresponds to a diffusion term one can build from characteristic quantities, namely turbulent velocity and length scale, is

$$\epsilon = C_\epsilon \frac{q^3}{l_\Delta}. \tag{7.37}$$

Here, we will use $C_\epsilon = 0.5$ for all our work.

Finally, we are left with the turbulence production tensor $\hat{\tau}(v_i, v_j)$. The production of turbulence energy, or more precisely, the flux of kinetic energy from resolved to subgrid-scales is most easily expressed using the symmetry of the latter tensor. Splitting into symmetric tracefree and diagonal part we write

$$\hat{\tau}(v_i, v_j) = \hat{\tau}_{ij} = \hat{\tau}^*_{ij} + \frac{1}{3}\delta_{ij}\langle\rho\rangle q^2. \tag{7.38}$$

For later simplicity, we also note that the here separated trace is commonly identified as turbulent pressure p_t. Hence, $\hat{\tau}_{ij} = \hat{\tau}^*_{ij} + p_t$. Moreover, we follow the old idea of Boussinesq [1877] and assume that $\hat{\tau}^*_{ij}$ has the same form as the stress tensor of a Newtonian fluid σ'_{ij}, also known as turbulent viscosity hypothesis. Strictly speaking, the turbulent viscosity hypothesis is well defined for fully developed, homogeneous turbulence. For its validity, the production of turbulent energy and its dissipation have to equal out when temporally averaged. In that sense Schmidt et al. [2006a] use the hypothesis for the SGS model we follow along that route for the work at hand. Hence, we write

$$\hat{\tau}^*_{ij} = -2\eta_t S^*_{ij} \tag{7.39}$$

where η_t is the turbulent dynamic viscosity $\eta_t = \langle\rho\rangle\nu_t = \langle\rho\rangle C_\nu l_\Delta q$ and a trace free part of the turbulent stress tensor is

$$S^*_{ij} = \frac{1}{2}\left(\frac{\partial}{\partial r_j}\hat{v}_i + \frac{\partial}{\partial r_i}\hat{v}_j\right) - \frac{1}{3}\delta_{ij}\frac{\partial}{\partial r_k}\hat{v}. \tag{7.40}$$

Henceforth, we can express the turbulence production tensor as

$$\hat{\tau}(v_i, v_j) = -2\langle\rho\rangle C_\nu l_\Delta q S^*_{ij} + \frac{1}{3}\delta_{ij}\langle\rho\rangle q^2, \tag{7.41}$$

where the last global parameter is calibrated to $C_\nu = 0.05$ by Schmidt et al. [2006a].

Note that at this point we have ultimately succeeded to express all terms in the filtered fluid Equations (7.28) to (7.31) in form of computable quantities. Combining these equations with the four closure Equations (7.35) to (7.41) and the corresponding values for the global parameters $C_\mathcal{D}$, C_λ, C_ϵ and C_ν we have arrived at a fully determined set of equations, readily usable for numerical experiments.

7.3. Subgrid-Scale Physics on an Adaptive Mesh

As described in the last section, we can use the filtered equations to solve for the dynamical evolution of a flow in our simulations. However, it is important to account for the fact that our subgrid-scale model of turbulent energy as well as the derived closures conceptualize the idea of an almost isotropic occurrence of velocity fluctuations. Henceforth, it is important to augment the concept of large-eddy simulations with adaptive mesh refinement in order to ensure isotropy in the resolved scales. In other words, whenever LES are insufficient to capture anisotropies stemming from large-scale flow features, the massive usage of AMR has to resolve these anisotropies of energy-containing scales in order to render the results of our subgrid-scale model to stay within reasonable bounds.

Technically, this implies that the additionally generated numerical quantity, the turbulent energy field, has to be evolved not only in space and time but also with respect to the grid resolution. As for all other quantities (i. e. density) Enzo interpolates values for a new fine grid from the coarser parent grid whenever the resolution is increased by AMR. Moreover, once a region is more resolved than with the root grid, the code averages values on the fine grid to replace the underlying coarse grid values. However, turbulent energy is essentially scale-dependend and we imperatively need to account for this dependence when refining or derefining the turbulent energy field.

From the Kolmogorov [1941] theory we know the scaling relation for incompressible turbulence and use this relation to adjust the turbulent energy on two differently refined levels

$$\frac{e_{t,1}}{e_{t,2}} = \frac{q_1^2}{q_2^2} \sim \left(\frac{l_{\Delta,1}}{l_{\Delta,2}}\right)^{2/3}. \tag{7.42}$$

However, for compressible turbulence when velocity fluctuations become comparable or larger than the speed of sound, modifications to the above relation are expedient. Unfortunately, it is yet unclear how exactly these modifications have to look like.

It is important to stress that this scaling relation is only applied to adjust the presumingly subsonic resolved scales while the subgrid-scales containing trans- and supersonic velocity fluctuations remain untouched.

Using the above scaling relation, the subgrid-scale model implementation adjusts the values of the turbulent energy field on the resolved levels according to a simple scheme whenever the resolution of a certain simulation area changes.

Refinement	Derefinement
Values from the parent grid are interpolated using the standard ENZO interpolation method.	Values on the fine grid are averaged and used to replace the underlying coarse grid values.
The values of velocity $\hat{v}_i$ and turbulent energy e_t on the new fine grid are corrected according to $\hat{v}_{i,\text{fine}} = \hat{v}_i \sqrt{1 + \frac{e_t}{e_{kin}}(1 - r^{-2/3})},$	The values of the remaining coarse grid zones which had been covered by a finer grid are corrected according to $e_{t,\text{coarse}} = e_t r^{2/3},$
$e_{t,\text{fine}} = e_t r^{-2/3}.$	$\hat{v}_{i,\text{coarse}} = \hat{v}_i \sqrt{1 - \frac{e_t}{e_{kin}}(r^{2/3} - 1)}.$
The resolved energy is adjusted to ensure energy conservation.	Energy conservation is ensured as well as positivity of energy values.

The factor r in the above equations is the label for the grid refinement level, where $r = 0$ identifies the rood grid. With these two simple algorithmic procedures we keep the turbulent energy field in sync with the adaptive mesh refinement.

7.4. SGS Model Specialties for Galaxy Simulations

Additionally to the above described SGS model and its realization, there are two more aspects we particularly use for simulating star formation in disk galaxies. An artificial limitation of the turbulent Mach number and the treatment of turbulent energy production in strong shocks.
First, a certain upper limit for the turbulent Mach number is present in all our simulations including the subgrid model. This accounts for the fact that low density gas can effectively be accelerated in the potential of a gravitational field. Yielding extreme velocity gradients, this would result in unphysically high production of turbulence energy owing to our implementation of the turbulent viscosity hypothesis. However, as indicated earlier, the turbulent viscosity hypothesis breaks down in such a scenario and it is advisable to, therefore, alter the production mechanism of turbulent energy in order to remain within reasonable bounds. We achieve this by limiting the turbulent Mach number to an upper value. We set $\mathscr{M}_{t,\max} = 5$ in all our subgrid simulations. This has severe influence on the subgrid-scale turbulence star formation algorithm which directly depends on the turbulent Mach number. As this dependence follows a negative power law relation (cf. Equation (4.21)) an upper limit in the Mach number denotes a lower limit for the star formation rate per free-fall time.
This is indeed an undesired effect, however, necessary for numerical stability of the current version of the SGS model. There are two reasons why we still claim to yield auspicious results from our simulations. Firstly, simulating turbulent Mach numbers up to $\mathscr{M} \approx 5$, we are well at the lower limit of the parameter space where most of star formation is assumed to take place. Therefore, while not yet able to fully cover the important parameter range, we are nevertheless in the interesting range. Secondly, note the low absolute value of the power law index of $\text{SFR}_{\text{ff}} \propto \mathscr{M}^{-0.32}$. Krumholz and McKee themselves single out this weak dependence and explain its reason. Holding α_{vir} fixed while increasing $\mathscr{M}$ increases the model inherent density limit x_{crit} and therefore renders less gas able to collapse as it must reach higher gas density to collapse. Contrarily, the increase in $\mathscr{M}$ also broadens the probability distribution function rendering more gas at higher densities able to collapse. The mutual cancellation of both effects results in the

weak Mach number dependence of the model. Hence, the limited turbulent Mach number certainly is a shortcoming of the model we need to keep in mind for the analysis, however, we are able to do reasonable physics at the lower end of the parameter space.

Second, it is necessary to additionally account for the most localized and anisotropic features that appear in our simulations. Even with AMR it might happen that the numerical scheme is not able to resolve all of these shocks to sufficient degrees of refinement in order to stretch out the anisotropies. Aside shocks, this is also true for strongly self-gravitating regions with sharp local gradients in the gravitational potential. For these cases it is advisable to reduce the influence of the subgrid model in order not to artificially influence the occurring shocks. Therefore, we use a simple shock detector,

$$-\frac{\partial \hat{v}_i}{\partial r_i} l_\Delta > c_s, \tag{7.43}$$

which identifies all cells with velocity increments larger than the local sound speed c_s. For all these cells we alter the production term of turbulent energy by updating the now local production parameter C_ν to be determined as

$$C_\nu = 0.05 \ \frac{c_s^2}{(l_\Delta d)^2}, \tag{7.44}$$

where we have used $d = \frac{\partial \hat{v}_i}{\partial r_i}$ to write the expression in an appealing way.
For strong shocks which automatically become highly resolved, hence are covered by cells having small lengths l_Δ, and at the same time having high values for the speed of sound, as well as large negative divergence of the velocity field, this effectively reduces the effects of the SGS algorithm as desired for non-isotropic local events.

This last Chapter (7) is a complete presentation of all relevant aspects of our subgrid model, with respect to our galaxy scale star formation simulations, and its implementation in the Enzo code. For more details on the conceptual work, we again refer readers to the work originally introducing and testing the model [Schmidt et al., 2006a,b]. Moreover, Maier et al. [2008] has served as a guideline for the presentation in this work and the paper by the latter authors already shows our endeavors to improve the model. In particular, several augmentations concerning the treatment of transsonic and supersonic velocity fluctuations have been developed and discussed above. Moreover, one of the major ongoing efforts in our group is the continuous improvement of the model towards an even better account of the effects of compressibility and high Mach number turbulent flows.

CHAPTER 8

Density Distribution of Gas in Star Forming Regions

For the development of their analytic star formation algorithm Krumholz and McKee [2005] assume that star formation takes place in molecular clouds that have lognormal density distributions. This basic assumption becomes important when estimating the amount of mass capable of gravitational collapse and star formation. It therefore has significant influence on the star formation rate. The latter authors give straight arguments for their assumptions and compare and fit their equations to numerical simulations yielding a calibrated parameterization ready for the implementation in numerical simulations. However, recent numerical experiments of our group [Schmidt et al., 2008b] question the assumption of a lognormal density distribution in supersonic, turbulent, isothermal gas. Therefore, we discuss the lognormal distribution in the following sections, report on the results of our experiments and draw conclusions for the implementation of the KM05 star formation theory.

8.1. The Lognormal distribution

In probability and statistics, the lognormal distribution is a distribution of any random variable whose logarithm is normally distributed. The positive definite continuous random variable X is lognormally distributed with the dependent parameters μ_L and σ_L^2 when the random variable Y has a normal distribution with the same parameters μ_L and σ_L^2, where μ_L and σ_L^2 are expectation value and standard deviation of the transformed random variable Y while μ and σ^2 are expectation value and standard deviation of X.

$$Y = \log X \tag{8.1}$$

Although the base of the logarithm does not matter in the sense that if $\log_a X$ is normally distributed, then so is $\log_b X$ for any two positive numbers $a, b \neq 1$, we will use the natural logarithm throughout this work if not stated otherwise.
The probability density and cumulative distribution functions for the lognormal distributions are

$$p(\rho)d\rho = \frac{1}{\rho\sqrt{2\pi}\sigma_\delta} \exp\left(-\frac{(\ln\rho - \overline{\ln\rho})^2}{2\sigma_\delta^2}\right)d\rho \tag{8.2}$$

$$d(\rho) = \frac{1}{2}\left[1 + \mathrm{erf}\left(\frac{\ln\rho - \overline{\ln\rho}}{\sigma_\delta\sqrt{2}}\right)\right], \tag{8.3}$$

where the density ρ is the quantity which is lognormally distributed (X) and $\delta = \ln\rho$ (Y) its normal substitution.
Using this substitution, we can rewrite equation (8.2) as

$$p(\delta)d\delta = \frac{1}{\sqrt{2\pi}\sigma_\delta} \exp\left(-\frac{(\delta - \mu_\delta)^2}{2\sigma_\delta^2}\right)d\delta \tag{8.4}$$

where we have also used $\frac{d\rho}{\rho} = d\ln\rho$ and $p(\rho)d\rho = p(\ln\rho)d\ln\rho$ and the substitution therein. We have labeled μ and σ with subscripts δ to stress that they are *mean* and *standard deviation* of the variables logarithm $\delta = \ln\rho$.

Equation (8.4) is commonly given in the literature as definition for a lognormal distribution (see e. g. Padoan and Nordlund [2002]).
Note that we have used the normalized volume density $\rho = \rho'/\rho_0$. The mean of the logarithm of density $\overline{\ln \rho}$ is determined by the standard deviation of the logarithm of density σ_δ.

$$\mu_\delta = \overline{\ln \rho} = -\frac{\sigma_\delta^2}{2} \tag{8.5}$$

Furthermore, the latter authors declare that the standard deviation is found to be a function of the rms Mach number $\mathscr{M}$ of the flow under consideration and report a correlation factor $\phi = \frac{1}{4}$.

$$\sigma_\delta^2 = \ln\left(1 + \phi \mathscr{M}_{\mathrm{rms}}^2\right) \tag{8.6}$$

We note that in this definition the rms Mach number is defined as three dimensional quantity $\mathscr{M} = |\vec{v}|/c_s$ and is related to rms Mach number in one dimensional simulations via $\mathscr{M}_{1D} = 1/\sqrt{3}\ \mathscr{M}_{3D}$.

The build up of density fluctuations in simulations of astrophysical flows can be described as a random multiplicative process. Once the density ρ is logarithmically parameterized as $\tilde{\delta} = \ln \rho$ or including a normalization as $\delta = \ln(\rho/\rho_0)$, the random process becomes additive at the level of the variable δ. Hence, δ is the sum of random density fluctuations. The sum of identical random processes is known to have a Gaussian distribution as a result of the Central Limit Theorem and the probability density function is thus expected to show normal distribution. Furthermore, Equation (8.5) is a result of the constraint of mass conservation or simply $\langle \rho/\rho_0 \rangle = 1$ requires the relation of μ_δ and σ_δ.

For completeness, we state the interdependence of expectation value and standard deviation of the normal and lognormal distribution[a].

$$\mu_\rho = \exp\left(\mu_\delta + \frac{\sigma_\delta^2}{2}\right) \tag{8.7}$$

$$\sigma_\rho^2 = \left[\exp\left(\sigma_\delta^2\right) - 1\right] \exp\left(2\mu_\delta + \sigma_\delta^2\right) \tag{8.8}$$

One can use this to derive the linear correlation of the empirically found logarithmic correlation of standard deviation and three dimensional rms Mach number. Passot and Vázquez-Semadeni [1998] use the correlation $\sigma^2 = \beta \mathscr{M}^2$ and report a value for the correlation factor $\beta = 1$ for their isothermal simulations. However, these are one dimensional simulations and so is their Mach number. Hence, we have to add a factor of 1/3 or $\phi \doteq \beta/3$ to reach accordance. Numerical evaluation then contrasts $\phi = 0.25$ and $\phi \simeq 0.33$ for Padoan and Nordlund [2002] and Passot and Vázquez-Semadeni [1998], respectively. Substitution of Equation (8.6) and Equation (8.5) in Equation (8.8) yields

$$\sigma_\rho^2 = \phi \mathscr{M}^2. \tag{8.9}$$

[a] This is only valid if the natural logarithm is used for the distribution function.

Clinging a little closer to probability theory and statistics we find the coefficient of variation η, which is a normalized measure of dispersion of a probability distribution.

$$\mu_\rho = \exp\left(\mu_\delta + \frac{\sigma_\delta^2}{2}\right) \rightarrow \mu_\rho^2 = \exp\left(2\mu_\delta + \sigma_\delta^2\right) \tag{8.10}$$

$$\sigma_\rho^2 = \left[\exp\left(\sigma_\delta^2\right) - 1\right]\mu_\rho^2 \tag{8.11}$$

$$\eta^2 = \frac{\sigma_\rho^2}{\mu_\rho^2} = \left[\exp\left(\sigma_\delta^2\right) - 1\right] \tag{8.12}$$

Again, substituting σ_δ^2 from Equation (8.6) gives

$$\eta^2 = \phi \mathscr{M}^2. \tag{8.13}$$

There is good reason for the correlation at hand. The coefficient of variation is most useful because the standard deviation of data is only meaningful in context of the mean of data. Therefore, when comparing largely different simulations the standard deviation strongly depends on units and scalings while the coefficient of correlation is a universal dimensionless number which can be compared across simulations, and more importantly, points towards a common source of the described variations. Obviously, the rms Mach number, yet another dimensionless number, seems the logical choice to characterize the magnitude of perturbations in the probability distribution of density in supersonic flows. Henceforth, the appearance of the universal scaling relation of the dispersion of density probability density function with the rms Mach number of the simulated flow in the literature is not surprising and can be interpreted as consequence of a correlation of two universally normalized quantities.

8.2. Compressively Driven Interstellar Turbulence

We have performed extensive three dimensional simulations of forced isothermal interstellar turbulence with Enzo. For this case we used the implementation of the piecewise-parabolic method (PPM) and performed static grid as well as adaptive mesh refinement simulations with an effective resolution of $N = 768^3$. The large-scale forcing is realized by an external stochastic field dominated by rotation-free modes. The forcing term is coupled to the momentum Equation (2.2) in the form

$$\rho \frac{D\boldsymbol{v}}{Dt} = -\boldsymbol{\nabla} p + \rho \boldsymbol{f}, \tag{8.14}$$

where we have used

$$\frac{D}{Dt} = \frac{\partial}{\partial t} + \boldsymbol{v} \cdot \boldsymbol{\nabla} \tag{8.15}$$

to rewrite the Lagrangian derivative. Note that $\rho \boldsymbol{f}$ is the external force density. Moreover, the turbulence simulations reported in this section do not include gravitational or viscous terms. The simulations are described in Schmidt et al. [2008b], here we only summarize the results concerning the density statistics and compare to other work in this field.

Previous theoretical and numerical studies favor lognormal statistics for the mass density of supersonic turbulence in isothermal gas [Vazquez-Semadeni, 1994, Padoan et al., 1997, Passot and Vázquez-Semadeni, 1998, Padoan and Nordlund, 2002]. This means that the distribution of $\delta = \ln(\rho/\rho_0)$ is Gaussian. Consistency with $\langle \rho/\rho_0 \rangle = 1$ requires the variance of δ being related to the mean via $\sigma_\delta^2 = -2\langle \delta \rangle$. However, as one can see in Figure (8.1), a normal distribution subject to this constraint does not properly fit the time-averaged δ-PDF from our simulation.

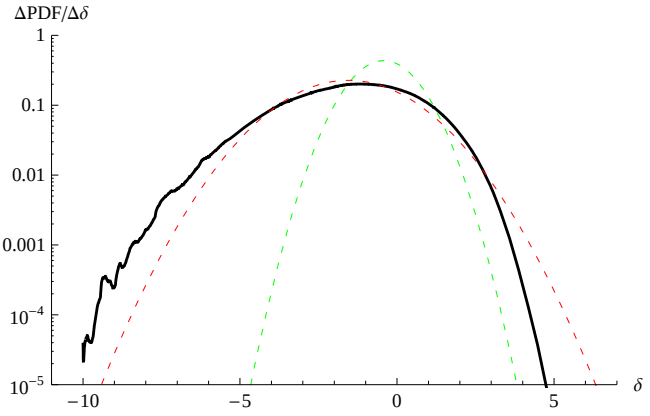

FIGURE 8.1. Temporally averaged probability density function of the logarithmic mass density fluctuations, $\ln(\rho/\rho_0)$, and lognormal fit functions (thin dashed lines).

The standard deviation of the closest possible fit is $\sigma_\delta \approx 1.76$. Padoan and Nordlund [2002] proposed that σ_δ can be parameterized in terms of the rms Mach number:

$$\sigma_\delta^2 = \ln\left(1 + 0.25\mathscr{M}_{\rm rms}^2\right). \tag{8.16}$$

We have $\mathscr{M}_{\rm rms} \approx 2.3$ in the interval of time over which the PDF of δ is averaged. For this Mach number, the above formula yields $\sigma_\delta \approx 0.92$. The corresponding PDF is also plotted for comparison in Figure (8.1). Clearly, compressively driven turbulence produces a substantially broader range of density fluctuations than predicted by Padoan and Nordlund. Kritsuk et al. [2007], on the other hand, found a narrower range in relation to the rms Mach number.

Since we have sampled the δ-PDFs over many integral time scales, the shape of our time-averaged PDF is very likely genuine. In test simulations, we have also excluded the possibilities that it is purely a resolution effect or a consequence of the nearly isothermal approximation. A skewed distribution of density fluctuations has important consequences. In Figure (8.2) the total mass of gas with density higher than a given threshold density

$$M(\rho) = (2L)^3 \int_\rho^\infty \rho' \mathrm{pdf}(\rho')\, d\rho' = \rho_0 (2L)^3 \int_\delta^\infty \exp(\delta)\ \mathrm{pdf}(\delta)\, d\delta', \tag{8.17}$$

is plotted for the time-averaged probability density function PDF(δ) from our simulation, closest lognormal PDF and the lognormal PDF with $\sigma_\delta \approx 0.92$, respectively. It is palpable that calculating $M(\rho)$ on the basis of the lognormal fit with $\sigma_\delta \approx 1.76$ in place of the numerical PDF implies enormously wrong mass fractions in the high-density peaks. On the other hand, the prediction of $M(\rho)$ based on the Padoan-Nordlund relation stated in Equation (8.16) underestimates the total mass of highly compressed gas by about one order of magnitude. For $\rho \gtrsim 100$ a numerical cutoff can be discerned, as the mass function corresponding to the numerical PDF plunges towards zero in the logarithmically scaled plot (b). The reason is that density fluctuations cannot become arbitrarily high as a result of the spatial discretization and, because of the discretization in time, the most intermittent events are too rare to show up in the statistics. The mass range affected by the numerical cutoff is $M(\rho) \lesssim 10^{-3}$. We found that this range largely overlaps with the mass range for the computation of clump mass spectra following the prescription by Padoan et al. [2007b]. The high sensitivity of mass spectra on numerical resolution has already been noted by Hennebelle and Audit [2007]. Consequently, it is mandatory to go to substantially higher resolutions which, in turn, necessitates the application of adaptive mesh refinement. Unlike the

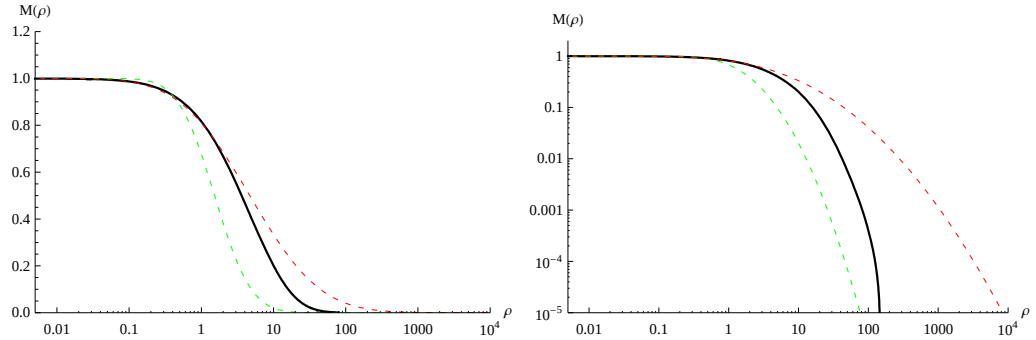

FIGURE 8.2. Integrated mass $M(\rho)$ in gas of density higher than ρ in linear scaling (a) and logarithmic scaling (b). The thick solid line results from the time-averaged PDF obtained from our simulation. The closest lognormal distribution and the lognormal distribution implied by the Padoan-Nordlund Relation (8.16) yield the dashed cures. While the former greatly overestimates the mass in the density peaks, the latter underestimates the fraction of over-dense gas.

AMR simulation at hand, extreme density peaks have to be followed to very high resolution and, at the same time, turbulent flow has to be treated self-consistently in less resolved regions of lower gas density. This becomes problematic in case of galactic scale simulations where the resolution limit is orders of magnitude above these density values.

8.3. Deviations from the Lognormal Distribution of Gas Densities

A justification for lognormal PDFs of the mass density based on analytical arguments was given by Passot and Vázquez-Semadeni [1998] for one-dimensional isothermal gas dynamics without external forces. To what extent do these arguments apply to three-dimensional turbulence with stochastic forcing? Setting the pressure $p = c_s^2 \rho$, where c_s is the isothermal speed of sound, the pressure gradient divided by the mass density is given by

$$\frac{1}{\rho} \boldsymbol{\nabla} p = c_s^2 \boldsymbol{\nabla} \delta. \tag{8.18}$$

Thus, we can write the first two Euler equations in the form

$$\frac{D\delta}{Dt} = -d, \tag{8.19}$$

$$\frac{D\boldsymbol{v}}{Dt} = -c_s^2 \boldsymbol{\nabla} \delta + \boldsymbol{f}. \tag{8.20}$$

The first equation means that infinitesimal Lagrangian changes of the density are given by $-d\ dt$. It is argued that density fluctuations are built up in a hierarchical process, meaning that δ evolves as a random process, where infinitesimal increments $\delta_+ dt$ (density enhancements) and decrements $\delta_- dt$ (density reductions) are added with equal probability independent of the value of δ. The central limit theorem then implies a Gaussian distribution of δ. This is the Wiener process. The Wiener process is a continuous-time stochastic process that generates Gaussian random vector deviates in the stochastic differential equation of the forcing algorithm (see Schmidt et al. [2008b]). These arguments also apply to the three-dimensional case.

However, the action of an external force can cause deviations from the lognormal statistics. In supersonic turbulence, the steepening of density gradients is associated with rising gas compression. This is indicated by a positive rate of compression, i. e., the negative time derivative of the divergence $d = \boldsymbol{\nabla} \boldsymbol{v}$. Applying the operator $\boldsymbol{\nabla} \cdot$ on Equation (8.14), it can be shown that the rate of compression is given by

$$-\frac{D}{Dt} d = \frac{1}{2} \left(|S|^2 - \omega^2 \right) + \boldsymbol{\nabla} \cdot \left(\frac{1}{\rho} \boldsymbol{\nabla} p - \boldsymbol{f} \right), \tag{8.21}$$

where $\boldsymbol{\omega} = \boldsymbol{\nabla} \times \boldsymbol{v}$ is the vorticity. Let us consider the equation for the rate of compression in the isothermal case:

$$-\frac{D}{Dt} d = \frac{1}{2} \left(|S|^2 - \omega^2 \right) + c_0^2 \boldsymbol{\nabla} \delta - \boldsymbol{\nabla} \cdot \boldsymbol{f}. \tag{8.22}$$

In regions, in which $\boldsymbol{\nabla} \cdot \boldsymbol{f} < 0$, the force tends to increase the rate of compression. The equation for the density fluctuations (cf. Equation (8.19)) implies that the corresponding fractional change of $-d\ dt$ results in a stronger increment $\delta_+ dt$ or a smaller decrement $\delta_- dt$, i. e., a force with positive convergence locally supports compression and weakens rarefaction, as one would expect. In the case $\boldsymbol{\nabla} \cdot \boldsymbol{f} > 0$, the force has the opposite effect. If the force field is stochastic, both effects will occur with equal probability at any time at any position (by the very construction of the force field). Hence, the net effect depends on the periods of time a particular fluid parcel is contracting ($-d > 0$) or expanding ($-d < 0$). Apart from that, the effect will weaken toward smaller scales and higher densities (because of scaling considerations). For a detailed analysis, Lagrangian density statistics would be required. From the existing simulation, we have only Eulerian statistics. Nevertheless, our considerations show that, in general, forces with a strong dilatational component may cause deviations form a lognormal distribution of the density fluctuations in isothermal gas. This is what we observe in our simulation.

8.4. The Density Distribution in the Star Formation Algorithm

As stated earlier, lognormality is one of the basic assumptions in the KM05 star formation prescription. However, the model still allows to introduce qualitative changes to the assumed density distribution function without corrupting the entire algorithm. In particular, the original model by KM05 also has two numerical factors which are determined by fitting the analytical equation to numerical simulations.
It was our original plan to repeat this calibration on the basis of the above described simulation of isothermal interstellar turbulence. However, as we discovered the importance of the employed forcing mode it became quickly obvious that the dilatationally forced simulations with significant deviations from lognormal density distributions would not be adequate to perform the desired calibration procedure. More work is underway to further investigate the issue at hand.

There are good arguments that compressive modes dominate the driving of interstellar turbulence on large scales. As described earlier, it is believed that especially supernova shock waves and the interaction of supernova bubbles are prime candidates for this driving. The influence of these mechanisms on the ISM would mostly be a result of compression effects, and consequently produce compressive modes. This reasoning for a more realistic driving was among the reasons for simulating compressive forcing in the first place.
As a consequence of this approach, it appears to be possible to improve the prescription of the probability distribution function of density in a supersonically turbulent isothermal gas considerably. Furthermore, this might strongly impact on the results of the star formation algorithm

proposed by KM05. However, we have not yet been able to find a similarly applicable analytic expression, as the lognormal distribution, which matches the PDF of our analysis more accurately. Additionally, more work is necessary to include self-gravity and thermal effects in these simulations to analyze gravitational contraction and perform improved calibrations of the numerical parameters in the algorithm.

Owing to these reasons and the primary focus on the implementation and application of the original KM05 model we resorted back to the original idea and calibration of Krumholz and McKee and will use the formulation and parameterization of the star formation algorithm given by the latter authors.

Summary of Numerics

The Part (II) of this thesis is concerned with the numerical aspects of our endeavor to simulate turbulence and star formation in disk galaxies. Therefore, we have started this part with a description of the general technical framework we are using. We have introduced the Enzo code and discussed the employed solver algorithms to evolve the hydrodynamical equations. Furthermore, we have described the important aspects of thermodynamical processes and their technical realization as well as the originally available particle creation and star formation routines.
Following this description of the public release version of Enzo, we presented our numerical setup of an isolated disk galaxy. Again, we have been following the natural order of scales and started the description by integrating our galaxies into the cosmological context. Proceeding from the details of the dark matter profile to the baryonic gas density profile we continued to explain our setup, and discussed the details of the numerical realization of cooling and heating processes. We closed the description of the galaxy setup by presenting our changes to the original star formation routines and the introduction of our new turbulence regulated algorithm.
Consequently, we continued with a detailed presentation of the turbulence subgrid-scale model which supplies the information necessary for the use of the latter star formation algorithm. Therefore, we have shown how to derive the governing equations yielding the turbulent subgrid-scale energy. Furthermore, we also added a detailed description of how we close these equations with appropriate subgrid-scale closures. We continued this explanation of the numerical details of the subgrid model by describing how we combine SGS and AMR, and concluded with the description of some specialties concerning our galaxy simulations.
With the complete technical description of the galaxy simulations at hand, we added a supplementary discussion on the assumption of a lognormal density distribution of gas in star formation regions. We started with the theoretical description of the assumed distribution which appears as basic element in the turbulence regulated star formation scenario. Subsequently, we described our numerical work which lead us to the conclusion to have serious doubt about the assumed lognormal distribution function. Finally, we concluded with a discussion why we nevertheless continue our present work with the originally proposed model.

Thus, we have finished the presentation of our numerical work and given all relevant conceptual and technical details. Next, we will proceed to Part (III) and show what we have been able to achieve using everything presented up to now.

Part III

Learning from Simulations

CHAPTER 9

Results of Numerical Simulations

Simulating star formation and especially turbulence regulated star formation in models of isolated disk galaxies is a quite challenging endeavor. In the preceding parts of this thesis we have described the theory and numerics we use to approach the problem. Now, we systematically analyze and present our simulation runs. We performed the common standard analyses (i. e. density and temperature distributions) and discuss them here. Moreover, we will give extensive details on how we analyze the particular star formation and turbulence content in our simulations. Finally, we draw conclusions and discuss shortcomings as well as prospective achievements of work using our subgrid-scale approach to model turbulence and star formation.

9.1. Redefining Initial Conditions

It is well known that setting up a full three-dimensional model of some dynamically stable astrophysical disk configuration is rather difficult. Rotational forces, gravity, the temperature profile and distribution of gas density have to have balanced forces in order for the disk not to disperse immediately. With our approach to set up a gas disk as described in Section (6.2) we do not attempt to construct such a system from scratch. We rather define the system's gross properties and let it self–consistently evolve towards the desired initial conditions. From the description of our setup in the latter section as well as in the work of Tasker and Bryan [2006] it is easy to see that using a constant initial temperature of $10^4\,\mathrm{K}$ the pressure profile directly depends on the gas density distribution. However, the rotational velocity in the gas disk is initialized only with respect to the gravitational potential. This leads to a dynamically unstable initial configuration. In Figure (9.1) we show three projections of the gas disk along the axis of rotation (face-on projections) of the original initial setup. The three projections are snapshots of the very

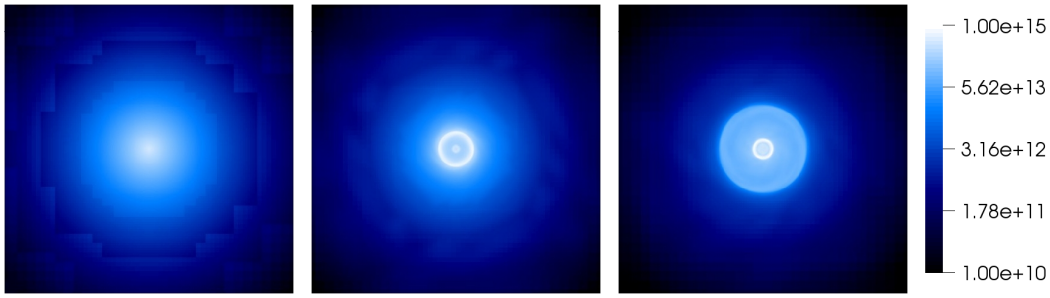

(a) 0 Myr (b) 50 Myr (c) 100 Myr

FIGURE 9.1. Face-on projections of the initial gas disk configuration. The pictures are 60 kpc across and show color coded gas density where the most dense gas $10^{15}\,\mathrm{M}_\odot\,\mathrm{Mpc}^{-2}$ is depicted white, while the lowest gas density $10^{10}\,\mathrm{M}_\odot\,\mathrm{Mpc}^{-2}$ is colored black.

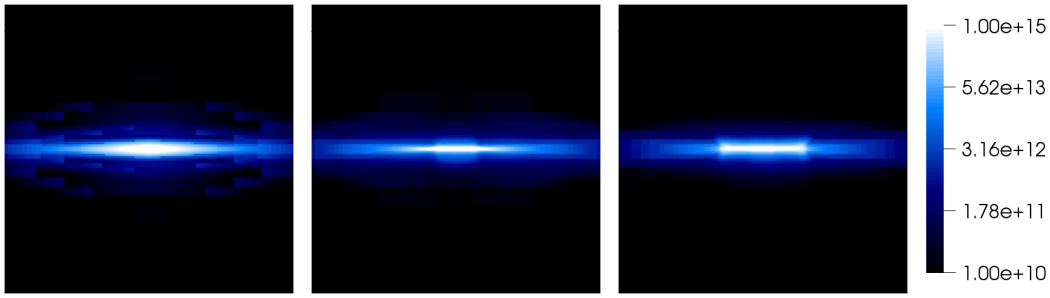

(a) 0 Myr (b) 50 Myr (c) 100 Myr

FIGURE 9.2. Side-on projections of the initial gas disk configuration. The pictures are again 60 kpc across and use the same color table as Figure (9.1)

early evolution of the disk and show the first 100 Myr of a simulation. As this is just a test of the initial conditions, this simulation does not use radiative cooling and the formation of sink particles is switched off. At first glance we see that the gas distribution dramatically changes its appearance in the early phase of the simulation. Qualitatively, we observe a contraction of the outer gas disk, while a strong circular shock wave appears in the center of the disk. This circular compression of gas travels radially outwards and is itself followed by other subsequent compression waves emerging from the disk center.

The appearance of this violent relaxation of initial conditions is even more eminent in the side-on projections of the disk. In Figure (9.2) we see the shock front sweeping up gas as it moves outwards. In simulations where the generation of sink particles was allowed in this early phase of the simulation, we saw a strong burst of particle generation following the circular ring of compressed gas radially travelling outwards through the disk. In fact, Tasker and Bryan [2008] also report to observe a strong initial star burst in their simulations and account for it by focussing the main part of their analysis on later times. Although the initial conditions are rather artificial in the first place and setting up a Milky Way style galaxy with the correct mass, but all in gas and none in stars, will certainly result in a rapid production of a stellar component as soon as allowed to dynamically evolve, we nevertheless decided not to have the latter process to be influenced by the relaxation waves occurring as a result of the initial conditions. Contrarily, we decided to evolve the initial setup, still without cooling and particle formation, until it reaches a dynamically stable configuration where it does not change its gross properties anymore.

For this reason, we evolve our simulations for a full standard simulation time, namely 1.4 Gyr before we switch to the dynamical phase of the simulation. Note that while neither radiative cooling is active nor does the code have to simulate the formation and evolution of particles, we only need a couple of hundred CPU hours to simulate towards stable initial conditions.
Consequently, we define new initial conditions with $t = 0$ Myr after 1.4 Gyr of the earlier simulation. Figure (9.3) shows again face-on and side-on projections of this state of the simulation. This is the configuration from which we restart our simulations. The most eminent difference between the old and the new initial conditions is the vertical thickness of the gas disk. Gas density now appears to decline much more slowly with distance to the galactic midplane, as moderately changing profiles are much less sensitive to small perturbations.

Moreover, from Figure (9.4) we also see significant differences in the temperature profile. While the original setup used a fixed temperature, we now see a narrow distribution of temperatures, approximately at a value one order of magnitude hotter than before. Note that the analysis of

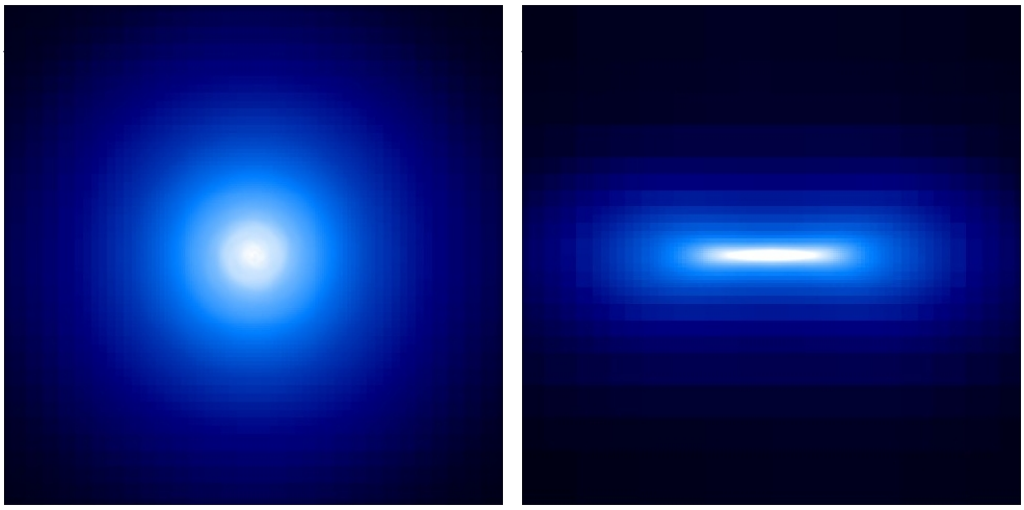

(a) 1.4 Gyr ≙ 0 Myr (b) 1.4 Gyr ≙ 0 Myr

FIGURE 9.3. New initial conditions of our simulations after 1.4 Gyr when the setup has reach a dynamically stable configuration.

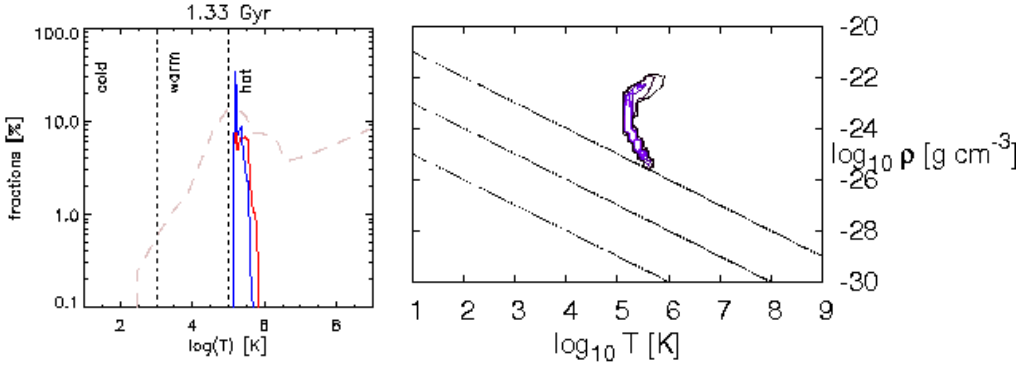

(a) Volume (blue) and mass (red) fractions of baryonic gas in the extraction volume.

(b) Pressure contours. The straight lines depict constant pressure.

FIGURE 9.4. Initial conditions of our simulations. Plot (a) shows the temperature of the gas while (b) shows how the temperature is related to the gas density.

this picture evaluates a volume centered on the galactic center comprising of three radial scale lengths (= 10.5 kpc) in radius and one vertical scale height (325 pc) as distance to the galactic midplane to focus on the main disk. Additionally, the right plot (b) in the last figure, depicts countours of pressure in the disk. We include this picture to clarify that we do not re-initialize our simulations with a disk in pressure equilibrium, but in order to avoid the effects of an artificial initial compression shock wave.

Unfortunately, it is hard to judge which consequences the excluded effects stemming from the original initial conditions can have on a simulation. In simulations not presented here, we have

seen that a significant amount of gas is transformed into particles by the outwards propagating shock. Firstly, this gas is not available for later star formation. Secondly, by acquiring properties of the generating cells, especially velocity and momentum, a major fraction of particles carries the imprint of the initial conditions far into the simulations. Thirdly, in cases with feedback the latter effect might be even more serious as particles now determine location and strength (owing to the coupling of feedback and particle creation time) of the feedback. Certainly, the artificial construction of initial conditions, the original way or our relaxed version, is a shortcoming of the simulations at hand. More importantly, we discuss this topic at length here, because it also certainly influences the comparability to the earlier work of Tasker and Bryan [2006] and Tasker and Bryan [2008]. However, we consider it an important improvement of the latter work.

9.2. Summary of Performed Simulations

In the remaining part of this and the following chapter we will disscuss several simulations, all using the new initial conditions. Generally, we develop two different branches of simulations. The first branch are simulations similar to those presented by Tasker and Bryan [2006] and Tasker and Bryan [2008] but with our new initial conditions and some differently motivated parameter choices. The second branch is devoted to our subgrid-scale approach to model turbulence effects below the resolution limit to regulate star formation.
All simulations have the same dark matter potential (cf. Section (6.1)) as well as initial gas and temperature distribution (cf. Section (9.1)). The common parameters of all simulations are a box size of 1 Mpc on a side, resolved by a root grid resolution of 128^3 including 8 levels of refinement. Refinement is based an a density difference criterion. We use an adiabatic equation of state and employ a ratio of specific heats of $\gamma = 5/3$. We do not simulate any chemistry but use a global mean molecular weight of $\mu = 1.2$ to mimic a mixture of atomic and molecular hydrogen. All our simulations use a standard number density of $n = 10^3\,\mathrm{cm}^{-3}$ particles per cubic centimeter as particle creation threshold.
On this common basis, we perform several different realizations of simulations. We start with a simulation using SF1 star formation algorithm with star formation efficiency $\epsilon = 0.5$ (cf. Equation(5.24)). Furthermore, a minimum sink particle mass of $M_{\mathrm{min}}^{\mathrm{sink}} = 10^4\,\mathrm{M}_\odot$ is used as described in Section (5.4). This parameter set is simulated once without feedback, hereafter termed *standard case* (SF1F0e50), and once including feedback from type II supernovae (SF1F1e50) as described in Section (5.5). Here we set the code to return a total fraction of $f_{\mathrm{ej}} = 0.25$ (cf. Equation (5.26)) of gas converted into particles, back into the simulation volume as gas during the evolution of particles. The feedback energy is set as $f_{\mathrm{SN}} = 10^{-5}$ as described in the latter section. Additionally, we study different simulations, one using a larger sink particle mass limit and one using relaxed particle creation criteria.

To develop the second branch of turbulence regulated star formation, we also perform simulations with varying star formation efficiency as well as with and without feedback. Finally, we perform the full turbulence regulated calculation and variations. We summarize the different realizations in Table (9.1).

9.3. Evolution of the Gas Disk

In this section, we discuss the evolution of the interstellar gas in the galactic disk. The particular properties of this evolution strongly depend on the particular type of simulation (including feedback or not, type of SF algorithm, SF efficiency,...). However, before we get into all the details, we introduce the general properties of our simulations and detail the employed analyses.
Therefore, we begin the discussion with the standard simulation with no feedback, no subgrid-scale model, the SF1 star formation algorithm and standard values for all other quantities.

Name	Star Formation Algorithm	Feedback	Min Particle Mass	Efficiency
SF1F0e50	SF1	No	$10^4\,M_\odot$	0.5
SF1F1e50	SF1	Yes	$10^4\,M_\odot$	0.5
SF1F0e50mpm	SF1	No	$10^5\,M_\odot$	0.5
SF2F0e50	SF2	No	$10^4\,M_\odot$	0.5
SF1F0e3	SF1	No	$10^4\,M_\odot$	0.03
SF1F1e3	SF1	Yes	$10^4\,M_\odot$	0.03
SF1F1e03	SF1	Yes	$10^4\,M_\odot$	0.003
SF1F0e50sgsMa5	SF1	No	$10^4\,M_\odot$	0.5, $\mathscr{M}_{t,\max} = 5$
SF3F0sgsMa10err	SF3 (incorrect particle gravity)	No	$10^4\,M_\odot$	KM05, $\mathscr{M}_{t,\max} = 10$
SF3F0sgsMa5	SF3	No	$10^4\,M_\odot$	KM05, $\mathscr{M}_{t,\max} = 5$
SF3F1sgsMa1	SF3	Yes	$10^4\,M_\odot$	KM05, $\mathscr{M}_{t,\max} = 1$

TABLE 9.1. Overview of performed simulations.

To discuss the structure and evolution of the baryonic gas in the galactic disk, we start with a visual inspection of the temporal evolution of face-on (cf. Figure (9.5)) and side-on (cf. Figure (9.6)) projections. In the very early phase of the evolution, during the first 50 Myr, we see how the central, most dense part of the disk becomes unstable and starts to fragment. After 20 Myr we already see how gas accumulates in fine filamentary sheets building a highly irregular web. In the immediate center of the disk, where the gas density was originally most pronounced, patches with significantly depleted gas density begin to show up.
Subsequently, the two-dimensional filaments start to break up into point or cloud like structures. The process of fragmentation again starts in the inner part of the disk and proceeds outwards. At 50 Myr we see small round accumulations of dense gas in the center of the disk, while the intermediate disk still shows filaments of dense gas. The outer part of the disk is yet completely untouched by the processes occurring in the disk center.
Moreover, during the further temporal evolution more and more of the filaments disappear and transform into clouds. In the frame depicting 100 Myr of simulation time, only an outer ring of gas filaments remains. Gas from the intermediate disk range has begun to be swept up and accumulates into these filaments. Additionally, larger eddy like structures appear in the inner part of the disk, stemming from merging smaller clouds.
This evolution continuous and the fragmentation proceeds further outward through the gas disk. During the following 100 Myr, large amounts of gas are transformed into stars (not depicted here). The number of clouds and larger accumulations of gas as well as their size is reduced significantly. Moreover, large voids of very low density gas start to appear at intermediate disk scale.
Subsequently, the depletion of gas in the inner and intermediate disk results in a continuous inflow of gas from the outer part. At 500 Myr we see a clear reduction of the overall gas density

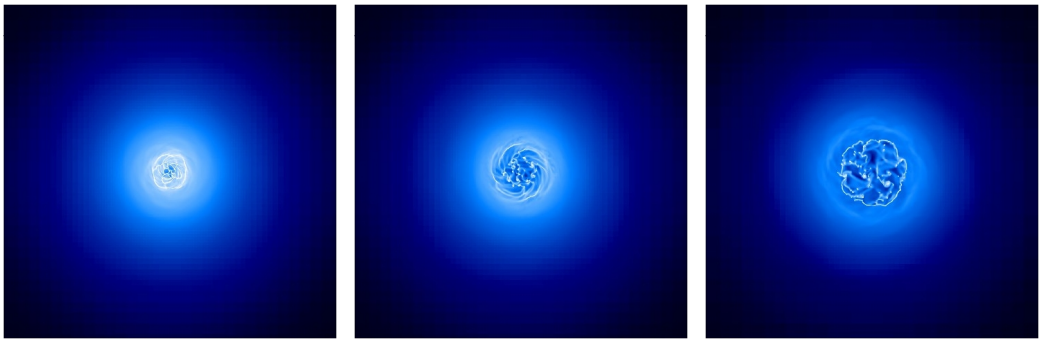

(a) 20 Myr (b) 50 Myr (c) 100 Myr

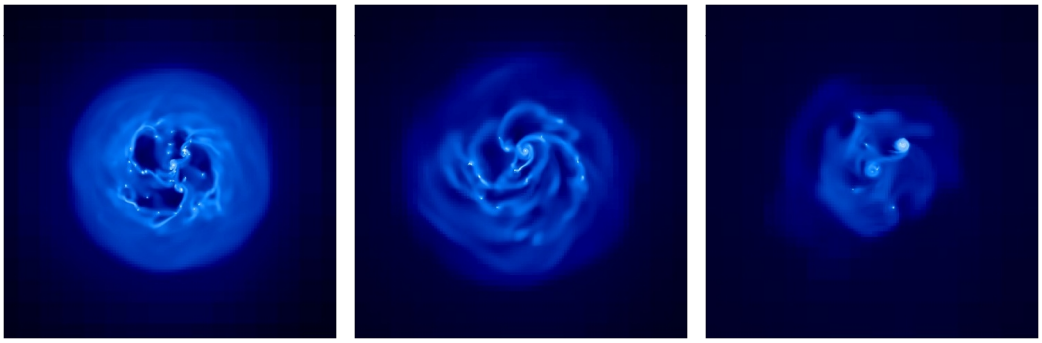

(d) 200 Myr (e) 500 Myr (f) 1000 Myr

FIGURE 9.5. SF1F0e50: Temporal evolution of the gas disk structure in projection along the axis of rotation. All pictures are 60 kpc across and the color table ranges from $10^{10}\,M_\odot\,Mpc^{-2}$ to $10^{15}\,M_\odot\,Mpc^{-2}$ as in Figure (9.1).

in the outer disk, while the number of dense clouds in the inner disk is also declining further. Note that all our disks are rotating counter-clockwise. We see both accretion from dense clouds into larger more massive objects as well as the stripping of gas from dense objects. This ram pressure stripping seems to be responsible for a significant part of the diffuse filaments appearing during this intermediate phase of disk evolution.
During the late time of evolution, up to 1 Gyr and until the simulation end at 1.4 Gyr, we mostly observe further gas depletion on all scales of the disk. The remaining gas seems to accumulate in only a couple of dense clouds, some still stripping gas of each other.

Although we cannot see much of the detailed structure of the galactic disk in the side-on projections of Figure (9.6) we nevertheless consider them to be very interesting. Most generally, it is obvious that the vertical disk scale changes significantly during the first 100 Myr. Vertically stratified gas, necessary for the stable initial conditions, settles down quickly. The gas available above and below the galactic midplane is most sensitive to the loss of pressure support as a result of the imminent cooling of the gas disk. This happens because vertical gas motions as a result of gravitational attraction are not stabilized by rotational forces. Hence, the disk quickly reaches an almost planar configuration.
Additionally, we can state that most of the structure emerging, evolving and dissolving during the simulation remain in or at least close to the galactic midplane. However, several clouds of

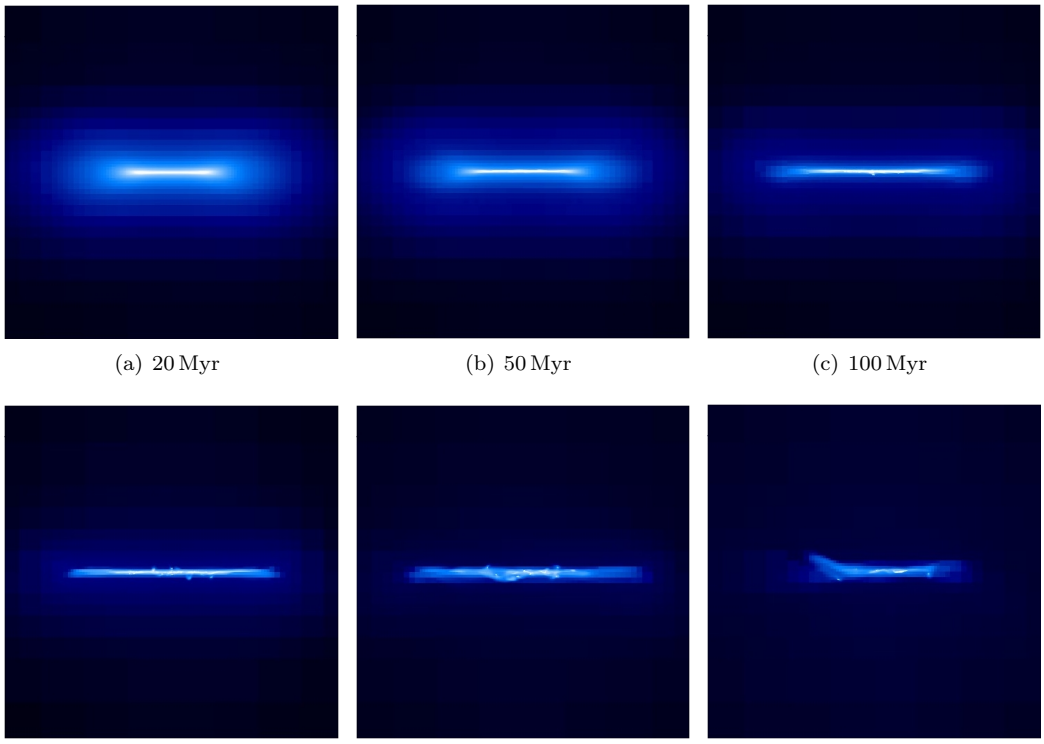

(a) 20 Myr (b) 50 Myr (c) 100 Myr

(d) 200 Myr (e) 500 Myr (f) 1000 Myr

FIGURE 9.6. SF1F0e50: Temporal evolution of the gas disk projected through the galactic plane. All frames have the same spacial extension and color table as figures above.

dense gas appear slightly off the midplane. This is most easily observable in the displayed frames at 200 Myr as well as 500 Myr. For this reason, several objects including stars that form therein have orbits around the galactic center which noticeably stretch into space off the disk. This effect appears to become more pronounced during the late phase of the simulation. At 1 Gyr we observe a distinct gas filament, at the left hand edge of the gas disk, which emerges as gas is stripped off a dense cloud on a strongly tilted orbit.

Aside this qualitative description of structure of instellar gas in the galactic disk, we also performed a quantitative analysis of the distribution of gas densities and their temporal evolution. Figure (9.7) shows nine subsequent plots of the PDF of the normalized logarithm of gas density δ. To perform this analysis, we define a standard extraction volume of the galactic disk. Namely, we extract a maximum resolution dataset of size 21 kpc width and 650 pc height, centered on the galactic midpoint. Note that these dimensions correspond to six radial scale lengths in width and two vertical scale length in height. The reason for this choice is twofold. First, we make a restriction in order to gain a technically feasible dataset for postprocessing, and second, choosing the extraction volume in terms of the used multiples of scale length and height ensures we focus our analysis on the inner gas disk.
For the analysis of the extracted volume, we then compute the volume-averaged natural logarithm of gas density as described in detail in Section (8). Furthermore, we analyze the distribution of

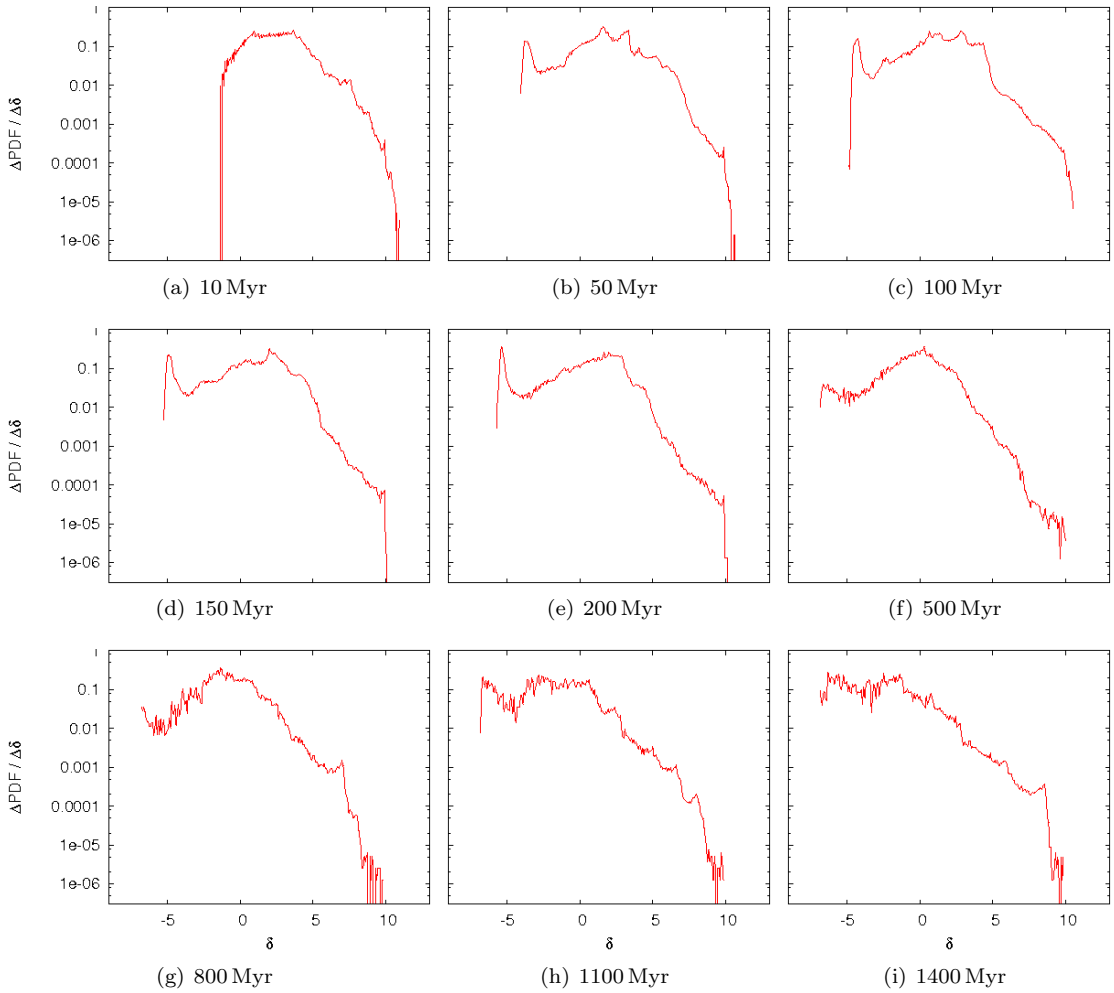

(a) 10 Myr (b) 50 Myr (c) 100 Myr

(d) 150 Myr (e) 200 Myr (f) 500 Myr

(g) 800 Myr (h) 1100 Myr (i) 1400 Myr

FIGURE 9.7. SF1F0e50: PDF of gas density. The plots depict the normalized logarithm of gas density. Therefore, the density scale of $\delta =]-5, 10[$ readily translates to $\rho =]6.74 \cdot 10^{-28}\,\mathrm{g\,cm^{-3}}, 2.20 \cdot 10^{-21}\,\mathrm{g\,cm^{-3}}[$ or $\rho =]10.0 \cdot 10^{-6}\,\mathrm{M_\odot\,pc^{-3}}, 32.5\,\mathrm{M_\odot\,pc^{-3}}[$.

this quantity δ to arrive at the density PDF.

The first plot in Figure (9.7) (a) depicts the initial gas configuration after 10 Myr. We observe a rather smooth distribution function which continuously falls off towards the high mass regime in a lognormal fashion. At intermediate gas density, the initial distribution shows a clear maximum with significant extent. Additionally, the amount of gas at lower densities again drops off as we go to smaller gas densities until we hit a certain minimum cutoff density. This cutoff stems from the choice of our extraction volume. As the initial gas density distribution falls off continuously with radius and height above the disk midplane, we define the cutoff density by choosing the extraction volume. Moreover, owing to the form of the distribution in this initial state, we see our choice of size of the extraction volume to be reasonable. We include not only dense and intermediate density gas but the analyzed volume also contains a certain fraction of low density

material.
Considering the temporal evolution of the distribution, several characteristics of the previous discussion show up. Firstly, highest gas densities appear in the very early phase of the simulation when the galactic center, the most dense part of the disk, fragments. Secondly, the distribution significantly broadens during its evolution building up a second maximum of extremely low density gas. Thirdly, as time proceeds the whole distribution shifts towards smaller densities.
In conclusion, qualitative visual inspection and quantitative statistical analysis show well defined evolution of the interstellar gas disk in agreement with other work. Li et al. [2005] use SPH simulations to simulate galaxy evolution. Although the details of their setup are different in several aspects[a], all simulations show the same general evolution of structure in the disk. Comparison to the early work of Tasker and Bryan [2006], who use a four times less massive gas disk but the originally unstable initial conditions also show generally the same pattern of fragmentation. A more detailed comparison is not applicable owing to the large differences in disk mass, size and initial conditions. More recent work of Tasker and Bryan [2008], this time using a much more massive gas disk ($6 \cdot 10^4\,\mathrm{M}_\odot$ compared to $1 \cdot 10^4\,\mathrm{M}_\odot$ in the early work) does not show the early evolution, but only corresponding gas disk visualizations at later simulation times. These figures show the same gross properties as our results. Moreover, we can also compare density PDFs to the latter work. Tasker and Bryan show these statistics in their Fig. (8). Comparing simulation run 'D', which best matches our standard case, to our corresponding Figure (9.7) shows both similarities and differences. The early bimodal profile and the late deterioration of the lognormal profile are similar in both simulations. The first feature is a consequence of thermal instability while the second follows as particle creation subsequently reduces the amount of high density gas in the disk. Both effects are certainly realized in both simulations. The early high density distribution and the late low density peak are different in both simulations. Here, we lack the information of our reference paper on the detailed early evolution of the gas disk. Therefore, it is useless to speculate about the lognormal nature of the high density tale at 377 Myr. The differences in the observed low density peaks at late time can be a result of the different logarithmic scaling of the analysis as well as different analysis resolutions.

We conclude this comparison by noting two major issues: Firstly, our simulations reproduce earlier work in an appropriate fashion on a level of qualitative comparison. All major aspects are reproduced in our simulations. Secondly, quantitative comparison is rather difficult as a result of the changes we have included in our work in order to circumvent problems we have identified in our realization of the originally described problem setup. Additionally, differences in the analysis in order to provide most useful information are an additional source of discrepancy. Nevertheless, we will continue to search for similarities and differences but stress that owing to the highly nonlinear nature of the problem we expect our simulations to show different results. Improving earlier work is one of the goals of this study.

9.4. Dynamics of Thermal Properties

Next we study the thermal properties of the interstellar medium of the galactic gas disk. We have described in Section (2.4) how we expect the buildup of a three-phase medium with cold, warm and hot gas. In this section we now investigate how our simulations reproduce the properties of the observed ISM and how well simulation and theory correspond.

To begin our study of the simulated ISM we again start with the same extraction volume as

[a]Simulation labelled G220-4 is closest to our own parameter setup.

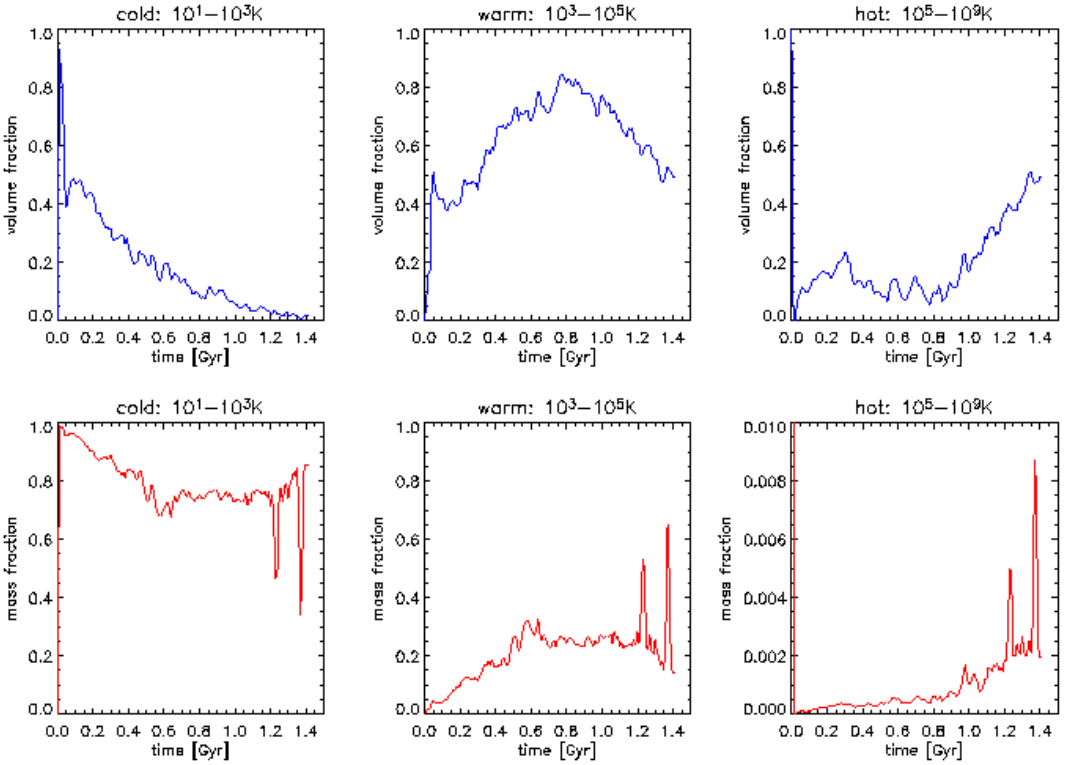

FIGURE 9.8. SF1F0e50: Top: Volume fraction of gas sampled into the expected three phases of the ISM. Bottom: Mass fraction of gas in the same temperature phases. Note the different scale of the 'hot' mass fraction plot.

used in the last section. We sample the volume fraction as well as the mass fraction contained in the extraction volume into three temperature categories. We chose these categories to correspond to the phases of the ISM. Figure (9.8) shows how the different phases evolve over time. Note that we depict absolute fractions in the way that adding up three values, one of every phase at the same instant in time, always yields a total of 100 % or a fraction of 1. Furthermore, it is important to realize that gas transformed into sink particles is not included in this analysis.

As we have seen during our discussion of initial conditions, all gas and therefore the complete extraction volume have temperatures typical for the hot phase at the beginning. This is an implication of our choice of setup and as soon as the dynamical evolution is started and cooling becomes active the gas immediately cools. We start the discussion at the point where the volume is occupied to equal parts by cold and warm gas, and when almost all mass is in the cold phase. As cold gas is rapidly transformed into sink particles we see a steady decline of the cold fraction while the warm fraction increases correspondingly. This is a result of the fact that the star formation process depletes large parts of the inner gas disk leaving behind low density gas as mentioned in the discussion of the density projections. This low density gas is easily heated up as a result of the adiabatic equation of state. After roughly 800 Myr we see a steady decline of the warm volume fraction while the hot fraction begins to rise correspondingly. At this point, the star formation process has not only depleted the inner disk substantially, but subsequent penetration of gas from the outer disk has lowered the overall gas density in a way that warm

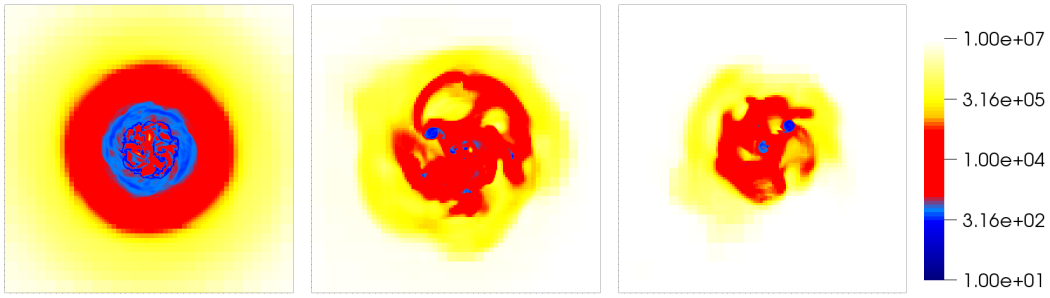

(a) 100 Myr (b) 700 Myr (c) 1000 Myr

FIGURE 9.9. SF1F0e50: Face-on projections of the gas temperature (K) in the galactic disk. Again the frames are 60 kpc across. We use a special color table to visualize the three components of the ISM.

and hot intergalactic gas begins to enter the extraction volume. This leads to the observed increase of the hot fraction and is clearly visible in Figure (9.9).

The mass fractions show a very similar behavior. Initially almost the complete mass is in the cold phase. As time proceeds and the volume occupied by dense gas declines, the mass of cold gas declines as well. However, as small blobs of cold dense gas can still carry enormous amounts of mass, the mass fraction in the cold phase does not fall below a value of 75 %. The attributes cold and dense are identical for gas at constant pressure, therefore most mass is concentrated in cold dense clumps. Towards the end of the simulation only small amounts of mass remain in gaseous form and the mass fraction in the hot phase starts to increase. However, note the hot mass distribution plot uses a different scale. The two spikes appearing in the mass fractions at late time correspond to two instants during the simulation when the remaining dense clumps of gas temporarily leave the extraction volume as a result of a tilted orbit at that late time (see the discussion of side-on density projection earlier). When this happens there is almost no cold gas left in the disk and fractions spike significantly.

Our sampling of gas temperature into three different regimes and the discussion above do not demonstrate the existence of a three-phase medium in our simulations. The discussion above is rather a description of how to interpret temperature distribution in the ISM assuming a three-phase configuration. In oder to solve this problem we show the same data in a continuous form in Figure (9.10).

The volume distribution shows a clear separation of two distinct phases at all times. We observe a broad peak in the warm regime which also extends into the cold regime and therefore contains a significant fraction of cold gas. At intermediate times it is confirmed that almost the whole extracted volume of the disk is occupied by the warm phase. This is what we expect when gas can cool efficiently in the disk and no feedback mechanisms to heat the gas are switched on. During the late evolution we observe again how hot material from outside the disk begins to penetrate the extraction volume and shows up in the analysis.

In conclusion, considering this first simulation without feedback, the observed bimodal temperature distribution shows a good first order realization of the real ISM in our model. Note that although the cold gas phase does not appear in these plots, it is nevertheless present. Cold gas has been transformed into sink particles which represent molecular clouds and the stars that form therein. We will discuss sink particles in the next section.

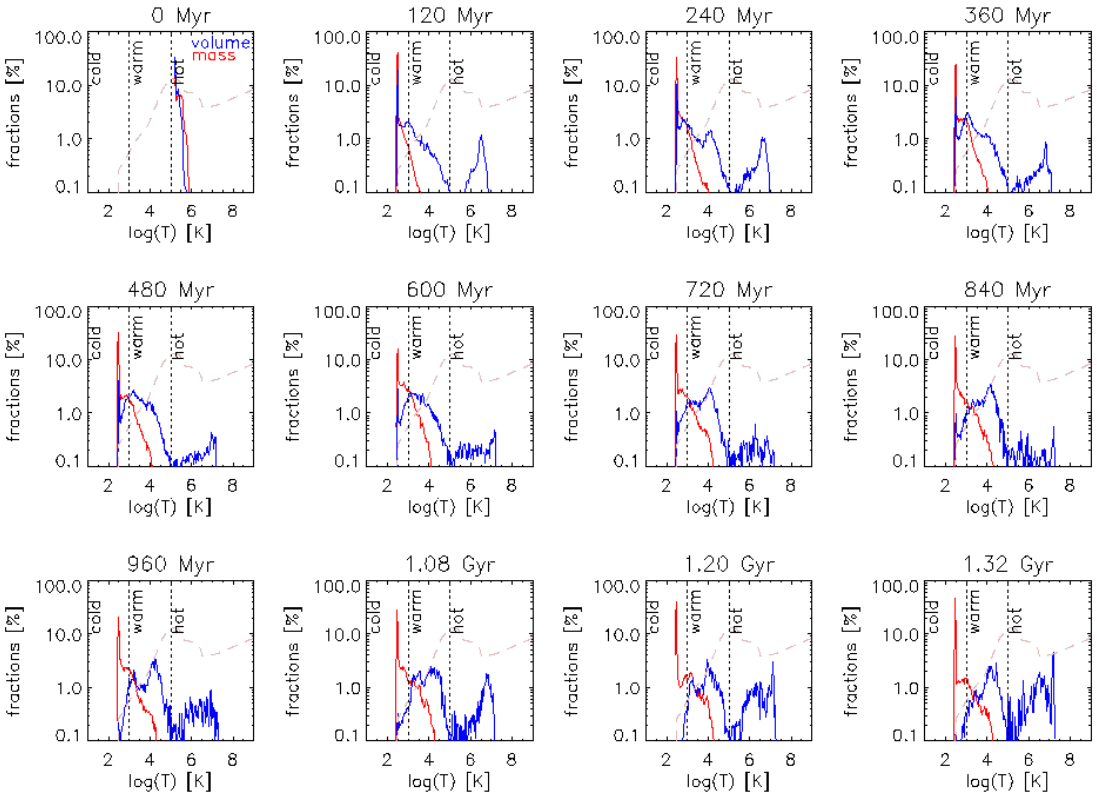

FIGURE 9.10. SF1F0e50: Temperature distribution in the simulated ISM. We depict again volume and mass fractions, this time in continuous plots covering the whole temperature regime. The dashed line depicts the employed cooling function, and vertical lines indicate our definition of phases in the ISM.

Moreover, we also see how the employed cooling curve (cf. Section (5.3) [page 54f]) directly shapes the structure of the ISM. The underlying dashed curve shows how the maximum of the cooling rate separates warm and hot gas phases. At this point, gas can cool most efficiently and the buildup of the warm component starts. Moreover, at 10^4 K the slope of the cooling curve flattens. Consequently, this leads to a significant accumulation of gas that cannot cool down to lower temperatures with the same efficiency as before. Cold gas below several hundred K contracts rapidly by gravitational effects and the volume fraction goes towards zero at our minimum temperature of 300 K.

Gas that is heated above the temperature where cooling is most efficient is easily heated to even higher temperatures owing to its low density. Here, we have a sensitive balance of radiative cooling and adiabatic heating. Henceforth, most of the high temperature gas accumulates at the point where cooling has the smallest effect. In other words, heating and cooling continuously change the gas temperature. We assume the heating to be uniform, but cooling is least efficient at 10^6 K. Therefore, we observe most hot gas around this temperature.

Considering the mass weighted distribution of temperatures, it is not surprising that all mass is concentrated in the cold and warm regime. The tiny fractions in the hot phase are off scale. Note that while the total amount of mass declines, the relative fractions are distributed in an almost constant fashion. The most eminent fact is that large amounts of mass (more than 20 % at all

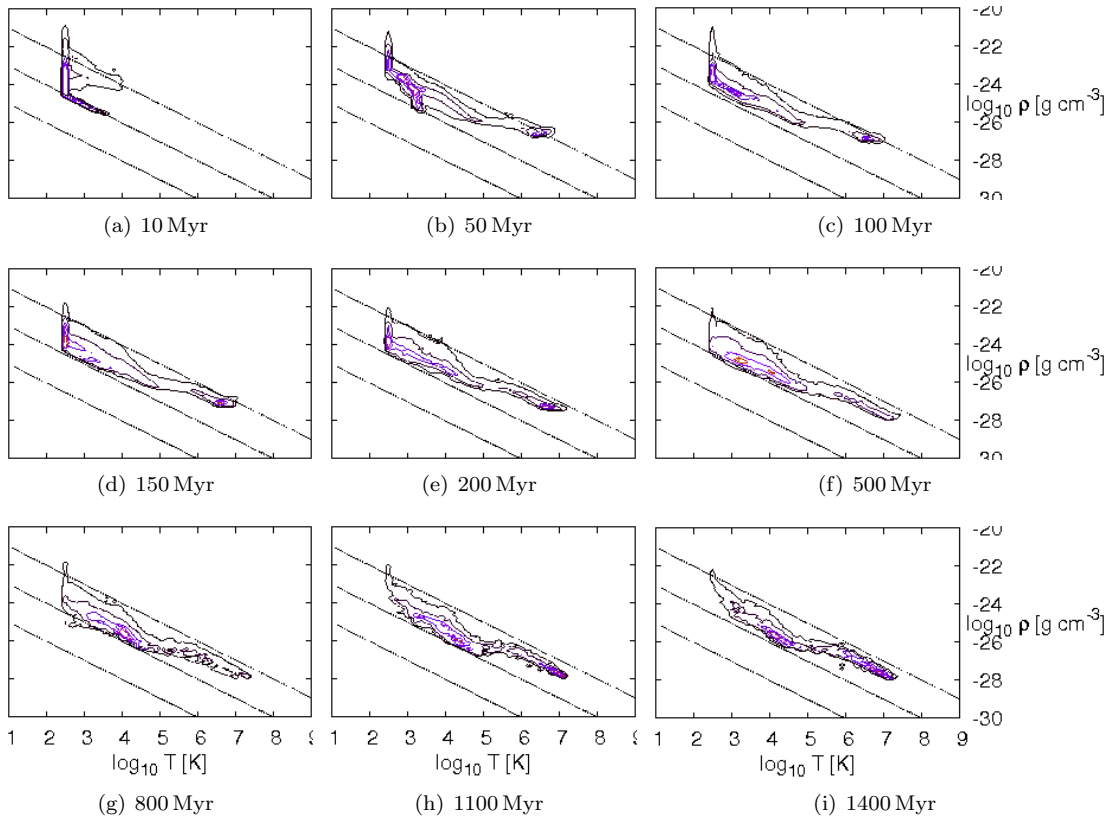

(a) 10 Myr (b) 50 Myr (c) 100 Myr

(d) 150 Myr (e) 200 Myr (f) 500 Myr

(g) 800 Myr (h) 1100 Myr (i) 1400 Myr

FIGURE 9.11. SF1F0e50: Contour diagrams of gas density versus temperature in the standard extraction volume of the galactic disk. Contour levels are 10^3, 10^4, $5 \cdot 10^4$, 10^5, $1.5 \cdot 10^5$ and refer to cell counts. The total number of cells in the extraction volume is $\sim 1 \cdot 10^7$. Straight lines depict isobars.

time) reside in the cold phase having the minimum temperature during the entire simulation.

Next, we investigate the gas pressure in the disk. Figure (9.11) shows pressure contours at various instants of time during the simulation. We see again that the initial conditions are out of equilibrium. Nevertheless, when cooling is activated and the full evolution of the disk starts, the gas quickly settles into a configuration where pressure is roughly constant for all temperatures. Additionally, the fine structure of these plots exhibits three features worth mentioning. Firstly, there is a certain fraction of overdense gas at the minimum temperature. If allowed, this gas would cool further, flattening the apparent spike in the distribution. Secondly, at the temperature of $\sim 10^5$ K where the cooling curve has its maximum (cf. Figure(5.2)), there appears to be a small break in the distribution, separating hot and lower temperature phases. Obviously, the hot phase in our simulations has slightly higher gas pressure than the warm phase. Thirdly, the warm phase shows a much broader occurrence of pressure values than the hot phase. This can certainly be attributed to the much larger amount of volume filled by the warm phase.

Comparing the thermal structure of the ISM in our simulation to Tasker and Bryan [2008]

again shows general agreement. Particularly, comparing the mapping of mass and volume fractions into different temperature regimes (cf. Fig. (11) of the latter work) even yields very close correspondence. This is not surprising, as we basically use the same numerical realization of cooling as these authors. Our small changes and corrections to the implementation, affecting specifically the low temperature regime where cooling is fast and efficient anyway, do not generate any noticeable differences in the analysis at hand. Additionally, the comparison of pressure contours also shows general concordance [Tasker and Bryan, 2008, Fig. 13].

Putting all this together, we have seen that already this first simulation reproduces the observed multi-phase structure of the ISM quite well. We have seen both the hot and warm gas in all analyses and were able to confirm the existence of these phases in approximate pressure equilibrium. Next, we turn towards the formation of sink particles and discuss the inherent cold phase as well as the formation of stars therein.

9.5. The Formation of Stars

If gas cools efficiently it quickly settles into cold and dense clumps. With the star formation algorithm active in the simulation, the code checks whether the conditions to convert gas into particles are fulfilled. If this is the case, the simulation generates particles and follows their evolution, including the formation of stars, through the subsequent calculation. Figure (9.12) shows the projected density of sink particles, representing the cold gas phase as well as the stellar component.
We observe how the initial collapse starts in the center of the disk where densities are highest and gas is cooling most efficiently. Subsequently, we see the buildup of a significant particle component growing continuously in radius over time. As there is no feedback in this simulation, the mass initially attributed to the particles at creation does not change over time. In other words, the gas component is continuously transformed into particles, resulting in the observed reduction of gas density and subsequent replacement of the gas disk by a disk of particles. Additionally, we observe how most of the larger associations of particles merge together building up only a couple of very massive clusters of particles. Already at 500 Myr we see only two of these clusters remaining. Although these two exist until the very end of the simulation, they continuously attract and disperse other particles while passing through the galactic disk. The stripping of particles by tidal effects is responsible for the spacial growth of the particle component as well as for its increasing diffusivity.

Next, we investigate the rate at which stars are formed inside sink particles. Therefore we analyze the cumulative mass that all sink particles transform into stars. We average this mass over timesteps of 10 Myr each and normalize to units of $M_\odot$ per yr. The corresponding plot is presented in Figure (9.13) (a).
We see that the star formation activity is strongest shortly after the start of the simulation. As we have seen earlier, the gas disk has cooled significantly at this point and more importantly, all material of the galaxy is yet in gaseous form available for sink/star formation. For the following evolution of the star formation rate, we consider two different effects. Firstly, the creation of new sink particles and therefore, of new sources of star formation. Secondly, the formation of stellar mass itself as described in Section (5.5). Both effects are tightly coupled and lead to the observed star formation rate.
To gain more information on the star formation mechanism and the physical nature of the locations of these events we analyze the formation of stars dependent on the local gas surface density. Therefore, we use the projected datasets visualized above and impose 40 concentric

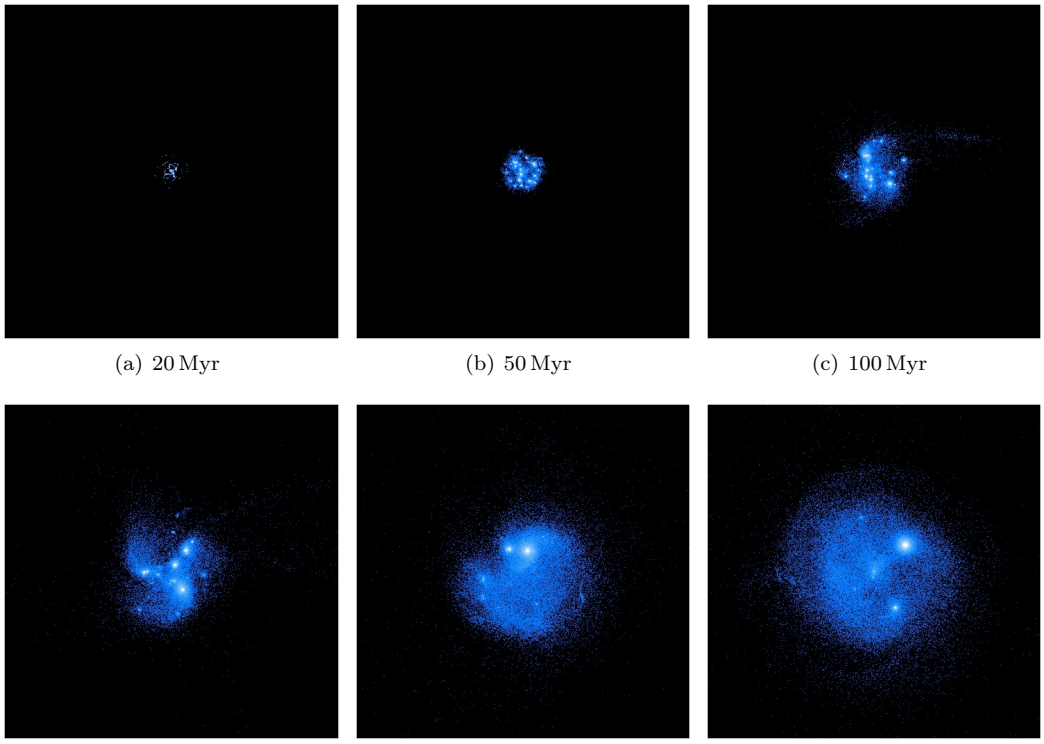

(a) 20 Myr (b) 50 Myr (c) 100 Myr

(d) 200 Myr (e) 500 Myr (f) 1000 Myr

FIGURE 9.12. SF1F0e50: Projected particle density. Note that we have stretched the scale of depicted values by one order of magnitude compared to earlier plots for better visualization. The maximum and minimum densities shown here are $10^{16}\,\mathrm{M}_\odot\,\mathrm{Mpc}^{-2}$ and $10^{10}\,\mathrm{M}_\odot\,\mathrm{Mpc}^{-2}$, respectively.

radial bins. Each of these bins is 350 pc in radius so we cover a total radius of 14 kpc, essentially the whole domain were any star formation happens. We record the average star formation rate as well as gas surface density for each of these radial bins at 140 instants of time, separated again by 10 Myr each. We plot this information, also known as local Schmidt-law, in Figure (9.13) (b). Although the data show a large scatter, it is nevertheless interesting to see the apparent correlation between local star formation rate and the corresponding gas surface density.

We have deliberately omitted a fit to the data points, although it is easy to fit a power law to the presented data. Even the slope of ~ 1.4 appears probably as good fit. Nevertheless, the large scatter, the double logarithmic scale of the plot and the obvious accumulation of data points towards small values renders such a fit rather meaningless in our opinion. However, Kennicutt [1998b, Fig. (3)] reports the same overall behavior from a large sample of 21 observed spiral galaxies. The author describes to observe the Schmidt-law with power law index ~ 1.4 at high densities. Moreover, an abrupt steepening below some density level, a critical threshold density for star formation, is reported. Li et al. [2006, Fig. (11)] show the same observations for five different simulation models of star formation in disk galaxies. These authors characterize the general features of their analysis in the same way. They report a tight correlation of Σ_{SFR} and Σ_{gas} as well as a dramatic drop at some gas surface density, interpreted as threshold for star

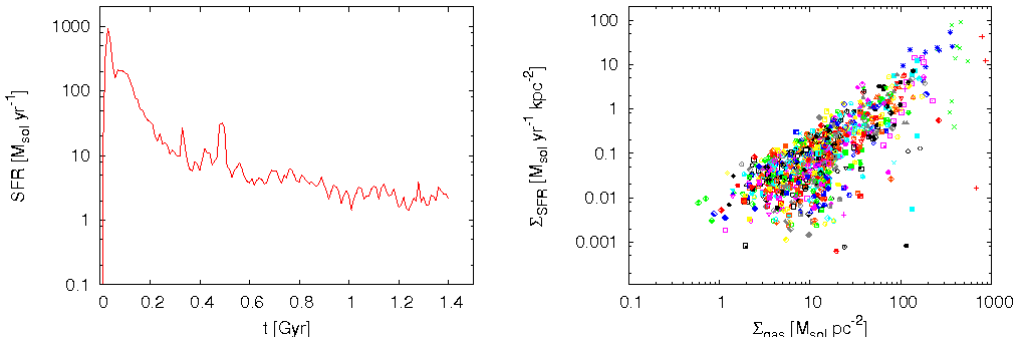

(a) Temporal evolution of the star formation rate.

(b) The local Schmidt-law.

FIGURE 9.13. SF1F0e50: Analysis of the star formation rate. The left frame depicts how the star formation rate changes over the course of a simulation, while the right frame shows the locally averaged dependence of the star formation rate on the gas surface density for all recorded data outputs.

formation.
As we do not have several different galaxies to analyze, we interpret our results in the fashion that different times during the evolution of our simulation are roughly representative of different galaxies in their different evolutional phases. Therefore, we interpret our results in the same fashion as the cited authors. As a result of the large scatter we will not claim to gain any distinct results, but state that our data agree reasonably with the conclusions presented above. We observe the Σ_{SFR}-Σ_{gas} correlation and attribute the trend towards low star formation rates at low gas surface densities as indication of a significant reduction of star formation accompanying the decline in density.

Finally, we analyze the simulated galaxy with respect to the global Schmidt-law. We perform the postprocessing in the same way as described by Li et al. [2006] and define a star formation region by using an analysis radius chosen to encircle 80 % of the mass present in sink particles. Again, we used the projected data of density and star formation rate. We identify all cells within the analysis radius and average their gas density as well as star formation rate values for each of our datasets over the entire galaxy. Therefore, we gain 140 datapoints (again, temporal separation is 10 Myr) representing the disk averaged gas surface density and star formation rate inside the 80 % particle mass limit. This relation, known as the global Schmidt-law, is shown in Figure (9.14) together with the analytic relation found by Kennicutt [1998b].
We augmented our analysis with color code to depict the time during the simulation when a specific data point is sampled. From this it becomes easily observable how star formation rate and gas density correlate during the course of the simulation. We also supply information on a power law fit of the presented data. However, we stress that this information is mostly included to visualize the general trends of different simulations. Even though the dataset in Figure (9.14) does not show any strong deviations from power law distribution, other datasets presented later do. We caution the reader not to overrate the stated numbers.
After all, from the analysis we see that simulation SF1F0e50 clearly overproduces stars during the entire simulation. The star formation rate is systematically larger than predicted by the KS relation. Moreover, at early times when gas surface density is most pronounced, the deviations are much stronger than at later times when the gas reservoir in the disk has been significantly

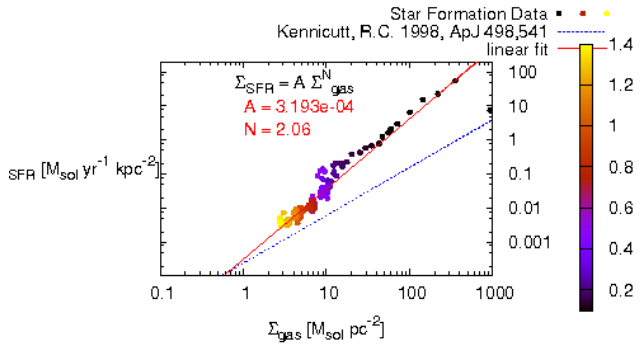

FIGURE 9.14. SF1F0e50: Comparison of simulation data to the analytic form of the KS relation. Datapoints are color coded to indicate the timestep they represent. The red solid line depicts a linear fit to the data, while the blue dashed line shows the analytic function as given by Kennicutt [1998b].

depleted. Obviously, the employed star formation routine does not represent the nature of star formation in a sufficiently realistic way in order to reproduce the fit to observational data.

9.6. Effects from Stellar Feedback

As we have seen in the previous section, our general simulation setup is capable of describing the gross properties of a Milky Way like disk galaxy. Moreover, we have already successfully realized the simulation of the general properties of the interstellar medium. However, particularly the parameterization of the dense cold gas phase and the inherent star formation in sink particles without any feedback has proven to be a rather inappropriate realization of the actual physics. Therefore, we will now investigate the influence of stellar feedback on the evolution of the ISM and subsequently the evolution of the whole galaxy. Particularly, we are interested whether the inclusion of feedback from type II supernovae is capable of significantly altering the properties of the previously analyzed star formation relations or not.

We base the investigation of feedback on the comparison of the simulation without feedback (SF1F0e50) to an identical simulation including the full thermal as well as kinetic feedback (SF1F1e50) as described in Section (5.5). At first glance, we expect two obvious effects of the feedback on the interstellar gas. Firstly, the input of hot gas from modelled stellar feedback should lead to an observable increase of low density gas. Secondly, additional shocks created by evolving bubbles of hot gas should cause an increase of significantly overdense gas. Putting both effects together, we expect to observe a broader density PDF in the feedback case than without feedback.
Figure (9.15) shows the results of our analysis. In fact, we observe a much broader distribution, especially in the low density regime of hot gas. Moreover, we also see a noticeable increase of high density material, however, only during the first 200 Myr. After that time, the high density fraction of gas falls significantly below the fraction in the simulation without feedback. This can be readily understood. We have seen earlier that star formation activity is strongest during the early phase of the simulations. Consequently, also feedback has its most severe influence during the early evolution of the simulation. As the activity declines so does the strength of the feedback, rendering it unable to produce density enhancements by shocks. Correspondingly, the strong early feedback generates an increased amount of hot, low density gas, while this effect gets largely overwhelmed by the later mixing of hot material from outside of the extraction volume.

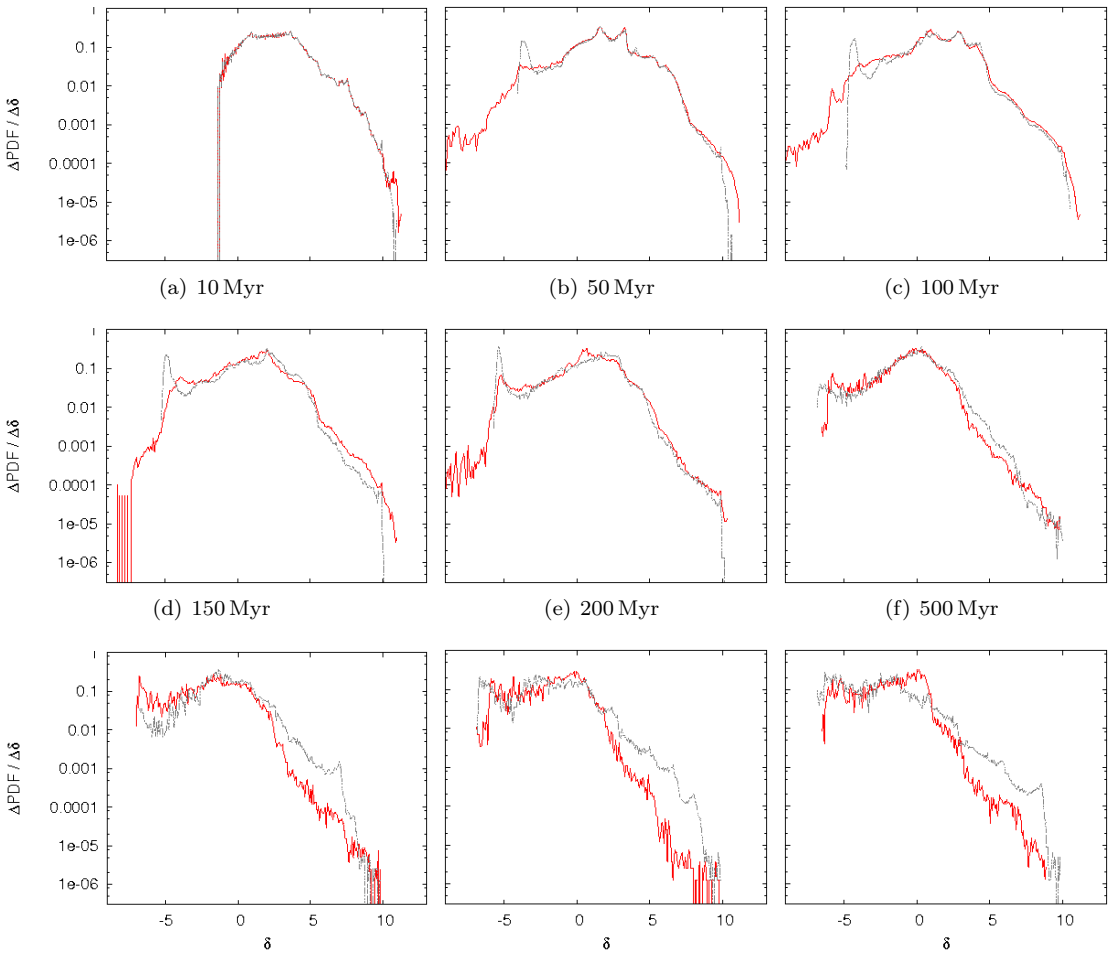

(a) 10 Myr (b) 50 Myr (c) 100 Myr

(d) 150 Myr (e) 200 Myr (f) 500 Myr

(g) 800 Myr (h) 1100 Myr (i) 1400 Myr

FIGURE 9.15. Comparison of density PDF of two identical simulations, one without feedback (SF1F0e50) (grey, dashed-dotted line) and the other including feedback from type II supernovae (SF1F1e50) (red, continuous line). Scales are again $\rho =]10.0 \cdot 10^{-6}\,\mathrm{M}_\odot\,\mathrm{pc}^{-3}, 32.5\,\mathrm{M}_\odot\,\mathrm{pc}^{-3}[$.

The strong reduction of high density material at late time is yet another consequence of the energy input owing to feedback. Feedback predominantly occurs at the locations where dense gas accumulates and forms stars. Now the feedback continuously disperses these associations of dense gas and stars. Most importantly, this effect becomes stronger as more and more material is transformed into stars while at the same time the overall gas disk becomes more and more depleted. Note that also feedback recycles gas from particles back into the ISM, this only happens to a certain fixed fraction of the initial particle mass. The remainder eventually ends up in stars.

We observe more of the details looking at the thermal properties of the gas (cf. Figure (9.16)). Particularly, the mass fractions of the different phases of the extracted inner disk region confirm the observations drawn from the PDFs, although the small increase of high density material

during the first half of the simulation is not clearly visible in the phase plots. However, the more eminent features, like the recycling of cold high density material during the second half of the simulation, is quite obvious. We see that most of this material ends up as warm gas, while the mass in the hot phase is also significantly increased. Note that the scale of the hot phase mass plot is still one order of magnitude less than the other plots. It appears that cooling is able to effectively reduce the temperature in the gas as long as gas densities are still large enough.
The volume fraction plots do not reveal such clear implications of feedback. Most generally, the volume changes are much less pronounced than the changes of the mass fractions. Nevertheless, with the exception of a small period of time around 700 Myr, the feedback simulations show more volume filled by warm gas than in case without feedback. The cold volume is continuously smaller than before, and also the hot volume is generally reduced. This is somewhat surprising as we would have expected the feedback to produce more bubbles of hot gas in the ISM. It is tempting to speculate that the increase of hot volume at 700 Myr displays the cumulative effects of such supernovae events. However, at this relatively late time of the evolution, we begin to see the effects of gas depletion and the mixing of hot gas from outside the disk into the extraction volume. Again, this effect appears to be somewhat reduced and delayed in the feedback case. We see two possible problems with the feedback implementation and its interpretation from this analysis. Firstly, as our feedback is still very rudimentary. Therefore, hot ejected gas possibly suffers from overcooling and cannot realisticly evolve during the simulation. Secondly, we define some analysis volume, which is unfortunately a rectangular box applied to analyze a circular disk structure. The choice of the extent of this volume, in radial direction as well as in height above the disk midplane, has strong influence on the depicted gas fractions.

We try to gain a better picture of the distribution of gas temperatures by investigating the thermal properties in the familiar face-on projections. Figure (9.17) reveals several distinct differences between the feedback and non-feedback (cf. Figure (9.9)) simulation. The first plot at 100 Myr has a much smaller ring of cold gas. We did not see this reduction of cold volume in the phase plots because most of the cold ring lies outside the extraction volume. However, considering solely the cold phase, this is still the warmest contribution while the even colder gas clumps are well within the analysis volume. Hence, we observe the reduction of cold gas mass. More interestingly, we see an almost complete extinction of cold dense gas in the later evolution at 700 Myr and 1000 Myr. Here, feedback clearly acts to dissolve cold regions of high density gas. Again, it is questionable whether we can identify the large region of hot gas at 700 Myr as the supernovae bubbles discussed earlier. They appear to form from the inside out, as we would expect as most initial star formation takes place in the inner disk and therefore places the sources of feedback there. However, we also see similar hot gas regions in the case without feedback (cf. Figure (9.9)). Further investigations on the detailed processes and structuring effects of feedback are necessary, but beyond the current scope of this thesis.
We therefore conclude the general discussion of thermal properties of our feedback implementation stating two main issues. On the one hand, feedback certainly needs more attention and a better understanding of its implications, especially on the evolution of hot and warm gas. On the other hand, we see that our feedback is capable of dispersing cold dense associations of gas after stars have formed therein. This might actually be the most important effect of feedback at the current state of our simulations. Future simulations, however, can possibly pay more attention to the interesting details of star formation feedback.

Nevertheless, the feedback as discussed above has important consequences on the overall star formation properties of the galaxy as it reshapes the temperature and gas density profiles. Figure (9.18) shows the corresponding effects. As expected, feedback enhances the star formation

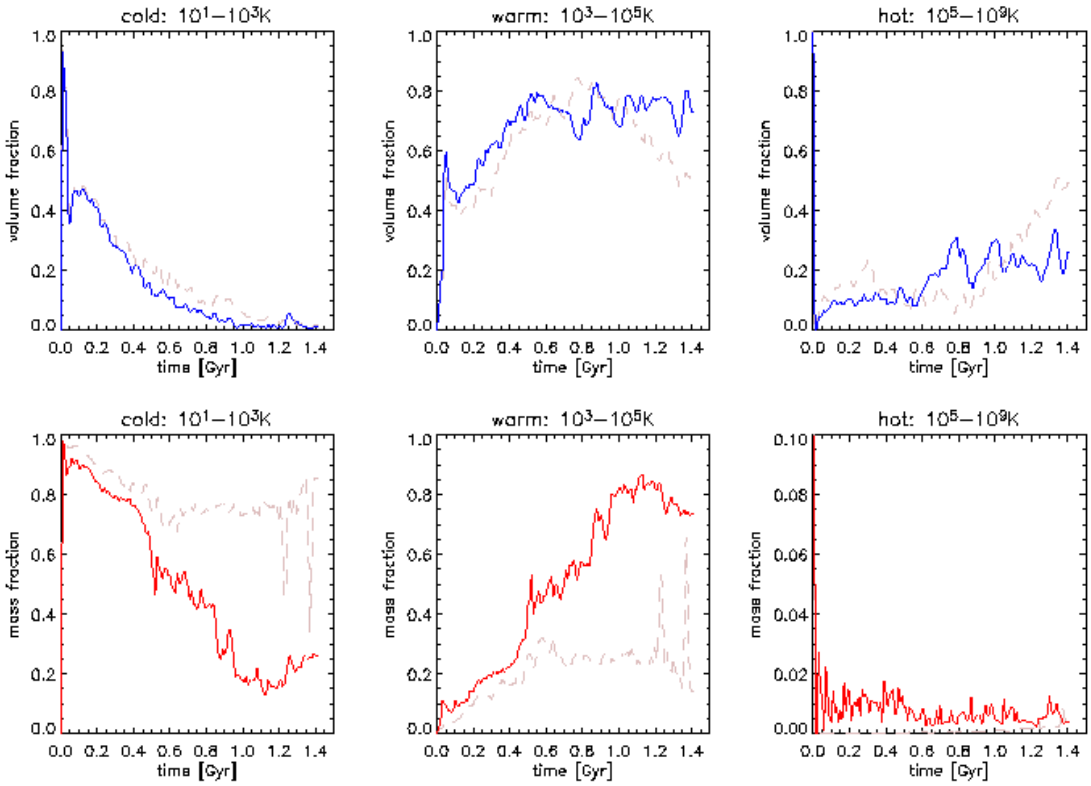

FIGURE 9.16. Comparison of volume (top) and mass (bottom) fractions of the ISM. The faded dashed plots represent the earlier discussed case without feedback (SF1F0e50), while the continuous lines are the case including feedback (SF1F1e50).

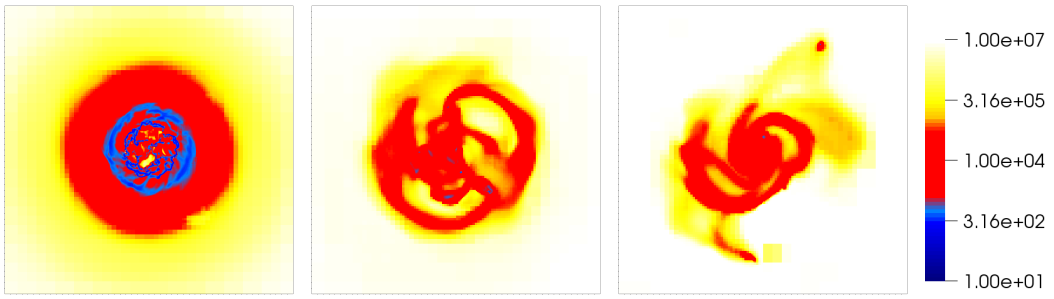

(a) 100 Myr (b) 700 Myr (c) 1000 Myr

FIGURE 9.17. SF1F1e50: Face-on projections of the gas temperature (K) in the galactic disk of the feedback simulation.

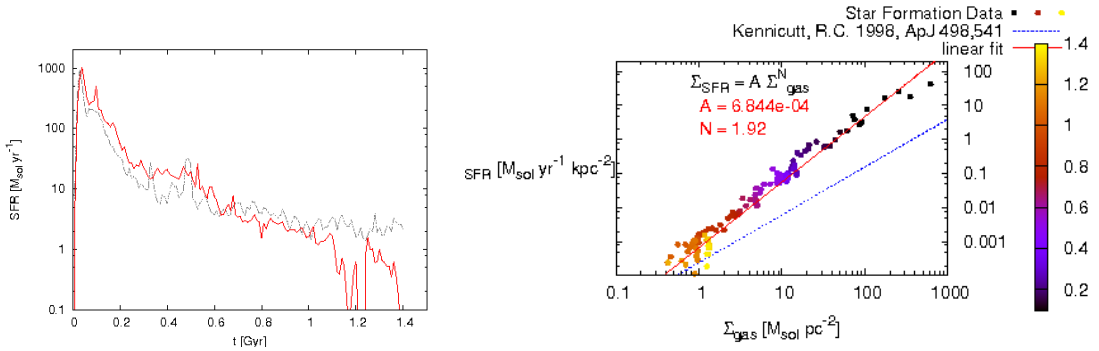

(a) Temporal evolution of the star formation rate.

(b) The global Schmidt-law in the feedback simulation.

FIGURE 9.18. (a) Comparison of the star formation rate in the simulation without feedback (SF1F0e50) (grey, dashed line) and the simulation including feedback from type II supernovae (SF1F1e50) (red, continuous line). (b) Analysis of feedback simulation data with respect to the KS relation.

rate compared to the non-feedback case for the first half of the simulations, as a result of increased gas densities. Conversely, during the second half, the star formation rate is reduced. This feature of feedback is apparent in both plots of the latter figure. The star formation history (9.18) (a) most clearly depicts this dual influence. Although the overall shape of the star formation evolution remains unchanged by feedback, particular differences are well defined. Moreover, at late times during the simulation when feedback has depleted most gas that has not yet been transformed into stars inside the particles, the star formation rate is dramatically declining. In the non-feedback case on the other hand, particles continue almost constantly to hold up the star formation rate.
The described behavior also leads to the changed dependence of the star formation rate on gas surface density. Figure (9.18) (b) shows that the simulated galaxy again has a very strong correlation as described by the KS relation. Several interesting features are apparent in this plot. Firstly, the slope $N = 1.92$ of the fitted power law is significantly smaller than in the case without feedback $N = 2.06$. Furthermore, star formation is shifted to much lower densities and rates for later times during the simulation. Here, obviously, the feedback reshapes the immediate surroundings of star formation locations through winds and outflows.
Putting all this together, it appears that initial effects from feedback lead to additional increase of density in the early gas rich galactic disk, increasing the global star formation rate. Consequently, the gas reservoir in the disk becomes depleted faster when feedback is active and the star formation rate falls off faster with feedback during the course of the simulation. However, feedback also returns some of the gas back to the ISM, otherwise locked up in dense clumps. This not only leads to expansion of star formation activity to lower gas density but also to a further reduction of star formation owing to continuous depletion of material in dense clumps.

Essentially, feedback is very important for the realization of some kind of gas recycling mechanism in our simulations. Additionally, feedback depletes dense regions, significantly lowering the star formation rate in evolved simulations.

9.7. Modifications to the Standard Case

Additionally to the simulations discussed above we also performed some test simulations to check how key parameters might change the results of our simulations. Here, we will present two of these additional simulations. For better comparison and to save computational resources, we decided to run these simulations without the inclusion of feedback. We investigate two major issues. Firstly, the influence of a certain mass threshold of particles, and secondly, the most radical simplification of the star formation algorithm, dismissing all criteria but overdensity for the creation of sink particles.

Influence of a Minimum Particle Mass. For our standard simulations we use the typical number density of $n = 10^3\,\mathrm{cm}^{-3}$ as density threshold for particle creation. In Section (5.4), we have already discussed how setting a lower mass limit for particles translates into an additional density threshold. Using a minimum particle mass of either $10^4\,\mathrm{M}_\odot$ or $10^5\,\mathrm{M}_\odot$ as for our simulations translates to a density limit of $n \approx 12\,\mathrm{cm}^{-3}$ and $n \approx 120\,\mathrm{cm}^{-3}$, respectively, at the finest level and subsequently smaller numbers are calculated as particles are possibly created at lower resolution ($n \approx 1.5\,\mathrm{cm}^{-3}$ and $n \approx 14.9\,\mathrm{cm}^{-3}$, at the second highest refinement level). Hence, the lower particle mass limit does *not* impose an additional dominating density threshold in our simulations at any time.
Nevertheless, setting the particle limit has other implications on the simulations. Note our motivation for setting a limiting particle mass in general: Firstly, this was for computational reasons, avoiding a computationally infeasible large number of particles. Secondly, and more importantly, we interpret our sink particles as molecular clouds. These clouds are known to have a certain amount of mass. Performing the most basic calculation, employing the smallest fiducial values for molecular clouds, namely, $n = 10^2\,\mathrm{cm}^{-3}$ (cf. Table (2.1)) and $R = 25\,\mathrm{pc}$ as in Chapter (3) we calculate a cloud mass of $\sim 10^5\,\mathrm{M}_\odot$. Note that the quoted number density is not to be confused with the density limit for particle creation. The number density is rather to be interpreted as density of gas represented by a particle which has been created once the density limit has been exceeded and is very likely to be much smaller than the limiting value itself. Molecular clouds are known to be much more complex than this trivial analysis suggests. Neither the assumption of a spherical configuration nor of a constant density value hold for real clouds. Clouds are known to have a vast spectrum of substructure, yet unfortunately little known in detail. Putting all this together, we are left with the question which numerically realized minimum mass is the best choice to model the real situation best. Fortunately, it appears we already know the right order of magnitude. For our standard case we use $10^4\,\mathrm{M}_\odot$, in order to better account for high density substructure in dense associations of gas.
Moreover, one can also argue that representing clouds by two or more particles is better than using just one. Assuming we have a gravitationally bound, dense parcel of gas we can either use one massive or several smaller particles. As we are not using a sophisticated particle algorithm such as one including merging of particles and accretion, the massive particle is a rather static entity in our simulations (except for feedback effects). However, several smaller particles would still closely stick together gravitationally as long as forces are strong enough. Contrarily, once gravitational pull from other objects, or similar violent forces, impact on the association of light particles a more dynamical evolution, which are likely to mimic a more realistic situation, can be simulated. These are the main reasons why we chose our small standard minimum particle mass. Nevertheless, we want to see how a simulation behaves which has a one order of magnitude larger mass limit.

In Figure (9.19) we compare our standard simulation to the latter case with higher mass limit

on the particles. The globally averaged star formation history (a) shows two distinct features. Firstly, the new simulation shows much stronger variations in magnitude than the standard simulation. Secondly, the overall temporal evolution is influenced in the sense that we observe an intermediate phase of higher star formation activity while towards the end of the simulation this trend is reversed. Both observations are readily understandable.
The variations in magnitude appear most pronounced in the second half of the simulation run. Here a large amount of the available gas has already been converted into stars. Hence, the buildup of large density enhancements, capable of forming a high mass sink, needs much longer than in the standard case and the star formation rate drops during that time. Once a new particle is created, the massive cloud quickly begins to form stars and the star formation rate rises again.
The same line of argument applies to the explanation of the temporal evolution. Initially, the disk has enough gas to produce the same global average of stars as in the standard case. After several hundred Myr when the disk still has a rather large amount of gaseous mass, massive particles form stars more effectively than a larger number of small particles. This effect quickly diminishes during the simulation and tips over at the end of the simulation when the gas disk becomes too depleted to produce new sink partiles and star formation in previously created particles has largely ceased.

Figure (9.19) (b) again shows the dependence of star formation rate on gas surface density, this time for the simulation with larger particle masses. Although the difference in the high surface density regime is rather inconspicuous, the latter simulation nevertheless shows slightly smaller star formation rates as a result of the additional mass limit. More interestingly, we see significant differences in the data points at later times, at lower surface density values, compared to the standard case. Firstly, data points are distributed over a much broader range of values. Secondly, we observe some kind of limit in gas surface density at roughly $\Sigma_{\mathrm{gas}} = 2\,\mathrm{M}_{\odot}\,\mathrm{pc}^{-2}$ where we have different star formation rates varying over almost two orders of magnitude for the same density value.
The spread appears to result from the fact that the creation of massive particles significantly changes the density of the corresponding cells while spawning lighter particles has a less dramatic effect on the overall density of the surrounding medium. Moreover, massive particles can move further away from their natal gas and still contribute significantly to the formation of stars. They also produce stars for more extended periods of time resulting in ongoing star formation at very low rates (and low gas densities) while the formation of particles has already largely ceased.
The observed variation of star formation rate at one specific gas surface density indicates that a large number of star forming particles is surrounded by a static envelope of gas. From the color coding we see that this star formation happens at the end of the simulation. In fact, we observe in the particle density projection (not shown here) that a large number of particles has built a very massive particle accumulation. Furthermore, the corresponding gas density plots also show how relatively large amounts of gas follow the gravitational attraction of the particle association and build a clump at the same position. Nevertheless, the relatively low gas surface density shows that the gas density is still too low to create new particles. Therefore, the gas density is just influenced owing to gravity of particles while the cumulative gas mass is to small for gas self-gravity to significantly fragment the gas to higher densities. Consequently, the gas density remains rather static, following the gravitational potential, while sink particles continue to form stars at the same location.

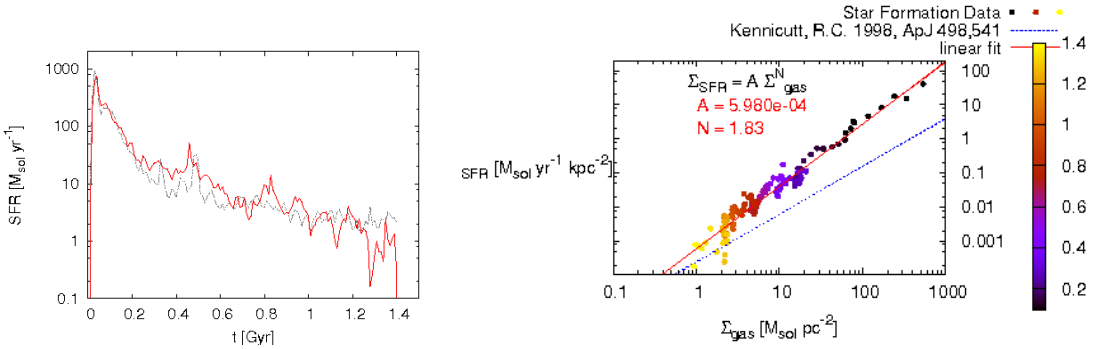

(a) Temporal evolution of the star formation rate.

(b) The global Schmidt-law for star formation with enlaged minimum particle mass.

FIGURE 9.19. (a) Comparison of the star formation rate in the simulation without feedback (SF1F0e50) (grey, dashed line) and the simulation including a larger minimum star particle mass (SF1F0e50mpm) (red, continuous line). (b) Analysis of enlarged minimum sink particle mass simulation data with respect to the KS relation.

Simplified Particle Creation. Finally, we investigate how the parameterization of particle and hence star formation influences the simulations. Section (5.4) [page 57f] gives all the details on the different criteria we require to be fulfilled before particles are created in the standard case. Here, we discuss a simulation disregarding all criteria but (a) and (b), namely, the numerical criterion that particle creating cells are not refined further, and a simple threshold density criterion, respectively.

We use the familiar plots to discuss similarities and differences. In Figure (9.20) (a) we observe that the star formation history of the first 300 Myr is almost completely identical to the standard case. This leads to the conclusion that the additional particle creation criteria do not significantly influence the simulation during this early evolution. More directly, it appears that whenever cells are dense enough to exceed the density threshold criterion, they also fulfill the other criteria, during this time. This is not surprising, considering the nature of the other criteria. Criterion (c) encodes converging flux, which is a very likely precondition to overdensity. (d) the timing condition is also likely to be fulfilled in rapidly cooling dense gas. Moreover, the Jeans criterion (e) as well as the minimum particle mass requirement (f) do not cause an abandonment of particle creation at the apparent high gas densities during the early simulation.

The situation changes, however, during the further evolution of the galaxy. After the identical initial evolution we observe a period of slightly higher star formation rate until approximately 600 Myr of simulation time. After that, the star formation rate is continuously below the rate in the standard case. This is a somewhat surprising evolution since we would generally expect a larger star formation rate without the confining effects of additional particle creation criteria. The period with slightly increased rate does not appear to be important enough to deplete the galaxy of enough gas to cause the later decline of star formation rate. Interestingly, we observe again a kink in the plot showing the correlation of star formation rate on gas surface density (Figure (9.20) (b)) beginning with data points taken at roughly the same time. Both the low star formation rate at late time and the fact that no star formation takes place below gas surface density of $\Sigma_{\mathrm{gas}} \leq 2\,\mathrm{M}_{\odot}\,\mathrm{pc}^{-2}$ appear to go back to the same reason. All simulations without feedback show the trend of building large associations of particles and congruent patches of gas

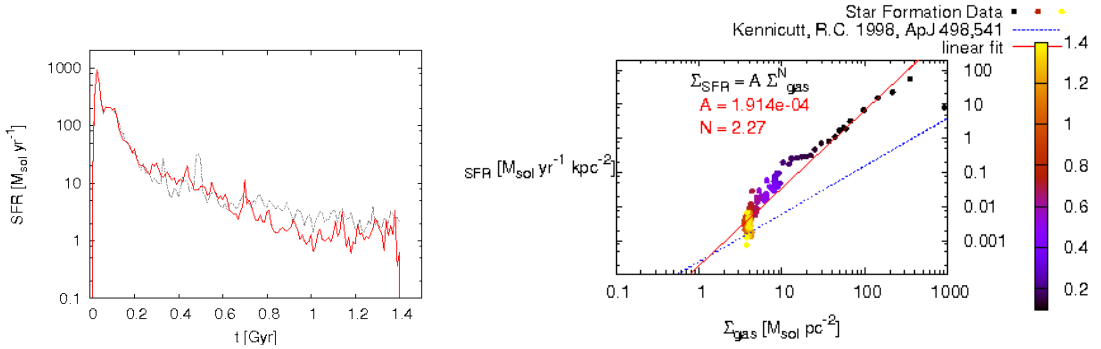

(a) Temporal evolution of the star formation rate.

(b) The global Schmidt-law for star formation with simplified criteria.

FIGURE 9.20. (a) Comparison of the star formation rate in the standard case simulation (SF1F0e50) (grey, dashed line) and the simulation with stripped star formation criteria (SF2F0e50) (red, continuous line). (b) Analysis of the simulation with simplified star formation criteria with respect to the KS relation.

during the second half of simulation time. With less restrictive creation criteria most particle and therefore star formation takes place in these locations, while otherwise the more strict criteria spread the creation through the disk and therefore lead to different star formation rates occurring at different gas surface densities. The overall small star formation rate can possibly be attributed to the relatively long timescales on which new gas becomes available as a result of accretion and infall. Hence, purely turning dense gas into sink particles is not a convincing mode to model star formation in molecular clouds.

We conclude this chapter with a general assessment of simulation routines and parameter choices. We have seen that simulations without feedback already develop a reasonable overall gas structure in the galactic disk. Nevertheless, feedback is essential to simulate the circulation of matter in the star formation process as well as to gain a more realistic interstellar medium. Our feedback serves both demands in an appropriate way. However, lots of interesting details have not yet been studied in detail in the above analysis. Moreover, the simulation parameters as well as the employed particle creation criteria, established as our standard case, have prooven to be the adequate choice for our goal to simulate star formation in isolated disk galaxies. The parameter studies in the last Section (9.7) have shown that simulations follow the temporal and structural evolution in most detail when the standard value for minimum particle mass is applied. Additionally, we have seen that in the spirit of our interpretation of sink particles, the complete set of particle creation criteria as in SF1 is best capable to yield a good representation of star forming gas clouds. With these findings, we now proceed and study the influence of turbulence regulation of the star formation process in subsequent simulations.

CHAPTER 10

Turbulence Regulated Star Formation

In the previous Chapter (9) we have described our standard simulations and how we perform analyses on the simulation data. We have described and interpreted the results and given an extended discussion of the nonlinear dependencies of algorithmic and parametric changes of different simulations. In conclusion, we have argued for our choice of standard parameter values and established the basis for the now pending inclusion of turbulence effects to regulate the star formation process.
In this Chapter (10) we show how we expect the turbulence regulated star formation algorithm to work and why. For this case we discuss several simulations motivated by the KM05 model and analyze their results. Finally, we present simulations of turbulence regulated star formation using the full model as proposed by Krumholz and McKee [2005].

10.1. The Efficiency Parameter

In all previous simulations we have always used a star formation efficiency parameter $\epsilon = 0.5$ as originally proposed by Tasker and Bryan [2006] for some of their Enzo simulations. In the algorithmic realization of star formation this efficiency parameter encodes, among other quantities (cf. Equation (5.24)), the fraction of gas that is transformed into sink particles and is eventually available for the formation of stars. Therefore, the efficiency parameter can be interpreted to determine the fraction of gas in a molecular cloud which gets transformed into stars.
The value of the efficiency parameter is rather controversial owing to the difficulties to determine the substructure, particularly, mass and time scales of molecular clouds by observations. Simulations such as our own do not have sufficient spatial and temporal resolution to resolve the physics. Hence, our solution to model these missing physics is the subgrid-scale approach to determine how efficiently gas is transformed into stars.
There is vast literature investigating this problem. Lada and Lada [2003] give an efficiency between $10 - 30\,\%$ for nearby embedded clusters gained from observations. Duerr et al. [1982] state that field stars form with much lower efficiency $1 - 5\,\%$ in giant molecular clouds, while Elmegreen and Efremov [1997] give a local efficiency of $20 - 50\,\%$ for the formation of bound stellar clusters. Matzner and McKee [2000] propose an analytical model including outflows and determine an efficiency for cluster formation of $30 - 50\,\%$. Finally, to mention just a few, recent work by Krumholz and Tan [2007] shows again that much lower values of the order of only several percent ($2\,\%$) are possible.

As we have seen in the last chapter, the value of $50\,\%$ efficiency usually employed in our standard case leads to star formation rates which are more than one order of magnitude to large. This result, together with the literature cited above, indicating much smaller efficiency values, raises the question which efficiency to expect from the KM05 model.
In order to answer this question and to get an order of magnitude estimate for $\mathrm{SFR}_{\mathrm{ff}}$ (cf. Equation (4.21)) we estimate the virial parameter α_{vir} and the turbulent Mach number $\mathscr{M}_t$. Both

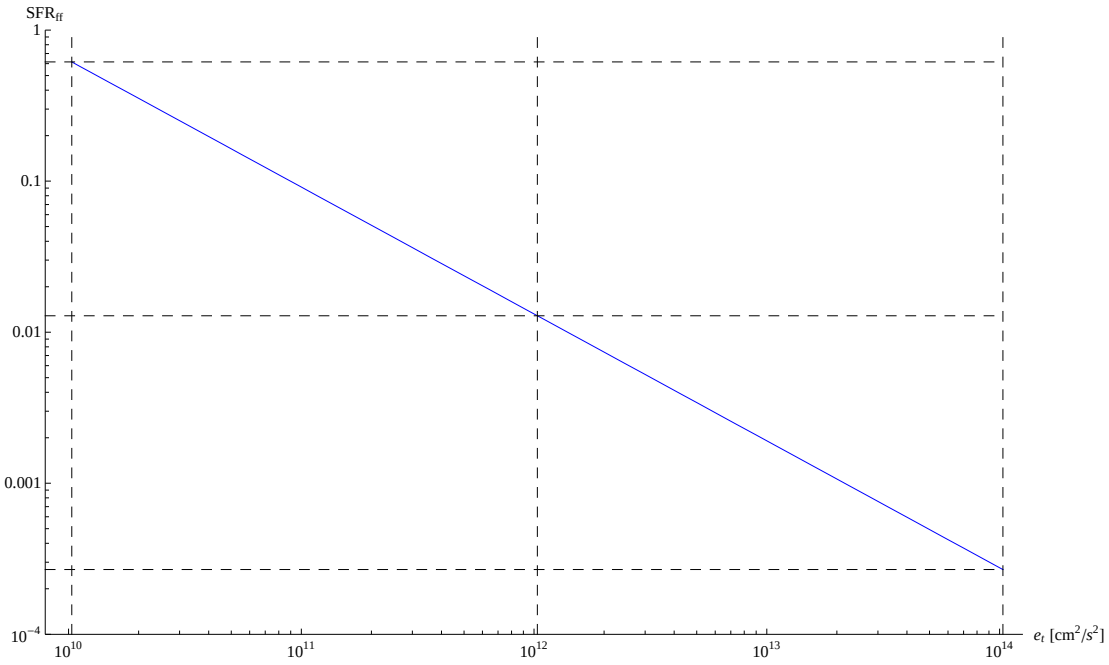

FIGURE 10.1. Order of magnitude estimate of possible star formation efficiency values depending on turbulent energy content of star forming simulation cells. The vertical lines indicate approximate turbulent Mach number of $\mathscr{M}_t = 1, 10, 100$ (from left to right), while the horizontal lines intersect the functional graph at these Mach number values and depicts the corresponding star formation efficiencies.

parameters can in turn be calculated on the basis of turbulent energy as described in Section (6.3), see Equations (6.22) and (6.23). Hence, we only need to estimate the turbulent energy in a star forming region to get $\mathrm{SFR}_{\mathrm{ff}}$.
Vice versa, we can also start from the Mach number and get the turbulent energy. As we are only interested in an qualitative estimate at this time, we can then use the energy to calculate the virial parameter and eventually the star formation efficiency. Hence, we pick a turbulent Mach number apparent in molecular clouds, and still computable in our simulation, namely $\mathscr{M}_t = 5$ and calculate a corresponding turbulent energy of $e_t \approx 2.6 \cdot 10^{11}\,\mathrm{cm}^2/\mathrm{s}^2$. Here, we use all standard values and set a temperature of 300 K as this is the minimum temperature realized during the simulation. For this energy, we furthermore calculate $\alpha_{\mathrm{vir}} \approx 1.1$ and finally get a star formation efficiency $\mathrm{SFR}_{\mathrm{ff}} \approx 0.041$ or 4.1 % from Equation (4.21).
Figure (10.1) shows the results of the procedure for turbulent Mach numbers $\mathscr{M}_t$ ranging from 1 to 100. The corresponding estimates of $\mathrm{SFR}_{\mathrm{ff}}$ range from 61.5 % to 0.03 %, respectively. Note that these numbers are not to be considered results from our simulations. They are only a rough estimate of what results we possibly expect from the KM05 model in the context of our simulations. Moreover, we particularly do not realize the extremely low values at high Mach numbers, as our simulations are restricted to turbulent Mach numbers smaller than 5 (cf. Section (7.4)).
We draw the conclusion that turbulence regulated star formation will have a much smaller efficiency than used in the previously presented simulations. In order to investigate this important issue, we decided to first study the effects of reduced efficiency without the full complication of

the dynamical computation of the star formation efficiency performed via subgrid model calculations. Instead we chose a fixed efficiency value of 3 %, as we would expect it to be realized during SGS simulation. This value is slightly lower than the previously calculated 4.1 % at $\mathscr{M}_t = 5$. The reasons are that we expect star formation to generally occur at larger Mach numbers and henceforth, with lower efficiency, but more physically, the efficiency of 0.03 is what we see to lie at the center of the parametric analysis given by Krumholz and McKee [2005] (see Figure (4.1) (a) and the frame indicating most probable star formation parameters therein.)

10.2. Simulations with Reduced Efficiency

We have performed two simulations with the low fixed efficiency of $\epsilon = 0.03$. The first simulation (SF1F0e3) is an exact recapitulation of the standard simulation, but with this different efficiency. The second simulation (SF1F1e3:) additionally includes feedback as discussed in Section (9.6).

Here, we start the analysis of simulation data by investigating the thermal properties of the simulated interstellar medium. In Figure (10.2) we overlay the gas phase distribution functions of the low efficiency simulations and the standard case. For the volume fractions, we only see marginal differences. The reader should keep in mind that all plots are normalized to the total gas mass at the specific instant in time. Gas already transformed into particles is not included. More interestingly, we also see general concordance of the mass distributions, although two distinct differences show up. Firstly, the low efficiency simulation without feedback produces much less cold gas and correspondingly more warm material during the second half of the simulation runs. The inclusion of feedback in the low efficiency case appears to alleviate this change. The strong fluctuations in the distribution functions show how the slow, low efficiency star formation only depletes certain regions inside the inner gas disk. These voids of hot, low density material exist for several Myr until the overall dynamics mix the gas phases again. Contrarily, in the feedback case, the stars that form do not only deplete gas but also supply it back into the low density regions. More importantly, feedback is a much stronger source of gas mixing and therefore quickly transfers surrounding gas into depleted areas.
Secondly, the feedback case shows a small but definitely larger amount of mass in the hot phase than both other simulations during the whole simulation. Again, note the different scale of this plot. This is the mass injected back into the ISM from evolving sink particles.
Next, we turn to investigate the star formation history in our simulations with reduced efficiency. Again, we compare both low efficiency simulations and the standard case (see Figure (10.3)). Several interesting differences have to be discussed. Firstly, both low efficiency simulations do not show the same strong initial star formation burst as the standard case. The maximum star formation rate only reaches approximately half the value of the standard case. Contrarily, after this initial spike, both low efficiency runs have continuously higher global star formation rates than the simulation with standard efficiency. These observations are not surprising. After all, low efficiency star formation produces a smaller star formation rate, even with a huge amount of overcritical gas, as present during the initial phase of the simulations. While the standard case produces stars with relatively high efficiency and thereby processes large amounts of gas, the low efficiency runs extend the entire process much longer over time and therefore generate stars at moderate rates for much longer.
After approximately 500 Myr both standard and slow star formation realizations have reached equal rates of star formation. However, while the rate still declines for the standard case, the low efficiency runs roughly maintain a constant rate for another 500 Myr. However, the feedback run shows significant fluctuations which even show a temporary increase of star formation activity. Again, continuous infall of unprocessed gas and the overall much smaller depletion of gas in the low efficiency simulations feed the continuous star formation process. The increase in the

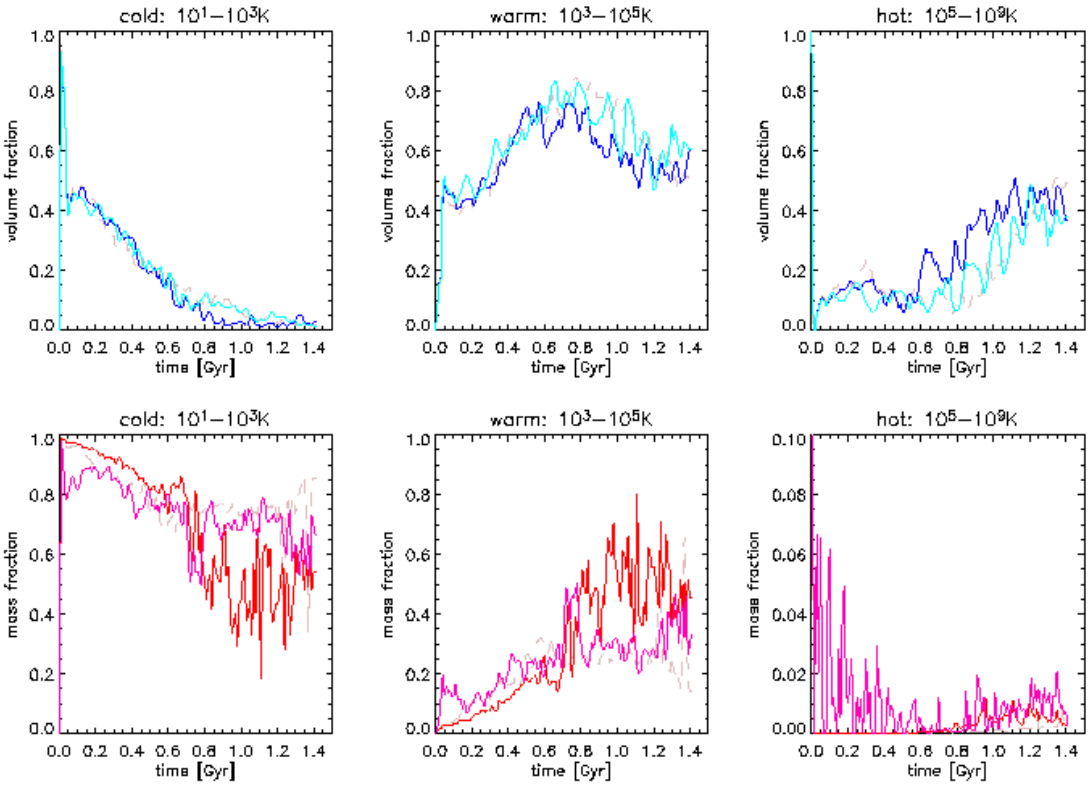

FIGURE 10.2. Top: Volume fractions of gas in the ISM in three different simulations. Bottom: Mass fraction of gas in the ISM. Grey dashed lines depict the standard ($\epsilon = 0.5$) simulation without feedback (SF1F0e50). Blue (SF1F0e3) and light blue (SF1F1e3) (including feedback) as well as red (SF1F0e3) and magenta (SF1F1e3) (including feedback) depict low efficiency simulations ($\epsilon = 0.03$)

feedback case is owed to a significant accumulation of remaining mass in a high density object with significant star formation. This region of high gas density is also able to collect additional gas from the surrounding ISM. As star formation proceeds, gas is transformed into stars and feedback starts to disperse the gas association again.

Towards the end of the simulations the star formation rate of the non-feedback run is generally reduced and fluctuates around a rather low value. In contrast, the simulations including feedback show a relatively constant star formation rate with only a small reduction of star formation activity. We readily attribute these observations to the fact that only small fractions of overdense gas are available during the final evolution of our simulations. However, this effect is reduced and delayed in the feedback simulation where gas is recycled back to the ISM.

The previously discussed differences also appear in the analysis of the global dependence of spatially averaged star formation rate and gas surface density, as shown in Figure (10.4). Both plots show the reduced star formation rate in the high density regime. Here. a general flattening and therefore collective reduction of star formation in highly overdense gas is apparent as expected for simulations turning overcritical material into stars much slower as a result of the reduced efficiency.

Additionally, the star formation rate in the non-feedback case stretches down to lower values as

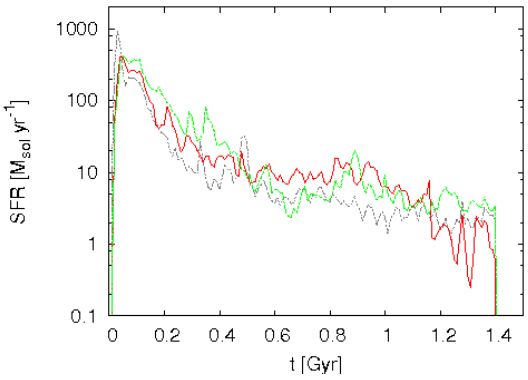

FIGURE 10.3. Temporal evolution of the globally averaged star formation rate of the standard simulation without feedback (SF1F0e50) (grey dashed), low efficiency simulation without feedback (SF1F0e3) (red) and low efficiency including feedback (SF1F1e3) (green)

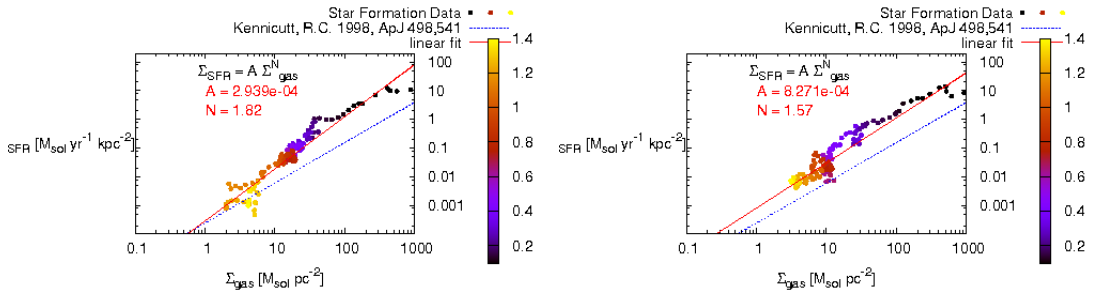

(a) Low efficiency simulation without feedback (SF1F0e3).

(b) Low efficiency simulation including feedback (SF1F1e3).

FIGURE 10.4. Comparison of simulation data to the analytic prediction of the KS relation. The time evolution of galaxies is color coded in the data points. The blue dashed line depicts the KS relation, while the red continuous line is a linear fit to the depicted simulation data.

well as corresponding gas surface densities. Contrarily, in the feedback case gas densities and star formation activity show both still larger values owing to the yet less pronounced effects of gas depletion.

Finally, the low efficiency simulation including feedback significantly raises the late time star formation rate at intermediate gas densities and we see how the simulation comes close to reproducing the power law correlation predicted by KS. Nevertheless, the star formation rate is generally still one order of magnitude too large.

We take this as an indication that the star formation algorithm proposed by KM05 in combination with feedback can be used in our simulations to yield results in better agreement with observed galactic properties than previous simulations with fixed efficiency.

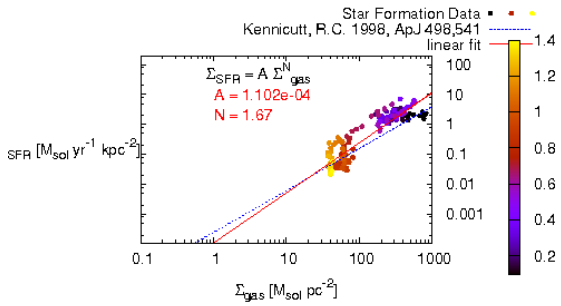

FIGURE 10.5. Comparison of simulation data to the analytic prediction of the KS relation. The simulation uses an artificially low star formation efficiency 0.3 % and includes feedback (SF1F1e03).

A Parameter Test. Above we have studied the influence of reduced star formation efficiency on our simulations. We have seen that although the reduced efficiency brings us closer to the desired reproduction of the global KS relation, particularly in the feedback case. However, data and observations still differ by roughly one order of magnitude. Although we have physically motivated the choice of our employed efficiency value above, we also had to account for the given algorithmic limitations in order to apply our subgrid-scale model, namely, a maximum value for $\mathscr{M}_t = 5$. Generally, high turbulent Mach numbers, possibly reaching values up to 50 in molecular clouds, can theoretically produce even smaller efficiencies of turning gas into stars. Although this cannot be interpreted as a single global efficiency for one molecular cloud object we consider it interesting to test whether an even lower efficiency parameter produces better agreement of simulation data and KS relation.
Therefore, we performed an additional study, repeating the low efficiency simulation including feedback presented above, but with efficiency parameter again reduced by one order of magnitude. We use $\epsilon = 0.003$ or 0.3 %.
Figure (10.5) shows the data analysis of this simulation. The simulation reproduces the normalization of the KS relation much better while using the artificially low star formation efficiency. The slope of our linear fit does not give any conclusive information, however, while the simulation still slightly overestimates the star formation rate at high gas surface density, it produces a better fit for the intermediate density range. Unfortunately, the simulation has not transformed enough gas into stars at the time it was stopped (1.4 Gyr) to show any low surface density star formation.

10.3. Galaxy Simulation with Subgrid Physics but No Coupling to Star Formation

We begin the discussion of simulations including the treatment of subgrid-scale turbulence by presenting an initial study of a disk galaxy simulation including the full SGS turbulence calculations, but the standard star formation algorithm as well as no feedback from star formation. In that sense the setup of this simulation is identical to our standard case simulation (cf. Section (9.2)) with the sole difference that we now include the complete subgrid model (cf. Chapter (7)) in the numerical calculation.
The reason for this study is to identify the primary effects of the SGS model on the overall

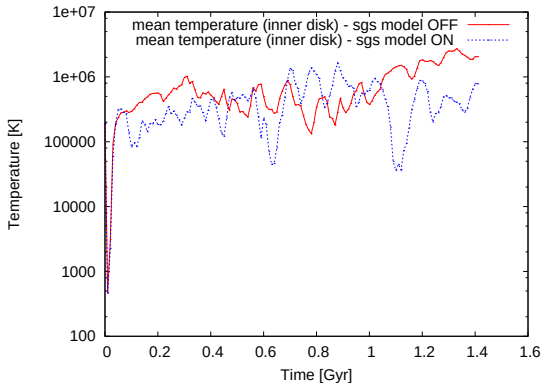

FIGURE 10.6. Comparison of mean temperature of our standard case simulation (SF1F0e50) (red continuous function) and a standard simulation including the full SGS turbulence model (SF1F0e50sgsMa5) (blue dashed function).

evolution of the galactic disk with as little secondary effects as possible. Although these secondary effects, e. g. the influence of the primarily different energy content in the ISM on the star formation process, is what we are ultimately interested in, we first focus on the primary effects. Consequently, we compare the SGS simulation to its standard case counterpart and look for differences and similarities.

Thermal Properties of the Inner Gas Disk. Figure (10.6) shows the averaged gas temperature of the inner gas disk for the standard simulation without subgrid model and the case with subgrid model but no direct coupling to the star formation algorithm.
Initially, both simulations are identical, but shortly after the beginning of their evolution, the mean temperature of both realizations begins to deviate. In the subgrid case, a certain fraction of turbulent energy starts to build up and therefore reduces the mean thermal energy content of the simulation. With this major difference, the mean temperature values evolve without significant events until approximately 500 Myr. At this point, the standard simulation shows a slight decrease in its mean temperature while the subgrid run develops a significant increase of temperature at the same time. Consequently, there is a period of several hundred Myr when the subgrid simulation has higher mean temperature in the inner disk than the run without SGS model. After roughly 1 Gyr the situation is reversed again. Moreover, we see a general increase of the mean temperature in the standard run, particularly during the second half of the simulation. We do not observe this trend in the subgrid simulation where the general trend is roughly constant. We have already seen this increase of temperature towards the end of simulation runs in the earlier discussion. The reason was that as gas depletion proceeds, more and more hot gas from the outer disk region falls into the extraction volume. While this is obviously the case for the standard run, the subgrid run depletes its gas reservoir much more slowly delaying the infall of hot material. In gas density projection plots (not shown here) this is also the most evident effect.
More detailed information is available from a comparison of Figure (10.7) and the corresponding Figure (9.10) of the standard case, showing the temperature distribution in both simulated disks. In correspondence with the discussion above, the most obvious difference is the reduction of high temperature material for the subgrid case. Particularly during the early and late evolution significantly less volume is occupied with high temperature material. At intermediate times, the distribution functions differ much less. Nevertheless, it is important to keep in mind that

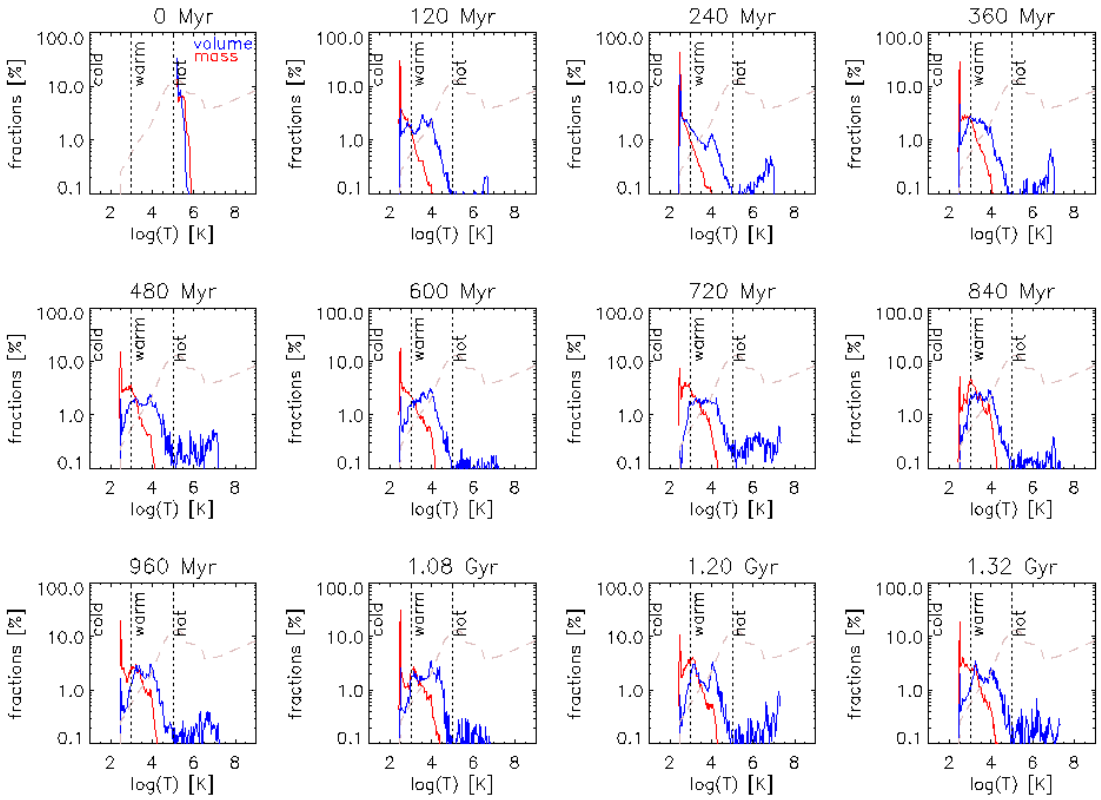

FIGURE 10.7. Temperature distribution in the simulated ISM for the simulation with full SGS model (SF1F0e50sgsMa5) but no coupling to star formation.

especially for the late evolution we can not compare absolute values as the fractions also depend on the amount of mass already transformed into particles.
Nevertheless, from these observations we identify two prime subgrid model effects. Firstly, the reduction of thermal gas energy during the buildup of a significant turbulent energy component, and secondly, increased mixing and stirring effects with more gas at intermediate temperatures.

Density Distribution in the Inner Gas Disk. The behavior discussed above is also evident from the comparison of gas density PDF as shown in Figure (10.8). We have picked three representative instants of time at 200 Myr, 800 Myr and 1.4 Gyr which clearly show how the distribution of gas densities is changed in the simulation run including the effects of unresolved turbulence. Especially the high density tail of both distribution functions are largely different, with significantly more material at high density in the standard case. Additionally, the standard case does not only show more gas at high density but also on the low density side of the distribution. Contrarily, the subgrid run shows much higher values at intermediate gas densities.
In this picture, the incorporation of the subgrid model results in an increase of gas at moderate densities. However, high density material capable of collapse is also present throughout the simulation. It appears that the subgrid model enhances the evolution of gas at intermediate density towards either lower or higher densities. Clearly, the density domain starting roughly at $n \sim 1\,\mathrm{cm}^{-3}$ up to the threshold density where gas is transformed into particles is significantly

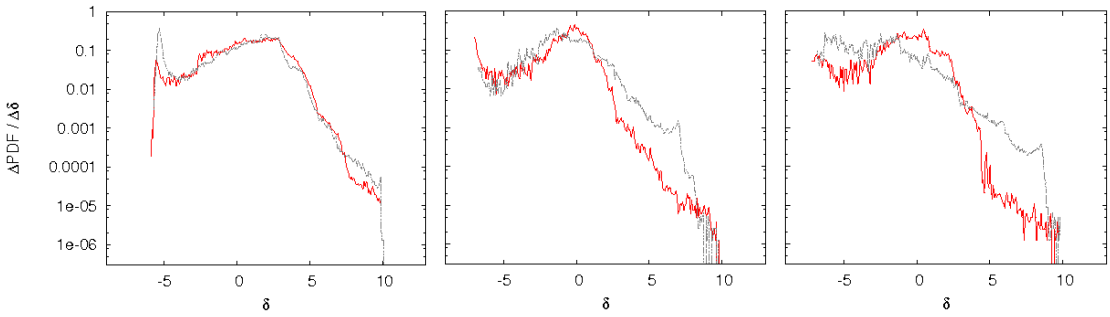

(a) 200 Myr (b) 800 Myr (c) 1400 Myr

FIGURE 10.8. Comparison of density PDF for the subgrid run without coupling to SF (SF1F0e50sgsMa5) (red, continuous line) and the standard run ((SF1F0e50)) (grey, dash-dotted line).

less occupied during the entire simulation.
Consequently, the star formation process is supplied less fast with new overdense material. This results in a shortened high star formation activity during the initial evolution and a reduction to moderate values. Subsequently however, there is enough dense material to maintain this moderate activity throughout the simulation.

Concluding this section, we have seen how already the passive inclusion of subgrid-scale turbulence has significant influence on the overall dynamics of a simulation. Summing up these latter aspects, the SGS model accounts for a significant amount of turbulent energy resulting in reduced thermal energy content. Furthermore, the SGS model leads to a concentration of gas at intermediate densities.
An order of magnitude estimate of the effect on the thermal energy content can be deduced from Figure (10.6). We focus on the first couple of hundred Myr because at later times nonlinear effects and different algorithms cause diverging evolution of the simulations. We observe that the difference in thermal energy is approximately of the same order as the thermal energy itself. From the definition of the turbulent Mach number $\mathscr{M}_t = \sqrt{2e_t}/c_s$ and the correlation of thermal energy and sound speed $e_{int} \sim c_s^2$ we see that turbulent energy reaches the same order of magnitude as the thermal energy $e_t \sim \mathscr{M}_t^2 \cdot e_{int}$ for supersonic turbulent Mach numbers. Figure (10.10) shows the turbulent Mach number for a simulation comparable during the early evolution. We see that the turbulent Mach number is supersonic on average in the inner part of the disk, corresponding to the analyzed temperature data. Hence, a turbulent energy content in the same order of magnitude as the thermal energy and the corresponding reduction of the thermal energy as observed in Figure (10.6) is what we expect for the discussed simulation.

10.4. Turbulence Regulated Star Formation with Limited Turbulent Mach Number

Next we start the discussion of simulations actively making use of the subgrid-scale information to determine the details of the star formation process. We begin the discussion of simulations with turbulence regulated star formation by presenting an initial study of a disk galaxy simulation including the full SGS turbulence calculation, the KM05 star formation algorithm but no feedback from star formation. As discussed earlier, we limit the turbulent Mach number to a

value of $\mathscr{M}_{t,\max} = 5$ in this and the subsequent simulations until stated otherwise. Therefore, the presented simulations differ in two major aspects to all previously discussed realizations.
Firstly, the calculation of the star formation efficiency has a real functional dependence on the subgrid-scale turbulence energy. Considering the discussion of fixed efficiency simulations in Chapter (9) and furthermore the analysis of theoretically determined lower, but still fixed efficiency in Section (10.1) of this chapter, this difference is twofold. On the one hand, the efficiency is uniquely determined for each particle formation process rendering the transformation of interstellar gas into a sink particle directly dependent on the unresolved physics of turbulence captured via the subgrid-scale model. On the other hand, the global average of star formation efficiency is expected to be quite different from the efficiency in the standard runs. However, compared to the fixed low efficiency runs, this difference might disappear or at least be much less pronounced as the discussion will show.
Secondly, the turbulence subgrid-scale model itself will have an direct influence on the simulation runs as discussed in the previous section.

To investigate the first issue of turbulence regulated efficiency we start with an analysis of the numerically computed efficiency values, based on the KM05 model. The simulation logs almost two million sink particle creation events during its full runtime of 1.4 Gyr. We average these events for time periods of 10 Myr and depict the resulting values in Figure (10.9).
The most apparent feature of this analysis is the fact that the dynamically computed efficiency is indeed one order of magnitude smaller than the previously used values of $\epsilon = 0.5$. We also see that the discussion of reduced fixed efficiency (cf. Section (10.1)), where we decided to run a simulation with fixed efficiency of $\epsilon = 0.03$ was a reasonable choice.
Considering the details of the presented graph, two aspects need to be mentioned. Firstly, the rather smooth characteristics are owed to the fact that almost two million original data points are accumulated and averaged in only 140 bins. Secondly, the temporal evolution of the efficiency values show clearly that the initial values are larger than later ones. We see a drop off during the first 300 Myr until a value of approximately $\epsilon \approx 0.05$ is reached. This behavior is not to be attributed to be an effect from the subgrid model. It reflects the large initial gas overdensity as a result of our initial conditions. The KM05 star formation efficiency is indirectly proportional to α_{vir} and the virial parameter itself is indirectly proportional to the gas mass in the corresponding cell. Therefore, the large initial overdensities produce small α_{vir} values, yielding increased efficiency values ϵ.

To analyze the evolution and influence of the subgrid model on the simulations, we depict the turbulent Mach number in slices through the disk midplane in Figure (10.10). The color coding clearly separates subsonic (blue) and supersonic (red) parts of the disk, while the transsonic regime is colored white. Initially, the turbulent Mach number is largest in the center of the disk where gas is rapidly cooling and gravitational fragmentation is forming cold dense clumps. During the subsequent evolution we observe a torus of supersonically supported gas around a more dynamically changing central disk part which contains patches of turbulent gas with the highest turbulent Mach numbers but at the same time also extended regions with no supersonic gas at all.

Problems with Subgrid-Scale Model and Feedback. After introducing the simulation including turbulence regulated star formation, the next step is to include feedback from formed stars as discussed previously (cf. Section (9.6)). However, the combination of our implementation of feedback together with the full subgrid model algorithm has encountered strong numerical

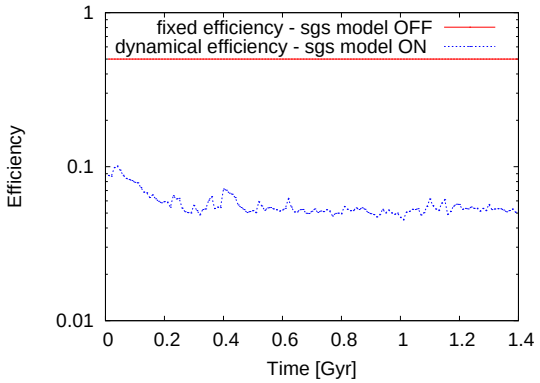

FIGURE 10.9. Efficiency parameter for the transformation of gas into particles. The red, constant line depicts the standard case fixed efficiency of 50 % ((SF1F0e50)) while the blue function shows temporally averaged values computed using the KM05 star formation algorithm (SF3F0sgsMa5).

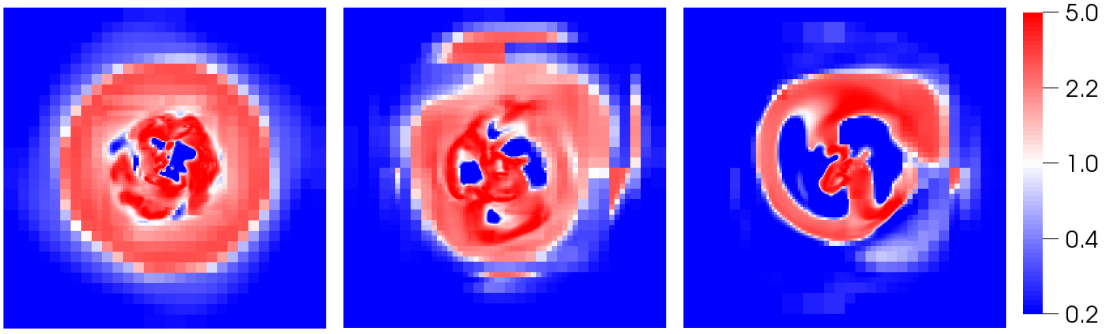

(a) 200 Myr (b) 800 Myr (c) 1400 Myr

FIGURE 10.10. SF3F0sgsMa5: Slices through the disk midplane depicting the turbulent Mach number. The artifacts in the middle frame are produced by the slicing algorithm of the visualization tool.

problems. The feedback algorithm effectively alters the energy content of particles and gas thermally as well as kinetically. This in combination with the subgrid model algorithm can have severe numerical effects, even with our amendments to the subgrid model to prevent unphysical production of turbulent energy described in Section (7.4). The general problem is caused by highly non-isotropic local feedback events happening at the locations of the parent particles but are not necessarily correlated to the original particle creation locations anymore. This results in the fact that feedback events can occur in marginally resolved regions. Therefore, the combination of feedback and subgrid model can result in an overproduction of turbulent energy which causes the numerical scheme to break down if not accounted for.
In order to perform a general problem assessment and check whether and in which way energy feedback worsens this situation, we experimented with a gross simplification of the feedback algorithm. Usually, the feedback is twofold, including mass and momentum feedback on the one hand, as well as thermal energy feedback on the other hand. In one particular simulation run (not presented here) we changed the feedback to only realize mass and momentum feedback but

omit changes to the thermal energy content. As expected, owing to the increased simplicity, the situation was improved slightly but the general problem is likely located closer to the production of turbulent energy than the explicit changes of the thermal energy content. It turned out that a reduction of the maximum turbulent Mach number, effectively setting a limit to the production of turbulent energy itself, is capable of resolving the problem. However, the realization and simulation of supersonic and highly supersonic Mach numbers is ultimately necessary to first account for the physics of real star formation environments and second to make use of the full potential of the KM05 star formation algorithm. More work and the continuous improvement of the subgrid model will yield advances into that direction.

The Correct Treatment of Particle Gravity. Additionally to the discussion presented so far we also want to draw attention to a particular problem of the Enzo code with respect to the simulation of particles produced and inserted dynamically into a simulation during runtime. Owing to some algorithmic shortcomings in the particle treatment, particularly, when individual particles move out of their parent grid, it is possible that these particles are not correctly attributed to the new grid that becomes responsible to provide information to compute the dynamical particle properties at the next timestep. When this happens, one direct effect is that gravitational forces are not applied to the corresponding particles until the algorithm reattributes particle and grid affiliations during the next global iteration of the grid structure. Henceforth, most of these particles leave the inner part of the galactic disk where they have been created and possibly even the entire computational domain. The total mass of particles usually lost in a galaxy simulation, as presented in this work, is only around 5 %. More important is the fact that particles that are not treated correctly by gravitational forces result in a largely falsified distribution and dynamical evolution of particles themselves. Consequently, the gravitational potential caused by the particle component is also incorrect. This directly effects the gas phase and is most severe in the inner part of the galactic disk.
One simple possibility to circumvent the entire problem is to shorten the root grid time-step of the simulation. Numerical experimentation has shown that using a root grid time-step reduced by a factor of $1/10$ is needed to realize a corrected simulation of particle dynamics. The factor of $1/10$ was determined via a convergence study of identical simulations with the only difference of the temporal extend in the root-grid timestep.

For all simulations presented in this work we have used this additional reduction of the root grid time-step.

We emphasize and present this problem here because we want to draw attention to two different but very instructive details. Firstly, the inadequate treatment of particle dynamics copes with a larger turbulent Mach number limit, owing to the weakend particle potential. Secondly, simulating incorrect particle dynamics yields much lower star formation efficiencies. Both effects are seemingly of little physical importance as the basic presumptions, or better, the underlying numerical simulations, are known to bear significant error. In this sense, we do not draw any quantitative conclusions. However, there are still some aspects worth mentioning.

We compare two simulations, the first using the original timing for the evolution of the grid hierarchy and the second using a ten times more frequent iteration of the grid structure. Additionally, these two simulations have different turbulent Mach numbers. While the simulation run depicted in Figure (10.11) (a) has a turbulent Mach number limit of $\mathscr{M}_t = 10$, the comparison run (b) has our standard value of $\mathscr{M}_t = 5$. This difference aside, both simulations are initialized equally, using the SF3 algorithm for star formation, no feedback and all other parameters in

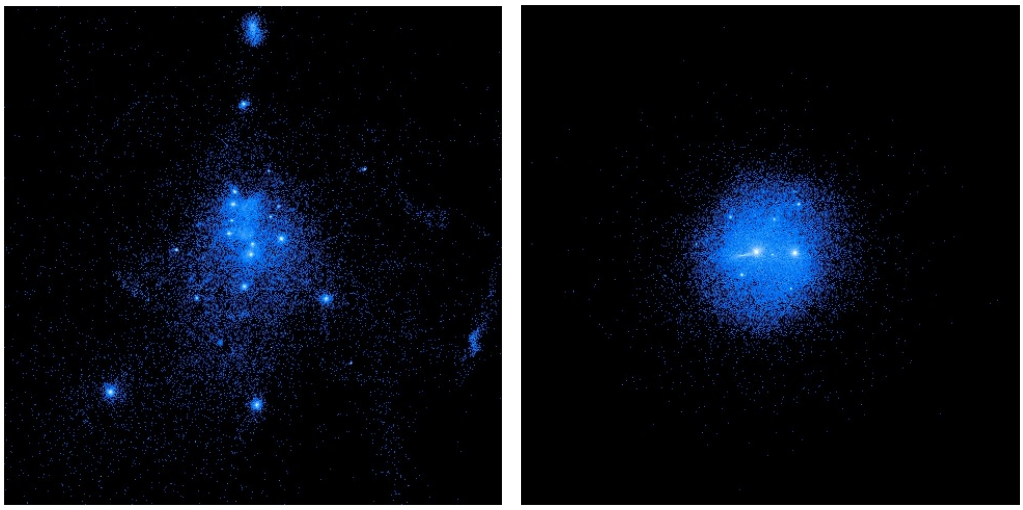

(a) incorrect particle treatment (b) decreased root grid time-step

FIGURE 10.11. Comparison of two simulations, left (a) uses an inadequate treatment of particles ((SF3F0sgsMa10err)), while right (b) uses a root grid time-step which has been shortened by $1/10$ to capture the correct particle dynamics ((SF3F0sgsMa5)).

standard configuration.
The flawed simulation is one of our early runs where it appeared that our scheme would be able to allow turbulent Mach numbers up to 10, later we had to accept that only smaller values can be realized in the current form of the subgrid model and we reduced the values correspondingly. However, the presented Figure (10.11) gives a strong hint towards the reason of difficulties. We observe that the particle distribution is much more centrally concentrated when particle dynamics are treated in the correct way. Moreover, the major peaks of particle density or correspondingly gravitational potential are significantly increased in the latter case. Both effects tilt the simulation towards a more extreme situation and add events and physical circumstances that are potentially more critical to the numerical scheme than in the simulation evolving a largely dispersed particle component.

Furthermore, we already stated that the flawed simulation determines relatively low star formation rates. Note that we have used the KM05 algorithm for the presented simulation. Figure (10.12) shows the dependence of star formation rate on gas surface density in our usual analysis. While it is certainly questionable to discuss the details of the plot it is nevertheless interesting to note that the general order of magnitude of the star formation rate is significantly lower in this flawed simulation.
Obviously, the gas component in the simulation is much less accumulated as a result of particle gravity, than is the case for the simulation with correct particle treatment. The dispersed particle component directly results in a correspondingly dispersed gas component. The reduced gas density, in consequence, yields a lower star formation rate. This points towards the possibility that dynamical effects of the gas and stellar components of a galactic disk may in fact have more significant influence on the overall evolution than expected before.

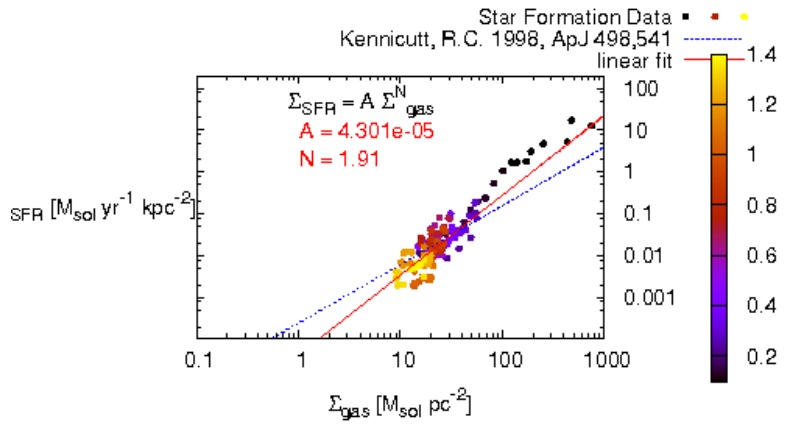

FIGURE 10.12. Order of magnitude estimate of star formation rate in a simulation ((SF3F0sgsMa10err)) with flawed treatment of particle dynamics.

Although it is dangerous to speculate based on certainly wrong data, it appears worth reinvestigating whether the assumption of an isolated galaxy with no dispersing effects from beyond the galaxy itself or the initial setup of a purely gaseous disk with no stellar component are best parameter choices.

Somewhere along the course of this thesis, we experimented with initial conditions including a significant stellar component. The generation of the initial conditions has been realized according to recent work of Li et al. [2005, 2006]. The latter authors have been so kind to supply us with the numerical realization of the analytical work of Mo et al. [1998] implemented by Springel and White [1999], Springel [2000]. This initial condition generator has been adopted to be used with ENZO, however, the possibility of such simulations was omitted in this thesis as we decided to focus our efforts towards the incorporation and applicability of the subgrid-scale treatment of turbulence. Future work might very well follow along the earlier approach and use largely different initial conditions prepared with the initial condition generator tool.

10.5. Low Turbulence Mach Number Regulated Galaxy Simulation with Feedback

Finally, we present a complete realization of all previously introduced and discussed aspects of turbulence regulated star formation in a full scale simulation of an isolated disk galaxy. In order to realize this goal, namely the joint simulation of the galactic gross properties together with the detailed interstellar medium including subgrid-scale turbulence to regulate star formation and furthermore including the buildup of a stellar component and a simplified representation of supernova type II feedback from these stars, we use the framework presented in the previous chapters. We use all standard parameter values as discussed and reasoned for earlier. The star formation is again realized via our implementation of the KM05 algorithm SF3 and the simulation includes feedback. The subgrid model is, however, configured in a more strict way, allowing only turbulence Mach numbers up to a value of $\mathscr{M} = 1$. Although we stress that this is not generally the largest possible value but at least an operational one. In the remainder of this Chapter (10) we now analyze and discuss this full scale turbulence regulated simulation (SF3F1sgsMa1).

The Galactic Disk. We begin with an investigation of the morphological structure of the galactic disk. Figure (10.13) shows the projection of gas surface density in the same fashion

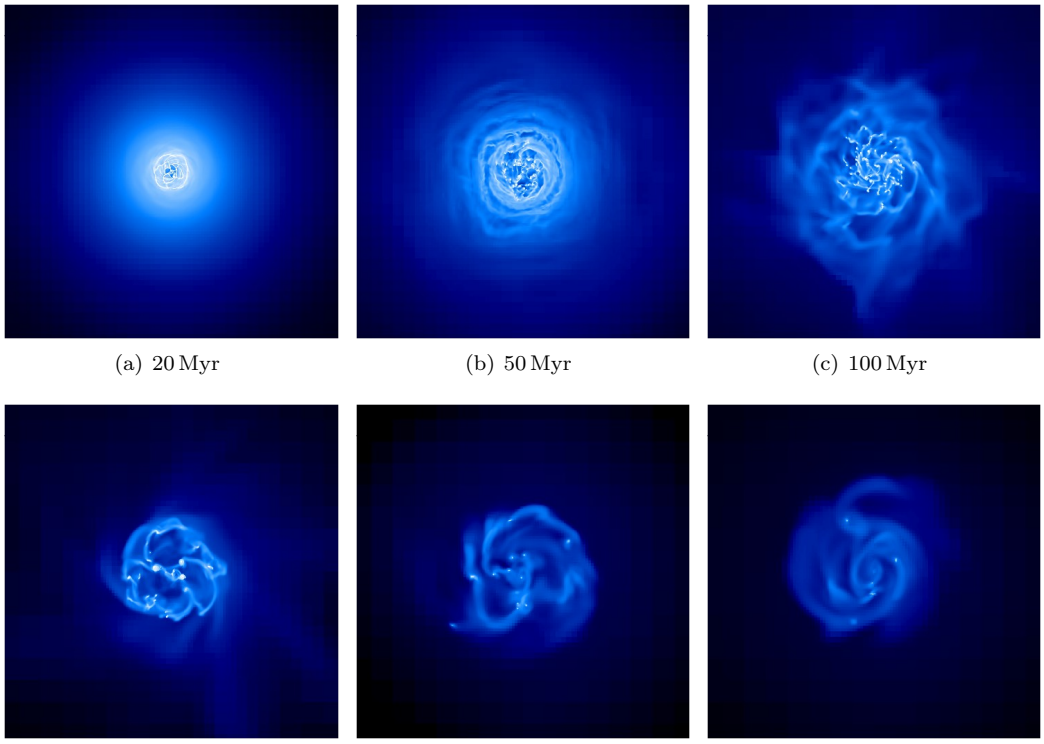

(a) 20 Myr (b) 50 Myr (c) 100 Myr

(d) 200 Myr (e) 500 Myr (f) 1000 Myr

FIGURE 10.13. SF3F1sgsMa1: Temporal evolution of the gas disk structure in projection along the axis of rotation. All pictures are 60 kpc across and the color table ranges from $10^{10}\,M_\odot\,Mpc^{-2}$ to $10^{15}\,M_\odot\,Mpc^{-2}$.

as introduced earlier (cf. Figure (9.1)). The general structural evolution with the early central fragmentation and the buildup of irregular web of filamentary density enhancements, as well as the subsequent fragmentation into small clumps of cold dense gas, follows the same pattern as in all other simulations. However, the filamentary structure is already disrupted by early feedback events. Furthermore, this significant influence from star formation feedback results in a much more irregular appearance of the interstellar medium. At approximately 50 Myr, shortly after the initial star formation burst, we observe several irregular rings of gas which result from feedback events originating in the central part of the disk where early formation of stars was most pronounced. During the next 100 Myr most of these shock density enhanced regions fragment and collapse towards the inner part of the disk. Consequently, the galactic disk is much more centrally concentrated although this is certainly also influenced by the slower, because less efficient, star formation process. At later times during the simulation, the disk settles into a less dynamical state where it only marginally changes in size and structural appearance.

Additionally, we also observe the effects of feedback in the side-on projections of the galactic disk shown in Figure (10.14). Large outflows and ejections of gas are visible throughout the entire disk. This is most pronounced during the early, most active star formation phase. As the simulation proceeds and the disk becomes more quiescent, the strength of outflows is largely reduced, too. The snapshots at 200 Myr and particularly at 500 Myr again show how the disk

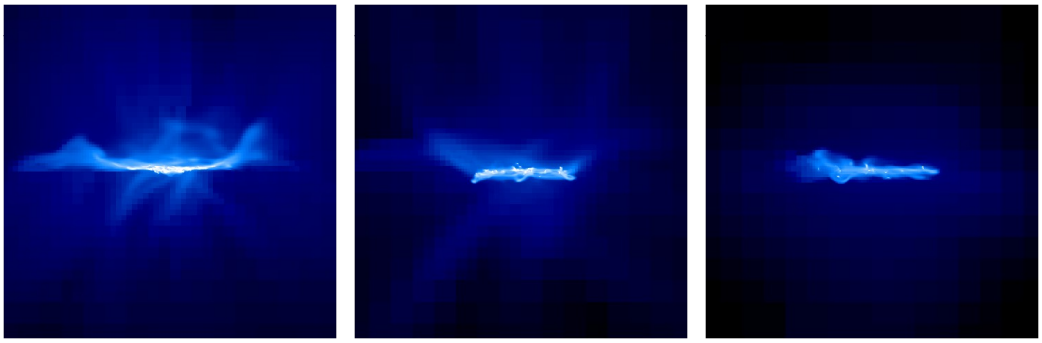

(a) 100 Myr (b) 200 Myr (c) 500 Myr

FIGURE 10.14. SF3F1sgsMa1: Temporal evolution of the gas disk projected through the galactic plane. All frames have the same spacial extension and color table as figures before.

is reshaped and gas is more centrally concentrated. After all, comparing this turbulence regulated simulation including feedback to the standard simulation case (fixed efficiency, no feedback, cf. Figure (9.5) and Figure (9.6)) shows a galactic disk with smaller extent in radial direction, but increased disk thickness.

Again, to gain a more quantitative evaluation we turn towards the analysis of gas density distribution in the central galactic disk. Figure (10.15) depicts the same analysis as presented for the standard case in Figure (9.7). Once more, feedback is the dominating factor which strongly broadens the density range in both directions, rendering significant fractions of gas to be existant at previously unoccupied ends of the distribution function. More dense gas is created via compression and subsequently repeated compression from feedback shocks. Low density gas is created via gas heating from feedback but more importantly, rarefaction as counterpart of shock compression. This behavior dominates for approximately 500 Myr. After that period of time we observe a shift in the distribution function describing rather continuous fractions of gas at low and intermediate gas densities while the high density wing of the distribution function is largely reduced. Towards the end of the simulation the galactic disk contains no high density material at all.

This is rather surprising from the point of view that feedback, including the circulation of gas from the ISM into stars and back into the ISM via mass ejection, is a channel to supply already processed material back into the galactic gas reservoir. This gas could then fragment and gravitationally collapse again to form new stars. To resolve this discrepancy, it is important to note that Figure (10.15) (i) is only partially representative for that late evolution of the gas disk. During the last hundred Myr we can indeed identify two distinct data outputs, at 1320 Myr and 1380 Myr, when the distribution shows gas at significant overdensity. Furthermore, the feedback deposits various, but rather small amounts of material continuously back into the ISM. Note that feedback was primarily modelled to mimic type II supernovae but also spread over time to account for the continuous outflows and winds. Therefore, feedback works to smooth the remaining galactic gas disk as the most violent events, namely the massive interaction of coincident events, become very rare.

Moreover, the presented simulation uses our turbulence regulated star formation realization. One implication is a reduced star formation efficiency which leads to slower transformation from

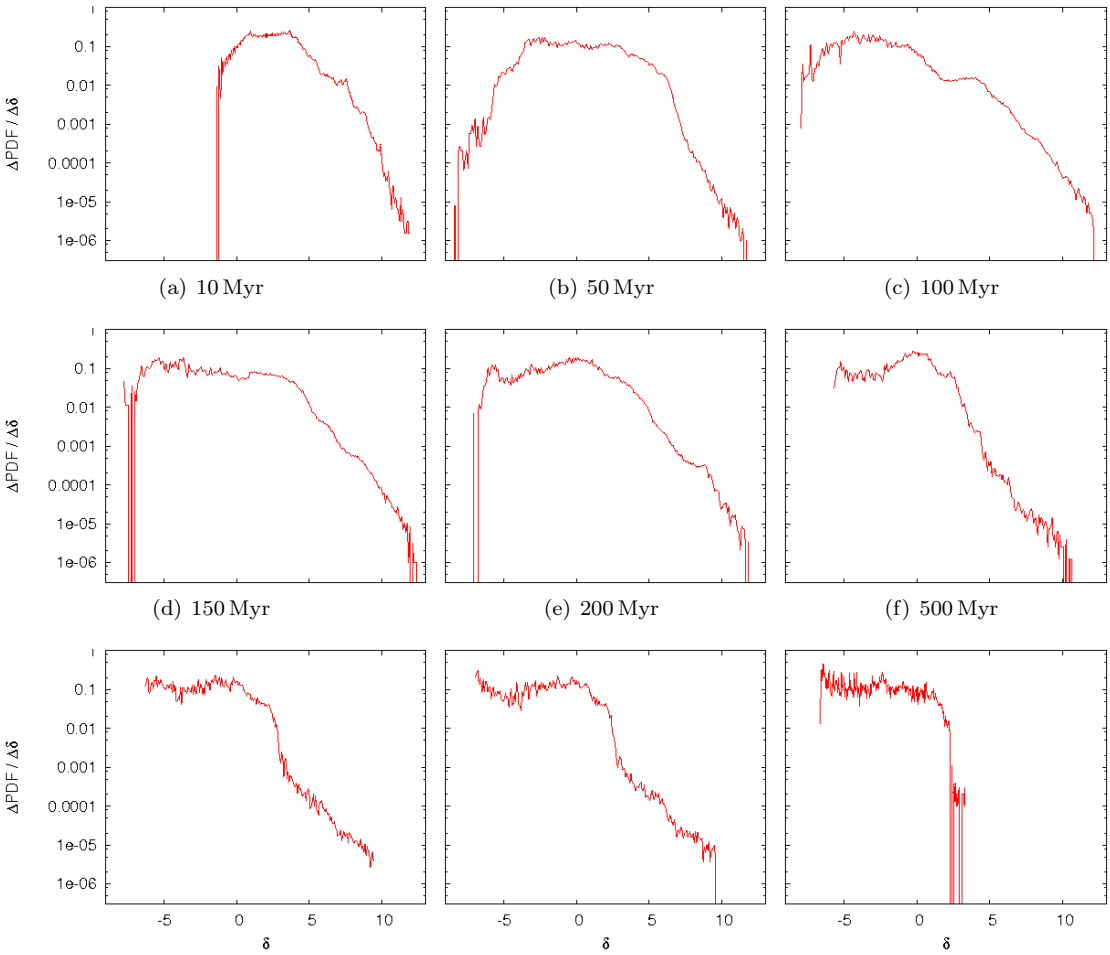

(a) 10 Myr (b) 50 Myr (c) 100 Myr

(d) 150 Myr (e) 200 Myr (f) 500 Myr

(g) 800 Myr (h) 1100 Myr (i) 1400 Myr

FIGURE 10.15. SF3F1sgsMa1: PDF of gas density. The plots depict the normalized logarithm of gas density. Therefore, the density scale of $\delta =]-5, 10[$ readily translates to $\rho =]6.74 \cdot 10^{-28}\,\mathrm{g\,cm^{-3}}, 2.20 \cdot 10^{-21}\,\mathrm{g\,cm^{-3}}[$ or $\rho =]10.0 \cdot 10^{-6}\,\mathrm{M_\odot\,pc^{-3}}, 32.5\,\mathrm{M_\odot\,pc^{-3}}[$.

gaseous phase into particles. Consequently, gas that is not immediately converted into particles once it reaches overdensity can easily be dispersed and redistributed by feedback, contributing to the previously described broadening of gas density distribution function.

Thermal Properties. The influence of star formation and feedback is not only evident in the density structure of the galaxy but also shows up in the thermal properties of the ISM. We analyze the evolution of thermal properties of the galactic gas in Figure (10.16) and compare to the standard case (cf. Figure (9.10)). In particular, the distribution of mass (red) shows a noticeable spread across the cold and warm phase during the first half of the simulation, in correspondence with the earlier discussion. An interesting additional peculiarity is the fact that several subsequent frames during the late evolution, particularly at 960 Myr, 1.08 Gyr and 1.20 Gyr, do

not show the pronounced low temperature peak in the mass distribution plot. This essentially demonstrates that no significant fraction of gas resides at or close to the minimum temperature without being transformed into particles or heated to higher temperatures. This is in accordance with the fact of the strongly reduced high density wing in the gas density distribution function at late times. A consequence of this is that we expect very low star formation activity for this time. Again, in accordance with the previous discussion, we observe a spike at 1.32 Gyr where we have also seen gas temporarily at high density in the distribution function.

The volume fractions depicted in the latter figure show the usual, expected picture of two distinct peaks, representing the corresponding warm and hot phase of the ISM. A noticeable difference to the standard case simulation is the fact that the hot fraction is significantly more pronounced during the entire simulation. This is again a consequence of continuous energy input from feedback which acts to particularly enhance to temperature in low density regions where cooling is less efficient.
However, it is important to note that there are still significant differences when comparing the latter simulation to the feedback augmented standard simulation presented in Section (9.6). These differences provide evidence for the fact that changes of particular aspects of a certain realization, like the inclusion of feedback or the utilization of a different star formation realization do by no means only implay straight forward linear changes to their dependencies. Oppositely, the entire simulation might be dramatically changed. The nonlinear interplay of all involved physics makes it very hard to identify the sources of change or their consequences.
Note, for example, the differences in the temperature phases of the standard simulation (Figure (9.9)), the standard simulation including feedback (Figure (9.17)) and the turbulence regulated simulation including feedback (Figure (10.17)). We have discussed the apparent differences between the first two in Section (9.6) and attributed the changes to the inclusion of feedback as this was essentially the only conceptual difference between both simulations. Now we observe the combined effects of a largely different star formation realization in combination with the feedback which is itself very different owing to the changes in the underlying stellar component. We will discuss this population in more detail shortly. Coming back to the thermal properties of the ISM, note that the turbulence regulated simulation completely lacks the very high temperature gas surrounding the central warm and hot accumulations of gas. In other words, although we still observe a well defined phase structure, the entire outer area of extraction volume presented in Figure (10.17) has approximately the same high temperature. The corresponding standard simulations show a clear trend towards higher temperature with distance to the galactic center. The combined effects of low efficiency star formation and the resulting feedback are the reasons for this behavior. Firstly, the slower transformation of gas also slows the infall of gas from the outer disk and therefore has a stabilizing effect as this simultaneously denotes a less efficient cooling. Less efficient cooling denotes less fragmentation and less infall of material towards the potential center.

More information is available from the study of the phase diagrams of the latter simulation presented in Figure (10.18). The first frame shows an identical start of the simulation in comparison to the standard case (cf. Figure (9.11)). In the subsequent evolution, we observe the broadening of gas density distribution function and reduction of high density material during the second half of the simulation. Furthermore, the disappearance of overpressured low temperature, large density peaks is in concordance with the above mentioned transformation of all overdense gas into particles.
Additionally, the plots reveal the fact that the simulated ISM has developed a fraction of gas that strongly deviates from the pressure balance of the stable phases. Interestingly, the phase

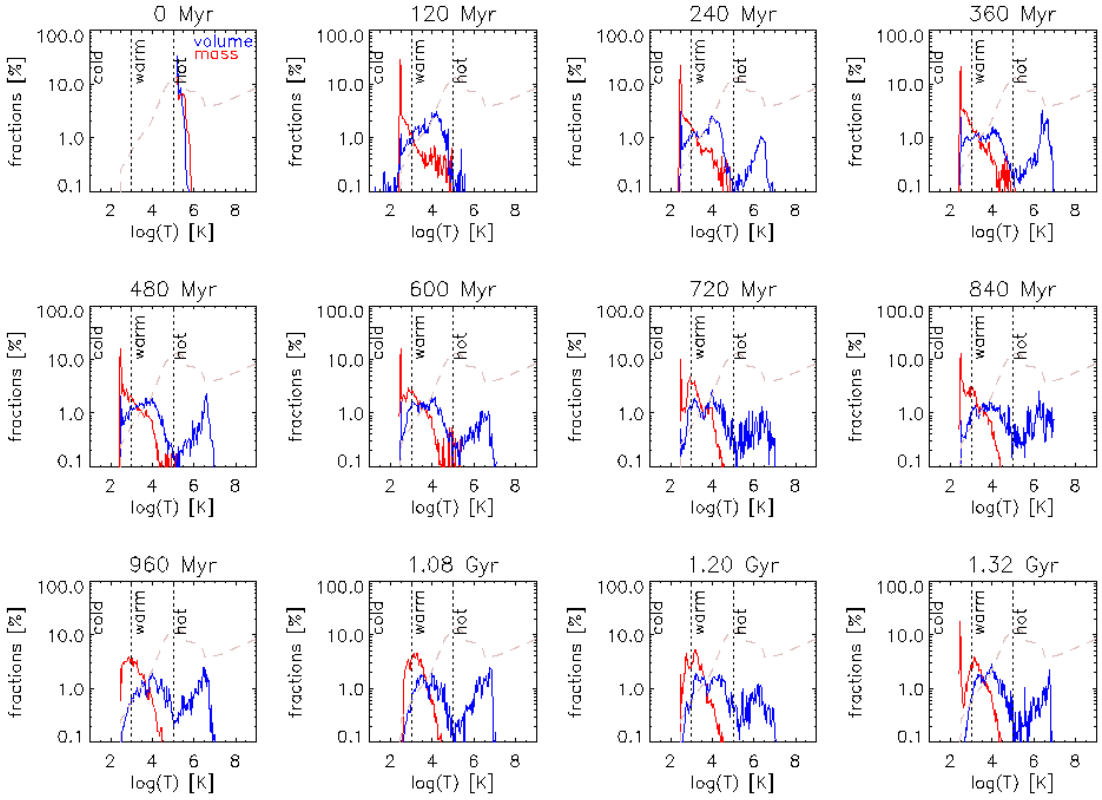

FIGURE 10.16. SF3F1sgsMa1: Temperature distribution in the simulated ISM. We depict again volume and mass fractions, this time in continuous plots covering the whole temperature regime. The dashed line depicts the employed cooling function, and vertical lines indicate our definition of phases in the ISM.

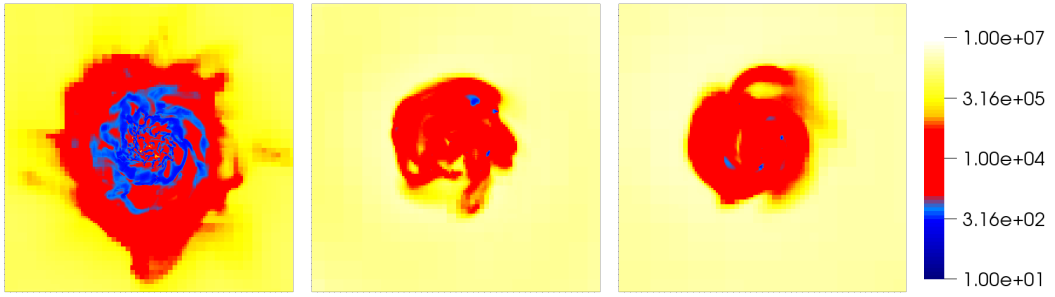

(a) 100 Myr (b) 700 Myr (c) 1000 Myr

FIGURE 10.17. SF3F1sgsMa1: Face-on projections of the gas temperature (K) in the galactic disk. Again the frames are 60 kpc across. We use a special color table to visualize the three components of the ISM.

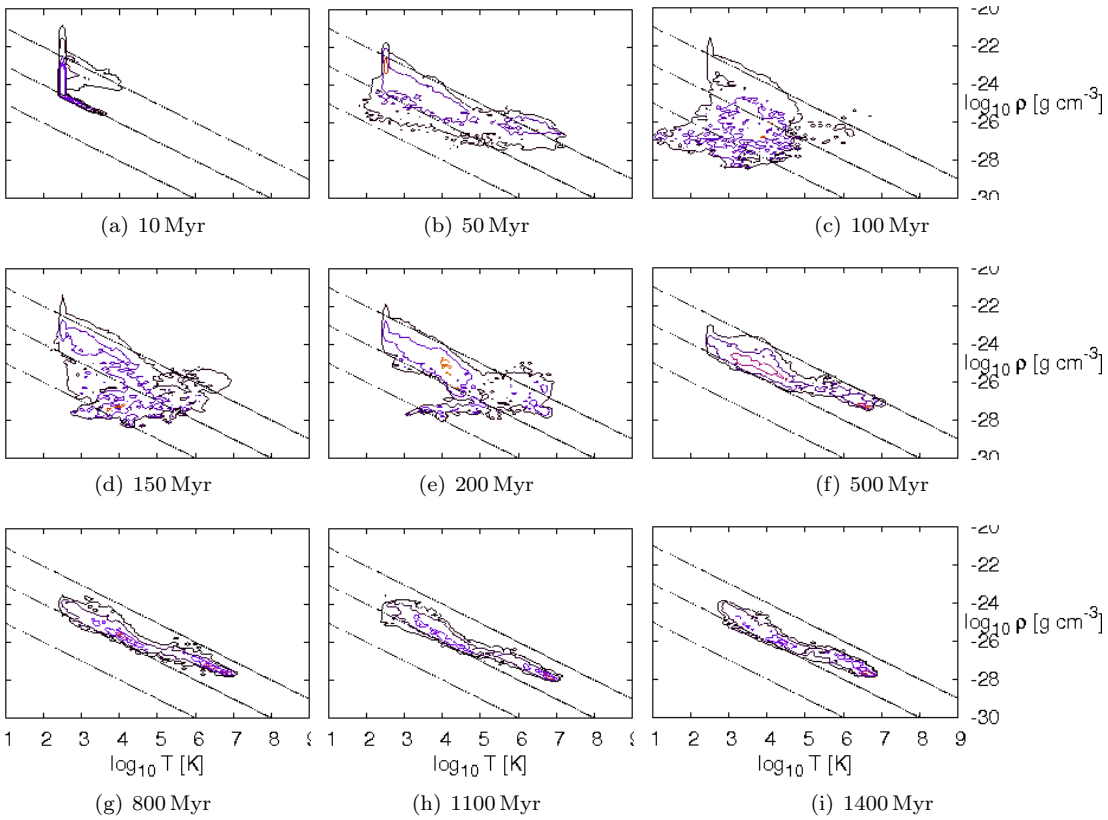

(a) 10 Myr (b) 50 Myr (c) 100 Myr

(d) 150 Myr (e) 200 Myr (f) 500 Myr

(g) 800 Myr (h) 1100 Myr (i) 1400 Myr

FIGURE 10.18. SF3F1sgsMa1: Contour diagrams of gas density versus temperature in the standard extraction volume of the galactic disk. Contour levels are 10^3, 10^4, $5 \cdot 10^4$, 10^5, $1.5 \cdot 10^5$ and refer to cell counts. The total number of cells in the extraction volume is $\sim 1 \cdot 10^7$. Straight lines depict isobars.

diagrams are not only broadened in density and towards higher temperatures, but likewise towards lower temperatures. Obviously the strong compression of gas and the correspondingly very efficient cooling leads to the fact that feedback indirectly also generates significant fractions of cold, star forming gas. This is particularly the case after a significant stellar component is formed during the first several tenth of Myr and up to approximately 500 Myr into the simulation when the star formation activity forming new massive stars has largely ceased.

Particle Distribution. The evolution of the particle distribution appears surprisingly similar to the standard case at first glance. However, we have to look carefully into the details of the projected particle density (Figure (10.19)) and keep in mind that particles represent dense cold gas as well as stars that form therein. The corresponding figure of the standard simulation is Figure (9.12).
The evolution again starts at the center of the galactic disk. Here, the first particles and consequently also the first stars form. Moreover, we observe that the initial particle distribution is spatially very confined and no particles are ejected or expelled from the galactic center at this time. This aspect confirms the earlier assumption that all early feedback originates from the

central region of the galaxy and can well generate the observed concentric density enhancements discussed in the beginning of this section.
A second conspicuous fact is that we can also observe a reduced amount of particles or likewise a particle distribution which is less extended as in the standard case simulation. This is particularly the case for the first three frames (a) to (c). On the one hand, the turbulence regulated star formation algorithm is known to have reduced efficiency, while on the other hand feedback acts to enhance density as well as to disperse dense star forming regions. A combination of both effects, most likely with temporal shift of the dominating part during the evolution affects the global evolution of the galaxy.

Another aspect of the particle component which needs to be discussed is its temporal evolution during the second part of the simulation. Here, the formation of new particles and stars is relatively low and we focus on the overall dynamics of the particle component. In the standard case with no feedback, we have seen how particles build up subsequently growing associations. Towards the end of the run the disk consisted of a small number of massive associations and a disk component. For the feedback case we expect this to be generally different and in fact observe more transient structures. Associations do not grow indefinitely but get dispersed after a certain time of evolution. Additionally, we observe the formation of a larger number of smaller associations most likely as a result of reduced star formation in combination with feedback spreads particle formation spatially as well as temporally.
As final remark, note the large cloud of particles appearing to the lower left of the particle distribution in Figure (10.19) (f). This is the dispersed remainder of a relatively large association of particles very similar to one of the outstanding white, high density occurrences apparent in all frames.

Star Formation. To gain a more quantitative picture we now study the star formation history of the turbulence regulated simulation. Figure (10.20) (a) shows the corresponding data. We observe the usual initial star formation burst followed by a prolonged period of high star formation activity. Around 500 Myr the star formation rate shows a short period of constant activity before the overall rate drops again. At the end of the simulation, star formation appears to stabilize at a relatively low rate. Although at 1.2 Gyr there is a significant break in this slow star formation evolution.
We have discussed how star formation algorithm and feedback influence the distribution of gas densities producing more gas at overdensities which becomes transformed into particles. After all, it seems surprising that the obviously increased star formation activity compared to the standard case (cf. Figure (9.13) (a)) does not produce a noticeably larger particle density in the previously presented projections. In fact, we saw the opposite, a smaller population of particles. However, at 500 Myr both simulations have similar particle components aside the different evolutionary histories. Moreover, during the further evolution, the turbulence regulated simulation including feedback significantly increases its particle component compared to the standard run. The explanation for these observations is the mass feedback which eventually recycles a total of 25 % of the particle mass back into the interstellar medium. Therefore, as long as the star formation rate is not larger than 25 % at any time, the overall particle density will be smaller than in the case without feedback. Moreover, the returned gas is available for the creation of new particles and this promotes the increased generation of particles and consequently stars at intermediate times. The turnover occurs roughly 200 Myr later as we have also seen in the previous discussion. Both density distribution functions temperature distribution as well as phase diagrams showed that the simulation does not have a noticeable amount of overdense cold gas

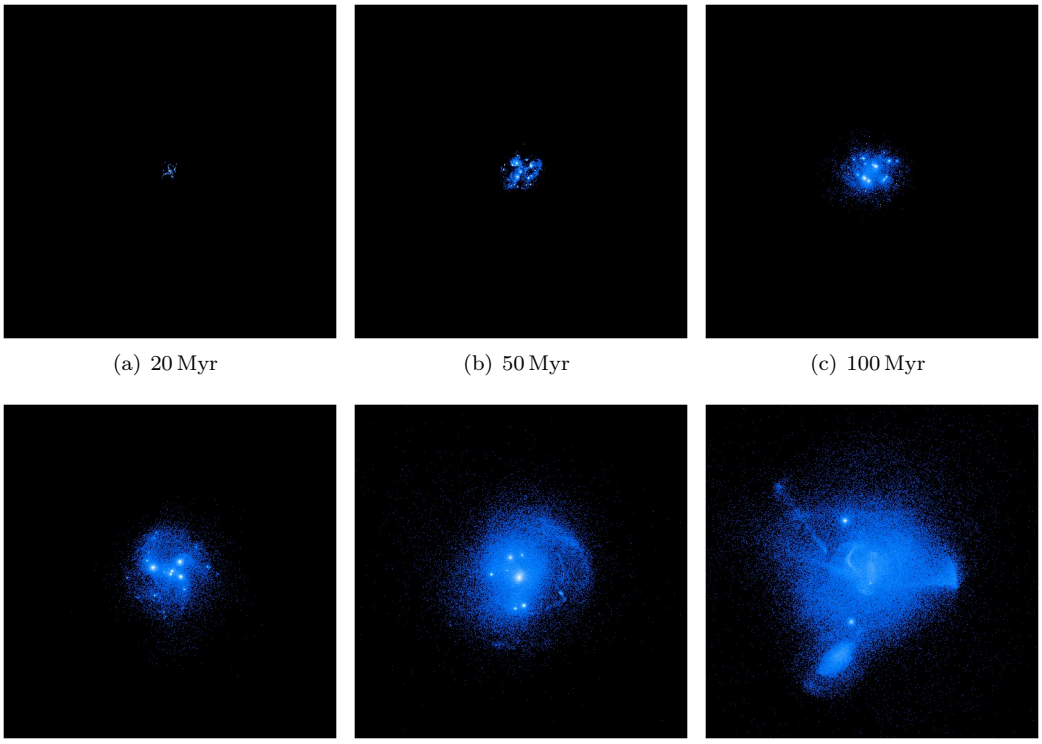

(a) 20 Myr (b) 50 Myr (c) 100 Myr

(d) 200 Myr (e) 500 Myr (f) 1000 Myr

FIGURE 10.19. SF3F1sgsMa1: Projected particle density. Note that we have stretched the scale of depicted values by one order of magnitude compared to earlier plots for better visualization. The maximum and minimum densities shown here are $10^{16}\,\mathrm{M}_\odot\,\mathrm{Mpc}^{-2}$ and $10^{10}\,\mathrm{M}_\odot\,\mathrm{Mpc}^{-2}$, respectively.

at this time. Most material has been transformed, while the remaining gas is rather smoothly distributed owing to the overall dynamics.

This behavior is reflected in the analysis of the dependence of star formation rate and gas surface density. Figure (10.20) (b) shows the analysis, although this time we have changed the data range to which we apply the fit to the first 750 Myr of the simulation. We again see that the simulation largely overrates the star formation rate by more than one order of magnitude. However, the combination of dynamical efficiency and feedback gives the correct slope for the first half of the simulation.
Contrarily, for the second half of the simulation the correlation is broken and depicts a much steeper slope. The data points show the behavior expected from the discussion of the star formation history. We observe a continuous decline of star formation rate until a minimum is reached at approximately 1.2 Gyr. Several hundred Myr before and after that instant of time the star formation efficiency corresponds to what is observed and described by the KS relation.

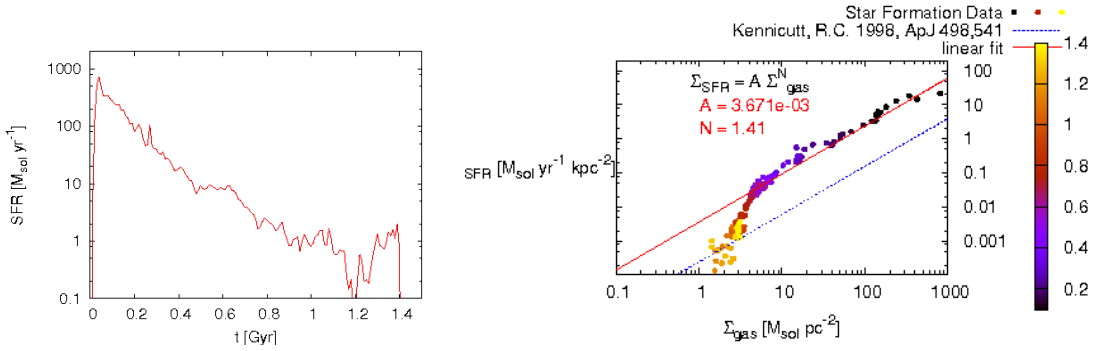

(a) Temporal evolution of the star formation rate.

(b) Global Schmidt-law.

FIGURE 10.20. SF3F1sgsMa1: Analysis of the star formation rate. The left frame depicts how the star formation rate changes over the course of a simulation, while the right frame shows the dependence of star formation rate on gas surface density. Note that we have cut the range to which we apply the fit to only include data of the first 750 Myr.

10.6. Thermal and Turbulent Pressure in the Galactic Disk

As we have seen in the previous discussion, our simulations are not yet able to reproduce the KS relation correctly. Nevertheless, we have seen how the implementation of the SGS model to realize the influence of turbulence has important consequences for the overall dynamics of the simulated disks. In our final analysis we investigate how the SGS model accounts for the effects of turbulent pressure and what the magnitude of this pressure component is compared to the thermal pressure.

Again, we focus on the inner, most actively star forming part of the galactic disk and perform the following analysis with the same extracted dataset as all previous studies. Figure (10.21) shows the comparison of thermal and turbulent pressure for two simulations with different star formation realizations, but the same limit on the turbulent Mach number. More precisely, we present the standard simulation (fixed efficiency) including the full SGS calculation but no coupling to the star formation algorithm (SF1F0e50sgsMa5) (cf. Section (10.3)) on the one hand and the turbulence regulated simulation with limited Mach number (SF3F0sgsMa5) (cf. Section (10.4)) on the other hand. Both simulations have $\mathscr{M}_{t,\mathrm{crit}} = 5$ and no feedback.

Figure (10.21) depicts a broad concordance of the pressure data of both simulations. Moreover, in the simulations with a relatively high limiting Mach number the turbulent pressure is significantly larger than the thermal pressure. This difference is approximately one order of magnitude throughout the entire simulation time.

The fact that we observe high initial values for both pressure components is once more owed to the initial conditions. Note that thermal pressure $p_{\mathrm{th}} = (\gamma - 1) \cdot \rho \cdot e_{gas}$ as well as turbulent pressure $p_{\mathrm{turb}} = 2/3 \cdot \rho \cdot e_t$ depend linearly on gas density which is most pronounced at the beginning of each simulation. Furthermore, the subsequent drop of pressure in the turbulence regulated case is a consequence of the rapid decline of gas density during this early simulation phase as a result of the much larger star formation activity of the simulation with respect to the displayed counterpart. As the simulations proceed, gas is continuously transformed into stars and this yields a corresponding decline in the pressure components. Towards the end of the runs,

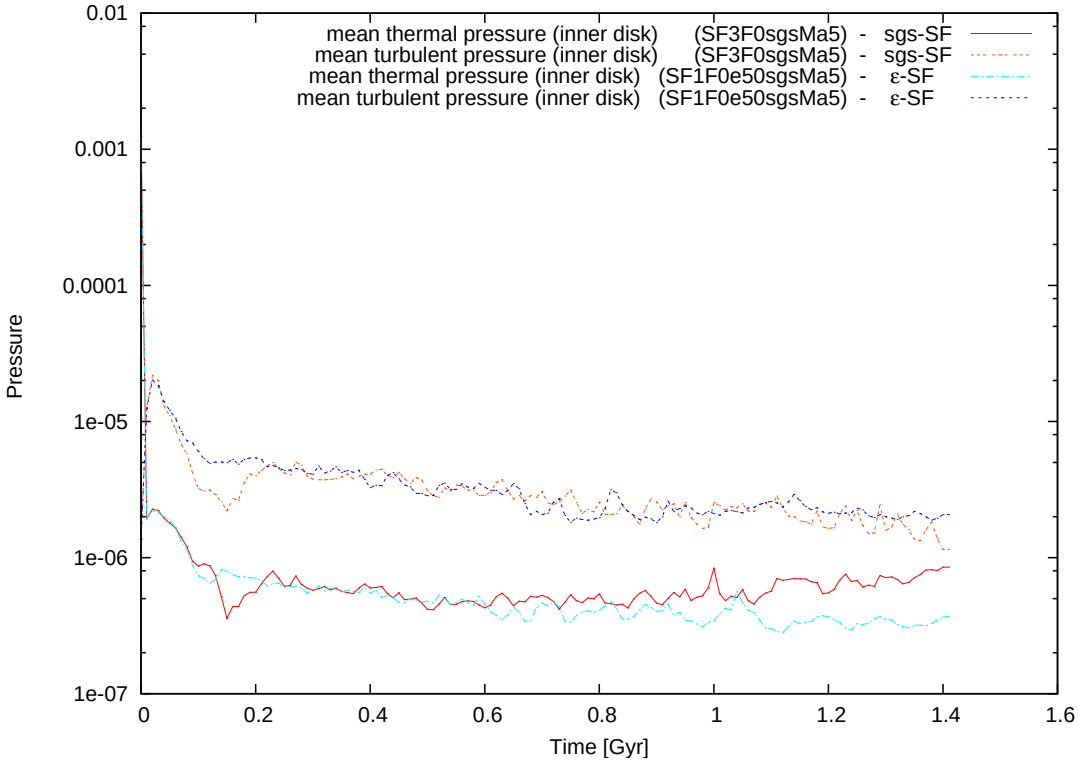

FIGURE 10.21. Comparison of thermal (lower graph) and turbulent (upper graph) pressure in two simulations. The labeling identifies the particular plots. All pressures are given in code units but can be scaled to cgs units via multiplication with $\mathbb{R}^2\mathbb{L}^2\mathbb{G}_0 \approx 6.35 \cdot 10^{-9}\mathrm{g/s^2cm}$.

the thermal pressure becomes influenced more strongly by the increase of gas temperature which can lead to slightly increased values. This is particularly the case for the turbulence regulated simulation, where an increasing mean temperature slightly raises the thermal pressure. The behavior of turbulent pressure remains rather constant. This is firstly a consequence of the only marginally changing disk gas density and secondly displays that also the global turbulent energy content of the inner disk remains rather constant.

In Figure (10.22) we compare the 'SGS-SF' turbulence regulated simulation described in the last paragraph to the previously presented simulation with $\mathscr{M}_{t,\mathrm{crit}} = 1$ (cf. Section (10.5)). We caution the reader to keep in mind the fact that the latter simulation includes feedback. However, the most important aspect of this comparison is the fact that the simulation with much lower limit on the turbulent Mach number has a strongly decreased turbulent pressure content. Not only is the turbulent pressure in this case smaller by more than one order of magnitude compared to the $\mathscr{M}_{t,\mathrm{crit}} = 5$ simulation but, moreover, the turbulent pressure is also almost one order of magnitude smaller than the thermal pressure. We see that the artificial reduction of the turbulent Mach number from $\mathscr{M}_{t,\mathrm{crit}} = 5$ to $\mathscr{M}_{t,\mathrm{crit}} = 1$ not only reduces the overall turbulent energy content of the galactic disk, but more importantly renders the turbulent contingent less significant than the thermal one. Henceforth, we can not expect turbulence to supply a significant pressure support to influence the gas dynamics of the galactic disk and eventually lead to a

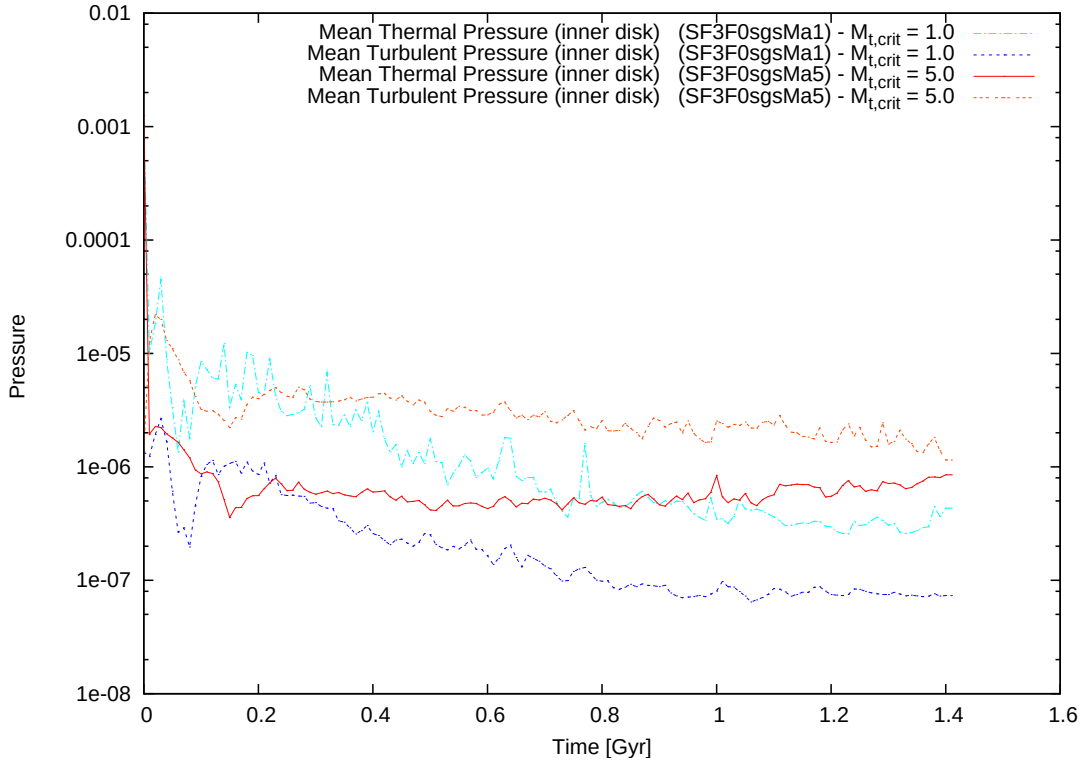

FIGURE 10.22. Comparison of mean thermal and turbulent pressure in two turbulence regulated simulations with different limits on the turbulent Mach number as displayed in the figure's labeling.

more realistic star formation rate in case of this too small Mach number limit.

As concluding remark we note that feedback results in fluctuations of the average gas temperature as discussed before and therefore leads to fluctuations in the thermal pressure function depicted in the figure above.

With Figure (10.22) as last visualization of simulation data we close the presentation of our numerical results. We will reflect the above disscussion, compare again to work by other authors and draw conclusion in the next Chapter (11).

CHAPTER 11

Conclusions and Prospects

In the previous Chapters (9) and (10), we have described our simulations and extensively discussed the particular results. Here we sum up and reflect the most important aspects, discuss achievements and shortcomings and finally point towards future applications of our work.

11.1. Simulation of Galactic Disk Systems

We have performed state of the art three-dimensional high-resolution simulations of an entire, although isolated, galactic disk system and studied the details of the overall evolution for 1.4 Gyr. Our simulations self-consistently include the fixed properties of a galactic dark matter halo. We start the full dynamical evolution of our simulations from relaxed stable initial conditions of the galactic gas disk configuration. Thermal properties of the interstellar medium are modelled via a classical approach to define a particular cooling function, and all simulations develop a good realization of a three-phase medium in approximate pressure equilibrium.
Furthermore, besides the global galactic properties and the realization of a realistic interstellar medium our simulations also include several of the most important physical processes to simulate galactic evolution on extended timescales. Namely, we not only include dark matter potential and cooling, but self-gravity and consequently the fragmentation of gas as well as subsequent star formation and feedback from type II supernovae.
Additionally, our work introduces and uses our new FEARLESS concept to combine semi-analytic modeling of physical processes with hydrodynamical simulations. We use a subgrid-scale model to capture turbulence effects below the numerical grid cutoff scale which not only directly influence the evolution of resolved hydrodynamical quantities but, moreover, allows us to directly implement the turbulence regulated star formation algorithm proposed by KM05.
To realize this approach we use adaptive mesh refinement to simulate the substructure of galactic disk systems down to the scale of molecular clouds ($\sim 30\,\mathrm{pc}$) and augment the simulation routines with a code to model the turbulent energy content on smaller, unresolved scales.
Moreover, we use the capabilities of Enzo to combine the grid based hydrodynamical simulation with an additional particle component to account for highly overdense material which becomes converted into dense, bound objects which eventually transform into stars. Finally, we model the coupling of this particle component to the interstellar medium via feedback mechanisms which not only recycle gas but also energy and momentum back into the surrounding galactic medium.

11.2. Shortcomings, Achievements and Future Projects

Our simulations present a continuous development of previous work but still leave several aspects open to significant advancement.
To begin with, we comment on the fact that several authors claim to observe spiral structure in their simulations. However, most often only snapshots of the overall evolution are presented and also these snapshots sometimes suggest some kind of spiral structure (cf. e. g. our Figure (9.5)(e)) a real spiral pattern as defined in the Hubble classification is neither investigated nor present. The reasons are that both kinds of global spiral structure, namely flocculent and grand design

spirals, are dependent on various global properties not realized in the corresponding simulations. Grand design spirals result from galactic interactions but most simulations, as our own, are dealing with isolated galactic systems. Moreover, spiral structure as described in density wave theory requires a dynamical interaction of dark matter halo, galactic gas and stellar component. Again, using a fixed dark matter potential as in our work excludes the simulation of such interactions and the corresponding structural influences on the galactic disk. Summarizing, we neither expect nor claim that our simulations show any real spiral structure. However, the realization of a dynamical dark matter halo or the realization of a dynamical galactic interaction, either via direct simulation or via semi-analytic modeling of the corresponding gravitational effects, has no general objections and are certainly interesting questions with respect to large scale galactic simulations.

However, our focus has been towards the smaller scale or internal properties of a galactic disk system. We have already discussed the problem of defining initial conditions in Section (9.1). We have seen that starting off with an completely gaseous disk is not only difficult to handle owing to the fact that such a system is by definition highly unstable, but also difficult to interpret as the initial star formation burst has significant influence on the overall evolution of the galactic disk. Although we have improved the generic situation significantly in our work as we circumvented the initial, radial compression shock wave which largely generated stars in earlier work (e. g. Tasker and Bryan [2006, 2008]), the overall initial conditions remain very artificial. Oppositely, it also appears unsuitable to simulate the complete formation and buildup process of a galactic object owing to its immense complexity. A reasonable approach would be to start from a set of more realistic initial conditions as realized by Li et al. [2005]. The latter authors are able to generate Milky Way like initial conditions with a dark matter halo very similar to our analytic profile and a galactic disk with variable fractions of baryonic mass in the gas disk and, correspondingly, the stellar component. As mentioned earlier, the tool to generate the latter initial conditions has already been adapted and tested for simulations with Enzo. Therefore, work along this path can start directly and investigate the benefits of our turbulence subgrid-scale model and star formation realizations.

Another aspect which has been slightly improved in our work but still bears large conceptual potential for advancements is the realization of heating and cooling in the interstellar medium. We have given extended details on our implementation of cooling in Section (5.3) and argued for our assumptions and choices. Furthermore, we have seen how this realization yields ISM properties in good concordance with observations. Nevertheless, a detailed treatment of chemical processes, the inclusion of additional radiation sources such as quasars and the implications of interstellar dust are important aspects all in their own right.
Gnedin et al. [2008] describe a phenomenological model for the formation of molecular hydrogen, applicable to simulations which are able to resolve molecular cloud scales such as our own. Their model includes the formation of H_2 on dust grains and accounts for shielding from photodissociation effects caused by the interstellar radiation field. The authors describe several recipes for star formation based on the calculated density of molecular hydrogen. In our simulations we follow Krumholz and McKee [2005] and assume that gas that is dense enough to exceed the threshold for star formation is entirely molecular. Here, a more detailed treatment in the spirit of Gnedin et al. can certainly improve our simulations. Particularly, the dependence of the molecular fraction on the metallicity of the ISM is an important issue. Especially, when the metallicity changes during the galactic evolution. However, an additional variable amount of molecular gas can also be interpreted as additional fraction of the overall gas content that is transformed into stars. Hence, including the treatment of molecular hydrogen can also be realized in a first order

approximation, as an additional efficiency parameter. A more physical treatment on the other hand requires again model assumptions as well as tuning of parameters to reach the reproduction of observational results.
The question one has to ask is concerning necessary effort and potential improvement. Heating and energy input from quasars are relatively simple to introduce in our framework and partly already existent in Enzo. However, the quality of this first order implementation is likely to yield only marginal effects, while a more complete realization poses significant difficulties owing to the additional level of complexity.
ISM chemistry itself is a completely different topic. Simple models can be used to add additional details to simulations. A holistic approach systematically analyzing and implementing the entire, highly complex problem will ultimately yield better contributions to galaxy scale simulations.

The transformation of dense parcels of gas into particles is our method of choice to account for highly overdense regions in the galactic disk. Other authors chose to employ higher minimum temperatures or, as in recent work by Agertz et al. [2008], use a polytropic equation of state. The latter authors succeed to maintain global stability of the numerical scheme and also prevent artificial fragmentation in a general way, as they tune their parameters to prevent gas from cooling below a certain temperature limit at certain maximum resolution. However, this also denies them to study the plethora of structure of the ISM, in particular the cold neutral medium as well as the molecular gas therein. Consequently, a phenomenological star formation parameterization is used, based on the KS relation. Oppositely, our realization of cooling and particle creation can possibly lead to some artificial fragmentation while capturing the structure of the ISM in much more detail. A possible solution to this problem would be increased numerical resolution as computing power reaches the next level. Prior to this, also a more sophisticated control of the adaptive mesh refinement can yield higher resolution in overdense regions while only increasing the computational demands to a still feasible level.
Another aspect of the stellar component certainly worth a close reinvestigation is the implemented feedback, modeled to mimic type II supernovae explosions. We did neither study the details of variations in the feedback governing parameters nor did we study particular feedback events and their influence on the overall galaxy scale simulation. However, feedback has shown to be a very important ingredient to a complete galactic simulation and particularly essential for the life-cycle of matter as well as the thermal properties of the ISM. Therefore, feedback appears as promising candidate for further interesting and beneficial studies, with respect to a better understanding of galactic disk systems.

After all, the turbulence regulated star formation algorithm which ultimately determines the star formation rate as a result of the turbulent subgrid-scale properties has proven a powerful alternative to previously employed star formation recipes which seem to largely overestimate the star formation efficiency in simulations of galactic scale.
However, the conceptual and numerical realization of the subgrid-scale model suffers from strong limitations as we had to artificially reduce the generation of turbulent energy by only allowing for certain maximum values of turbulent Mach number. The eventual reduction of this turbulent Mach number limit to the transsonic regime and the corresponding exclusion of supersonic subgrid-scale turbulence effects in the feedback case greatly impacted on the influence and quality of the SGS calculations. Unfortunately, the artificial limit draws off the predictive power as well as impact on the simulations of the otherwise quite promising subgrid model approach.
Consequently, a next development step of the SGS model including the realization of even slightly higher turbulent Mach numbers of the order of one magnitude will enable the FEARLESS approach to turbulence regulated star formation to regain its conceptual power. The possible

simulation of even higher turbulent Mach numbers will ultimately be a highly interesting task and potentially very important towards a deeper understanding of star formation, turbulence, the ISM and eventually the global evolution of entire galactic systems.

Finally, we conclude this reflection of the presented work with noting that also generally neglected pieces like radiative transfer and magnetic fields are important parts to the complete picture of galaxy scale simulations.

11.3. Conclusions and Essence

We summarize our main conclusions here:

- Initial conditions with all galactic baryonic mass in the gas disk represent a rather artificial setup. Imprints of this choice of initial conditions can be manifest throughout the simulations. Therefore, a more realistic initial configuration is generally preferable.

- Gravitational contraction and turbulent fragmentation initialize rapid densification of galactic gas, starting at the disk center. While the exact fragmentation processes in a galactic disk system are largely dependent on the particular simulation properties (e. g. star formation, feedback, ...), the global evolution leads to a central concentration of the remaining gas disk.

- The realization of gas cooling as parameterized with our cooling function naturally produces an interstellar medium with three distinct gas phases which are in approximate pressure equilibrium. The influence of star formation and feedback lead to significant deviations from this behavior and generate gas off equilibrium conditions.

- The particle and stellar component in our simulations follow the gravitational fragmentation and grow from the inner galactic disk outwards. Feedback acts to disperse large associations of particles and leads to spatially enhanced stellar component.

- We observe a well defined functional dependence of gas surface density and star formation rate in all our simulations which can well be described as power law dependence. The corresponding power law indices as well as the normalization generally deviate from the observed KS relation in our simulations. A systematic trend could not be identified, however, feedback in combination with the turbulence regulated star formation algorithm show the best agreement with observations. Nevertheless, the normalization of the star formation rate is still an order of magnitude too large. However, this overproduction of stars is not surprising as we could not account for supersonic subgrid-scale turbulence in the corresponding simulation. Additionally, we observe a break in the simulated KS relation, indicating largely reduced star formation activity during late simulation times when gas surface densities are globally reduced.

- Recent work indicates that star formation efficiencies are as low as only a few percent considering the gas of molecular clouds eventually turned into stars. Our implementation of the KM05 star formation algorithm as turbulence regulated alternative to previous fixed efficiency realizations confirms the results of low star formation efficiencies in turbulent molecular clouds.

- The control of the subgrid-scale model and the yet necessary artificial limitation of the production of turbulent energy in simulations of full galaxy scale complexity also limits the SGS model capabilities during the calculation of the correct star formation rates. New SGS algorithm development steps are likely to quickly overcome this problem.

- The combination of semi-analytic modeling of turbulence effects below the resolved grid-scale with hydrodynamical simulations, as realized in our FEARLESS approach, is a powerful technique to study highly complex entities with important physics on all scales.

Summary of Results

Part (III) of this thesis is devoted to the results of our numerical studies. The first set of presented simulations represents the state of the art large scale galactic simulations with a parametric recipe for star formation. We started the evaluation of simulations with a detailed description of how and why we define our particular initial conditions. From this starting point, we systematically discussed the physical properties of the simulated galactic disk systems. We have begun with the description of the gas disk and its thermodynamical evolution, followed by a detailed discussion of the star formation process. We have ended the description of this kind of simulations with an investigation of feedback effects from the evolved stellar component as well as a discussion of the importance and choice of different simulation parameters.
Furthermore, we have presented a second set of simulations motivated by and finally including the star formation recipe developed by KM05. Here, the presentation started with a general assessment of the possible simulation results of a star formation realization using the KM05 algorithm and a discussion of corresponding simulations. Following these proof of principle simulations we finally presented our simulations of galactic disks with turbulence regulated star formation in several variations. Beginning with a study of the implications of the subgrid-scale model to capture unresolved turbulence we subsequently presented simulations with full turbulent regulated star formation and eventually the inclusion of feedback and discussed the various implications and results of these highly complex simulations.
Concluding this work, we have summarized our findings and reflected the performed simulations as well as the discussed results. Additionally, we have pointed towards some future applications and identified most promising projects continuing the work presented in this thesis. Finally, we have condensed our most significant findings into several bullet points.

Part IV

Appendices

APPENDIX A

Cooling via Bremsstrahlung

To estimate the length scale of an early galactic system which can cool efficiently via thermal Bremsstrahlung, we use the integrated power density of thermal Bremsstrahlung

$$P_{\rm Brems} \propto (n_e r_e^3)^2 \left(\frac{k_b T}{m_e c^2}\right)^{1/2} \frac{m_e c^3}{r_e^4}\alpha = \tag{A.1}$$

$$= n_e^2 e^6 \frac{\sqrt{k_b T}}{m_e^{3/2}\hbar c^3}, \tag{A.2}$$

where n_e is the number density of electrons, r_e is the classical radius of electron, m_e is its mass and c is the speed of light. We have used $r_e = e^2/m_e c^2$ and $\alpha = e^2/\hbar c$. This yields the cooling time as

$$t_{\rm cool} \propto \frac{\sqrt{k_b T}}{n_e e^6} m_e^{3/2}\hbar c^3. \tag{A.3}$$

For the collapse or free–fall time we use $M \propto n_e m_h R^3$ and write

$$t_{\rm grav} \propto \left(\frac{GM}{R^3}\right)^{-1/2} = \tag{A.4}$$

$$\propto \left(\frac{G n_e m_h R^3}{R^3}\right)^{-1/2} = (G n_e m_h)^{-1/2}\,. \tag{A.5}$$

Equating for $t_{\rm cool} \approx t_{\rm grav}$ we get

$$\frac{1}{\sqrt{G n_e m_h}} \approx \frac{\sqrt{k_b T} m_e^{3/2}\hbar c^3}{n_e e^6} \tag{A.6}$$

$$\frac{1}{\sqrt{G n_e m_h}} \approx R\frac{\sqrt{G n_e m_h^2} m_e^{3/2}\hbar c^3}{n_e e^6} \tag{A.7}$$

$$R \approx \frac{e^6}{G m_h^{3/2} m_e^{3/2}\hbar c^3} \tag{A.8}$$

This can be rewritten as

$$R \approx \frac{\alpha^3}{\alpha_G}\left(\frac{m_p}{m_e}\right)^{1/2}\left(\frac{\lambda_e}{2\pi}\right), \tag{A.9}$$

where we have used the constant for gravitational coupling $\alpha_G = G m_p^2/\hbar c$ and the Compton wavelength $\lambda_e = h/m_e c$.

Equating this, including all coefficients, yields the typical length scale of an efficiently cooling system, roughly 75 kpc.

APPENDIX B

Derivation of the Virial Theorem

Stahler and Palla [2005] show a short but comprehensive derivation of the virial theorem in their Appendix D. For completeness, we copy from the latter authors and show their derivation here. At some points we have made amendments or additional comments.

The derivation starts with the equation of motion for an inviscid fluid including terms of gravitational acceleration and magnetic effects.

$$\rho \frac{D\boldsymbol{v}}{Dt} = -\boldsymbol{\nabla} P - \rho \boldsymbol{\nabla} \Phi_g + \frac{1}{c} \boldsymbol{j} \times \boldsymbol{B} \tag{B.1}$$

Equation (B.1) is written using the convective or Euler time derivative of the fluid velocity $\boldsymbol{v}$.

$$\frac{D\boldsymbol{v}}{Dt} = \left(\frac{\partial \boldsymbol{v}}{\partial t} \right)_x + (\boldsymbol{v}\boldsymbol{\nabla})\boldsymbol{v} \tag{B.2}$$

To tackle the last term in Equation (B.1), the magnetic force term, Ampère's law is used.

$$\boldsymbol{\nabla} \times \boldsymbol{B} = \frac{4\pi}{c} \boldsymbol{j} + \underbrace{\frac{1}{c} \left(\frac{\partial \boldsymbol{E}}{\partial t} \right)_x}_{\text{ignored}} \tag{B.3}$$

Here, the displacement current of the electric field $\boldsymbol{E}$ will be ignored for the further derivation as changes in the electric field are expected to be relatively slow.

$$\boldsymbol{\nabla} \times \boldsymbol{B} = \frac{4\pi}{c} \boldsymbol{j} \tag{B.4}$$

$$\frac{1}{4\pi} (\boldsymbol{\nabla} \times \boldsymbol{B}) = \frac{1}{c} \boldsymbol{j} \tag{B.5}$$

$$\begin{aligned} \frac{1}{c} \boldsymbol{j} \times \boldsymbol{B} &= \frac{1}{4\pi} (\boldsymbol{\nabla} \times \boldsymbol{B}) \times \boldsymbol{B} \\ &= -\boldsymbol{B} \times \frac{1}{4\pi} (\boldsymbol{\nabla} \times \boldsymbol{B}) \\ &= \boldsymbol{\nabla} (-\boldsymbol{B} \frac{1}{4\pi} \boldsymbol{B}) - (-\boldsymbol{B}\boldsymbol{\nabla}) \frac{1}{4\pi} \boldsymbol{B} \\ &= -\frac{1}{8\pi} \boldsymbol{\nabla} |\boldsymbol{B}|^2 + \frac{1}{4\pi} (\boldsymbol{B}\boldsymbol{\nabla}) \boldsymbol{B} \end{aligned} \tag{B.6}$$

A short transformation of vector identities yields Equation (B.6) which can be used to recast the equation of motion.

$$\underbrace{\rho \frac{D\boldsymbol{v}}{Dt}}_{❶} = \underbrace{-\boldsymbol{\nabla} P}_{❷} \underbrace{- \rho \boldsymbol{\nabla} \Phi_g}_{❸} + \underbrace{\frac{1}{4\pi} (\boldsymbol{B}\boldsymbol{\nabla}) \boldsymbol{B}}_{❹} \underbrace{- \frac{1}{8\pi} \boldsymbol{\nabla} |\boldsymbol{B}|^2}_{❺} \tag{B.7}$$

For the following calculation the scalar product of Equation (B.7) and $\boldsymbol{r}$ is taken and integrated over volume. Furthermore, the authors use carthesian coordinates and adopt the short form of

writing partial derivatives. They also use the convention for summation of repeated indices by Einstein. The identities $\partial_i x_i = 3$ and $\partial_i X_j = \delta_{ij}$ are employed.

Subsequently, we will work our way through the labeled terms of Equation (B.7).
First, Equation (B.2) is used to rewrite the first term ❶ as

$$\int \rho x_i \left(\frac{\partial v_i}{\partial t}\right)_x d^3\boldsymbol{x} + \int \rho x_i v_j \partial_j v_i d^3\boldsymbol{x}. \tag{B.8}$$

The first integrand is rewritten

$$\rho x_i \left(\frac{\partial v_i}{\partial t}\right)_x = \rho \left[\frac{\partial (x_i v_i)}{\partial t}\right]_x, \tag{B.9}$$

and the second term yields

$$\begin{aligned} \rho x_i v_j \partial_j v_i &= \rho v_j \partial_j (x_i v_i) - \rho v_j v_i \partial_j x_i \\ &= \partial_j (\rho v_j x_i v_i) - (x_i v_i)\partial_j (\rho v_j) - \rho v_j v_i \delta_{ij} \\ &= \partial_j (\rho v_j x_i v_i) + \left(\frac{\partial \rho}{\partial t}\right)_x (x_i v_i) - (\rho v_i v_i), \end{aligned} \tag{B.10}$$

where the equation of mass continuity was used to replace $\partial_j(\rho v_j) \equiv \boldsymbol{\nabla} \cdot (\rho \boldsymbol{v})$.
The first term in Equation (B.10) is the divergence of a vector and will vanish after volume integration if no external mass flux is present. Hence, reuniting Equations (B.9) and (B.10) gives

$$\int \rho x_i \left(\frac{\partial v_i}{\partial t}\right)_x d^3\boldsymbol{x} + \int \rho x_i v_j \partial_j v_i d^3\boldsymbol{x} = \frac{\partial}{\partial t} \int \rho x_i v_i d^3\boldsymbol{x} - 2\mathfrak{T}, \tag{B.11}$$

where the kinetic energy

$$\mathfrak{T} \equiv \frac{1}{2} \int \rho |\boldsymbol{v}|^2 d^3\boldsymbol{x} \tag{B.12}$$

has been replaced.
The remaining integrand is

$$\begin{aligned} \rho x_i v_i &= \frac{1}{2} \rho v_i \partial_i (x_j x_j) \\ &= \frac{1}{2} \partial_i (\rho v_i x_j x_j) - \frac{1}{2} x_j x_j \partial_i (\rho v_i) \\ &= \frac{1}{2} \partial_i (\rho v_i x_j x_j) + \frac{1}{2} \left(\frac{\partial \rho}{\partial t}\right)_x x_j x_j. \end{aligned} \tag{B.13}$$

Invoking again the absence of external mass flux, this yields

$$\int \rho x_i v_i d^3\boldsymbol{x} = \frac{1}{2} \frac{\partial I}{\partial t}, \tag{B.14}$$

where the scalar I was introduced to represent the moment of inertia

$$I \equiv \int \rho x_j x_j d^3\boldsymbol{x}. \tag{B.15}$$

Finally, using Equation (B.14) in (B.11) gives

$$\int \rho x_i \left(\frac{\partial v_i}{\partial t}\right)_x d^3\boldsymbol{x} + \int \rho x_i v_j \partial_j v_i d^3\boldsymbol{x} = \frac{1}{2} \frac{\partial^2 I}{\partial t^2} - 2\mathfrak{T} \tag{B.16}$$

Next are the terms on the right hand side of Equation (B.7).
Term ❷ can be rewritten

$$-\int x_i \partial_i P d^3\boldsymbol{x} = -\int \partial_i(x_i P) d^3\boldsymbol{x} + \int (\partial_i x_i) P d^3\boldsymbol{x} = -\int P\boldsymbol{r}\cdot\boldsymbol{n} d^2\boldsymbol{x} + 3\int P d^3\boldsymbol{x}, \tag{B.17}$$

where $\boldsymbol{n}$ is the normal vector of the surface of integration, pointing outwards.
For nonrelativistic fluid, the internal pressure is two-thirds the energy density in thermal motion, hence it follows

$$-\int x_i \partial_i P d^3\boldsymbol{x} = -\int P\boldsymbol{r}\cdot\boldsymbol{n} d^2\boldsymbol{x} + 2\mathcal{U}, \tag{B.18}$$

where the thermal energy was defined as

$$\mathcal{U} \equiv \frac{3}{2}\int n k_b T d^3\boldsymbol{x} = \frac{3}{2}\int P d^3\boldsymbol{x}. \tag{B.19}$$

To tackle the gravity Term ❸, first, the potential is rewritten as integral over all mass elements in the volume:

$$\Phi_g(\boldsymbol{r}) = -G\int \frac{\rho(\boldsymbol{r}')}{|\boldsymbol{r}-\boldsymbol{r}'|} d^3\boldsymbol{x} \tag{B.20}$$

This yields

$$-\int \rho x_i \partial_i \Phi_g d^3\boldsymbol{x} = -G\iint \rho(\boldsymbol{r})\rho(\boldsymbol{r}')\frac{x_i(x_i - x_i')}{|\boldsymbol{r}-\boldsymbol{r}'|^3} d^3\boldsymbol{x}' d^3\boldsymbol{x}, \tag{B.21}$$

where the following identity was used

$$\partial_i \frac{1}{|\boldsymbol{r}-\boldsymbol{r}'|} = -\frac{(x_i - x_i')}{|\boldsymbol{r}-\boldsymbol{r}'|^3}. \tag{B.22}$$

Equation (B.22) has the dummy variables $\boldsymbol{r}$ and $\boldsymbol{r}'$ inside the double integral. After changing the order of integration, the resulting expression can be added to the original integral, doubling its value. It follows that

$$-\int \rho x_i \partial_i \Phi_g d^3\boldsymbol{x} = -\frac{1}{2}G\iint \rho(\boldsymbol{r})\rho(\boldsymbol{r}')\frac{|\boldsymbol{r}-\boldsymbol{r}'|^2}{|\boldsymbol{r}-\boldsymbol{r}'|^3} d^3\boldsymbol{x}' d^3\boldsymbol{x} = \frac{1}{2}\int \rho(\boldsymbol{r})\Phi_g(\boldsymbol{r}) d^3\boldsymbol{x} = \mathcal{W}, \tag{B.23}$$

where $\mathcal{W}$ is the gravitational potential energy

$$\mathcal{W} \equiv \frac{1}{2}\int \rho \Phi_g d^3\boldsymbol{x}. \tag{B.24}$$

Yet, there are only the magnetic terms left. Integration of term ❹ leads to

$$\frac{1}{4\pi}\int x_i B_j \partial_j B_i d^3\boldsymbol{x} = \frac{1}{4\pi}\int \partial_j(x_i B_j B_i) d^3\boldsymbol{x} - \frac{1}{4\pi}\int B_i \partial_j(x_i B_j) d^3\boldsymbol{x} = \frac{1}{4\pi}\int \partial_j(x_i B_j B_i) d^3\boldsymbol{x} - \frac{1}{4\pi}\int B_i B_i d^3\boldsymbol{x} = \frac{1}{4\pi}\int (\boldsymbol{r}\cdot\boldsymbol{B})\boldsymbol{B}\cdot\boldsymbol{n} d^2\boldsymbol{x} - 2\mathcal{M}, \tag{B.25}$$

where $\mathcal{M}$ is the magnetic energy

$$\mathcal{M} \equiv \frac{1}{8\pi}\int |\boldsymbol{B}|^2 d^3\boldsymbol{x}. \tag{B.26}$$

Maxwell's equation $\partial_j B_j \equiv \boldsymbol{\nabla}\cdot\boldsymbol{B} = 0$ was used to eliminate one integral in Equation (B.25). Finally, the last term ❺ can be integrated and gives

$$\begin{aligned} -\frac{1}{8\pi}\int x_i\partial_i(B_jB_i)d^3\boldsymbol{x} &= -\frac{1}{8\pi}\int \partial_i(x_iB_jB_j)d^3\boldsymbol{x} \\ &\quad +\frac{1}{8\pi}\int(\partial_i x_i)B_jB_jd^3\boldsymbol{x} \\ &= -\frac{1}{8\pi}\int B^2\boldsymbol{r}\cdot\boldsymbol{n}d^2\boldsymbol{x} + 3\mathcal{M}. \end{aligned} \tag{B.27}$$

In conclusion, we are left with the following results from Equations (B.16), (B.18), (B.23), (B.25) and (B.27).

$$\underbrace{\int \rho x_i\left(\frac{\partial v_i}{\partial t}\right)_x d^3\boldsymbol{x} + \int \rho x_i v_j\partial_j v_i d^3\boldsymbol{x}}_{❶} = \frac{1}{2}\frac{\partial^2 I}{\partial t^2} - 2\mathcal{T} \tag{B.28}$$

$$\underbrace{-\int x_i\partial_i P d^3\boldsymbol{x}}_{❷} = -\int P\boldsymbol{r}\cdot\boldsymbol{n}d^2\boldsymbol{x} + 2\mathcal{U} \tag{B.29}$$

$$\underbrace{-\int \rho x_i\partial_i\Phi_g d^3\boldsymbol{x}}_{❸} = \mathcal{W} \tag{B.30}$$

$$\underbrace{\frac{1}{4\pi}\int x_iB_j\partial_jB_i d^3\boldsymbol{x}}_{❹} = \frac{1}{4\pi}\int(\boldsymbol{r}\cdot\boldsymbol{B})\boldsymbol{B}\cdot\boldsymbol{n}d^2\boldsymbol{x} - 2\mathcal{M} \tag{B.31}$$

$$\underbrace{-\frac{1}{8\pi}\int x_i\partial_i(B_jB_i)d^3\boldsymbol{x}}_{❺} = -\frac{1}{8\pi}\int B^2\boldsymbol{r}\cdot\boldsymbol{n}d^2\boldsymbol{x} + 3\mathcal{M} \tag{B.32}$$

Evaluating these lines we easily see the overall result:

$$\begin{aligned} \frac{1}{2}\frac{\partial^2 I}{\partial t^2} &= 2\mathcal{T} + 2\mathcal{U} + \mathcal{W} + \mathcal{M} \\ &\quad -\int\left(P + \frac{B^2}{8\pi}\right)\boldsymbol{r}\cdot\boldsymbol{n}d^2\boldsymbol{x} + \frac{1}{4\pi}\int(\boldsymbol{r}\cdot\boldsymbol{B})\boldsymbol{B}\cdot\boldsymbol{n}d^2\boldsymbol{x}. \end{aligned} \tag{B.33}$$

The first line of Equation (B.33) is the simplified version of the virial theorem most often quoted in astrophysical applications. The reason for this is, as mentioned by Stahler and Palla that it is possible to ignore the surface integrals for the sake of simplicity. This approximation is only valid for strongly self-gravitating entities such as giant molecular cloud complexes. Therefore, throughout this work, we will only be engaged with the short form of the virial theorem:

$$\frac{1}{2}\frac{\partial^2 I}{\partial t^2} = 2\mathcal{T} + 2\mathcal{U} + \mathcal{W} + \mathcal{M} \tag{B.34}$$

APPENDIX C

Scaling Relations

Here some important technical details on the scaling from real to simulated quantities will be described.

The Enzo code was historically developed as a cosmological simulation framework and later adopted to simulate scale free problems like pure hydrodynamical turbulence. The code is written in a fashion which assumes that all computational quantities are numbers of the order of unity. In other words, rather than using cgs units and a density value of e. g. $1.0 \cdot 10^{-23}\,\mathrm{g/cm^3}$ the code is most stable when computations are performed with numbers close to one.
For the cosmological case, the code adheres a set of routines to convert the user set parameters into values of the order of magnitude of one, while for the pure hydro case units are generally meaningless and usually all quantities are scaled during the postprocessing and therefore the computational scale can just be set arbitrarily.
However, as soon as additional physics like self-gravity or cooling enter the hydrodynamical computation the freedom of scales is lost and quantities interdepend on basis of their physical units. To realize meaningful computations with Enzo we follow Robinson et al. [2004] and use scaling relations below to scale physical problem parameters to numbers expedient for Enzo calculations.

$$\rho_{enzo} = \rho_{\mathrm{cgs}} \;/\; \mathbb{R} \tag{C.1}$$

$$l_{enzo} = l_{\mathrm{cgs}} \;/\; \mathbb{L} \tag{C.2}$$

$$t_{enzo} = t_{\mathrm{cgs}} \;/\; \sqrt{\frac{\mathbb{L}}{\mathbb{G}}} \tag{C.3}$$

$$G_{enzo} = G_{\mathrm{cgs}} \;/\; \mathbb{G}_0 \tag{C.4}$$

$$e_{enzo} = e_{\mathrm{cgs}} \;/\; (\mathbb{L} * \mathbb{G}) \tag{C.5}$$

$$v_{enzo} = v_{\mathrm{cgs}} \;/\; \sqrt{\mathbb{L} * \mathbb{G}} \tag{C.6}$$

$$g_{enzo} = g_{\mathrm{cgs}} / \mathbb{G} \tag{C.7}$$

$$m_{enzo} = m_{\mathrm{cgs}} / (\mathbb{R} * \mathbb{L}^3) \tag{C.8}$$

Equations (C.1) to (C.8) are not independent and from dimensional analysis it follows that $\mathbb{G} = \mathbb{G}_0 * \mathbb{L} * \mathbb{R}$. Therefore, equations (C.1), (C.2) and (C.4) completely define the scaling relations as all other scalings can be computed as compositions of them, however, we list the complete scaling relations for convenience. Usually, we omit the subscript *cgs* but use it here for unambiguousness. Dimensional analysis immediately shows that $\sqrt{\mathbb{L}/\mathbb{G}} = \mathbb{T}$, $\sqrt{\mathbb{L}\mathbb{G}} = \mathbb{V}$, $\mathbb{L}\mathbb{G} = \mathbb{E}$ and $\mathbb{R}\mathbb{L}^3 = \mathbb{M}$.

To be complete, we also repeat the scaling factors for transforming cooling and heating rates as described and calculated in Section (6.2).

$$\mathbb{C} = \frac{\mathbb{L}^2}{\mathbb{T}^3\mathbb{R}} m_h^2 \tag{C.9}$$

$$\mathbb{H} = \frac{\mathbb{L}^2}{\mathbb{T}^3} m_h \tag{C.10}$$

Bibliography

O. Agertz, G. Lake, R. Teyssier, B. Moore, L. Mayer, and A. B. Romeo. Large scale galactic turbulence: can self-gravity drive the observed HI velocity dispersions? *ArXiv e-prints*, October 2008.

E. Audit and P. Hennebelle. Thermal condensation in a turbulent atomic hydrogen flow. *Astron. & Astrophys.*, 433:1–13, April 2005. doi: 10.1051/0004-6361:20041474.

C. M. Baugh. A primer on hierarchical galaxy formation: the semi-analytical approach. *Reports on Progress in Physics*, 69:3101–3156, December 2006. doi: 10.1088/0034-4885/69/12/R02.

F. Bertoldi and C. F. McKee. Pressure-confined clumps in magnetized molecular clouds. *Astrophys. J.*, 395:140–157, August 1992. doi: 10.1086/171638.

S. Bonazzola, J. Heyvaerts, E. Falgarone, M. Perault, and J. L. Puget. Jeans collapse in a turbulent medium. *A&A*, 172:293–298, January 1987.

W. B. Bonnor. Boyle's Law and gravitational instability. *Mon. Not. R. Astron. Soc.*, 116:351–+, 1956.

T. L. Bourke, P. C. Myers, G. Robinson, and A. R. Hyland. New OH Zeeman Measurements of Magnetic Field Strengths in Molecular Clouds. *Astrophys. J.*, 554:916–932, June 2001. doi: 10.1086/321405.

J. Boussinesq. Théorie de l'Écoulement Tourbillant. *Mem. PrÃ©sentÃ©s par Divers Savants Acad. Sci. Inst. Fr.*, 23:46–50, 1877.

G. L. Bryan, M. L. Norman, J. M. Stone, R. Cen, and J. P. Ostriker. A piecewise parabolic method for cosmological hydrodynamics. *Computer Physics Communications*, 89:149–168, August 1995.

R. Cen and J. P. Ostriker. Galaxy formation and physical bias. *Astrophys. J., Lett.*, 399: L113–L116, November 1992. doi: 10.1086/186620.

G. Chabrier. Galactic Stellar and Substellar Initial Mass Function. *PASP*, 115:763–795, July 2003.

S. Chandrasekhar. The Fluctuations of Density in Isotropic Turbulence. *Proceedings of the Royal Society of London. Series A, Mathematical and Physical Sciences (1934-1990)*, 210: 18–25, December 1951a. doi: 10.1098/rspa.1951.0227.

S. Chandrasekhar. The Gravitational Instability of an Infinite Homogeneous Turbulent Medium. *Proceedings of the Royal Society of London. Series A, Mathematical and Physical Sciences (1934-1990)*, 210:18–25, December 1951b. doi: 10.1098/rspa.1951.0228.

D. A. Clarke, J. M. Stone, and M. L. Norman. MHD Jet Simulations in Three Dimensions. In *Bulletin of the American Astronomical Society*, volume 22 of *Bulletin of the American Astronomical Society*, pages 801–+, March 1990.

D. C. Collins and M. L. Norman. Devolopment of an AMR MHD module for the code Enzo. In *Bulletin of the American Astronomical Society*, volume 36 of *Bulletin of the American Astronomical Society*, pages 1605–+, December 2004.

R. M. Crutcher. Magnetic Fields in Molecular Clouds: Observations Confront Theory. *Astrophys. J.*, 520:706–713, August 1999. doi: 10.1086/307483.

R. M. Crutcher, T. H. Troland, A. A. Goodman, C. Heiles, I. Kazes, and P. C. Myers. OH Zeeman observations of dark clouds. *Astrophys. J.*, 407:175–184, April 1993. doi: 10.1086/172503.

A. Dalgarno and R. A. McCray. Heating and Ionization of HI Regions. *Annu. Rev. Astron. Astrophys.*, 10:375–+, 1972. doi: 10.1146/annurev.aa.10.090172.002111.

D. Downes and P. M. Solomon. Rotating Nuclear Rings and Extreme Starbursts in Ultraluminous Galaxies. *Astrophys. J.*, 507:615–654, November 1998. doi: 10.1086/306339.

R. Duerr, C. L. Imhoff, and C. J. Lada. Star formation in the Lambda Orionis region. I - The distribution of young objects. *ApJ*, 261:135–150, October 1982. doi: 10.1086/160325.

R. Ebert. Über die Verdichtung von H I-Gebieten. Mit 5 Textabbildungen. *Zeitschrift fur Astrophysik*, 37:217–+, 1955.

B. G. Elmegreen. Star Formation at Compressed Interfaces in Turbulent Self-gravitating Clouds. *Astrophys. J., Lett.*, 419:L29+, December 1993. doi: 10.1086/187129.

B. G. Elmegreen and Y. N. Efremov. A Universal Formation Mechanism for Open and Globular Clusters in Turbulent Gas. *ApJ*, 480:235–+, May 1997. doi: 10.1086/303966.

A. Favre. Statistical equations of turbulent gases. *SIAM: Problems of hydrodynamics and continuum mechanics*, pages 231–266, 1969.

K. Ferriere. Effect of an ensemble of explosions on the Galactic dynamo. I - General formulation. *Astrophys. J.*, 389:286–296, April 1992. doi: 10.1086/171204.

K. M. Ferrière. The interstellar environment of our galaxy. *Reviews of Modern Physics*, 73: 1031–1066, October 2001.

G. B. Field, D. W. Goldsmith, and H. J. Habing. Cosmic-Ray Heating of the Interstellar Gas. *Astrophys. J., Lett.*, 155:L149+, March 1969.

M. Germano. Turbulence - The filtering approach. *Journal of Fluid Mechanics*, 238:325–336, May 1992.

N. Y. Gnedin, K. Tassis, and A. V. Kravtsov. Modeling Molecular Hydrogen and Star Formation in Cosmological Simulations. *ArXiv e-prints*, October 2008.

P. Goldreich and S. Sridhar. Toward a theory of interstellar turbulence. 2: Strong alfvenic turbulence. *Astrophys. J.*, 438:763–775, January 1995. doi: 10.1086/175121.

P. Goldreich and S. Sridhar. Magnetohydrodynamic Turbulence Revisited. *Astrophys. J.*, 485: 680–+, August 1997. doi: 10.1086/304442.

E. J. Hallman, B. W. O'Shea, J. O. Burns, M. L. Norman, R. Harkness, and R. Wagner. The Santa Fe Light Cone Simulation Project. I. Confusion and the Warm-Hot Intergalactic Medium in Upcoming Sunyaev-Zel'dovich Effect Surveys. *Astrophys. J.*, 671:27–39, December 2007. doi: 10.1086/522912.

P. Hennebelle and E. Audit. On the structure of the turbulent interstellar atomic hydrogen. I. Physical characteristics. Influence and nature of turbulence in a thermally bistable flow. *Astron. & Astrophys.*, 465:431–443, April 2007. doi: 10.1051/0004-6361:20066139.

M. H. Heyer and C. M. Brunt. The Universality of Turbulence in Galactic Molecular Clouds. *Astrophys. J., Lett.*, 615:L45–L48, November 2004. doi: 10.1086/425978.

J. H. Hunter, Jr. The influence of initial velocity fields upon star formation. *Astrophys. J.*, 233: 946–949, November 1979. doi: 10.1086/157457.

R. C. Kennicutt, Jr. The star formation law in galactic disks. *Astrophys. J.*, 344:685–703, September 1989. doi: 10.1086/167834.

R. C. Kennicutt, Jr. Star Formation in Galaxies Along the Hubble Sequence. *Annu. Rev. Astron. Astrophys.*, 36:189–232, 1998a. doi: 10.1146/annurev.astro.36.1.189.

R. C. Kennicutt, Jr. The Global Schmidt Law in Star-forming Galaxies. *Astrophys. J.*, 498: 541–+, May 1998b. doi: 10.1086/305588.

R. S. Klessen, F. Heitsch, and M.-M. Mac Low. Gravitational Collapse in Turbulent Molecular Clouds. I. Gasdynamical Turbulence. *Astrophys. J.*, 535:887–906, June 2000. doi: 10.1086/

308891.

A. Klypin, H. Zhao, and R. S. Somerville. ΛCDM-based Models for the Milky Way and M31. I. Dynamical Models. *Astrophys. J.*, 573:597–613, July 2002. doi: 10.1086/340656.

A. Kolmogorov. The Local Structure of Turbulence in Incompressible Viscous Fluid for Very Large Reynolds' Numbers. *Akademiia Nauk SSSR Doklady*, 30:301–305, 1941.

H. Koyama and S.-I. Inutsuka. Molecular Cloud Formation in Shock-compressed Layers. *Astrophys. J.*, 532:980–993, April 2000. doi: 10.1086/308594.

H. Koyama and S.-i. Inutsuka. An Origin of Supersonic Motions in Interstellar Clouds. *Astrophys. J., Lett.*, 564:L97–L100, January 2002. doi: 10.1086/338978.

A. G. Kritsuk and M. L. Norman. Thermal Instability-induced Interstellar Turbulence. *Astrophys. J., Lett.*, 569:L127–L131, April 2002. doi: 10.1086/340785.

A. G. Kritsuk, P. Padoan, R. Wagner, and M. L. Norman. Scaling laws and intermittency in highly compressible turbulence. In *Turbulence and Nonlinear Processes in Astrophysical Plasmas*, volume 932 of *American Institute of Physics Conference Series*, pages 393–399, August 2007. doi: 10.1063/1.2778991.

P. Kroupa. On the variation of the initial mass function. *MNRAS*, 322:231–246, April 2001.

M. R. Krumholz and C. F. McKee. A General Theory of Turbulence-regulated Star Formation, from Spirals to Ultraluminous Infrared Galaxies. *Astrophys. J.*, 630:250–268, September 2005. doi: 10.1086/431734.

M. R. Krumholz and J. C. Tan. Slow Star Formation in Dense Gas: Evidence and Implications. *Astrophys. J.*, 654:304–315, January 2007. doi: 10.1086/509101.

C. J. Lada and E. A. Lada. Embedded Clusters in Molecular Clouds. *ARA&A*, 41:57–115, 2003. doi: 10.1146/annurev.astro.41.011802.094844.

R. B. Larson. Turbulence and star formation in molecular clouds. *Mon. Not. R. Astron. Soc.*, 194:809–826, March 1981.

J. Lequeux. *The interstellar medium*. The interstellar medium, Translation from the French language edition of: Le Milieu Interstellaire by James Lequeux, EDP Sciences, 2003 Edited by J. Lequeux. Astronomy and astrophysics library, Berlin: Springer, 2005, 2005.

Y. Li, M.-M. Mac Low, and R. S. Klessen. Star Formation in Isolated Disk Galaxies. I. Models and Characteristics of Nonlinear Gravitational Collapse. *Astrophys. J.*, 626:823–843, June 2005. doi: 10.1086/430205.

Y. Li, M.-M. Mac Low, and R. S. Klessen. Star Formation in Isolated Disk Galaxies. II. Schmidt Laws and Efficiency of Gravitational Collapse. *Astrophys. J.*, 639:879–896, March 2006. doi: 10.1086/499350.

M.-M. Mac Low. The Energy Dissipation Rate of Supersonic, Magnetohydrodynamic Turbulence in Molecular Clouds. *Astrophys. J.*, 524:169–178, October 1999. doi: 10.1086/307784.

M.-M. Mac Low and R. S. Klessen. Control of star formation by supersonic turbulence. *Reviews of Modern Physics*, 76:125–194, January 2004.

M.-M. Mac Low, R. S. Klessen, A. Burkert, and M. D. Smith. Kinetic Energy Decay Rates of Supersonic and Super-Alfvénic Turbulence in Star-Forming Clouds. *Physical Review Letters*, 80:2754–2757, March 1998.

A. Maier, L. Iapichino, W. Schmidt, and J. Niemeyer. Adaptively refined large-eddy simulations of a galaxy cluster. *in preparation*, 2008.

C. D. Matzner and C. F. McKee. Efficiencies of Low-Mass Star and Star Cluster Formation. *ApJ*, 545:364–378, December 2000. doi: 10.1086/317785.

C. F. McKee and E. C. Ostriker. Theory of Star Formation. *Annu. Rev. Astron. Astrophys.*, 45: 565–687, September 2007. doi: 10.1146/annurev.astro.45.051806.110602.

C. F. McKee and J. P. Williams. The Luminosity Function of OB Associations in the Galaxy. *Astrophys. J.*, 476:144–+, February 1997. doi: 10.1086/303587.

G. E. Miller and J. M. Scalo. The initial mass function and stellar birthrate in the solar neighborhood. *ApJS*, 41:513–547, November 1979. doi: 10.1086/190629.

H. J. Mo, S. Mao, and S. D. M. White. The formation of galactic discs. *MNRAS*, 295:319–336, April 1998.

J. F. Navarro, C. S. Frenk, and S. D. M. White. The Structure of Cold Dark Matter Halos. *Astrophys. J.*, 462:563–+, May 1996. doi: 10.1086/177173.

J. F. Navarro, C. S. Frenk, and S. D. M. White. A Universal Density Profile from Hierarchical Clustering. *Astrophys. J.*, 490:493–+, December 1997. doi: 10.1086/304888.

M. L. Norman, G. L. Bryan, R. Harkness, J. Bordner, D. Reynolds, B. O'Shea, and R. Wagner. Simulating Cosmological Evolution with Enzo. *ArXiv e-prints*, 705, May 2007.

B. W. O'Shea, G. Bryan, J. Bordner, M. L. Norman, T. Abel, R. Harkness, and A. Kritsuk. Introducing Enzo, an AMR Cosmology Application. *ArXiv Astrophysics e-prints*, March 2004.

E. C. Ostriker, C. F. Gammie, and J. M. Stone. Kinetic and Structural Evolution of Self-gravitating, Magnetized Clouds: 2.5-dimensional Simulations of Decaying Turbulence. *Astrophys. J.*, 513:259–274, March 1999. doi: 10.1086/306842.

P. Padoan and Å. Nordlund. The Stellar Initial Mass Function from Turbulent Fragmentation. *Astrophys. J.*, 576:870–879, September 2002. doi: 10.1086/341790.

P. Padoan, A. Nordlund, and B. J. T. Jones. The universality of the stellar initial mass function. *Mon. Not. R. Astron. Soc.*, 288:145–152, June 1997.

P. Padoan, Å. Nordlund, A. G. Kritsuk, M. L. Norman, and P. S. Li. Two Regimes of Turbulent Fragmentation and the Stellar Initial Mass Function from Primordial to Present-Day Star Formation. *ApJ*, 661:972–981, June 2007a. doi: 10.1086/516623.

P. Padoan, Å. Nordlund, A. G. Kritsuk, M. L. Norman, and P. S. Li. The mass distribution of unstable cores in turbulent magnetized clouds. In B. G. Elmegreen and J. Palous, editors, *IAU Symposium*, volume 237 of *IAU Symposium*, pages 283–291, 2007b. doi: 10.1017/S1743921307001615.

T. Passot and E. Vázquez-Semadeni. Density probability distribution in one-dimensional polytropic gas dynamics. *Phys. Rev. E*, 58:4501–4510, October 1998.

R. R. Rafikov. The local axisymmetric instability criterion in a thin, rotating, multicomponent disc. *Mon. Not. R. Astron. Soc.*, 323:445–452, May 2001. doi: 10.1046/j.1365-8711.2001.04201.x.

J. C. Raymond, D. P. Cox, and B. W. Smith. Radiative cooling of a low-density plasma. *Astrophys. J.*, 204:290–292, February 1976.

J. A. Regan, M. G. Haehnelt, and M. Viel. Numerical simulations of the Lyman α forest - a comparison of GADGET-2 and ENZO. *Mon. Not. R. Astron. Soc.*, 374:196–205, January 2007. doi: 10.1111/j.1365-2966.2006.11132.x.

K. Robinson, L. J. Dursi, P. M. Ricker, R. Rosner, A. C. Calder, M. Zingale, J. W. Truran, T. Linde, A. Caceres, B. Fryxell, K. Olson, K. Riley, A. Siegel, and N. Vladimirova. Morphology of Rising Hydrodynamic and Magnetohydrodynamic Bubbles from Numerical Simulations. *Astrophys. J.*, 601:621–643, February 2004. doi: 10.1086/380817.

A. Rosen and J. N. Bregman. Global Models of the Interstellar Medium in Disk Galaxies. *Astrophys. J.*, 440:634–+, February 1995. doi: 10.1086/175303.

V. S. Safronov. On the gravitational instability in flattened systems with axial symmetry and non-uniform rotation. *Annales d'Astrophysique*, 23:979–+, February 1960.

P. Sagaut. *Large eddy simulation for incompressible flows: An introduction*. The Physics and Chemistry of the Interstellar Medium, by A. G. G. M. Tielens, pp. . ISBN 0521826349. Berlin: Springer-Verlag, 2006., 2006.

E. E. Salpeter. The Luminosity Function and Stellar Evolution. *ApJ*, 121:161–+, January 1955.

M. Schmidt. The Rate of Star Formation. *Astrophys. J.*, 129:243–+, March 1959.

M. Schmidt. The Rate of Star Formation. II. The Rate of Formation of Stars of Different Mass. *Astrophys. J.*, 137:758–+, April 1963.

W. Schmidt, J. C. Niemeyer, and W. Hillebrandt. A localised subgrid scale model for fluid dynamical simulations in astrophysics. I. Theory and numerical tests. *Astron. & Astrophys.*, 450:265–281, April 2006a. doi: 10.1051/0004-6361:20053617.

W. Schmidt, J. C. Niemeyer, W. Hillebrandt, and F. K. Röpke. A localised subgrid scale model for fluid dynamical simulations in astrophysics. II. Application to type Ia supernovae. *Astron. & Astrophys.*, 450:283–294, April 2006b. doi: 10.1051/0004-6361:20053618.

W. Schmidt, C. Federrath, M. Hupp, S. Kern, and J. C. Niemeyer. Numerical simulations of compressively driven interstellar turbulence: I. Isothermal gas. *ArXiv e-prints*, 809, September 2008a.

W. Schmidt, Ch. Federrath, M. Hupp, S. Kern, and J. C. Niemeyer. Numerical simulations of compressively driven interstellar turbulence: I. Isothermal gas. *Astron. & Astrophys. in prep*, 2008b.

J. A. Sellwood and S. A. Balbus. Differential Rotation and Turbulence in Extended H I Disks. *Astrophys. J.*, 511:660–665, February 1999. doi: 10.1086/306728.

Z.-S. She and E. Leveque. Universal scaling laws in fully developed turbulence. *Physical Review Letters*, 72:336–339, January 1994. doi: 10.1103/PhysRevLett.72.336.

P. M. Solomon, A. R. Rivolo, J. Barrett, and A. Yahil. Mass, luminosity, and line width relations of Galactic molecular clouds. *Astrophys. J.*, 319:730–741, August 1987. doi: 10.1086/165493.

V. Springel. Modelling star formation and feedback in simulations of interacting galaxies. *MNRAS*, 312:859–879, March 2000.

V. Springel and S. D. M. White. Tidal tails in cold dark matter cosmologies. *MNRAS*, 307: 162–178, July 1999.

V. Springel, S. D. M. White, A. Jenkins, C. S. Frenk, N. Yoshida, L. Gao, J. Navarro, R. Thacker, D. Croton, J. Helly, J. A. Peacock, S. Cole, P. Thomas, H. Couchman, A. Evrard, J. Colberg, and F. Pearce. Simulations of the formation, evolution and clustering of galaxies and quasars. *Nature*, 435:629–636, June 2005. doi: 10.1038/nature03597.

S. W. Stahler and F. Palla. *The Formation of Stars*. The Formation of Stars, by Steven W. Stahler, Francesco Palla, pp. 865. ISBN 3-527-40559-3. Wiley-VCH , January 2005., January 2005.

J. M. Stone and M. L. Norman. ZEUS-2D: A radiation magnetohydrodynamics code for astrophysical flows in two space dimensions. I - The hydrodynamic algorithms and tests. *Astrophys. J., Suppl.*, 80:753–790, June 1992a. doi: 10.1086/191680.

J. M. Stone and M. L. Norman. ZEUS-2D: A Radiation Magnetohydrodynamics Code for Astrophysical Flows in Two Space Dimensions. II. The Magnetohydrodynamic Algorithms and Tests. *Astrophys. J., Suppl.*, 80:791–+, June 1992b. doi: 10.1086/191681.

J. M. Stone, D. Mihalas, and M. L. Norman. ZEUS-2D: A radiation magnetohydrodynamics code for astrophysical flows in two space dimensions. III - The radiation hydrodynamic algorithms and tests. *Astrophys. J., Suppl.*, 80:819–845, June 1992. doi: 10.1086/191682.

E. J. Tasker and G. L. Bryan. Simulating Star Formation and Feedback in Galactic Disk Models. *Astrophys. J.*, 641:878–890, April 2006. doi: 10.1086/500567.

E. J. Tasker and G. L. Bryan. The Effect of the Interstellar Model on Star Formation Properties in Galactic Disks. *Astrophys. J.*, 673:810–831, February 2008. doi: 10.1086/523889.

A. G. G. M. Tielens. *The Physics and Chemistry of the Interstellar Medium*. The Physics and Chemistry of the Interstellar Medium, by A. G. G. M. Tielens, pp. . ISBN 0521826349. Cambridge, UK: Cambridge University Press, 2005., September 2005.

A. Toomre. On the gravitational stability of a disk of stars. *Astrophys. J.*, 139:1217–1238, May 1964.

E. Vazquez-Semadeni. Hierarchical Structure in Nearly Pressureless Flows as a Consequence of Self-similar Statistics. *Astrophys. J.*, 423:681–+, March 1994. doi: 10.1086/173847.

E. Vazquez-Semadeni and A. Gazol. Gravitational instability in turbulent, non-uniform media. *A&A*, 303:204–+, November 1995.

E. Vázquez-Semadeni, J. Ballesteros-Paredes, and R. S. Klessen. A Holistic Scenario of Turbulent Molecular Cloud Evolution and Control of the Star Formation Efficiency: First Tests. *Astrophys. J., Lett.*, 585:L131–L134, March 2003. doi: 10.1086/374325.

E. Vázquez-Semadeni, G. C. Gómez, A. K. Jappsen, J. Ballesteros-Paredes, R. F. González, and R. S. Klessen. Molecular Cloud Evolution. II. From Cloud Formation to the Early Stages of Star Formation in Decaying Conditions. *Astrophys. J.*, 657:870–883, March 2007. doi: 10.1086/510771.

E. Vazquez-Semadent, T. Passot, and A. Pouquet. A turbulent model for the interstellar medium. 1: Threshold star formation and self-gravity. *Astrophys. J.*, 441:702–725, March 1995. doi: 10.1086/175393.

K. Wada, G. Meurer, and C. A. Norman. Gravity-driven Turbulence in Galactic Disks. *Astrophys. J.*, 577:197–205, September 2002. doi: 10.1086/342151.

P. Wang, T. Abel, and W. Zhang. Relativistic Hydrodynamic Flows Using Spatial and Temporal Adaptive Structured Mesh Refinement. *Astrophys. J., Suppl.*, 176:467–483, June 2008. doi: 10.1086/529434.

J. P. Williams, L. Blitz, and C. F. McKee. The Structure and Evolution of Molecular Clouds: from Clumps to Cores to the IMF. *Protostars and Planets IV*, pages 97–+, May 2000.

M. G. Wolfire, D. Hollenbach, C. F. McKee, A. G. G. M. Tielens, and E. L. O. Bakes. The neutral atomic phases of the interstellar medium. *Astrophys. J.*, 443:152–168, April 1995. doi: 10.1086/175510.

M. G. Wolfire, C. F. McKee, D. Hollenbach, and A. G. G. M. Tielens. Neutral Atomic Phases of the Interstellar Medium in the Galaxy. *Astrophys. J.*, 587:278–311, April 2003. doi: 10.1086/368016.

P. Woodward and P. Colella. The numerical simulation of two-dimensional fluid flow with strong shocks. *Journal of Computational Physics*, 54:115–173, April 1984.

H. Xu, D. C. Collins, M. L. Norman, S. Li, and H. Li. A Cosmological AMR MHD Module for Enzo. In *First Stars III*, volume 990 of *American Institute of Physics Conference Series*, pages 36–38, March 2008. doi: 10.1063/1.2905583.

Acknowledgment

To begin with, I am grateful to Professor Jens C. Niemeyer for giving me the opportunity to work in the extraordinary field of numerical astrophysics and the unique surroundings of his group. His exceptional knowledge of physics gave me a jump start into the project and his commitment to the Research Training Group (RTG)[a] created a solid framework in which this thesis could thrive.
I like to thank the assistant to the Professor, Wolfram Schmidt, for sharing some of his insights on the tremendous field of turbulence research and the explanations of his understanding of numerical simulations. Most of the conceptual work as well as large parts of the numerical implementation of the subgrid-scale model, presented and used in this thesis, are the result of Dr. Schmidt's enduring work.
Many thanks to Luigi Iapichino for always having a minute or two to discuss a problem at hand. I am indebted to him for giving me a handle on the Enzo code in the first place and for discussing particularities along all the way. Moreover, his professional as well as personal experience has always been a firm guideline.

Special thanks to my fellow colleagues at the office who have also become friends over the years. A lot of the original work on the tools to analyze our simulations has been developed together with Christoph Federrath during his diploma time in Würzburg. The first year team was completed by Melanie Keller and Andreas Maier. Continuing as well as new projects with Franco Ciaraldi-Schoolmann, Markus Niklaus, Sebastian Kern and lately Daniel Seifried enriched our group with new personalities as well as a huge diversity of knowledge. Especially, the late night poker sessions, political discussions and the broad spectrum of office moods, form highly professional tension to hilarious insanity, have been welcome diversions not only during long coding days.

Of course our hydro group does not exclusively comprise all people which have directly and indirectly contributed to this work. I want to particularly thank Felix Spanier and Aleksandar Rakić from the department of astrophysics for many discussions on professional and personal topics as well as for sharing their expertise and experience with me.

This work was funded and carried out in the framework of the Research Training Group (GK1147/1). I am grateful to the Deutsche Forschungsgemeinschaft for supporting my dissertation project as well as the projects of fellow colleagues, astrophysicists ans particle physicists. The Research Training Group has been an extraordinary institution which not only advanced the cross-topic exchange of knowledge but also enabled its students to attend outstanding programs.
Here, I like to thank the organizing committee of the Kavli Institute of Theoretical Physics (KITP) Program *Star Formation Through Cosmic Time*, Tom Abel, Alyssa Goodman, Chris McKee and Paolo Padoan, for inviting me to participate in the program and providing so many

[a] Deutsche Forschungsgemeinschaft, DFG, GK1147/1

new ideas. Especially, I like to express my gratitude to Alexei Kritsuk, Simon Glover, Patrick Hennebelle, David Collins, Mark Krumholz and Peng Weng for sharing their expertise and discussing a broad variety of problems.

Moreover, I like to thank Ralf Klessen and his team for several invitations to Heidelberg, interesting discussions promoting my work and the continuous interest on the progress of my dissertation. Particularly, the exchange of ideas with Hsiang-Hsu Wang has been of great mutual advantage.

Additionally, this work is based on different numerical frameworks. Many people work to maintain and advance these frameworks. My special thanks go to the entire Enzo team, but especially to Brian O'Shea for continuously answering question on the Enzo mailing list, to Elizabeth Tasker for providing some insights into her galaxy simulation coding and to Yuexing Li for providing the initial condition generator code.

After my work is done up to the point that the research for this thesis is completed, I am grateful to the members of the project evaluating RTG committee Jens Niemeyer, Karl Mannheim and Christian Klingenberg as well as to the referees of this work for their time and efforts assessing my performance.

Per aspera ad astra